An Automated Sunspot Identification and Tracking Algorithm to Investigate the Rotation of Sunspots

Charlotte Victoria Proverbs

A thesis submitted in partial fulfilment
of the requirements for the degree of
Doctor of Philosophy

Jeremiah Horrocks Institute for Mathematics, Physics and Astronomy
University of Lancashire

September 2025

Declaration

Type of Award: Doctor of Philosophy

School: Engineering and Computing

I declare that while registered as a candidate for the research degree, I have not been a registered candidate or enrolled student for another award of the University or other academic or professional institution.

I declare that no material contained in the thesis has been used in any other submission for an academic award and is solely my own work.

No proof-reading service was used in the compilation of this thesis.

Charlotte Victoria Proverbs

September 2025

Abstract

Sunspots are areas in the Sun's photosphere where the intense magnetic field can pass through from the solar interior, where it is generated, into the Sun's atmosphere where it dominates the dynamics of the solar corona. Motions of sunspots cause the coronal magnetic field to become deformed with the effect that energy can be stored in the coronal magnetic field. This energy can be released through eruptive events such as solar flares. Sunspots are known to rotate about their umbral centres. This rotation contributes to the build-up of energy within an active region that can be released during an eruptive solar event, such as a solar flare. This thesis aims to investigate the relationship between rotational forms of sunspot dynamics by conducting a statistical survey of sunspot rotation and sunspot pair corotation.

To generate the statistical sample, a fully automatic sunspot identification and tracking method is developed. This method is tested on a previously analysed four-month dataset that was generated using a semi-automatic sunspot rotation tool. The new method has many advantages over the previous method, as the automatic nature enables more sunspots to be systematically identified, and these sunspots are identified earlier and tracked for longer. The new method is able to identify when sunspots are undergoing structural changes, such as splitting or mergers, and track these variations successfully.

The method is applied to a twelve-month series of observations covering the rise-phase and initial peak of solar cycle 25. Within the sample there are 560 sunspots across 189 active regions, and 71% of active regions generate sufficient energy due

to sunspot rotation to account for the radiated flare energy, with 32% of active regions generating an excess of 10 times the amount of energy required for the flaring activity. The method is also applied to two case-study active regions that triggered intense space weather events in 2024, AR 13664 and AR 13842. These active regions were found to build-up rotation energy differently to each other, with AR 13664 requiring the contribution from all sunspots within the active region, and AR 13842 being dominated by the rotation profile of the largest sunspot.

A method to measure the angular variation between sunspot pairs is developed, and the method is applied to all active regions within the four-month and twelve-month samples, and the two case study active regions. It is found that 49% of active regions exhibit more than 180° of corotation, and the net active region corotation was found to have a positive correlation with the radiated flare energy.

The work in this thesis shows that sunspot rotation can generate enough energy within an active region to account for flaring activity, and suggests that the level of corotation present in an active region correlates with the volume of flaring activity.

Contents

List of Tables

List of Figures

Acknowledgements

I have been fortunate to receive an incredible amount of support throughout my PhD journey, both academically and otherwise. Firstly I would like to thank my supervisor, Daniel Brown, for his guidance and encouragement throughout my studies, alongside answering any and every question I could throw his way. I would also like to thank the STFC for the financial support throughout the PhD.

I'd also like to thank the friends that I have made within the Jeremiah Horrocks Institute, specifically Simon Ebo, Ruth Hyndman, Josh Stanway, Matt Teasdale, and Ethan Carter. From kitchen trips to lunch hours that engulfed entire afternoons, this journey wouldn't have been half as enjoyable without your company.

I am also thankful to my father, for inspiring me to pursue research, and my mother and sister, for lightening my mood and providing many words of encouragements throughout the years. Finally, I would like to thank my partner, Thomas Say, for grounding me when I felt overwhelmed, and for his kindness, understanding, and patience throughout this journey.

Chapter 1

Introduction

Sunspots are darker and cooler regions on the solar photosphere, occurring where the magnetic field protrudes from the solar interior. They have been observed to rotate about their umbral centres at approximately one degree per hour for several days, occasionally leading to an eruption or a solar flare (Sturrock et al., 2015; Brown & Walker, 2021; Brown et al., 2003). In this thesis we design a fully automatic method to measure sunspot dynamics, including rotation. This chapter defines what sunspots are and the connection sunspots have to solar events, such as solar flares. The objective of the work and the thesis structure is discussed.

1.1 Solar Structure

The Sun is a giant ball of plasma that comprises mostly of hydrogen (92%) and helium (8%). The solar interior can be separated into three regions: the core, the radiative zone, and the convection zone. The core of the Sun extends from the centre to $0.25\mathrm{R}_{\odot}$ and has a typical temperature of 15 million degrees K. The nuclear energy generated by nuclear fusion in the core 'leaks' continuously outwards into the radiative zone. The radiative zone ranges between $0.25 - 0.7\mathrm{R}_{\odot}$, and the predominant method of energy transport is radiation. The photons within this

region are absorbed and re-emitted continually, so it can take millions of years for the energy to travel outside of this zone. The density of the plasma drops over the range of the radiative zone, causing the temperature to also decrease. At the base of the radiative zone the temperature is 7 million degrees K, and at the top of the radiative zone the temperature is 2 million degrees K.

In-between the radiative zone and the convection zone is the tachocline. This is a strong shear layer where much of the Sun's large-scale magnetic field is believed to be generated (Priest, 2014). In the convection zone the dominant form of energy transport is convection. Hot plasma rises in convection cells to the surface, where it cools and drops back down. The temperature of the convection zone is 2 million degrees K at the base, decreasing to 5700° K at the top. The convective motions are visible on the photosphere of the Sun in the form of granules. The convection zone is the outer-most internal layer of the Sun. The photosphere is the Sun's visible surface layer, and is a few kilometres thick (Priest, 2014). It is on this layer that features such as granules, pores, and sunspots can be observed.

1.2 Sunspots

Sunspots represent regions where the internal solar magnetic field protrudes through the photosphere. The intense magnetic field restricts the convection cells, causing the region to become cooler and appear darker. The umbra is the darker central region of a sunspot, and the penumbra is the lighter annulus surrounding the umbra. A light bridge is a narrow, bright feature that can form across the umbra of a sunspot, occasionally extending into the penumbra. These features are illustrated in Figure 1.1. Sunspot light bridges form during the merging and fragmentation of umbral regions. These regions have a weaker and more horizontal magnetic field than the surrounding umbra (Beckers & Schröter, 1969), and are convective in origin (Lagg et al., 2014). Smaller umbral regions with little to no penumbra are called pores.

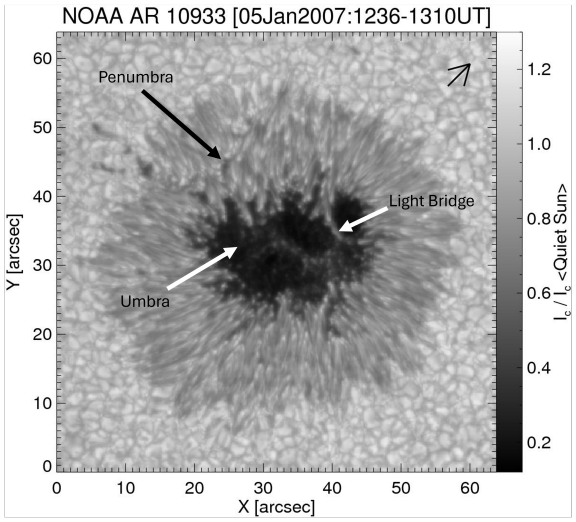

Figure 1.1: Continuum intensity image of a sunspot observed by Hinode SOT-SP. The locations of the umbra, penumbra and a light bridge are highlighted. The larger arrow points to disc centre. Adapted from Tiwari et al. (2015).

Figure 1.3 shows the difference between a sunspot and a pore.

1.2.1 Sunspot Lifecycle

The formation of a sunspot begins with the coalescence of pores and small magnetic flux tubes into larger pores (McIntosh, 1981; Thomas & Weiss, 2012). Once these pores reach a sufficient level of magnetic flux, typically $\sim 10^{20}$ Mx (Leka & Skumanich, 1998), the penumbra begins to form and the pore becomes a sunspot. The penumbra can form in less than 20 minutes, but the sunspot will continue to grow for a few days.

The decay phase of a sunspot begins almost immediately after the growth phase ends, and is much longer. A study of over 36,000 sunspot groups by Howard (1992) (using Mount Wilson observations from 1917-1985) found the daily changes in sunspot area for growing regions was 502% day^{-1}, whilst the daily change was -45% day^{-1} for decaying groups. Sunspot lifetimes also range broadly, with some smaller sunspots existing for a few hours, and some of the largest sunspots lasting

for multiple solar rotations. The leading sunspots within an active region tend to achieve a stable, round shape, and can exist for several months, whilst the smaller following sunspots do not achieve this, and can last for a few days. The lifetime (T) of a larger sunspot is typically proportional to the maximum area of the sunspot (A_{max}), and follow the Gnevyshev—Waldmeier rule

$$A_{max} = D_{GW}T \tag{1.1}$$

where $D_{GW} \simeq 10 \times 10^{-6} A_{\odot/2}$ day^{-1}, and $A_{\odot/2}$ is the surface area of a solar hemisphere (Gnevyshev, 1938; Waldmeier, 1955). This linear relationship was confirmed and refined by Petrovay & van Driel-Gesztelyi (1997) ($D_{GW} = (10.89 \pm 0.18) \times 10^{-6} A_{\odot/2}$) and more recently by Nagovitsyn, Ivanov & Skorbezh (2019) ($D_{GW} = (13.0 \pm 1.1) \times 10^{-6} A_{\odot/2}$).

The decay phase of a sunspot can also be separated between the leading and following sunspots. Following sunspots tend to fragment rapidly as they are torn apart due to convection a few days after formation, following the appearance of bright dots within the umbra (Zwaan, 1968). Leading sunspots tend to follow a gradual decay process, where the sunspot slowly shrinks in size due to the gradual dissipation of magnetic flux to the surrounding area. This continues until the sunspot becomes a pore or fragments (Thomas & Weiss, 2012).

As a sunspot approaches the solar limb, the limb-side penumbra is broader than the disc-side penumbra, this is because the sunspot appears depressed in comparison to the quiet Sun. This effect is the Wilson depression (Wilson & Maskelyne, 1774). Within the sunspot the temperature and gas pressure are lower, leading to a lower opacity (Löptien et al., 2018). This depression can be specified using the geometric depth (z_W) as a function of the optical depth (τ_{500}) and the horizontal position within the sunspot, and is currently estimated to be in the range 500-700 km (Thomas & Weiss, 2012; Löptien et al., 2020).

1.2.2 Sunspot Magnetic Field

Sunspots were discovered to be magnetic phenomena by Hale (1908). There are two theoretical models of the magnetic structure of sunspots, the monolithic model and the cluster model. Both of these models are illustrated in Figure 1.2. The monolith model (Cowling, 1946) assumes the sunspot is a single, monolithic magnetic flux tube above and below the solar surface, whereas the cluster model (Parker, 1979) (also known as the jellyfish or spaghetti model) assumes that the field splits into multiple flux tubes that spread out just below the photosphere. Observational and theoretical works have attempted to verify both of these methods, but they remain inconclusive (Cho, Chae & Madjarska, 2021). The magnetic fields of sunspots are twisted due to sunspot motions such as rotation, and the umbral magnetic field is vertical, with the penumbral magnetic field becoming more horizontal with increased radial distance from the centre of the sunspot. The magnetic field strength ranges between 2.5 and 4 kG within the umbra (Livingston, 2002; Siu-Tapia et al., 2019), and the typical magnetic field strength within the penumbra varies between 1.5-2.5 kG, and drops to 0.5 kG at the outer limits (Lites, Scharmer & Skumanich, 1990). The penumbra has a characteristic pattern of bright and dark radial filaments, known as penumbral fibrils (Scharmer et al., 2008). These fibrils last between 0.5-6 hours and are used to measure the rotation of a sunspot by Walker (2018); Brown & Walker (2021).

Plasma Beta

The plasma beta is the ratio of the plasma pressure to the magnetic pressure, and is given by

$$\beta = \frac{2\mu p_0}{B_0^2} \tag{1.2}$$

where μ is the permeability, p_0 is the plasma pressure, and B_0 is the magnetic field strength (Priest, 2014). If the plasma beta is much smaller than 1, we have a 'low-β' plasma and the magnetic force dominates. In the solar atmosphere, the plasma beta

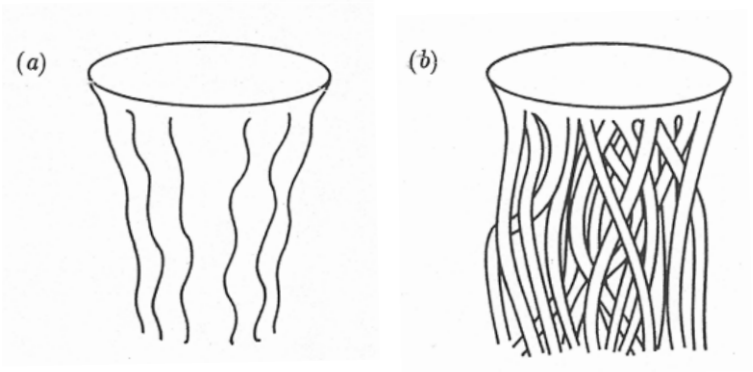

Figure 1.2: Sketch of the monolith (a) and cluster (b) models of a sunspot (from Thomas & Weiss (1992)).

decreases rapidly with height, and can be given by

$$\beta = 3.5 \times 10^{-21}\ n_0\ T_0\ B_0^{-2} \tag{1.3}$$

In the photosphere the plasma beta is high, so the plasma pressure dominates the magnetic field. The magnetic fields of sunspots and their active regions are rooted in the photosphere, but extend into the low-β corona. Surface flows and flux emergence drive the evolution of the photospheric magnetic field (e.g. sunspot rotation), and builds up free energy in the corona that can power solar flares via magnetic reconnection (Liu et al., 2016; Priest & Forbes, 2002; Su et al., 2013).

Magnetic Helicity

Magnetic helicity measures the twisting and kinking of a flux tube around itself, referred to as self-helicity, and the linkage between different flux tubes, referred to as mutual helicity (Priest, 2014). The free magnetic energy (or magnetic energy) is the excess energy of a magnetic configuration in comparison to the minimum-energy state (Régnier & Priest, 2007). The motion of magnetic footpoints in the photosphere (such as sunspots) can build-up the magnetic helicity within an active region until it is ejected by magnetic eruptions (Priest, 2014). The magnetic helicity

in a closed volume (V), bounded by a surface (S) is

$$H_0 = \int_V \mathbf{A} \cdot \mathbf{B} \; dV \tag{1.4}$$

where $\mathbf{A}$ is the vector potential, and H_0 is gauge invariant if the volume is mathematically closed, but not if magnetic field lines enter or leave it (Priest, 2014). The rate of change of magnetic helicity is

$$\frac{dH}{dt} = -2 \int_V \mathbf{E} \cdot \mathbf{B} \; dV + 2 \int_S \mathbf{A}_p \times \mathbf{E} \cdot \mathbf{n} \; dS \tag{1.5}$$

where a gauge ($\mathbf{A}_p$) has been chosen that satisfies $\nabla \cdot \mathbf{A}_p = 0$ and has $\mathbf{A}_p \cdot \mathbf{n} = 0$ on S. If the footpoint motions on the surface are considered, this becomes

$$\frac{dH}{dt} = 2 \int \int (\mathbf{B} \cdot \mathbf{A}_p) v_z - (\mathbf{v} \cdot \mathbf{A}_p) B_z \; dxdy \tag{1.6}$$

where the first term represents the effect of the emergence of structures that carry helicity through the surface, and the second term represents the injection by footpoint shuffling of helicity into fields already present in the volume (Priest, 2014).

When considering a plane surface S threaded by the footpoints of N thin flux tubes of magnetic flux $\phi_{m(i)}$, if the motion of each magnetic footpoint consists of a translation and a uniform rotation at a rate ω_i, the rate of helicity change is

$$\frac{dH}{dt} = -\frac{1}{2\pi} \left[\sum_{i=1}^{N} \omega_i F_{m(i)+}^2 \sum_{i=1}^{N} \sum_{j=1}^{N} \dot{\theta}_{ij} F_{m(i)} F_{m(j)} \right] \tag{1.7}$$

where $\dot{\theta}_{ij}$ is the time derivative of the relative angle (θ_{ij}) between footpoints i and j (Berger, 1984). The first term in Equation 1.7 represents the self-helicity of each flux tube due to internal twist, whilst the second term represents the mutual helicity. Sunspot rotation only contributes to the first term, so for the purposes of this thesis (following the work of Walker (2018)) the second term is assumed to be zero. If we assume that flux tubs are straight with uniform twist, the self-helicity of a flux tube can be given by

$$H = \frac{1}{2\pi} \theta \phi^2 \tag{1.8}$$

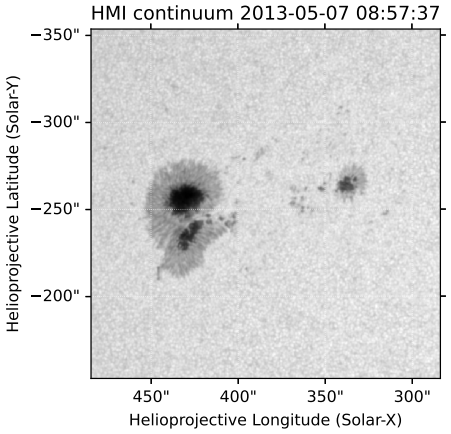

Figure 1.3: SDO/HMI continuum image of the photosphere. There are two sunspots on the left of the image, and a pore on the right of the image.

where θ is the twist (or sunspot rotation), and ϕ is the magnetic flux, implying that the self-helicity can be calculated by measuring the rotation of the magnetic footpoint (the sunspot).

1.2.3 Sunspot Group Classifications

Active regions are groups of sunspots, and they are defined by their magnetic complexity. The Mount Wilson (or Hale et al. (1919)) classification system defines an active region that contains a single sunspot or multiple sunspots of the same polarity as α. Active regions that contain sunspots of opposite polarity are designated β, γ is appended to the above previous classes to indicate a more complex active region, and δ is assigned to active regions that contain sunspots of opposite polarity within the same penumbra. This classification structure is broad enough to cover most active regions that have been observed on the Sun.

1.3 Solar Activity

Solar activity (or solar magnetic activity) is the manifestation of the Sun's magnetic field and includes the emission of electromagnetic radiation, plasma and magnetic flux during events such as coronal mass ejections. Sunspots are an example of solar activity on the photosphere, where the solar magnetic field disrupts convection, cooling parts of the photosphere, resulting in darker areas. This section will discuss the solar cycle and different forms of solar activity.

1.3.1 Solar Cycle

The Sun follows a 22-year cycle of Solar activity, split into two 11-year halves (Figure 1.4). For each 11-year cycle the sunspot number increases very rapidly and falls more slowly, and these variations are accompanied with variations in the latitudinal distribution of sunspots. The Babcock (1961) model of the solar cycle splits the process into five stages, beginning three years before the start of a new solar cycle. Stage one describes an initial dipole field, which is amplified in stage two due to the differential rotation of the Sun. Bipolar magnetic regions form from the rising flux ropes during stage three, and sunspots also form during this stage. The main dipole magnetic field then begins to neutralise and disperse during stage 4, before the dipole field reverses in stage 5 as a result of the foregoing processes. These five stages take around 11 years to complete, the cycle then repeats, completing the full cycle after 22 years. There are three features of the solar cycle that inform the observed evolution of active regions. Most sunspots are latitudinally confined between $\pm 5^{\circ}$ and $\pm 35^{\circ}$, and Spörer's Law states that as the solar cycle develops the average latitude will drift towards the equator (Spörer, 1880). This can be seen in upper panel of Figure 1.4. Leading sunspots are also more inclined to the equator in comparison to the trailing sunspots in the same active region (Joy's law) (Hale et al., 1919), and the polarity of leading sunspots across different hemispheres is

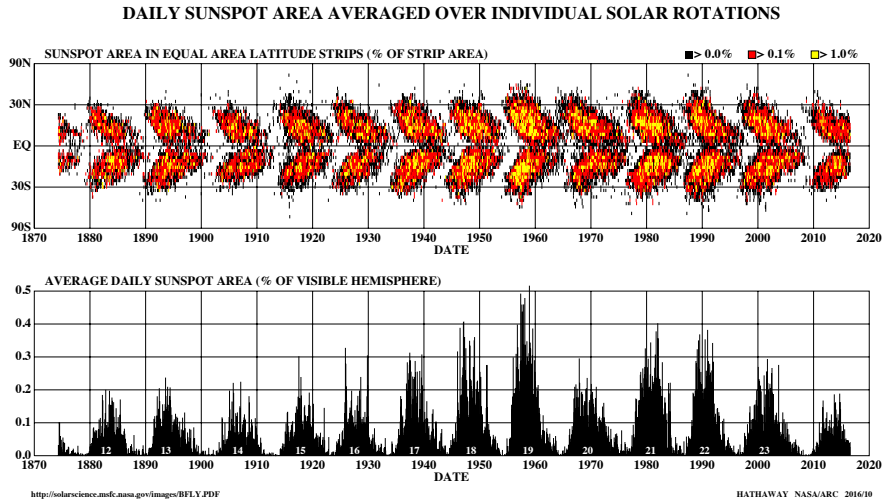

Figure 1.4: A butterfly diagram showing the latitudes of sunspots for each rotation of the Sun since May 1874. Image credit: NASA

always opposite (Hale's law) (Hale & Nicholson, 1925).

1.3.2 Solar Flares and Coronal Mass Ejections

Electromagnetic radiation, plasma and magnetic flux is emitted by the Sun by solar events, causing geomagnetic storms. These storms can be impactful to life on Earth, especially during solar maximum. During these periods, there is an increase in auroral activity and the risk of potential disruption to radio transmissions and power grids. It is currently understood that the complex solar magnetic field is the underlying cause of solar activity, such as sunspots, flares and coronal mass ejections (CMEs). Solar flares and coronal mass ejections can occur from the same active region, however these events do not cause each other, and are most likely triggered by the release of energy from an active region following magnetic reconnection (Webb & Howard, 2012). This work focuses on the energy output from solar flares that are connected to sunspot active regions.

CHAPTER 1

Solar Flares

Solar flares are classified as A, B, C, M or X-Class, based on their peak 1-8 Å flux near Earth, which is measured by the Geostationary Operational Environmental Satellites (GOES) (see section 1.4.2). Each class has a peak flux ten-times larger than that of the previous class. Each class is divided into 9 sub-classes, so an X5 Class flare is 1.25 times larger than an X4 Class flare. Flares are believed to be triggered by magnetic reconnection, and are often accompanied by coronal mass ejections and solar energetic particle events, driving space weather (Schrijver et al., 2011; Aulanier, Janvier & Schmieder, 2012; Masson et al., 2009). Solar flares go through multiple stages during the eruption period, during the pre-flare phase the soft X-Ray intensity increases for tens of minutes. An impulsive stage may occur for 100-1000 seconds, indicated by the appearance of a microwave and hard X-ray burst, before the rise phase begins. This phase typically lasts around 5 minutes, and is signified by a rapid increase in intensity and area of soft X-Ray emission. The coronal plasma is also heated to over 10 million degrees. The main phase consists of the intensity slowly decreasing, this usually lasts around one hour, but can take up to a day (Priest, 2014).

The most intense geomagnetic storm in recorded history was the Carrington Event of September 1859. An X45 class flare occurred on 1 September 1859, and the accompanying coronal mass ejection caused aurora to be viewed in the Northern Hemisphere as far south as the Caribbean (Cliver & Dietrich, 2013). The event also cause telegraph systems to fail, along with electrical fires and a few isolated instances of electric shock (Shea & Smart, 2006). If such an event were to occur in the modern-day, a significant risk would be posed to electrical power utilities and satellite infrastructure (Ritter et al., 2020). Even a minor event, such as the February 2022 geomagnetic storm, caused the loss of thirty-eight SpaceX Starlink satellites. A study by Fang et al. (2022), alongside the SpaceX team, recommended

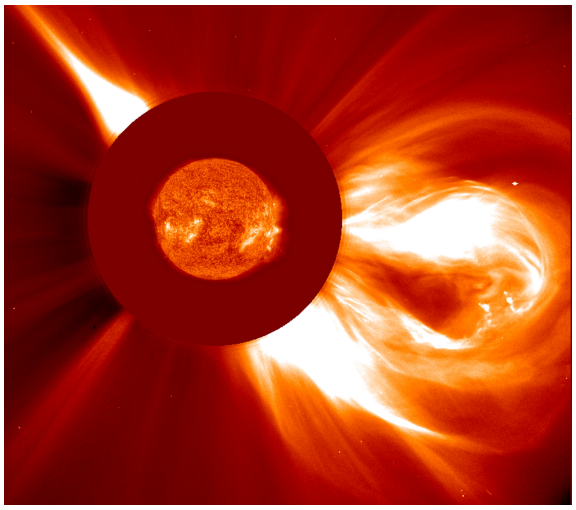

Figure 1.5: A composite image showing the 2 December 2003 CME with an EIT 304 image of the Sun superimposed on a LASCO C2 image showing details in the CME. Image credit: SOHO

to establish alerts and warnings for similar geomagnetic conditions in relation to satellite launches to ensure the events of February 2022 are not repeated. To further understanding and enable the prediction of space weather events, the study of solar activity is required.

Coronal Mass Ejections

Coronal mass ejections are huge eruptions of coronal plasma moving outward into interplanetary space (Foukal, 2004). When twisted flux bundles emerge from the convection zone into the solar atmosphere, they carry currents with them from below the photosphere (Leka et al., 1996). Surface motions cause the system to evolve to a state where stable equilibrium is no longer possible, and the field erupts (Forbes et al., 2006). If the eruption is strong enough, between 2×10^{14} g and 4×10^{16} g of plasma will be ejected into interplanetary space (Kallenrode, 2004). The kinetic energy of a CME is comparable to the energy released by a solar flare, and a CME can carry up to 10^{32} erg (Priest, 2014). CMEs typically have a loop-like structure,

with different types of CMEs including spikes, multiple-spikes, clouds, fans, and streamer blow outs (Howard et al., 1985). An image of a typical CME is shown in Figure 1.5.

There are several basic features of CMEs. The frequency of CMEs varies with the solar cycle, during solar minimum there is typically one CME per week, whereas at solar maximum there can be multiple CMEs per day (Svestka, Jackson & Machado, 1992). CMEs tend to be evenly distributed over both hemispheres, and are most commonly found within $\pm 30^{\circ}$ of the equator, reflecting the latitudinal distribution of sunspots (Burkepile & St. Cyr, 1993). The diameter of a CME can exceed that of the Sun, and the angular width is independent of the solar cycle, with typical values between 20° and 60° (Howard et al., 1985). A statistical study of 19,000 CMEs over solar cycles 23 and 24 found that the vast majority of CMEs had 'intermediate' width (i.e. between 20° and 200°) (Blessy et al., 2024). CME speeds also don't vary with the solar cycle, and can range between 10 km s^{-1} - 2,000 km s^{-1} (Kallenrode, 2004), though wide CMEs (angular width $> 200^{\circ}$) have been found to have much higher speeds than intermediate and narrow CMEs, with 74.19% of wide CMEs having an average speed of greater than 500 km s^{-1} during solar cycle 24, whereas only 14.5% and 10.67% of intermediate and narrow CMEs exceeded this value (Blessy et al., 2024).

1.4 Instrumentation

This section will discuss the different solar observations used to conduct this work. For this work, the Solar Dynamics Observatory Helioseismic and Magnetic Imager (SDO/HMI) is used to observe sunspots, and the Geostationary Operational Environment Satellites (GOES) are used to calculate the bolometric flare energy. The National Oceanic and Atmospheric Administration (NOAA) Solar Region Summary (SRS) database provides the active region data used for this work.

1.4.1 The Solar Dynamics Observatory

The Solar Dynamics Observatory is the main data source for this work, an image of SDO with the instruments labelled is shown in Figure 1.6. The satellite was launched in February 2010 and has been providing continuous data since May 2010. There are three science instruments on SDO, the Helioseismic and Magnetic Imager (HMI), the Atmospheric Imaging Assembly (AIA), and the Extreme Ultraviolet Variability Experiment (EVE). HMI observes the oscillations and the magnetic field at the photosphere, AIA observes the solar corona in seven EUV and three UV/visible channels, and EVE measures the EUV irradiance of the Sun (Scherrer et al., 2012; Lemen et al., 2012; Woods et al., 2012).

The Helioseismic and Magnetic Imager

Data from SDO/HMI will be used for this work, which measures the 6173 Å Fe I absorption line to produce continuum intensity, Doppler shift and magnetic field data (Wachter et al., 2012; Schou et al., 2012). Specifically, the focus will be on the continuum data, which produces 4096×4096 pixel full disc images every 45 seconds at a spatial resolution of 0.5 arcseconds per pixel (Scherrer et al., 2012). The use of the SDO/HMI data will allow multiple long periods of data to be analysed from varying points in the solar cycle, providing an understanding of how sunspot dynamics impact solar activity.

1.4.2 The Geostationary Operational Environment Satellite

The GOES satellites are used throughout this work to estimate the bolometric energy output of solar flares in relation to their assigned active regions. The GOES mission began in 1975 and has been monitoring the irradiance of the Sun ever since. The GOES-15 satellite is used for the 2013 data, and the GOES-17 and GOES-18 satellites are used for the 2023 - 2024 datasets. The GOES missions measure the

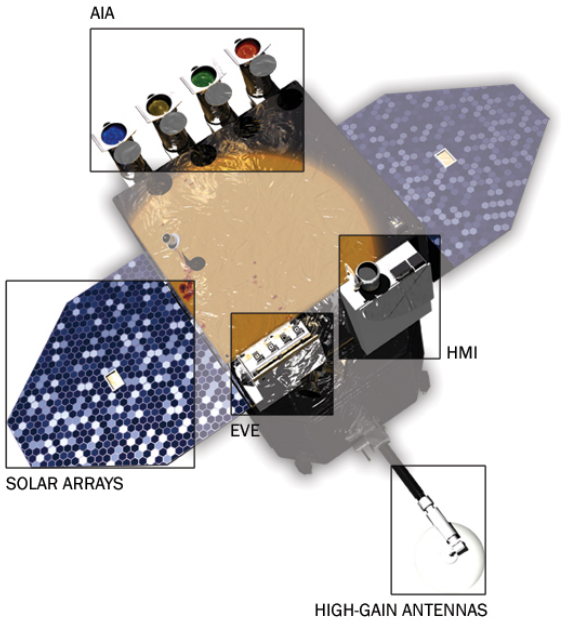

Figure 1.6: Image of the Solar Dynamics Observatory with the three instruments labelled. The Helioseismic and Magnetic Imager is located on the right side of the observatory. Image credit: NASA.

soft X-Ray measurements in two broadband energy ranges ($0.5 - 4$ Åand $1 - 8$ Å), and these measurements are used to categorise flares by their peak flux.

1.5 Sunspot Rotation

Sunspot dynamics are intrinsically linked to variations in the atmospheric magnetic field and have the ability to build-up energy into active regions during the lead up to solar events, such as coronal mass ejections and solar flares (Kumar et al., 2013; Vemareddy, Cheng & Ravindra, 2016). These dynamics can include sunspot rotation (Brown & Walker, 2021), pair interactions, shear (Kazachenko et al., 2009) and structural changes including splitting and merging (Louis et al., 2014).

Sunspots have been observed to rotate about their umbral centres at a rate of a few degrees per hour (Brown et al., 2003). Evidence of sunspot rotation was first discovered by Evershed (1910), and since this time multiple case studies have investigated this form of sunspot dynamics, such as Brown et al. (2003); Brown & Walker (2021); Li & Liu (2015); Yan & Qu (2007). As sunspots form the footpoints of magnetic flux tubes, observing and tracking these dynamics can provide an insight to the motions of the flux tubes. The rotation of the sunspot, or the magnetic footpoint, could add or subtract twist into the flux tube, which would add or remove magnetic helicity from the system (Longcope & Welsch, 2000). This motion can increase the stored energy of the active region, which can be released in the form of solar events such as solar flares. The study of sunspot rotation is therefore crucial to understand the development of the magnetic conditions required for these events (Sturrock et al., 2015).

The relationship between different types of solar activity and sunspot rotation has been investigated, with relations identified across limited case studies such as Li & Liu (2015) and Grimes, Pintér & Morgan (2020). Both studies found that solar flares were most likely to occur as the sunspot rotation rate reached its maximum,

implying that the latter could be the source of the build-up of magnetic energy in the corona itself, caused by the large-scale twisting of magnetic flux tubes (Yan, Qu & Kong, 2008). Sunspot rotation has also been linked to coronal mass ejections through individual case studies of CMEs and a related active region, for example Yan et al. (2012); Török et al. (2013); Yan et al. (2018).

Some statistical studies investigating the relationship between sunspot rotation and solar events have been conducted, however the literature in this area is relatively sparse. Yan, Qu & Xu (2008) statistically analysed 182 rotating sunspots using data from SOHO/MDI, TRACE and Hinode from December 1996 - December 2007. This study found that there were 12% more rotating sunspots in the northern hemisphere than in the southern hemisphere, and that there were more rotating sunspots during the maximum of solar cycle 23.

Another study by Li & Zhang (2009) chose 20 flare events that showed flare ribbons sweeping across sunspot umbra to analyse. They found that the main sunspot within each region rotated in all cases, and the secondary sunspot rotated in 19 of the cases. The average total rotation of the systems was 193°, and the shear of the sunspots was opposite to the rotational direction of the main sunspot in 14 cases.

Zhu, Alexander & Tian (2012) calculated the sunspot rotation from SOHO/MDI magnetograms using the DAVE technique (Schuck, 2006) on 132 sunspots across 95 active regions. This study found that out of the 82 emerging sunspots, 63 sunspots exhibit a rotation velocity of $> 0.4°\mathrm{h}^{-1}$, and out of the 50 non-emerging sunspots 14 exhibited $> 0.4°\mathrm{h}^{-1}$ rotation velocity, implying that there is a relationship between flux emergence and sunspot rotation.

Walker (2018) conducted two statistical surveys on sunspot rotation, one studying active regions that released X-Class flares, and another that analysed a continuous four-month period from 1 May 2013 - 31 August 2013. The X-Class sample

contained 76 sunspots from 26 active regions, and the four-month sample contained 56 sunspots from 38 active regions. This study found that, on average, the bolometric flare radiation is 60% of the sunspot rotation energy, suggesting that sunspot rotation is generally able to generate sufficient energy to account for the flaring activity within an active region.

1.5.1 Sunspot Corotation

Flux tubes connect sunspots within an active region, so studying how sunspots are interacting can provide an insight into the overall variations within the active region magnetic structure. Recent studies have investigated how the footpoints of flux tubes (including sunspots) vary during the evolution of an active region (Zhang et al., 2025), and Dhakal & Zhang (2024) found that bipoles that emerged around existing bipoles and approached the magnetic pole of opposite polarity would form strong gradient polarity inversion lines and would increase the shearing motion and flux cancellation of the active region. The shearing and orbital motions of magnetic bipoles within an active region have been found to facilitate the magnetic reconnection that formed a flare arcade beneath a flux rope before the onset of a coronal mass ejection (James et al., 2017, 2020). It is theorised that coronal mass ejections are driven by the ideal magnetohydrodynamic torus instability (Kliem & Török, 2006). There is a critical height at which the torus instability drives coronal mass ejections, and this varies during the lifetime of an active region. A study of 42 active regions by James, Williams & O'Kane (2022) found that the rate of CMEs increase when the critical height is rising, and the critical height is proportional to the separation of magnetic polarities. This relationship was confirmed by a statistical study of over 20,000 magnetograms, which found that the critical height (h_c) is

$$h_c = 0.5d + 7.35 \tag{1.9}$$

where d is the separation between opposite magnetic polarities (James et al., 2024). This work also found that the logarithm of magnetic flux is proportional to the logarithm of polarity separation, following the power law $\Phi \sim d^{1.14}$ for active regions (James et al., 2024).

For this work we define sunspot corotation as the movement of a sunspot pair about each other. We do not consider the sunspot polarity in this definition. By measuring this metric we can investigate the overall dynamics of an active region, and determine if the overall strain that the twisting, wrapping, and reconnection of flux tubes builds in an active region relates to the amount and intensity of solar activity.

Determining how different sunspot dynamics can impact and drive solar activity will improve the understanding of the solar magnetic field, which will in turn provide more information about the mechanisms that drive space weather. Intense solar activity, and the resulting space weather, can cause communication systems and satellites to fail, with obvious detriments to modern society (Siscoe, 2000). A thorough understanding of the origins of space weather and solar events could aid in the prediction and preparation for intense space weather storms, which would reduce the overall noticeable impact on Earth (Singh & Singh, 2003). To fully determine whether sunspot dynamics consistently provide enough energy build-up within an active region to account for the flaring activity, a statistical survey is required. The majority of studies into sunspot dynamics and flaring activity focus on case study active regions, whereas the analysis of a continuous series of data, including active regions with no or little flaring activity, would provide a more robust correlation determination of this relationship.

1.6 Energy Balance

The energy within a solar active region can be balanced in terms of input and output processes by

$$E_{rot} + E_{shear} + E_{emerge} + E_{other} = E_{fl-rad} + E_{CME} + E_{c-heat} + E_{other} \quad (1.10)$$

where E_{rot} is the energy built-up by sunspot rotation, E_{shear} is the energy input by shearing motions, E_{emerge} is the energy input by flux emergence, and E_{other} is the energy input by other sources. E_{fl-rad} is the energy output from flare radiation, E_{CME} is the energy output from CMEs, E_{c-heat} is the energy output from coronal heating, and E_{other} is the energy output from other sources (Walker, 2018).

The work undertaken in this thesis works towards balancing the input and output of energy from a solar active region. Equation 1.10 lists some of the possible input and output processes (Walker, 2018). This work only considers the energy built-up in an active region due to sunspot rotation (E_{rot}), and the energy output by flare radiation (E_{fl-rad}).

1.7 Thesis Structure

This work intends to conduct a statistical analysis of sunspot dynamics, specifically rotation, and their role in providing the build-up of energy within an active region that could be released during a solar flare.

In this thesis, a fully automatic method to identify and track sunspots is developed using data from the Solar Dynamics Observatory's Helioseismic and Magnetic Imager. Chapter 2 will describe this automatic method and also provide an overview of the methods used by Walker (2018) to calculate the active region energy due to sunspot rotation, and the estimated bolometric flare energy output of the active region from GOES time series data.

Chapter 3 will compare the results of the fully automatic sunspot identification method (the Proverbs method), with a previous semi-automatic method developed by Walker (2018) (the Walker method). The test period covers a four-month sample of active regions, running from 1 May - 31 August 2013. The number of sunspots identified per active region will be discussed, and differences between the sunspot duration and areas will also be compared. The rotation of each sunspot identified by both methods is calculated, and the differences between the rotation profiles are highlighted.

In chapter 4 the Proverbs method is applied to a twelve-month continuous sample of active regions that falls over the peak of solar cycle 25. All sunspots within active regions visible between 1 March 2023 - 1 March 2024 are tracked, and the data is input into the sunspot rotation method. The relationships between different sunspot and active region properties (such as area, duration, and rotation) and the flare energy outputs are investigated. Active regions that experience no or low flaring activity are included in the sample.

Two active regions that exhibited an uncommonly large amount of solar activity are studied in chapter 5. AR 13664 and AR 13842 are both linked to auroral events in 2024, and the study of these active regions provides case studies for incredibly complex and high energy active regions. The tracked sunspot motions are fed into the sunspot rotation and rotation energy methods, and the flare energy output is compared to different sunspot properties.

A new method to measure the corotation of sunspot pairs is introduced in chapter 6, this method is applied to all suitable active regions from the four-month and twelve-month sample, alongside the two case study active regions from chapter 5. The amount of corotation within an active region is compared to the estimated flare energy output of the active region.

The final chapter, chapter 7, summarises the results from chapters 3-6. This

chapter also discusses the potential avenues for future work in this field, and the implications of the collected results.

Chapter 2

A method to estimate the rotational and flare energy within an active region

This chapter describes the method used to identify and track sunspots using continuum data from the Solar Dynamics Observatory's Helioseismic and Magnetic Imager, specifically the HMI.IC_45S data series. An overview of the methods developed by Walker (2018) and Brown & Walker (2021) to calculate the rotation energy and the estimated radiated flare energy loss are also discussed.

2.1 An automatic method to identify and track sunspots

The sunspot identification and tracking method utilises three separate processes, sunspot identification, linking sunspots between frames and sunspot structure determination. The identification method can be applied to each observation in any

order using parallelisation. The SDO/HMI FITS files are inputted into the identification algorithm and the output is a file of metadata per observation containing sunspot characteristics, such as area, radius and weighted centre of mass for all sunspots visible in the observation. The second process uses the metadata files to connect sunspots between observations so their location can be tracked over the entire observation period and assigns each sunspot to its corresponding active region. The final process determines the final structure of the sunspot, once the observation has been put into the context of the surrounding frames. A second linking process is also applied to correctly record splitting sunspots. The following section will discuss these methods in detail.

2.1.1 Sunspot Identification Method

The sunspot identification method can be separated into smaller stages, as shown by Figure 2.1. The data is first corrected for limb darkening effects, and the umbral regions of the sunspots are identified. The structure of the sunspots are determined and properties are extracted and recorded per observation.

Data Preparation

Over the the lifetime of a sunspot the observed intensity of the umbral and penumbral regions can vary due to limb darkening effects. In order for the umbral pixel intensity threshold to be defined this effect must be corrected. The limb darkening correction used for this work is discussed in detail in Brown & Walker (2021). The observations are corrected using

$$I_{corr}(x, y) = \frac{I(x, y)}{\sum_{i=0}^{4} a_i \cos^i \theta} \tag{2.1}$$

where (x, y) is the location of the pixel being corrected, and $\cos(\theta)$ is

$$\cos(\theta) = \sqrt{1 - \frac{(x^2 + y^2)}{r_s^2}} \tag{2.2}$$

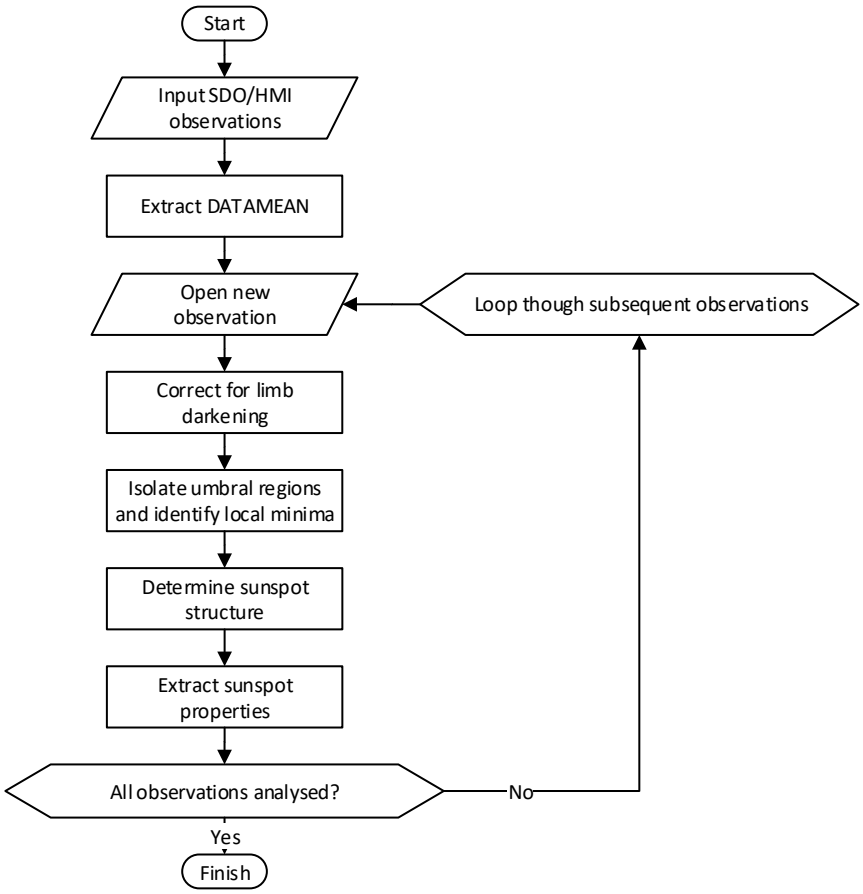

Figure 2.1: Method flow chart of the sunspot identification algorithm.

where r_s is the radius of the Sun, also in pixels. An example of the limb darkening correction process is shown in Figure 2.2.

Once the limb darkening effects have been corrected for, a fixed pixel intensity threshold can be set for the umbral region of the sunspot. The DATAMEAN value is extracted from the header of all of the observations under analysis and the mean of those values is calculated using

$$\bar{I} = \frac{1}{N} \sum_{i=1}^{N} \text{DATAMEAN}_i \tag{2.3}$$

The umbral region of the sunspot is defined as

$$I_{pix} \leq 0.6\bar{I} \tag{2.4}$$

and the penumbral region of the sunspot is defined by

$$0.6\bar{I} < I_{pix} \leq 1.05\bar{I} \tag{2.5}$$

These regions are highlighted in Figure 2.3.

Sunspot Identification

The process then moves to a frame-by-frame approach. All pixels with an intensity greater than the umbral intensity threshold (as defined by Equation 2.4) are masked out of the frame. Groups of connected umbral pixels are identified and extracted into smaller sub-arrays. A 5×5 box-car filter is applied to the data to remove excess noise and ensure that identified local minima are minima of the signal rather than the noise. The local minima were then extracted from each sub-array and compared with each other to determine the structure of the umbral region.

Different process are applied to the sub-arrays based on how many local minima are present. If there is only one local minima within the sub-array then all of the umbral pixels within the array are determined to be connected as one sunspot, this scenario is presented as case (iii) in Figure 2.4.

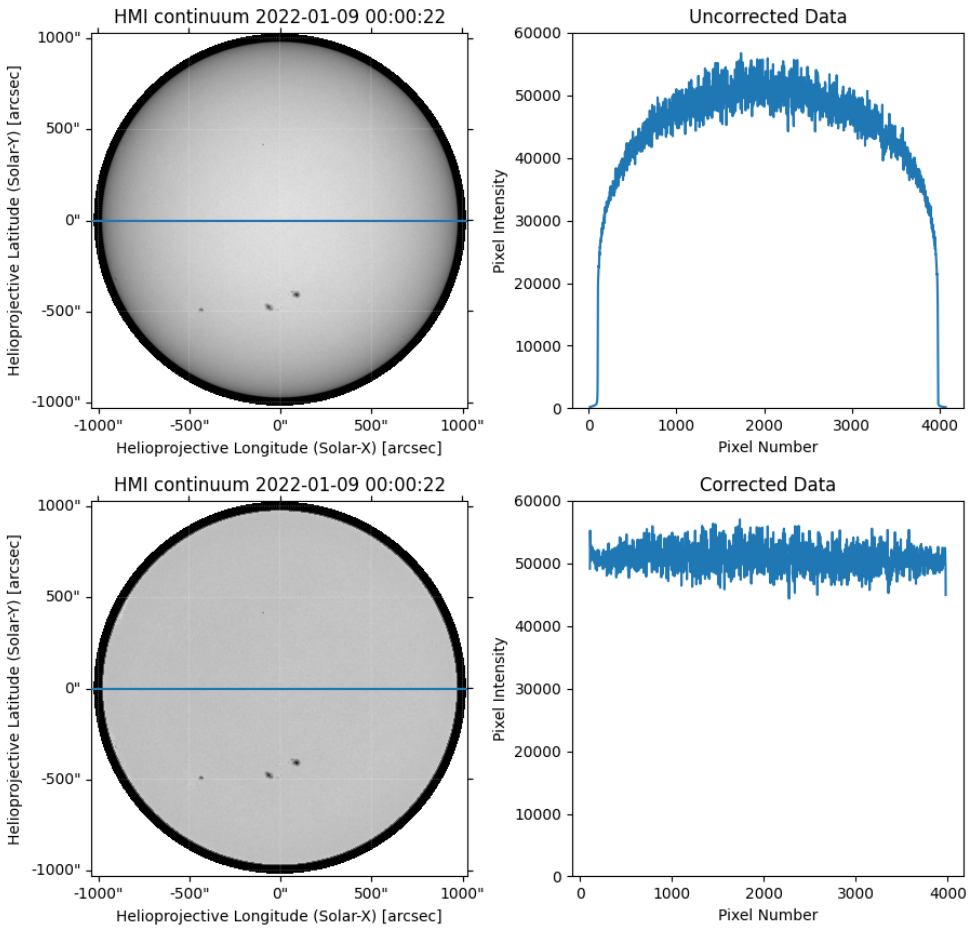

Figure 2.2: The top panel displays the SDO/HMI data without limb correction, and the lower panel shows the data once the limb darkening correction algorithm has been applied.

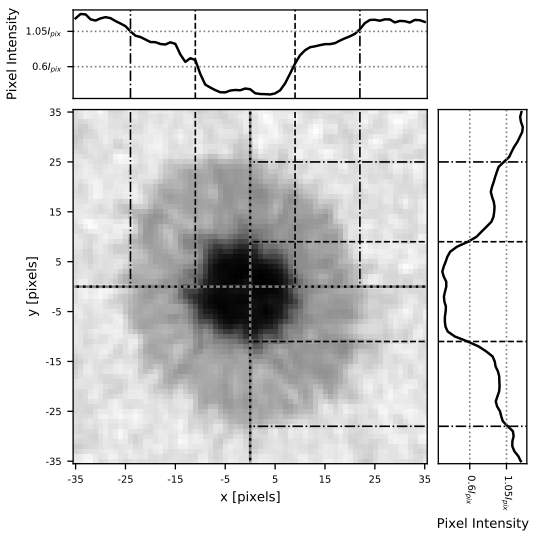

Figure 2.3: A reprojected SDO/HMI image with the horizontal and vertical intensity profiles across the centre of the sunspot. The umbral and penumbral thresholds are plotted on the sunspot image and the intensity profiles.

If there are multiple minima within one array a different process was followed. The local minima are sorted by ascending intensity. The local minima with the smallest intensity is considered to be part of a sunspot component. All the other minima are compared (in ascending order) to the smallest local minima to determine whether they are connected or not (i.e. within the same component). To determine if the minima are connected, a line of intensity is interpolated between the two minima. The minima are considered to be connected if

$$\frac{d_i}{D_i} < 0.2 \tag{2.6}$$

where d_i is the difference between the intensity peak of the interpolated line and the minima intensity, and D_i is the difference between the maximum umbral limit ($0.6\bar{I}$) and the minima intensity. If the minima are determined to be connected, the interpolated line would take the form of Figure 2.5a, and the second minima is added to the component. This scenario is presented in Figure 2.4, case (i). Here there are three local minima within the umbral region that are part of the same

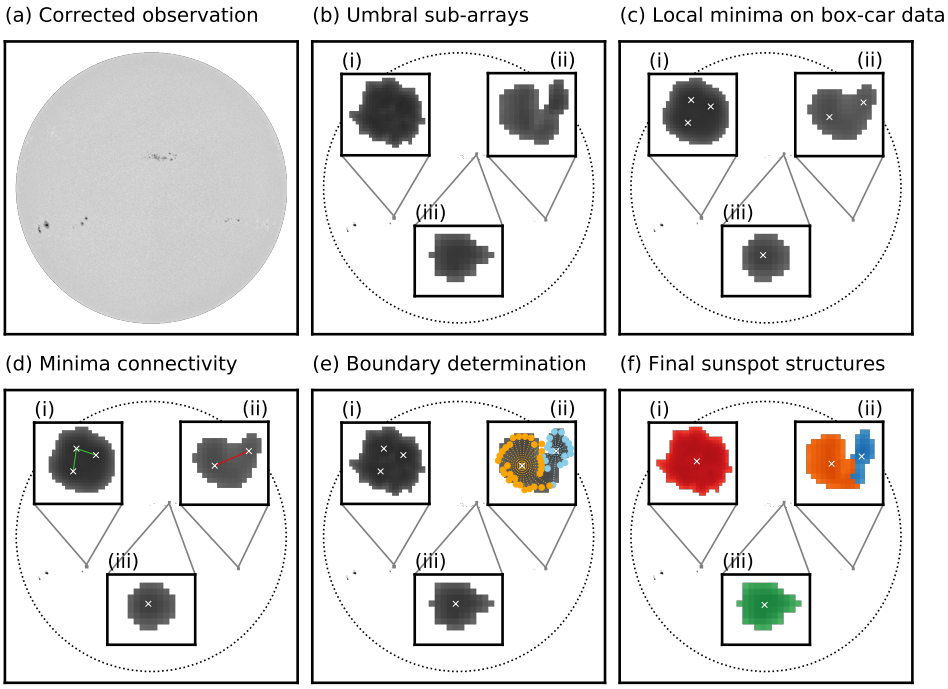

Figure 2.4: Sunspot structure determination. (a) The limb corrected SDO/HMI observation. (b) The sub-arrays containing the islands of umbral pixels. (c) The local minima location within the filtered sub-arrays. (d) The links between the local minima. (e) The boundaries of the sub-structure within the sub-arrays. (f) The final sunspot structure.

sunspot structure. The minima are considered to be unconnected and part of two separate components within the same umbral region and sub-array if

$$\frac{d_i}{D_i} > 0.4 \tag{2.7}$$

An example of this is shown in Figure 2.4 case (ii). If the minima comparison is

$$0.2 < \frac{d_i}{D_i} < 0.4 \tag{2.8}$$

the structure of the umbral region is classed as undecided and a final decision is made once the behaviour of the sunspot can be placed in the context of the surrounding linked observations. Generally the sunspots that fall in this category are at risk of either splitting or merging in the surrounding frames. Examples of these relations are represented in Figure 2.5d.

This process is repeated between every minima in the sub-array to determine which minima are connected and how many different sunspots are within the umbral region. If all of the minima within the umbral region are considered to be part of the same sunspot, all of the pixels within the umbral region are assigned to the single sunspot. If there are multiple sunspots within one umbral region, the boundary between the sunspots must be identified. For each sub-array an estimate for the maximum radius of the sunspot is calculated by interpolating a line radially outwards from each local minima at 90° increments until a turning point or the umbral intensity threshold was reached, using

$$\hat{r} = \frac{1}{4}\sum_{i=1}^{4} r_i \tag{2.9}$$

The inverse of this estimated radius defines the angle increment used for the boundary definition

$$\hat{r}\delta\theta = 1 \Rightarrow \delta\theta = \frac{1}{\hat{r}} \tag{2.10}$$

Using this method, one increment change in the angle around the local minima is equivalent to moving one pixel along the circumference of the umbral region. A line

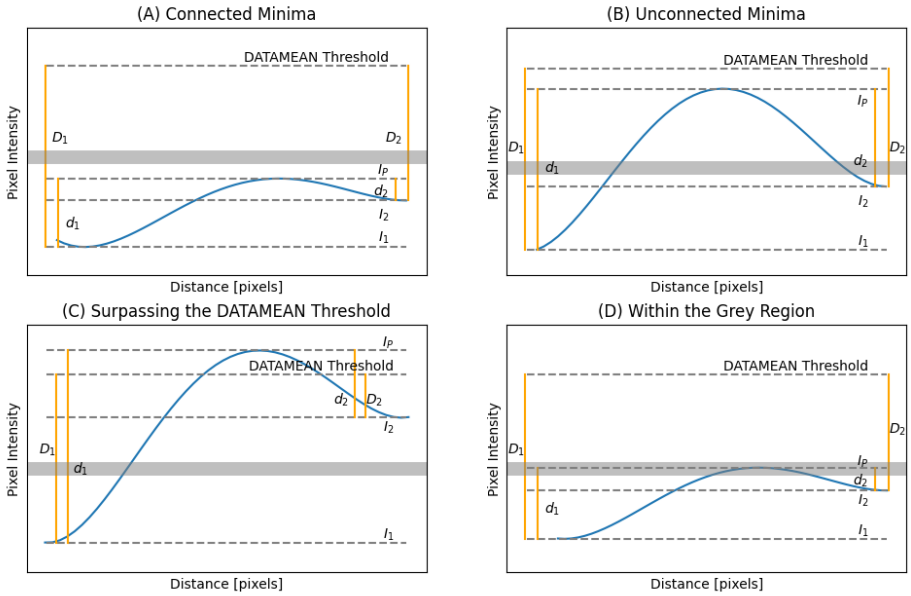

Figure 2.5: The blue line represents the interpolated intensity between two minima. $I_{1,2}$ is the intensity at each minima, I_P is the intensity at the maximum value between the minima and $D_{1,2}$ and $d_{1,2}$ are the differences between the $I_{1,2}$ and the DATAMEAN threshold and I_P, respectively. If the peak between the minima does not reach the grey region the minima are considered to be connected (A). If the peak between the minima does reach the grey region the minima are considered to be unconnected (B). If I_P surpasses the DATAMEAN threshold (C) the minima are considered to be unconnected. If I_P lands within the grey region (D) the minima are recorded as being temporarily connected but at risk of separating in future frames.

is then interpolated radially outwards from the local minima at increments of one pixel until either the edge of the umbral region is reached or a there is a turning point in the intensity. This pixel is considered to be the boundary of the sunspot. This is repeated through 360° for each local minima within the umbral region (Figure 2.4e). All of the pixels within these boundaries are collected and assigned to the correct sunspot. If there are any unassigned pixels within the sub array these are assigned to the closest sunspot in the sub-array.

The pixels assigned to each sunspot are then used to calculate the centre of mass of the sunspot, the centre of mass weighted for intensity, the maximum radius, the area, the structure and linking criterion alongside the errors associated with these parameters. Once all sunspots are identified in the current frame, the process is then repeated for the next file in the data set. As the order that the observations are analysed does not impact the results for the sunspot identification process, this step can be conducted in a parallel manner.

2.1.2 Sunspot Linking Method

Once all of the sunspots in the data set are identified, they are linked between frames to allow the tracking of sunspots. All of the sunspots in the first frame are assigned integer numbers from $1 - n$ where n is the number of sunspots in the frame. All observations in the subsequent frame are compared to the previous observation to determine if the sunspots are linked to any previous sunspot or if they are new emerging sunspots.

The current observation under analysis is referred to as frame t, with sunspot weighted centre of mass (x_t, y_t) and the previous observation is referred to as frame $t - 1$, with sunspot weighted centre of mass (x_{t-1}, y_{t-1}). The effect of the Sun's differential rotation between frame t and frame $t - 1$ is removed from observation t, these sunspots are then referred to as $\bar{t}$, $(\bar{x}_t, \bar{y}_t)$. The distances between the sunspot

from frame $\bar{t}$ and all sunspots from the previous frame $t-1$ are given by

$$d = \sqrt{(\bar{x}_t - x_{t-1})^2 + (\bar{y}_t - y_{t-1})^2} \tag{2.11}$$

We require the distance d to be less that the mean radius of the sunspots in the frames under comparison

$$r_{crit} = \frac{1}{2}(r_t + r_{t-1}) \tag{2.12}$$

in order for the sunspots to be considered the same sunspot from different observations.

There are two special cases that occur during the linking process. Firstly, multiple sunspots from frame t could track back and satisfy the linking criteria for a single sunspot in frame $t-1$. These sunspots typically fall within the 'undecided' region (Equation 2.8) from the structure identification process. The sunspots are then recorded as two separate structures, to be more thoroughly checked once the structural changes are placed in the context of the surrounding observations. In this case the sunspots are considered to be potentially splitting as they were connected in the previous frame but disconnected in the current frame. The other special case occurs when a single sunspot in the current frame (frame t) tracks back to multiple sunspots in the previous frame (frame $t-1$). In this case the sunspot also typically has an 'undecided' structure and is considered to be potentially merging in frame $t-1$ to a single sunspot in frame t.

If no sunspots from the previous frames fulfil this criteria, then the process is repeated between frames t and $t-2$. The maximum time between frames that could be compared is set to one hour. This process is repeated for all frames in the dataset. Each sunspot is then assigned to the closest active region using the data available from NOAA SRS.

2.1.3 Sunspot Structure Determination

To finalise the linking of the sunspots, each observation is placed within the context of the active region. A linear convolution filter (with window size 100) is applied to the recorded sunspot area of each sunspot, the smoothed area result is deducted from the original area recording to isolate the unexpected variations. Observations where the sunspot structure criteria falls within Equation 2.8 are extracted. Consecutive observations where sunspots fall within the 'undecided' region are confirmed to be splitting or merging sunspots. If these observations are not consecutive and the area variation exceeded 55 pixels, the sunspots are considered to be part of the same structure. These temporary variations in the sunspot structure are generally caused by light-bridges forming across the umbra. Once the components are merged together the recorded values are combined and attributes such as the weighted centre of mass and area are recalculated using the new pixel allocations.

A second sunspot linking method is then applied to the data, to connect sunspots together that would not have been considered the same sunspot from different observations before the structure determination method. The final hour of data for sunspot A is extracted and the mean weighted centre of mass coordinates, mean radius and median reprojected area is calculated from these observations.

A new area criterion is calculated for the second sunspot linking run. To determine the new area criterion, a median filter, with a kernel size of 61 observations, is applied to the area of 14 sunspots varying in area from 49π - 350π. The standard deviation of the residual area was calculated for each of the observed sunspots and the relationship between the standard deviation and the sunspot area is used to define the area limit. The area limit is defined by

$$A_{\text{lim}} = A_{\text{area}} \pm \sigma \tag{2.13}$$

$$\sigma = 5 \times (0.0592 \times A_{\text{area}} + 4.6658) \tag{2.14}$$

where σ is the area limit factor and A_{area} is the area of sunspot A. We consider sunspots A and B to be connected if they fulfil three criteria:

- The first observation of sunspot B is within ten-hours of the final observation of sunspot A
- The median area from the first hour of observations for sunspot B is within A_{lim}
- The distance between the mean centre of mass for sunspots A and B is less than the mean radius of sunspot A.

The second linking process is the final stage of the sunspot identification and tracking method. The metadata for each active region is recorded and ready to input into sunspot dynamic methods.

2.2 Sunspot Rotation

To calculate the sunspot rotation, we use the method developed by Brown & Walker (2021) and Walker (2018). A summary of this method is provided in this section.

The active region metadata from the previous section is input into the rotation method. The weighted centre of mass of the sunspot is transformed to the disc centre to remove the projection effects present when the sunspot is near the solar limb, whilst preserving solar north. The rotation matrices are calculated using the relative location of the sunspot with respect to the disc centre

$$\underline{\mathbf{A}} = \begin{bmatrix} \cos(\alpha) & 0 & -\sin(\alpha) \\ 0 & 1 & 0 \\ \sin(\alpha) & 0 & \cos(\alpha) \end{bmatrix}, \text{ and } \underline{\mathbf{B}} = \begin{bmatrix} 1 & 0 & 0 \\ 0 & \cos(\beta) & -\sin(\beta) \\ 0 & \sin(\beta) & \cos(\beta) \end{bmatrix} \tag{2.15}$$

where

$$\sin(\alpha) = \frac{x_{cen}}{\sqrt{r_s^2 - y_{cen}^2}}, \text{ and } \sin\beta = \frac{y_{cen}}{r_s} \tag{2.16}$$

where x_{cen}, y_{cen} is the relative (x, y) coordinate of the sunspot with respect to the centre of the solar disc, and r_s is the radius of the Sun. The application of Equation 2.15 supplies the transformed location of the position about the sunspot centre (x_{ss}, y_{ss}). Generally the transformed points are not at pixel centres, so the intensity values between pixels are calculated using

$$I_{r,\theta} = (1 - \delta_i)((1 - \delta_j)I_{i,j} + \delta_j I_{i,j+1}) + \delta_i((1 - \delta_j)I_{i+1,j} + \delta_j I_{i+1,j+1}) \tag{2.17}$$

where

$$x_{ss} = i + \delta_i, \text{ and } y_{ss} = j + \delta_j \tag{2.18}$$

Here $I_{i,j}$ is the intensity value (i, j) of the image pixel. The inner and outer radius of the penumbra is calculated using the metadata, and the sunspot is uncurled.

The horizontal motion of features in the penumbra are tracked to determine the rotational motion of the sunspot using peaks and troughs in the penumbral structure. These turning points are compared to previous observations to track them over the observational period. From this data the average rotational profile is calculated.

The net and absolute cumulative sunspot rotation is calculated to represent the maximum and minimum possible injection of twist due to rotation, respectively. The mid cumulative sunspot rotation is calculated using

$$R_{mid} = \frac{|R_{net}| + R_{abs}}{2} \tag{2.19}$$

The uncertainty on on R_{mid} is scaled by the difference in R_{net} and R_{abs} as there is a combination of random errors on the measurement of rotation, but these errors are predominantly taken to be uniformly distributed in range. The uncertainty is given by

$$\delta R^2_{mid} = \frac{1}{4}[\delta R^2_{net} + \delta R^2_{abs}] + \frac{(R_{abs} - |R_{net}|)^2}{12} \tag{2.20}$$

The cumulative rotation profiles for each active region are used to estimate the energy contribution due to sunspot rotation. The next section will discuss how this is calculated.

2.3 Rotation Energy

The method to estimate the active region energy contribution due to sunspot rotation follows that outlined by Walker (2018).

An average magnetic flux is calculated from the average sunspot area using

$$\phi = 10^{12.17} A^{1.09} \tag{2.21}$$

from Li, Ai & Wang (2001), where ϕ is the magnetic flux in Maxwells and A is the sunspot area in km^2. The area is converted from pixels to km^2 using the accepted value of 725.27km^2 per arcsecond at 1 AU, along with the SDO/HMI spatial resolution of 0.504 arcseconds per pixel, resulting in the conversion 133619 km^2/pixel^2.

The added self-helicity of a flux tube due to the sunspot rotation is calculated using

$$\Delta H = -\frac{1}{2\pi} \Delta\theta \phi^2 \tag{2.22}$$

where ΔH is the change in helicity, and $\Delta\theta$ is the total rotation of the sunspot (Vemareddy, Ambastha & Maurya, 2012). Finally, the magnetic helicity is used to estimate the magnetic energy injected into the active region due to the sunspot rotation. This relationship has been defined by Tziotziou, Georgoulis & Raouafi (2012), and is given by

$$|H| = 1.37 \times 10^{14} E^{0.897} \tag{2.23}$$

where $|H|$ is the unsigned helicity and E is the magnetic energy. This magnetic energy is compared to the flare energy output. The next section will discuss the method used to calculate the radiated flare energy.

2.4 Flare Energy

The Heliophysics Event Knowledgebase (HEK) is used to query flare events associated with the active regions under analysis. In this work we consider all flares, with

no distinction as to whether the flares are accompanied by a coronal mass ejection or not. The start, peak and end times for each flare are extracted. The end time of the flare is defined in the HEK database as the time when the flux reaches 50% of the peak flux of the flare. For this analysis the end time of the flare is either the time the flux reaches 5% above the background flux level, or the onset of the next flare. The GOES time series for the flare is used alongside a SUNPY built-in method to extract the temperature and emission measure of the flare. The SUNPY function follows the methods described in White, Thomas & Schwartz (2005).

The emission measure and temperature are used to calculate the optically thin radiative energy loss rate in erg s^{-1} using

$$L_{rad} = 10^{49} EM \frac{6 \times 10^{-22}}{(T/10^5)^{\frac{1}{2}}} \tag{2.24}$$

derived by Cox & Tucker (1969), where EM is the emission measure in 10^{49} cm^{-3}, and T is the temperature in Kelvin. This equation assumed an isothermal hot plasma. L_{rad} is summed over the duration of the flare to generate the total optically thin energy loss in ergs, this is then converted to the radiated bolometric energy loss (in ergs) using the factor 5.2 ± 2.3. This factor is based on work by Emslie et al. (2012) who compared the optically thin radiative energy loss and the bolometric energy loss over 38 X-Class flares and found that the bolometric energy loss is, on average, 5.2 ± 2.3 times larger than the optically thin radiative energy loss.

The method we use for this work varies slightly from the method used in Walker (2018) as we were unable to exactly replicate the values produced in Walker (2018) using the described methodology. Figure 2.6 shows the difference between the Proverbs and Walker calculated bolometric energy loss for the flares within the four-month testing region. The results from the Walker sample are slightly higher, however the results are generally scattered around the $x = y$ line.

This method is used to calculate the bolometric energy loss for each active region throughout this work. A few minor inconsistencies have been noticed with the HEK

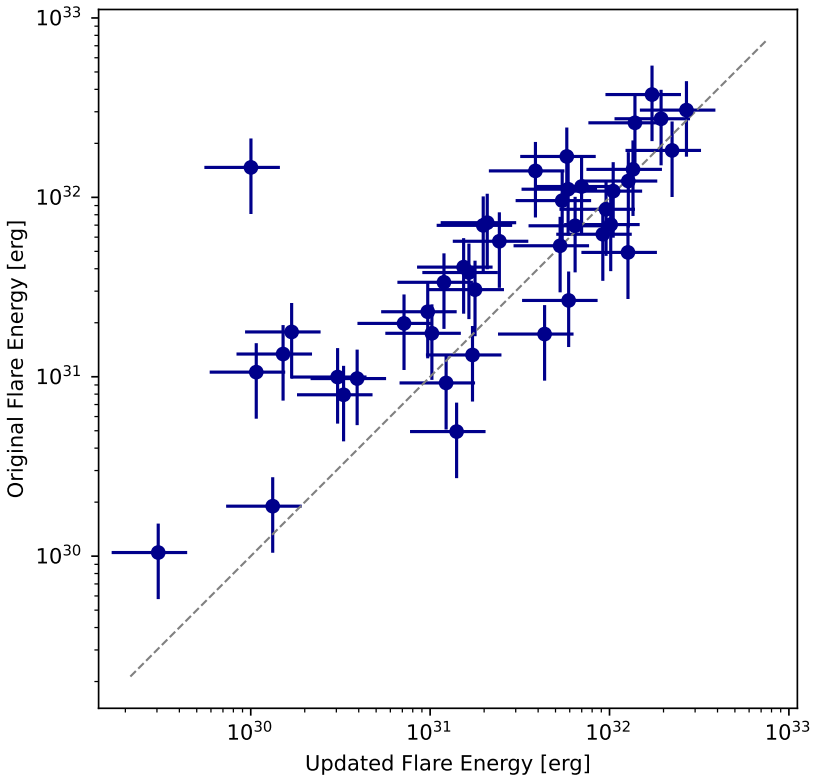

Figure 2.6: A scatter plot showing the difference between the updated Proverbs flare energy calculation (x-axis), and the flare energy calculations used by Walker (y-axis). The dashed line shows the $x = y$ line for the data.

data from 2023 - 2024. Flares with incorrect peak and end times have not been included in this analysis, however the majority of C, M and X-Class flares were not impacted, so the calculated energies are considered a good minimum energy output for active regions.

Chapter 3

Comparing the results of the Proverbs method against a semi-automatic method over a four-month sample of active regions

3.1 Introduction

The automatic sunspot identification and tracking method (the Proverbs method) from chapter 2 is applied to a four-month sample of active regions that has been previously analysed using a semi-automatic method by Walker (2018). This chapter will compare the results from both methods to determine the validity of the Proverbs method. The results for each active region will be compared, including sunspot properties such as the number of sunspots within an active region, the amount of time each sunspot is successfully tracked for, the area of each sunspot,

and the sunspot rotation profiles. Instances where the Walker method appears to out perform the Proverbs method, or where the Proverbs method greatly exceeds the Walker method, are extracted and presented as case study active regions.

3.1.1 The Sample

The four-month sample covers the period 1 May 2013 - 31 August 2013. Figure 3.1 shows where this period falls within solar cycle 24. To allow a fair comparison with the Walker method, the same sunspot criteria is applied. To allow analysis, the sunspot must fulfil the following criteria for at least 24 hours:

- The reprojected area of the sunspot must be greater than 49 pixels^2 ($\sim$ 40 Mm^2), based on the radius of an ideal circular sunspot of 7-pixels
- The sunspot must have an effective angular extent between $-60°$ and $60°$

The Walker method also excluded sunspots that experienced splits or mergers during the observation period. These sunspots will not be excluded from this analysis as the new Proverbs method is designed to handle these types of sunspot structures.

CHAPTER 3

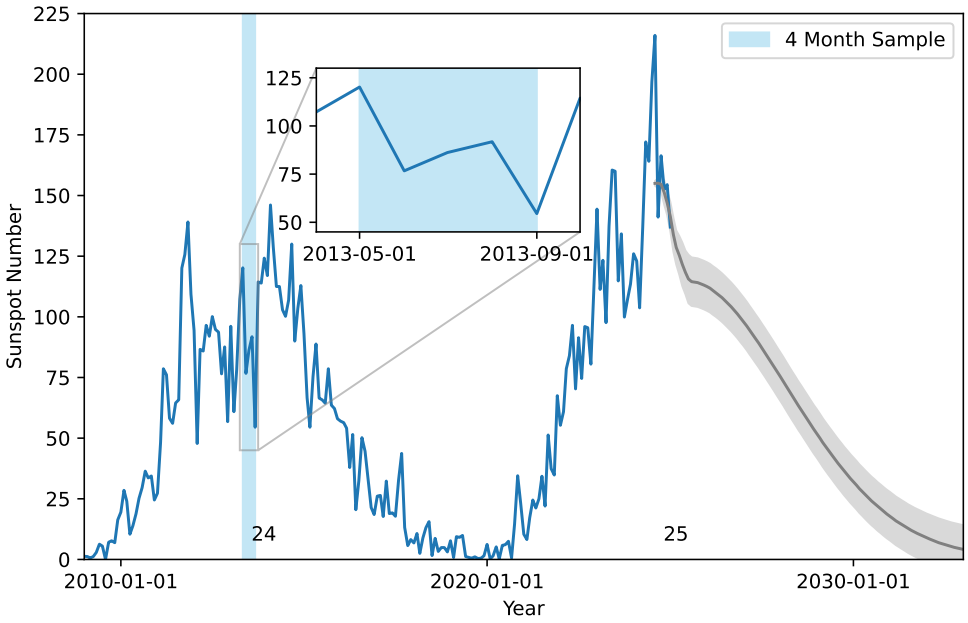

Figure 3.1: Solar cycles 24 and 25 presented using recorded and predicted sunspot number data from NOAA since 1 January 2008. The blue shaded region represents the four-month sample period. The inset figure shows the activity over this period in more detail.

3.2 Results

This section will compare the Proverbs dataset with the previously semi-automatically identified sunspot dataset from Walker (2018).

3.2.1 Sunspot Number Comparison

Over the four-month series, running from 1 May - 31 August 2013, the Proverbs method is able to identify 107 sunspots over 49 active regions and Walker (2018) identified 56 sunspots over 38 active regions. The number of sunspots identified per method and per active region is shown in Figure 3.2. The Proverbs method is able to identify 54 of the sunspots found by Walker, the two non-identified sunspots are from AR 11824 and AR 11835. These active regions are discussed in this section.

The Proverbs method is able to identify 51 more sunspots than Walker, including 11 active regions that did not have associated sunspots in the Walker dataset (active regions 11730, 11736, 11739, 11774, 11778, 11813, 11814, 11820, 11827, 11830 and 11836). Generally the 54 communally identified sunspots show good agreement, with the Proverbs method showing an increased ability to track the structural changes within the umbral regions of the sunspots in comparison to the Walker method. An example of an active region with good agreement, AR 11808, is discussed this section.

The Proverbs method typically identifies more sunspots per active region, with a greater sensitivity to smaller sunspots than the Walker method, as presented in Figure 3.3. The Proverbs method is designed to detect changes in the structure of sunspots, and to be able to identify splitting and merging sunspots, so it is expected that smaller sunspots would be identified using this method that were not identified using the Walker method. Where the Walker method identifies one large sunspot, the Proverbs method may find multiple smaller sunspots within one penumbral region.

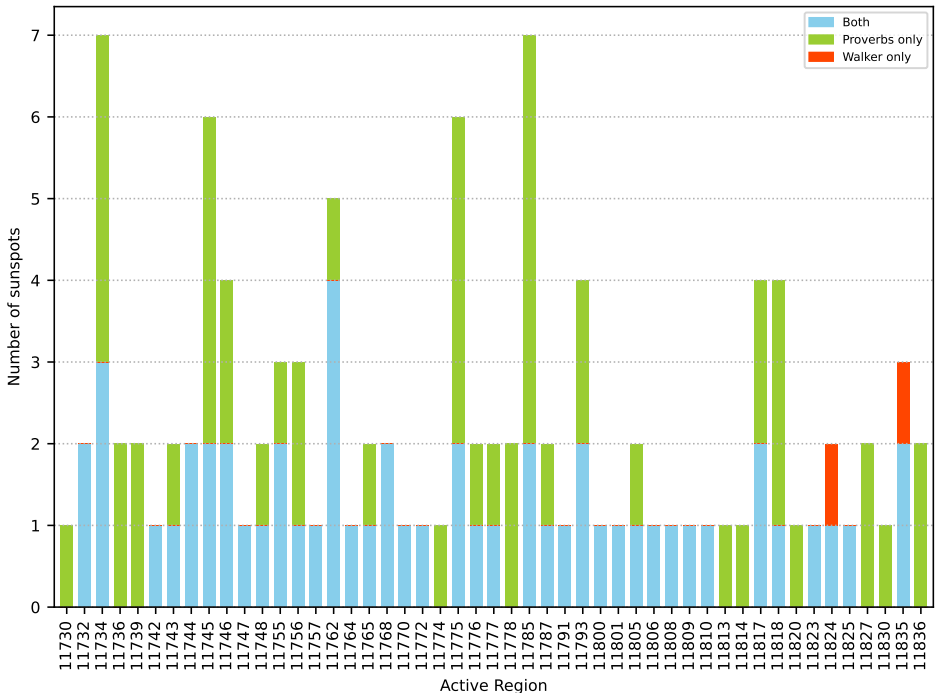

Figure 3.2: A histogram showing the number of sunspots identified per active region by the two sunspot identification methods. Sunspots identified by both methods are highlighted in blue, by only the Proverbs method in green and by only the Walker method in red.

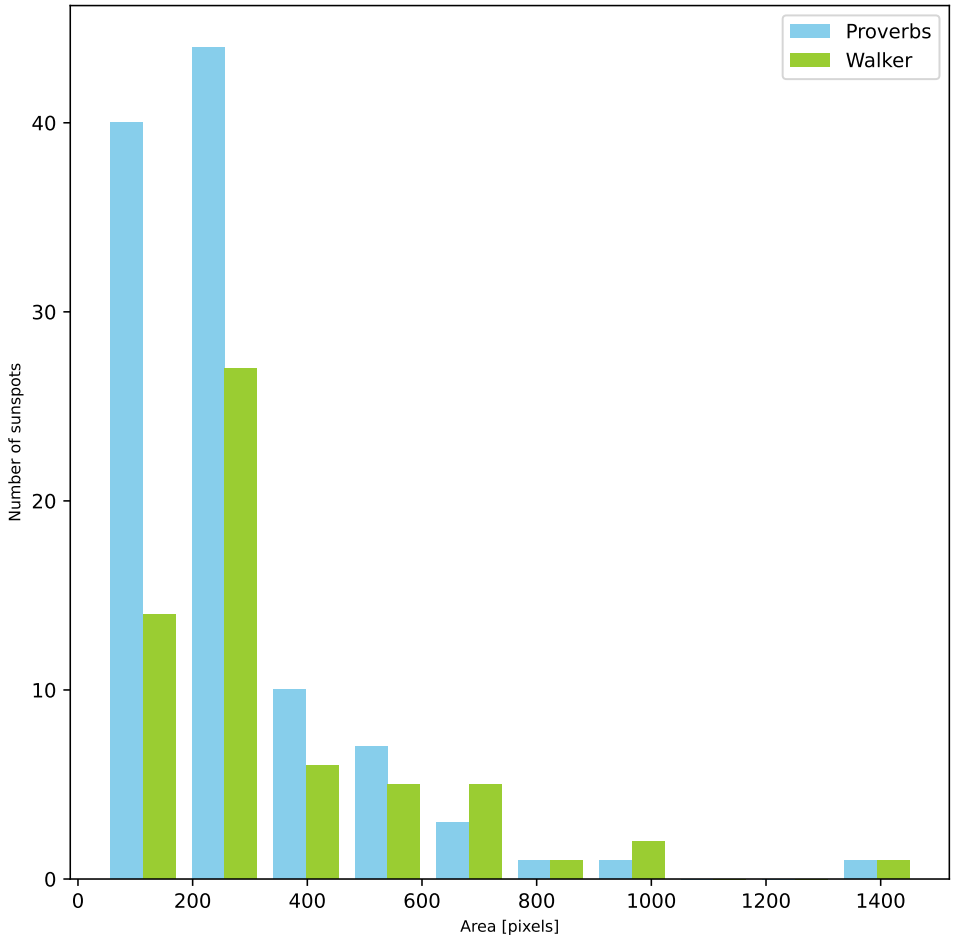

Figure 3.3: A histogram showing the area distribution of sunspots identified with the Proverbs method, and the Walker method.

Active region 11836 is included in the analysis for completeness, however this active region may not have been included in the original Walker dataset as the final observation of this active region occurs after the end of the sample period.

Analysis of AR11824

In AR 11824, Walker identifies two sunspots whereas the Proverbs method only identifies one, Figure 3.4 shows images of the active regions from two different observations, alongside the area profiles and the differences in centre of mass between the two sunspots. Walker applies a selection criteria where each sunspot under analysis must have a reprojected umbral area of greater than 49π pixels^2 and have an effective angular extent of between $-60°$ and $60°$ for at least 24 hours for inclusion in the sample. We apply the same selection criteria for this comparison.

Figure 3.4c shows that Walker considers sunspot W_B to have an area above the threshold for 24.6 hours, whereas Fig. 3.4d shows that sunspot P_B in the Proverbs result is only above the threshold for 16.95 hours, so the sunspot did not pass the selection criteria and is not included in the Proverbs sample. The Proverbs method is able to identify that sunspot P_B is undergoing an umbral split, so records the decrease in area. The Walker method however is more suited to tracking the bulk kinematics of the sunspots, so considers sunspot W_B to be a larger structure for an extended period.

Analysis of AR11835

AR 11835 undergoes a structural change where the umbral region splits into two components. Figures 3.5a and b show the active region during and after the split, respectively. Both the Walker and Proverbs method for identifying sunspots consider AR 11835 to be undergoing a split. In the Walker dataset the pre-split umbral region is considered one sunspot, and the two regions that separate are considered to be two

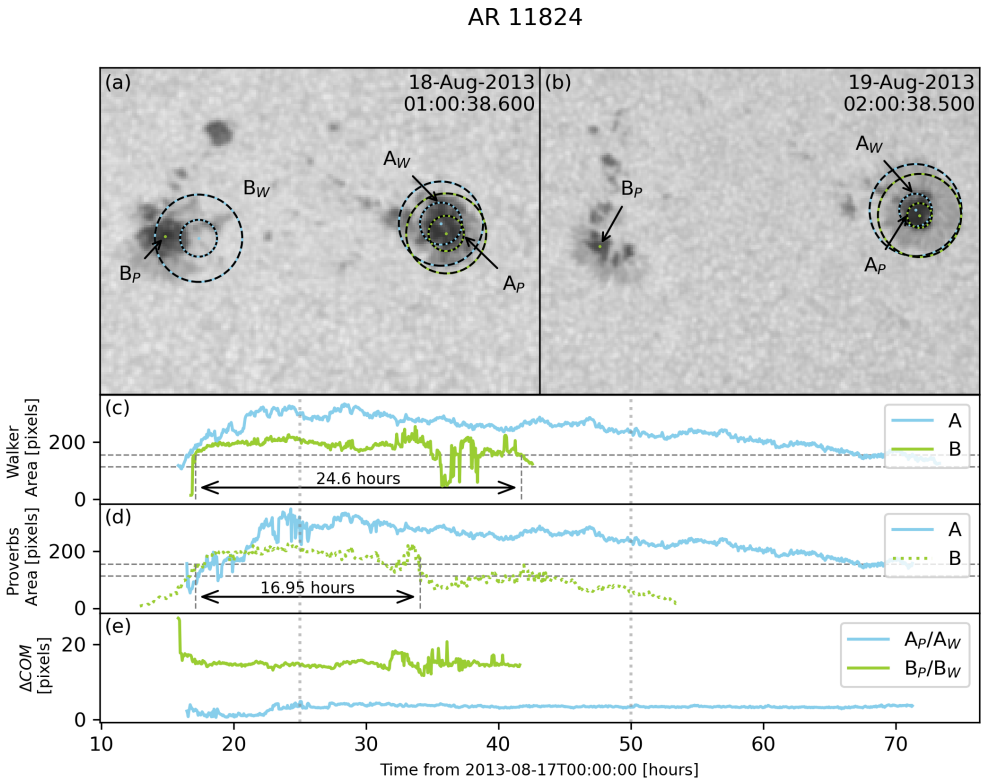

Figure 3.4: Tracking profiles for AR 11824: (**a,b**) images of the sunspots from 18 August 2013 at 01:00:38 UT and 19 August 2013 at 02:00:38 UT, respectively, with the identified penumbral and umbral radii overlaid from both identification methods; (**c**): the reprojected umbral area profile for the sunspots identified by the Walker method; (**d**): the reprojected umbral area profile for the sunspots identified by the Proverbs method; (**e**): the difference in recorded sunspot centre of mass for the comparable sunspots identified by both methods.

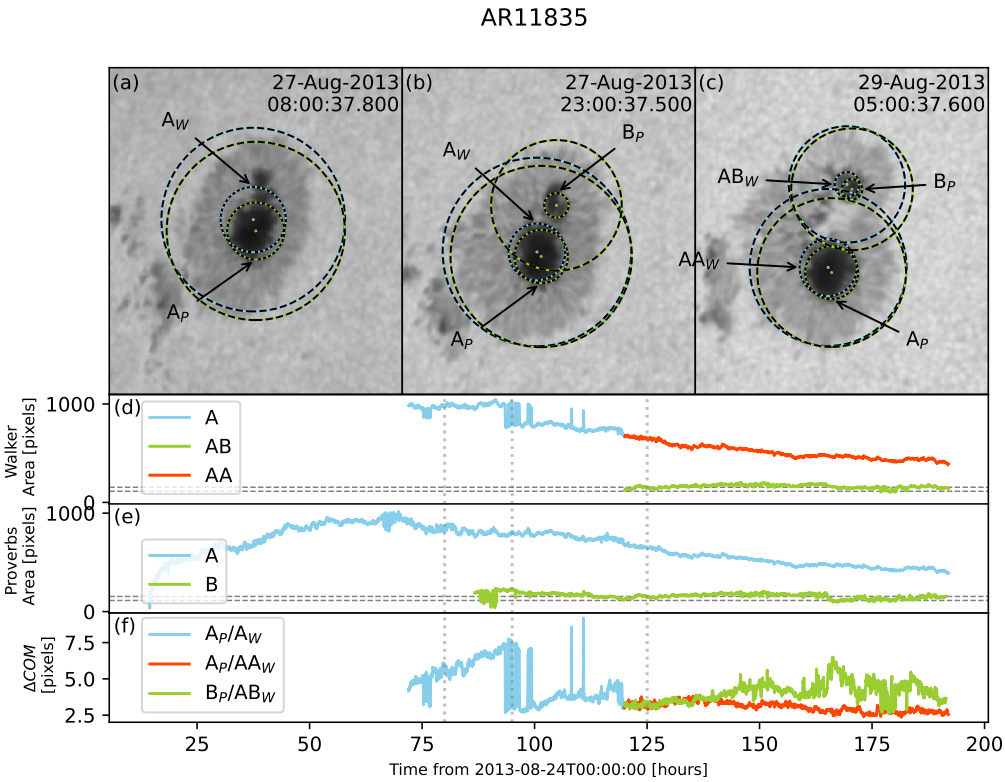

Figure 3.5: Tracking profiles for AR 11835: (**a,b,c**) image of the sunspots from 27 August 2013 at 08:00:37 UT, 27 August 2013 at 23:00:37 UT and 29 August 2013 at 05:00:37 UT, respectively, with the identified penumbral and umbral radii overlaid from both identification methods; (**d**): the reprojected umbral area profile for the sunspots identified by the Walker method; (**e**): the reprojected umbral area profile for the sunspots identified by the Proverbs method; (**f**): the difference in recorded sunspot centre of mass for the comparable sunspots identified by both methods.

additional sunspots (W_A, W_{AA}, W_{AB}), as shown by Figure 3.5. The Proverbs method was designed to handle structural variations within umbral regions, so records the sunspot continuously before and after the split as one sunspot, with an additional sunspot for the splitting component (P_A, P_B). When comparing the number of sunspots, the difference in split-handling changes the total sunspot number between the two datasets, although they both record the same sunspots. Figure 3.5e shows that the recorded structures do exhibit good agreement despite the difference in labelling.

Analysis of AR11808

This example illustrates how for simple sunspot structures the two methods perform comparably. AR 11808 consists of a large, circular sunspot that elongates as it travels across the solar disk, the areas and the differences in sunspot centres are presented in Figure 3.6. There is some difference in centre of mass during the maximal point of elongation (Figure 3.6b and e), but overall the two methods show good agreement. The Proverbs method identified the sunspot approximately 24 hours earlier than the Walker method, but the identified areas are very similar throughout the observations and the distance between centres is consistently below 5 pixels. Overall the methods show good agreement with this active region.

Analysis of AR11748

This example illustrates how the Proverbs method out performs the Walker method. AR 11748 is a complex active region containing multiple smaller structures. The area profiles and the differences in sunspot centres are presented in Figure 3.7. Walker identifies a single sunspot in the observations of this active region (A_W), whereas the Proverbs method identifies a second larger sunspot that appears on the solar disk for approximately 75 hours (B_P). Sunspot A_W and A_P have very similar

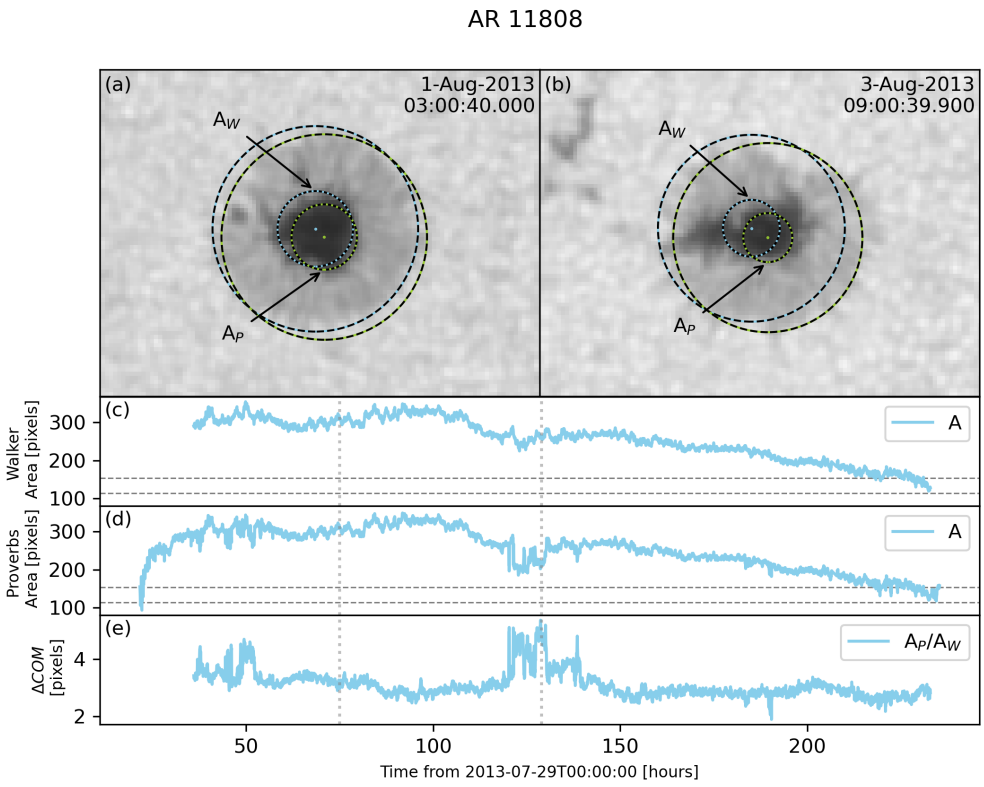

Figure 3.6: Tracking profiles for AR 11808: (**a,b**) image of the sunspots from 1 August 2013 at 03:00:40 UT and 3 August 2013 at 09:00:40 UT, respectively, with the identified penumbral and umbral radii overlaid from both identification methods; (**c**): the reprojected umbral area profile for the sunspots identified by the Walker method; (**d**): the reprojected umbral area profile for the sunspots identified by the Proverbs method; (**e**): the difference in recorded sunspot centre of mass for the comparable sunspots identified by both methods.

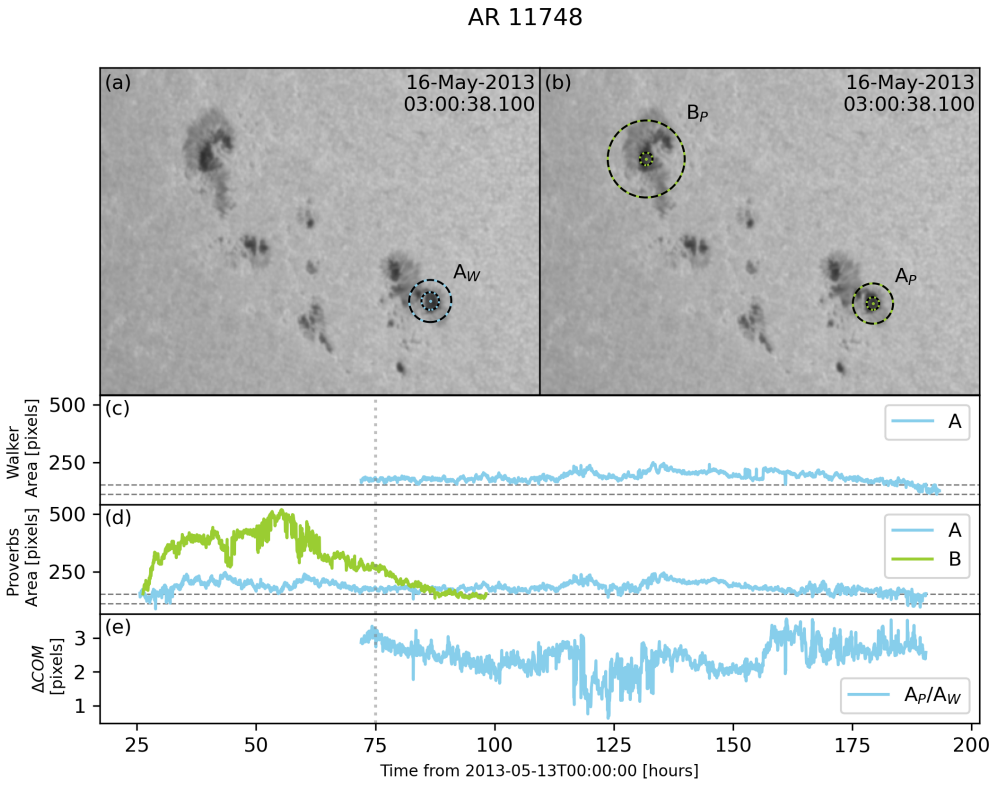

Figure 3.7: Tracking profiles for AR 11748: (**a,b**) image of the sunspots from 16 May 2013 at 03:00:38 UT, with the identified penumbral and umbral radii overlaid from both identification methods; (**c**): the reprojected umbral area profile for the sunspots identified by the Walker method; (**d**): the reprojected umbral area profile for the sunspots identified by the Proverbs method; (**e**): the difference in recorded sunspot centre of mass for the comparable sunspots identified by both methods.

umbral centre locations for the periods where they are identified by both methods, varying between 1-4 pixels difference. Sunspot A_P is observed for 50 hours more than sunspot A_W.

The next section investigates the difference in sunspot durations between the Walker method and the Proverbs method.

3.2.2 Duration Comparison

Figure 3.8 compares the duration of the 54 sunspots identified by both the Walker and Proverbs methods. We consider the duration to be the number of hours that a sunspot was successfully tracked by either the Walker or the Proverbs method. Generally, the Proverbs method was able to identify sunspots for a longer duration, with thirteen of the sunspots found using the Proverbs method being tracked for at least forty-eight hours more than with the Walker method. There is one extreme case, AR 11823 (noted as point A in Figure 3.8), where the Proverbs method tracked a sunspot for over 275 hours, whilst the Walker method only tracked the sunspot for 24 hours. There are three sunspots that are tracked using the Walker method for over forty-eight hours more than with the Proverbs method, AR 11756, 11734 and 11732 (point B, C and D in Figure 3.8, respectively).

Analysis of AR 11823

Active region 11823 is shown by Figure 3.9. The two photospheric observations (Figure 3.9a and b) show the active region on the 17 and 21 August 2013. The sunspot is clearly visible in both observations. As illustrated in the Walker area plot (Figure 3.9b), the Walker data covers a 24 hour period and does not track the sunspot beyond 18 August 2013 00:06. The Proverbs data successfully identifies the sunspot for the full duration of the active region. The short observational period could be a mistake in the Walker dataset, as the sunspot is clearly visible until 26

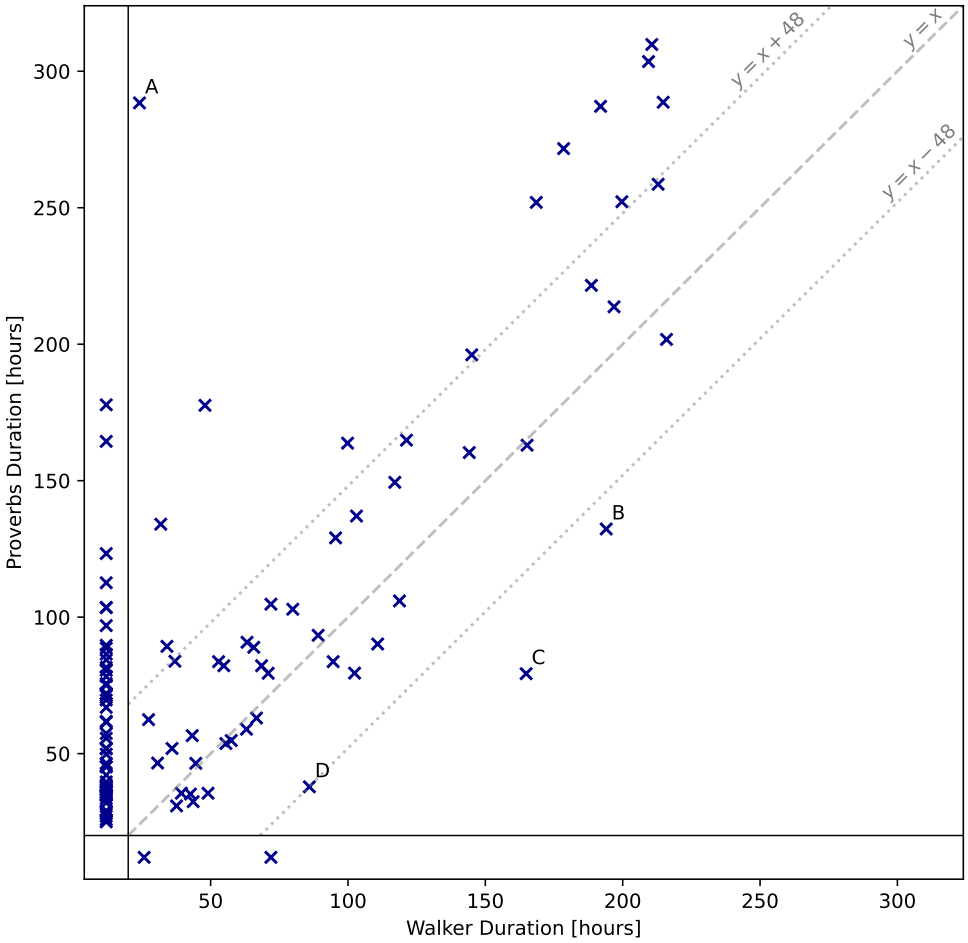

Figure 3.8: Duration comparison of sunspots identified by the Walker method and the Proverbs method. Sunspots identified only by Proverbs are plotting on the left of the figure, and sunspots identified only by Walker are at the bottom of the figure.

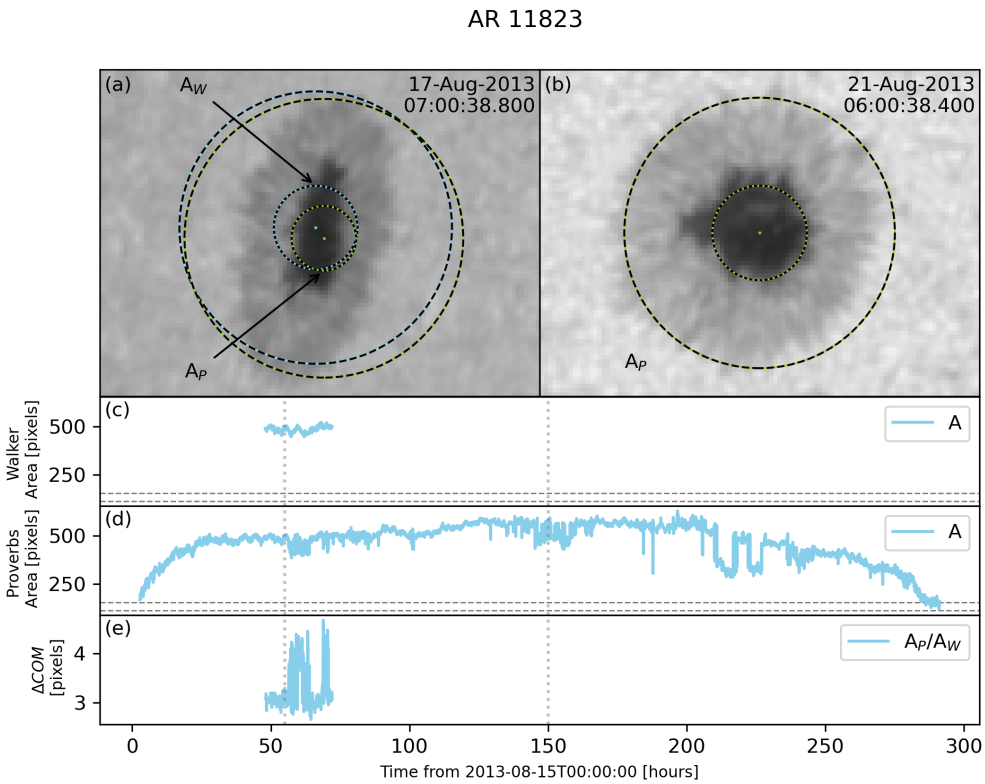

Figure 3.9: Tracking profiles for AR 11823: (**a,b**) image of the sunspots from 17 August 2013 at 07:00:39 UT and 21 August 2013 at 06:00:38 UT, respectively, with the identified penumbral and umbral radii overlaid from both identification methods; (**c**): the reprojected umbral area profile for the sunspots identified by the Walker method; (**d**): the reprojected umbral area profile for the sunspots identified by the Proverbs method; (**e**): the difference in recorded sunspot centre of mass for the comparable sunspots identified by both methods.

August in the Proverbs dataset. Within the overlapping observations the methods have good agreement with area, and show a variation of 3-4 pixels between the sunspot centres.

Analysis of AR 11756

The Walker method tracks sunspot A_W for over 200 hours, and the Proverbs method tracks sunspot A_P for 150 hours. Figure 3.10c and 3.10d show that the Proverbs method identifies sunspot A_P 24 hours before the Walker method first identifies the sunspot, but the Walker method continues to track the sunspot for much longer. This active region undergoes a split at 110 hours. The Walker method identifies this structural change but merges the umbral regions back together afterward. The Proverbs method identifies the change in umbral structure slightly earlier, and tracks each component separately (A_P and B_P). Because of this, the full duration of sunspot A_W is much longer than the duration of sunspot A_P, but the remaining component in the Proverbs dataset, sunspot B_P, is tracked for 25 hours beyond the final observation of sunspot A_W, so the combined components A_P and B_P are tracked for longer than A_W.

Analysis of AR 11734

Active region 11734 also contains a sunspot that has a longer duration in the Walker dataset than in the Proverbs dataset, sunspots C_W and C_P. This active region is presented in Figure 3.11. Figure 3.11a shows the active region at the final observation for sunspot C_P. As shown by the figure, the Proverbs method is more sensitive to variations in umbral structures, and identifies sunspot C_W as three smaller sunspots, C_P, D_P and G_P. Sunspots C_P and G_P dissipate between the observations represented by Figure 3.11, whilst sunspot D_P persists before splitting again and forming sunspot F_P. This active region has a very complex structure, and when combing the

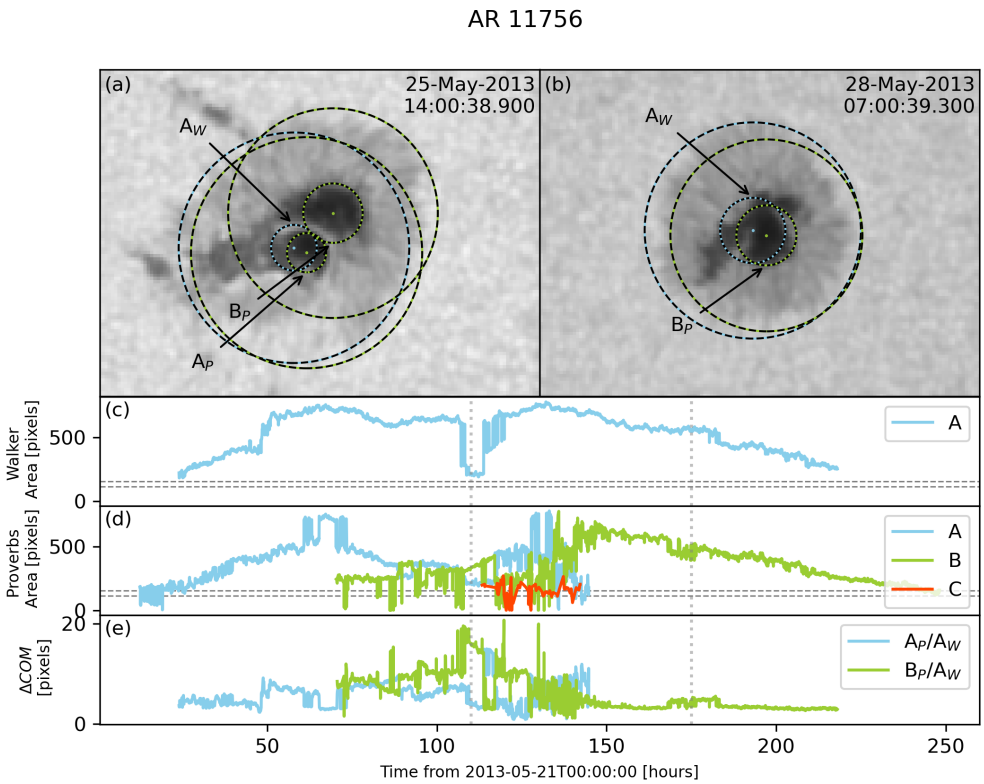

Figure 3.10: Tracking profiles for AR 11756: (**a,b**) image of the sunspots from 25 May 2013 at 14:00:39 UT and 28 May 2013 at 07:00:39 UT, respectively, with the identified penumbral and umbral radii overlaid from both identification methods; (**c**): the reprojected umbral area profile for the sunspots identified by the Walker method; (**d**): the reprojected umbral area profile for the sunspots identified by the Proverbs method; (**e**): the difference in recorded sunspot centre of mass for the comparable sunspots identified by both methods.

observations of each of the sunspots associated with C_W, the durations are much more similar.

Analysis of AR 11732

The Walker method was able to identify a sunspot in active region 11732 (Figure 3.12) that was observed for over 48 hours longer than the corresponding sunspot identified using the Proverbs method (sunspots B_W and B_P). The trailing sunspot in the active region undergoes a split between the observations presented in Figure 3.12a and 3.12b. The larger component of this sunspot dissipates into the penumbral region and falls below the umbral intensity threshold. This is found in both methods. The secondary split (C_P) is identified in the Proverbs method, but never exceeds the area threshold for the rotation analysis and so is not included in the final dataset. The Walker method considers sunspot C_P to be the same structure as the earlier identified B_W. When comparing the duration of observations of sunspots B_W, B_P and C_P, the Proverbs method identifies these structures for almost 100 hours longer than the Walker method.

3.2.3 Rotation Comparison

The rotation profile of each sunspot about its umbral centre was calculated for both the Walker and Proverbs method, and the cumulative rotation of each sunspot is shown as a scatter plot in Figure 3.13. As shown by the rotation comparison, the majority of commonly identified sunspots in the Proverbs dataset have a rotation of $\pm 45^\circ$ of the Walker method rotation calculations. This is a relatively large spread. However, Figure 3.14 shows how the situation improves when only the rotation during the overlapping periods is considered. The rotations have more similar rotation profiles, with three notable outliers, active region 11762, 11809 and 11793 (A, B and C, respectively). These active regions are discussed in further detail in the following

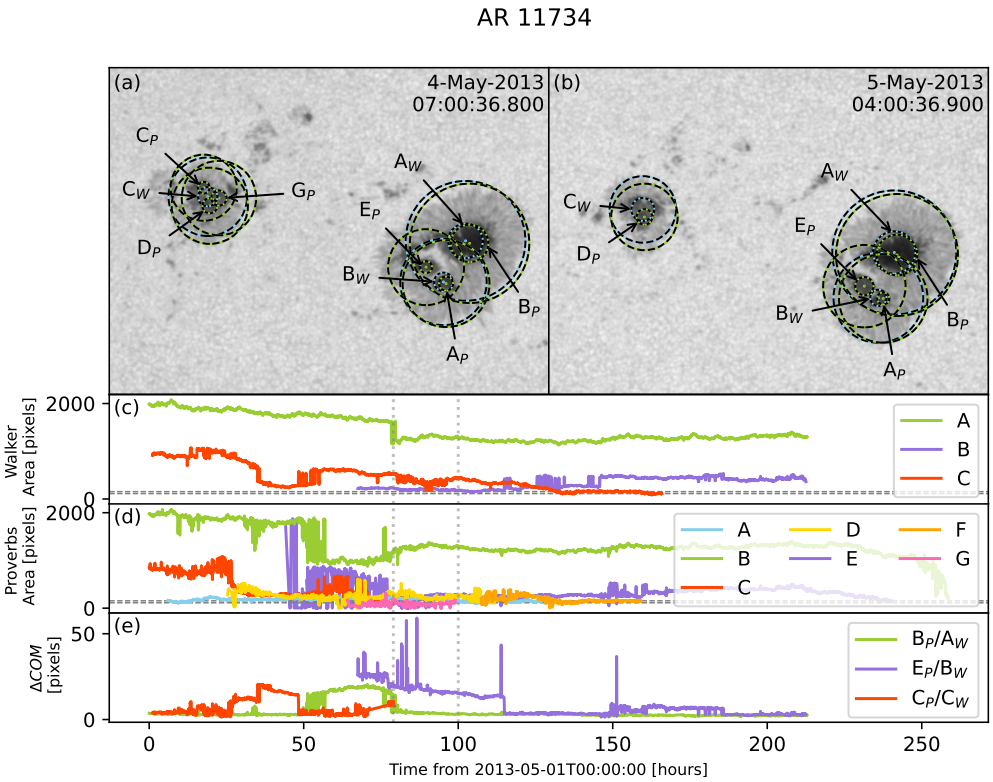

Figure 3.11: Tracking profiles for AR 11734: (**a,b**) image of the sunspots from 4 May 2013 at 07:00:36 UT and 5 May 2013 at 04:00:37 UT, respectively, with the identified penumbral and umbral radii overlaid from both identification methods; (**c**): the reprojected umbral area profile for the sunspots identified by the Walker method; (**d**): the reprojected umbral area profile for the sunspots identified by the Proverbs method; (**e**): the difference in recorded sunspot centre of mass for the comparable sunspots identified by both methods.

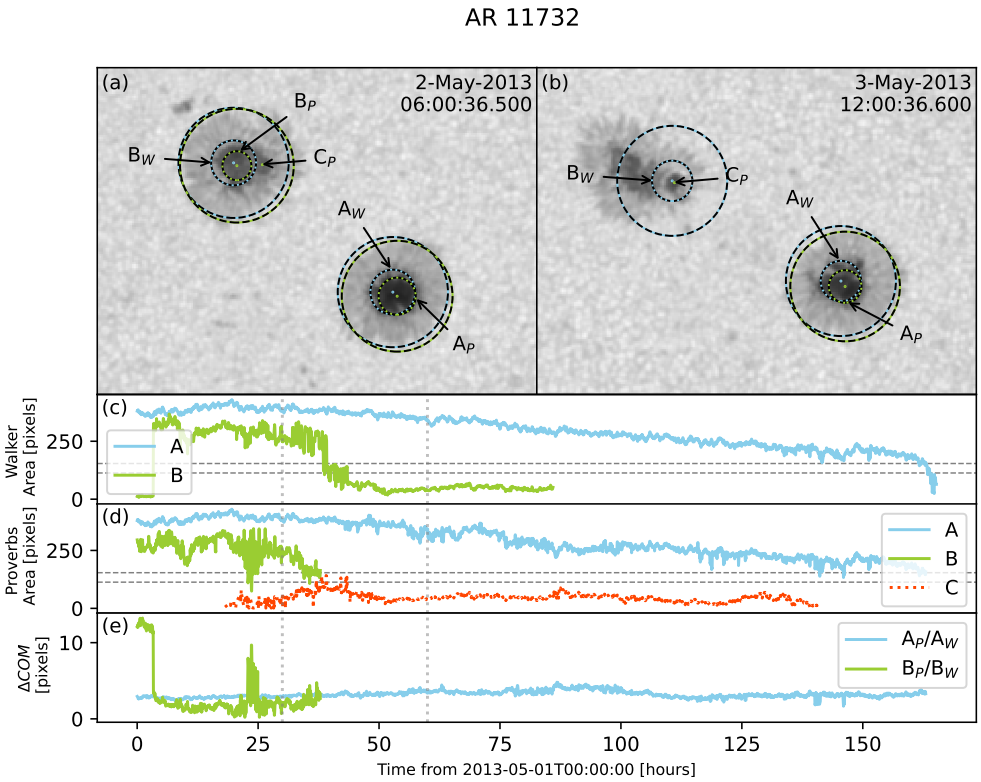

Figure 3.12: Tracking profiles for AR 11732: (**a,b**) image of the sunspots from 2 May 2013 at 06:00:37 UT and 3 May 2013 at 12:00:37 UT, respectively, with the identified penumbral and umbral radii overlaid from both identification methods; (**c**): the reprojected umbral area profile for the sunspots identified by the Walker method; (**d**): the reprojected umbral area profile for the sunspots identified by the Proverbs method; (**e**): the difference in recorded sunspot centre of mass for the comparable sunspots identified by both methods.

sections.

Analysis of AR 11762

From A in Figure 3.14, active region 11762 contains a sunspot (A_P and B_W) that is recorded to experience over 45° more rotation using the Walker method than the Proverbs method. Interestingly, when using Figure 3.13 to compare the two rotation profiles, the total rotation over both full observational periods is nearly the same. Figure 3.15e shows the greatest variation in rotation occurs at the start of the observation period for both methods, and this difference is also recorded in the change of centre of mass (Figure 3.15g). Subsequent observations have a much more similar rotation pattern.

Analysis of AR 11809

Active region 11809 is represented by point B in Figure 3.13 and 3.14. In Figure 3.14 AR 11809 displays almost 0° of rotation when using the Proverbs dataset, and almost 45° of rotation when using the Walker set, but in Figure 3.13 both methods observe approximately $-45°$ of rotation. The sunspots of interest within this active region are A_P and A_W, the rotation profiles of these sunspots are shown in Figure 3.16.

The Proverbs method identifies sunspot A_P over fifty hours earlier than the Walker method, observing over 25° of rotation in this period. At the beginning of the joint observation period the Proverbs method tracks a clockwise rotation whereas the Walker method tracks an anti-clockwise rotation. During this observation period the sunspot is undergoing a split, Figures 3.16a, b, c, and d show the sunspot centre for the Walker and Proverbs method displayed over the photospheric data. The Proverbs method is able to identify this split and continues to track the larger centre of mass, the Walker method continues to track the full structure, causing the increase

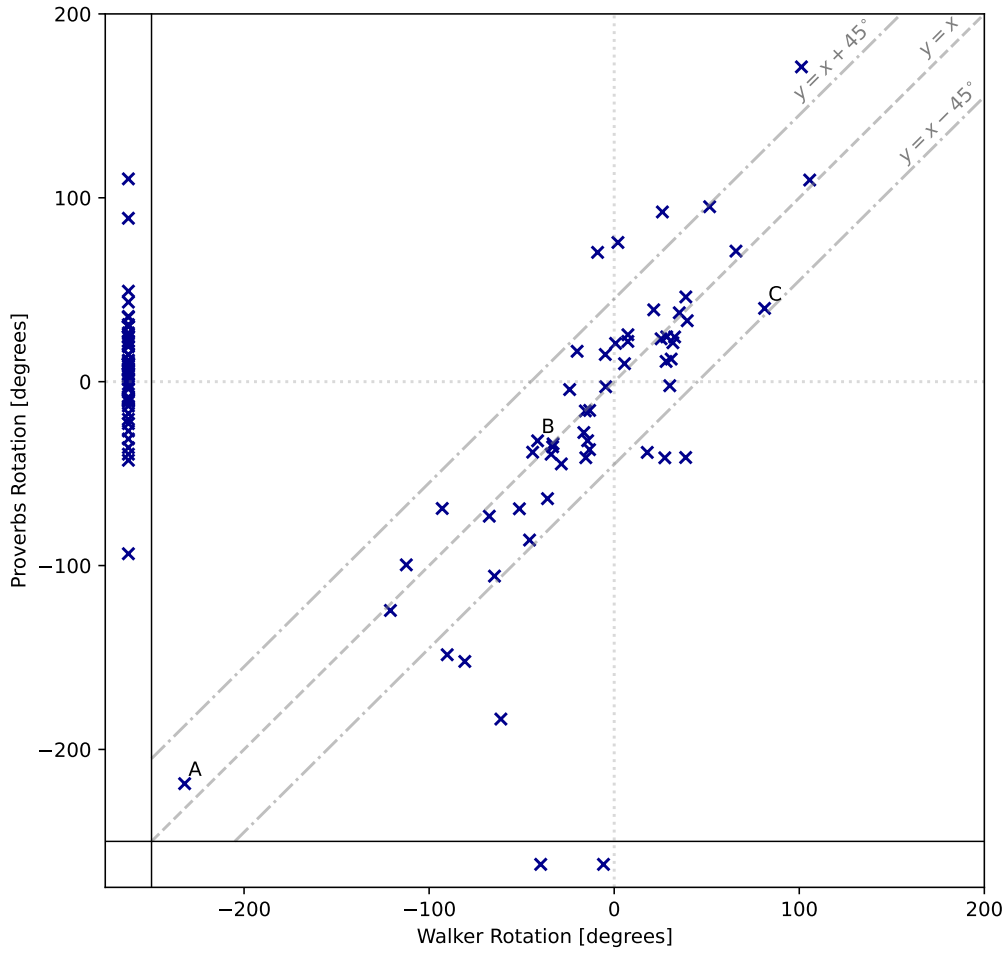

Figure 3.13: Net rotation comparison (in degrees) of sunspots identified using the Walker method and the Proverbs method. Sunspots only tracked using the Proverbs method are on the left of the figure, and sunspots only tracked using the Walker method are at the bottom of the figure.

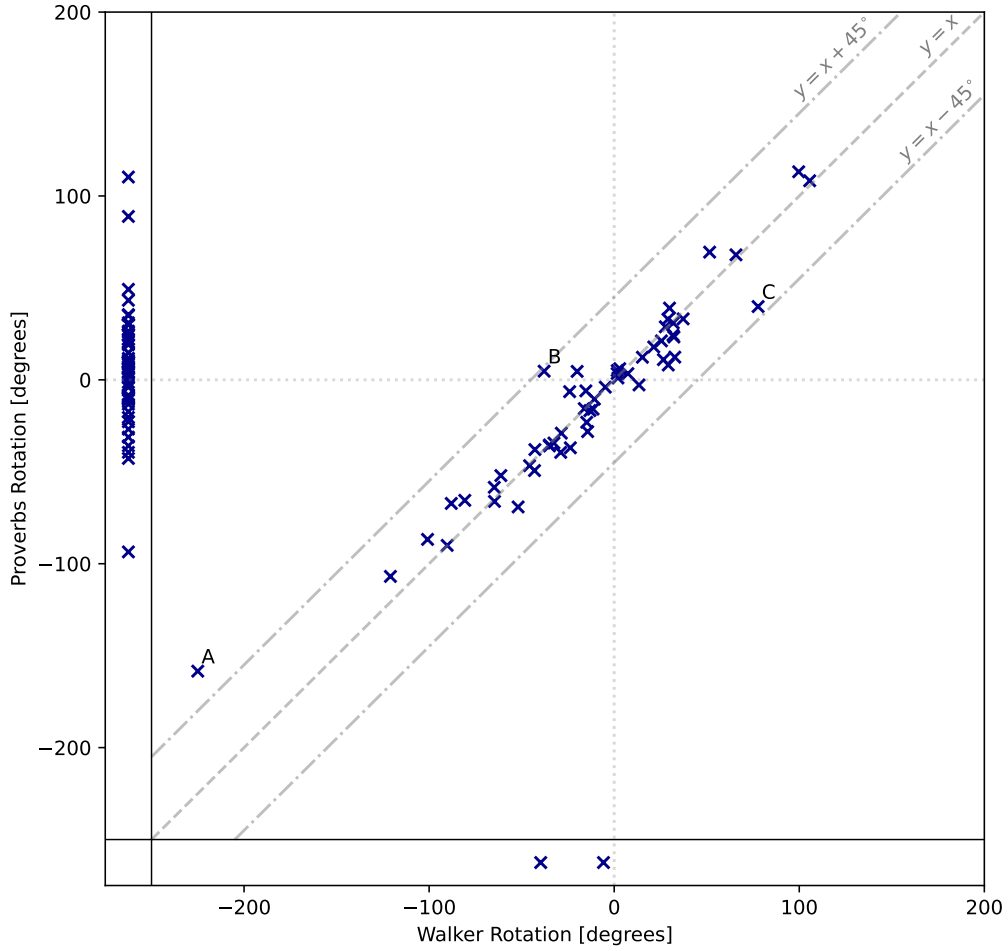

Figure 3.14: Net rotation comparison (in degrees) of sunspots identified using the Walker method and the Proverbs method using only observations found with both methods. Sunspots only tracked using the Proverbs method are on the left of the figure, and sunspots only tracked using the Walker method are at the bottom of the figure.

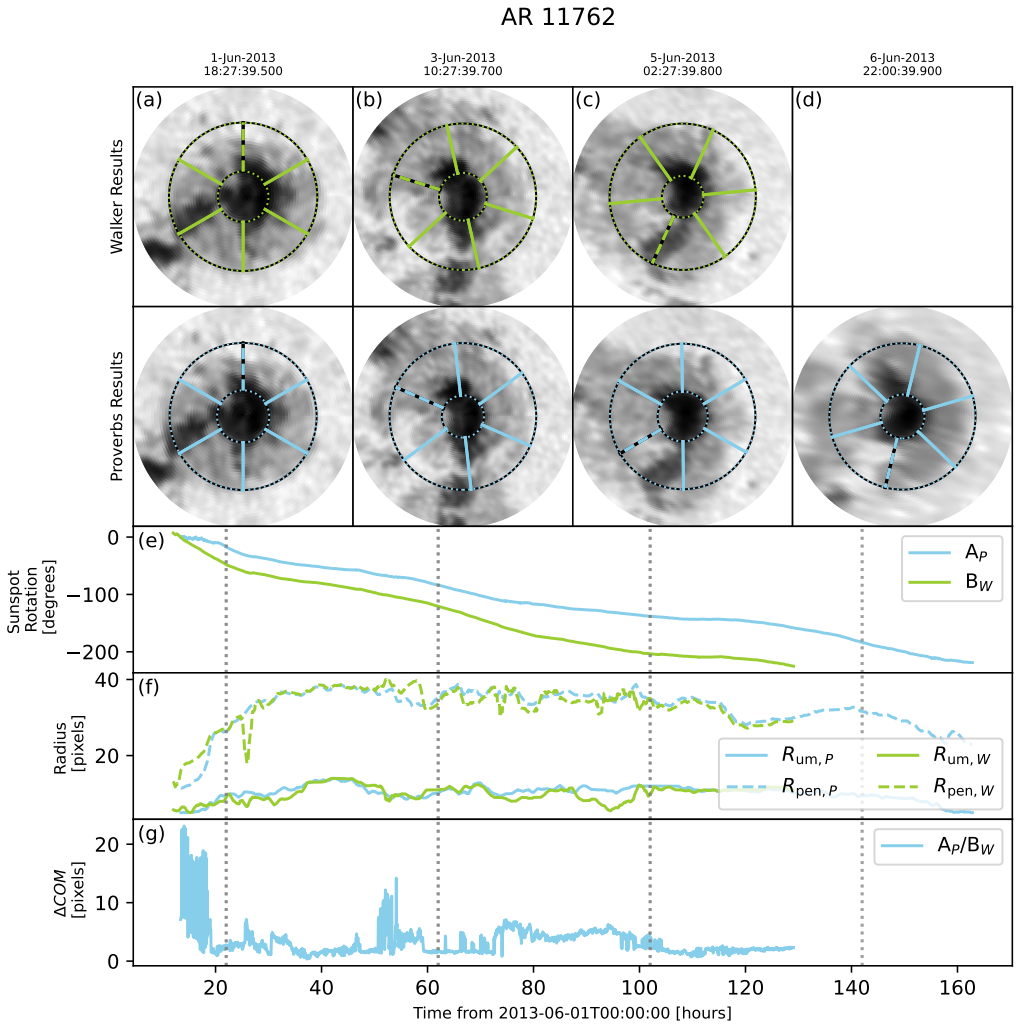

Figure 3.15: Rotation profiles for AR 11762: (**a, b, c, d**) reprojected image of the target sunspot to the solar centre from 1 June 2013 at 18:27:40 UT, 3 June 2013 at 10:27:40 UT, 5 June 2013 at 02:27:40 UT and 6 June 2013 at 22:00:40, respectively, with the identified penumbral and umbral radii overlaid and the rotation indicated by the dashed spoke; (**e**) the recorded net rotations of the sunspot in degrees using the Walker and Proverbs data; (**f**) the penumbral and umbral radii profiles of the sunspot from the Walker and Proverbs datasets; (**g**) the difference in recorded sunspot centre of mass for the comparable sunspots identified by both methods.

in ΔCOM shown in Figure 3.16g. The penumbral bounds for the Walker observation contain umbral pixels, this could lead to the difference in rotation direction shown in Figure 3.16e. After this initial rotation difference the rotation profiles become very similar between the two methods, with the difference in final cumulative rotation mostly being contributed by the initial difference in rotation direction.

Analysis of AR 11793

Rotation comparison C from Figures 3.13 and 3.14 compares the rotation profile from sunspots C_P and B_W from active region 11793. The rotation profile of these sunspots is presented in Figure 3.17e. Over the observed period, the Proverbs method identifies less rotation per observation. At 230 hours the difference between the rotation profiles of the two methods is approximately 10°. After this point the sunspot appears to begin a slight split, this is visible in Figure 3.17c, and shown by the decrease in umbral area for sunspot C_P (Figure 3.17f) and the sudden increase in difference in centre of mass (Figure 3.17g). The Walker method does not identify the split, and the rotation profile continues in a similar manner. The Proverbs method does identify the split, considering the left-most side of the umbral region to be the continuation of the sunspot, and the rotation profile begins to plateau. Both methods identify a change in rotation direction towards the end of the observational period. The Proverbs method shows a steeper negative inclination than the Walker method, resulting in a final rotation difference of 40°.

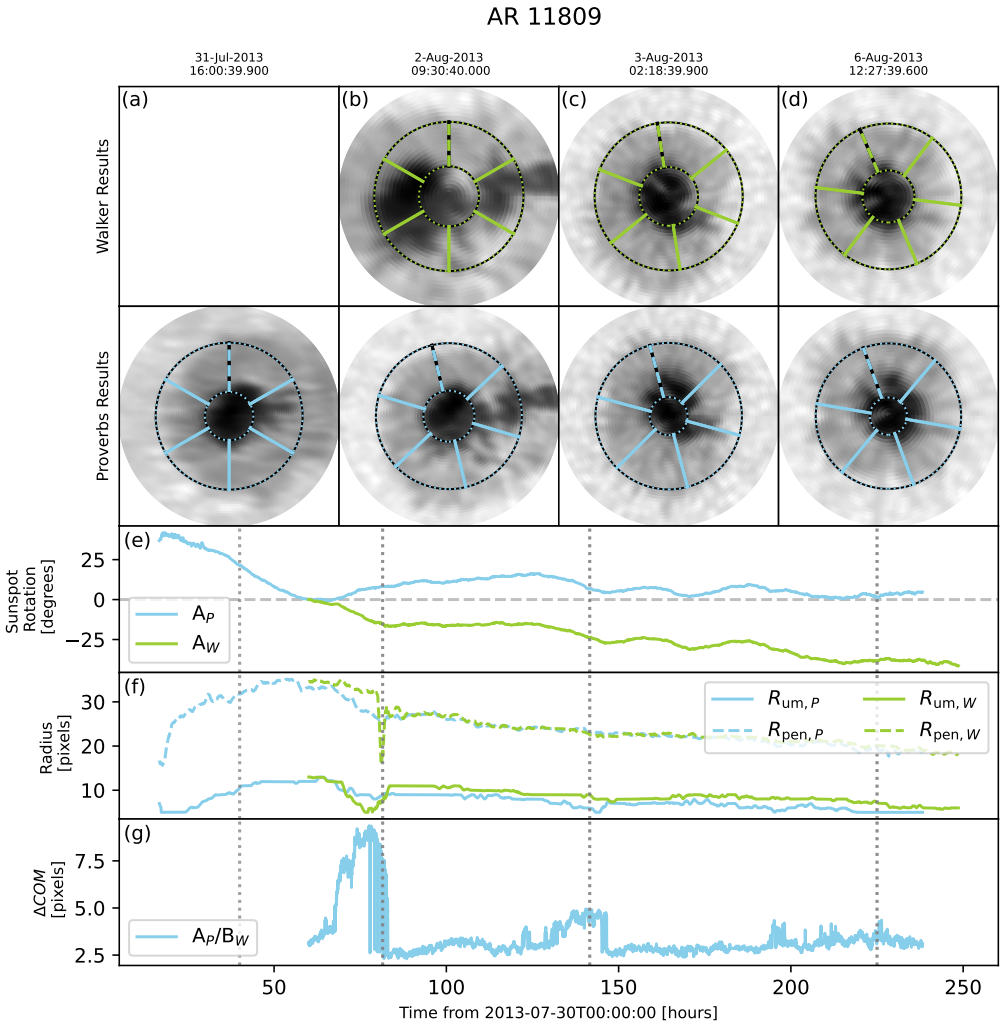

Figure 3.16: Rotation profiles for AR 11809: (**a, b, c, d**) reprojected image of the target sunspot to the solar centre from 31 July 2013 at 16:00:39 UT, 2 August 2013 at 09:30:40 UT, 3 August 2013 at 02:18:40 UT and 6 August 2013 at 12:27:40, respectively, with the identified penumbral and umbral radii overlaid and the rotation indicated by the dashed spoke; (**e**) the recorded net rotations of the sunspot in degrees using the Walker and Proverbs data; (**f**) the penumbral and umbral radii profiles of the sunspot from the Walker and Proverbs datasets; (**g**) the difference in recorded sunspot centre of mass for the comparable sunspots identified by both methods.

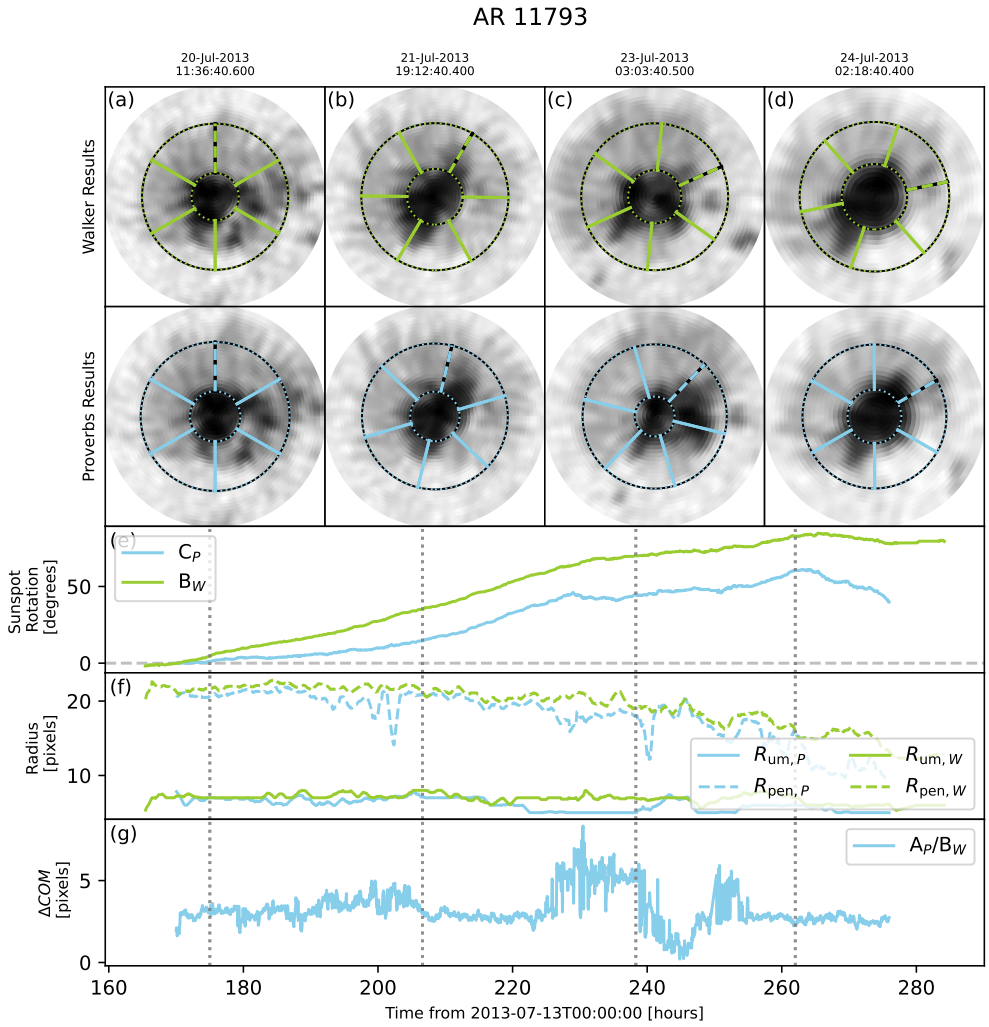

Figure 3.17: Rotation profiles for AR 11793: (**a, b, c, d**) reprojected image of the target sunspot to the solar centre from 20 July 2013 at 11:38:41 UT, 21 July 2013 at 19:12:40 UT, 23 July 2013 at 03:03:41 UT and 24 July 2013 at 10:21:40, respectively, with the identified penumbral and umbral radii overlaid and the rotation indicated by the dashed spoke; (**e**) the recorded net rotations of the sunspot in degrees using the Walker and Proverbs data; (**f**) the penumbral and umbral radii profiles of the sunspot from the Walker and Proverbs datasets; (**g**) the difference in recorded sunspot centre of mass for the comparable sunspots identified by both methods.

3.3 Discussion and Conclusions

This chapter has detailed the results of a new method to automatically identify and track sunspots using data from the Solar Dynamics Observatory's Helioseismic and Magnetic Imager, the Proverbs method. The resulting metadata from this method can be fed into various sunspot dynamic analysis methods to investigate the correlation with sunspot dynamics and the build up of energy within active regions. The method is able to identify variations in the umbral structure of a sunspot, such as sunspot splitting and mergers, and track each component accurately.

The method is tested on a four-month sample of data that had been previously analysed using a semi-automatic method by Walker (2018). Three characteristics are compared, is the Proverbs method able to identify all sunspots found by the Walker method, is the Proverbs method able to track each commonly-found sunspot for the same duration as the Walker method, and how do the rotation profiles of the sunspots compare between methods.

The Proverbs method was able to identify 107 sunspots over 49 active regions, including 54 of the 56 sunspots that were found using the Walker method, with the two unidentified sunspots belonging to active regions 11824 and 11835. The missing sunspot from AR 11824 was identified using the Proverbs method, but the sunspot split into two structures approximately 17 hours after identification. Due to this structural change the sunspot did not meet Walker's 24-hour size criteria for the rotation analysis, and was not included in the final Proverbs dataset. The Walker method identified a structural change, but was not designed to handle splitting or merging sunspots, so considered the sunspots to be a single structure for 24.6 hours, so it was included in the final dataset. The Walker method also identified an extra sunspot in AR 11835, however this sunspot is included in the Proverbs dataset. Both methods identify the splitting of sunspot A_P and A_W, however the Walker method records this sunspot after the split as sunspot AA_W, whilst the Proverbs

method records the sunspot as a continuation of A_P. Due to the difference in naming convention, it appears that the Walker method identifies a sunspot that the Proverbs method does not, however this is not the case. Generally the Proverbs method was able to reliably detect more complex sunspot structures than the Walker method.

When comparing the duration of the commonly identified sunspots, the Proverbs method is typically able to identify sunspots for longer than the Walker method, with thirteen sunspots being visible in the Proverbs method for over 48-hours longer than in the Walker method. The periods observed by both methods had very good agreement, with less than 10 pixels variation between the centre of the sunspots for most observations. There were three cases where Walker was able to track a sunspot for at least forty-eight hours longer than those identified with the Proverbs method. These active regions are AR 11756, 11734 and 11732. In each of these cases the Proverbs method was able to detect structural changes within the sunspot under investigation. Each of these sunspots split into multiple, smaller sunspots over the observation period, with some of these components dissipating into the penumbra. Because of the added sensitivity regarding sunspot splits and merges from the Proverbs method, the duration of these splitting sunspots is much less than with the Walker method, which typically ignores this substructure and considers them to be one single sunspot.

The rotation about umbral centres was calculated for each sunspot using the tracking data from both methods. When comparing all observations of the 54 common sunspots, there was a large amount of variation between the methods, with 10 sunspots having a difference in rotation greater than 45°. When only comparing the rotation during overlapping observations per sunspot, there was much greater agreement between the two methods, with only one sunspot having more than 45° difference between the methods.

Overall, the Proverbs method has a few key advantages over the Walker method.

Firstly, the Proverbs method is fully automatic, whereas the Walker method required initial identification and additional parameterisation to be included by hand for each sunspot under analysis. As all sunspots that fulfil the rotation criteria are identified without manual interference, the Proverbs method is able to identify 53 more sunspots than the Walker method over this period. The Proverbs method was also able to identify many smaller sunspots, and generally was able to detect sunspots earlier and track them for longer, having knock on effects to the rotation calculations. Secondly, the method is more sensitive to structural changes within the umbral region of a sunspot. The method has successfully tracked the splitting and merging of sunspots throughout the four-month sample, this was a weakness of the Walker method, which successfully tracked the larger scale movements of sunspots but struggled to identify the small-scale variations.

Even in the few cases where the Walker method appears to 'outperform' the Proverbs method, further investigation shows this to not be the case, rather the Proverbs method has handled splitting and mergers more elegantly leading to differences in classification rather than a failure to identify sunspots.

Chapter 4

Investigating the relationship between sunspot rotation and solar flares in a twelve-month sample of active regions

4.1 Introduction

As the sunspot identification and tracking method has shown good agreement with the four-month testing period, (chapter 3), the method can now be applied to an extended dataset to generate a larger statistical sample. The benefit of looking at extended periods is that the sample will contain a range of activity levels, from ARs exhibiting no or low numbers of flares up to highly active regions that produce several X and M-Class flares. This chapter will discuss the analysis of a twelve-month statistical sample from the rise phase of solar cycle 25.

4.1.1 The Sample

The twelve-month sample is defined by date and some of the selection criteria detailed in Walker (2018). The sunspot effective umbral radius must be greater than seven-pixels and the sunspot must have an effective angular extent between $-60°$ and $60°$ for at least twenty-four hours. Walker (2018) used one criterion that is not followed in this work: the exclusion of interacting sunspots (including umbral splits and mergers). The Proverbs method was designed to reliably track sunspots undergoing these structural changes, so these sunspots are included in the analysis.

The time period of 1 March 2023 - 28 February 2024 (highlighted in Figure 4.1) is chosen as it covers the lead up to the maximum of solar cycle 25. Out of the 189 active regions identified, 103 ARs have flares, whilst 86 ARs have no flares. In total there are 730 flares associated with active regions within the sample period, six of these were X-Class flares, ninety-eight were M-Class flares, and 626 were C-Class flares.

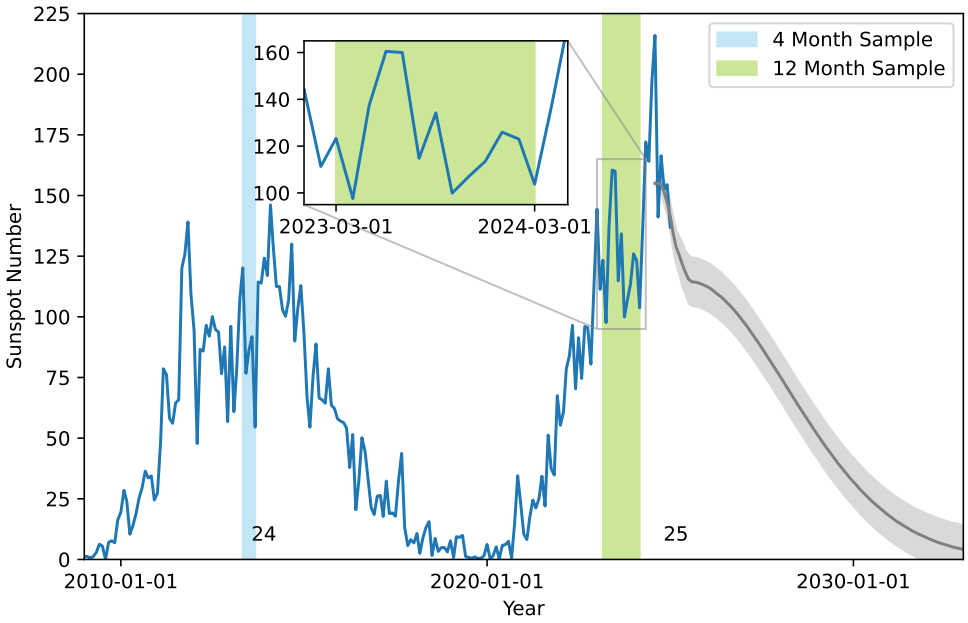

Figure 4.1: Solar cycles 24 and 25 presented using recorded and predicted sunspot number data from NOAA since 1 January 2008. The blue shaded region represents the four-month sample period, the green shaded region represents the twelve-month sample. The inset figure shows the activity over this period in more detail.

4.2 Analysis

The sunspots that pass the analysis criteria (listed in section 3.1.1) are fed into to the rotation algorithm created by Brown & Walker (2021). Following Walker (2018) the rotations are summed to generate R_{net}, R_{mid} and R_{abs} for each active region, and the estimated energy build-up within the active regions is calculated using the method discussed in section 2.3 using the rotation values for each active region under analysis. The sunspot area is converted into sunspot magnetic flux, and the added helicity is calculated using the sunspot flux and rotation. This helicity is converted into estimated sunspot energy and this is summed across the active region. The energy output from bolometric flare radiation is calculated using the method in section 2.4.

4.3 Results

This section will discuss the area and rotation properties of the active regions within the twelve-month statistical sample.

4.3.1 Sunspot Area

There are 560 sunspots in this period within 189 active regions, Figure 4.2 displays the area distribution of the sunspots under analysis. The majority of sunspots within the sample have a reprojected area of less than 500 pixels, whilst two sunspots have an area greater than 2500 pixels, sunspots 13363A and 13590A. The area of an active region is determined by summing the sunspot areas, the active region area is compared to the estimated bolometric flare energy output in Figure 4.3. Points below the dotted line belong to active regions with no assigned flares. The active region umbral areas ranged from 107 - 10819 pixels, with an average value of 973 pixels. The error from the umbral area calculations varied between 0.35 - 404 pixels,

with an average value of 11 pixels. The active region with the largest combined umbral area and the largest flaring output is active region 13576, which contains three sunspots with individual umbral areas exceeding 1000 pixels.

Figure 4.3 shows that relationship between active region area and the flaring energy. The correlation analysis produces a correlation coefficient of $r = 0.4$ with a P-value of 0.0002, so smaller active regions are less likely to flare, whilst larger active regions with more sunspots are more likely to exhibit higher energy flaring activity. However, there is a limited discernible pattern due to the scatter of the data, so other mechanisms are having an appreciable effect.

The active region area probability distribution of both the flaring and non-flaring active regions is shown in Figure 4.4. The maximum probability difference between the flaring and non-flaring regions is 0.3 with a P-value of 6×10^{-11}, so the difference between the distributions is significant. The figure suggests that active regions with a smaller total umbral area are less likely to experience flaring activity. The next section will evaluate the correlation between sunspot rotation and flaring activity.

4.3.2 Sunspot Rotation

Out of the 189 active regions analysed as part of the sample, 4 active regions had at least one X-Class flare (13533, 13575, 13576 and 13590). Active regions 13576 and 13590 also had over 14 sunspots that fulfilled the analysis criteria (19 and 15, respectively). AR 13576 also exhibited over 500° of rotation, alongside active regions 13296, 13354, 13435, 13500 and 13559.

The individual sunspot rotations are combined to estimate the net and absolute rotation values of each active region under analysis, and the results are presented in Table B.1, alongside the flares associated with each active region.

The rotation profiles of the active regions are calculated using the method outlined in section 2.2. Figure 4.5 shows the net and absolute rotation for each sunspot

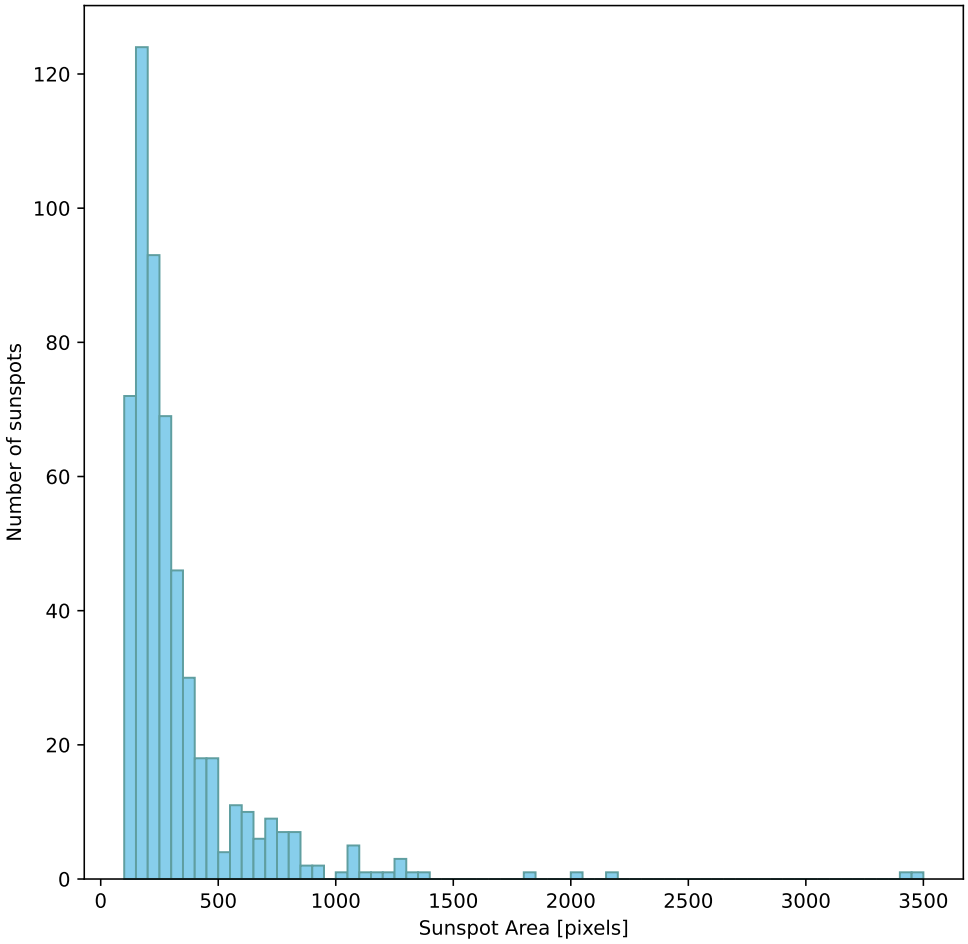

Figure 4.2: Histogram showing the distribution of average reprojected areas of sunspots within the twelve-month sample.

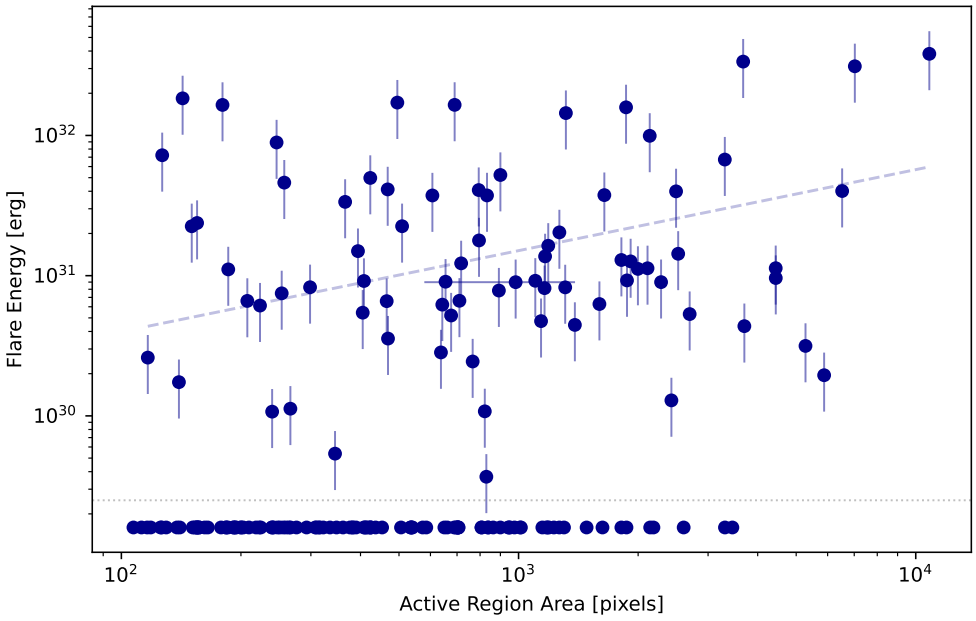

Figure 4.3: Active region umbral area versus flare energy in erg. Points below the dotted grey line represent active regions that have no associated flares. The blue dashed line shows the linear regression of the plot.

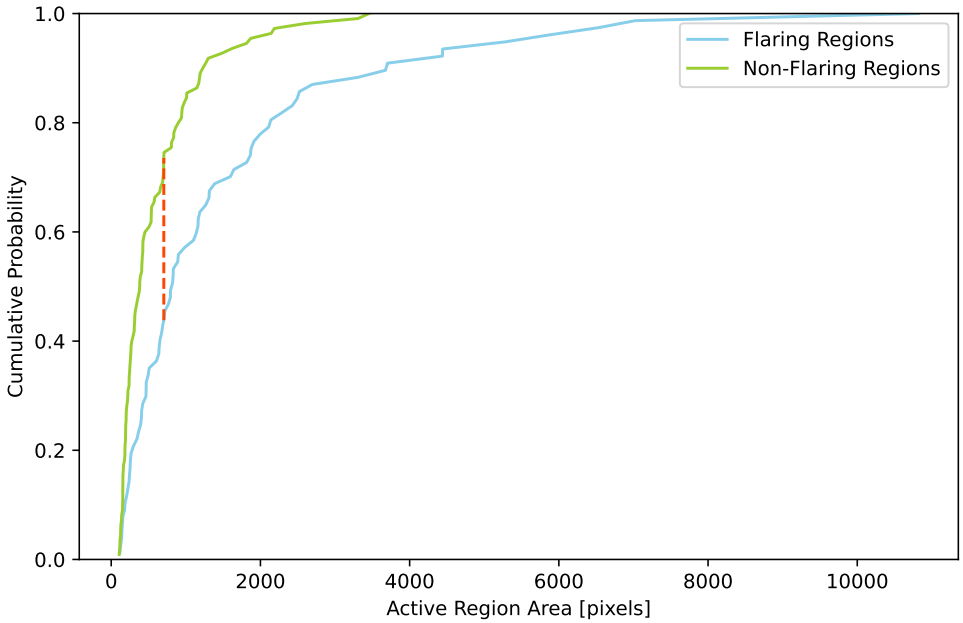

Figure 4.4: Probability distributions of active region areas for flaring and non-flaring regions. The blue line represents the flaring ARs, the green line represents the area distribution for non-flaring regions, and the red dashed line is the maximum difference between the two distributions (0.3 $P = 6 \times 10^{-11}$).

within the sample period. Within the sample, 450 of the sunspots exhibited less than 60° of net rotation (80%), with 338 (60%) of those sunspots rotating less than 30°. 53 sunspots (9%) rotated more than 90°, and the maximum net rotation by a single sunspot was $400° \pm 22°$. In terms of absolute rotation, 320 (57%) sunspots have less than 60° rotation, and 142 (25%) sunspots had over 90° rotation. The maximum absolute sunspot rotation was $405° \pm 22°$. Generally the absolute sunspot rotation is more widely distributed, but both distributions show most sunspots have rotation profiles of less than 30°.

Figure 4.6 shows the combined rotation distributions over active regions, rather than individual sunspots. R_{mid} was calculated for each active region using the method discussed in section 2.2 and Equation 2.19. Similar to the results from Figure 4.5, the majority of active regions exhibited $< 60°$ of net rotation (52%), with 31% of active regions having $> 90°$ net rotation. The absolute rotation distribution was skewed to be much higher, with only 12% of active regions exhibiting $< 60°$, whilst 71% of active regions display $> 90°$ of rotation. The mid rotation plot has a more even distribution, with 24% of active regions displayed $< 60°$ of rotation, whilst 60% of active regions exhibit $> 90°$ of rotation. The maximum rotation from a single active region was $489° \pm 79$ net from AR 13559, $656° \pm 331°$ mid and $1224° \pm 62°$ absolute from AR 13354. The mid rotation error is very high because it is scaled to the difference between the net and absolute rotation profiles, for this active region the net rotation is $89° \pm 62°$ and the absolute rotation is $1224° \pm 62°$.

The net, mid and absolute rotation of each active region is compared to the flare energy output in Figure 4.7. The active region rotation is presented in degrees on the x-axis, and the bolometric flare energy is on the y-axis. There is no significant correlation between rotation and energy in R_{net}, R_{mid} and R_{abs}, with correlation coefficients and P-Values of $r = 0.25$ and $P = 0.1$, $r = 0.24$ and $P = 0.1$, and $r = 0.25$ and $P = 0.1$. The points at the bottom of each sub-figure represent the

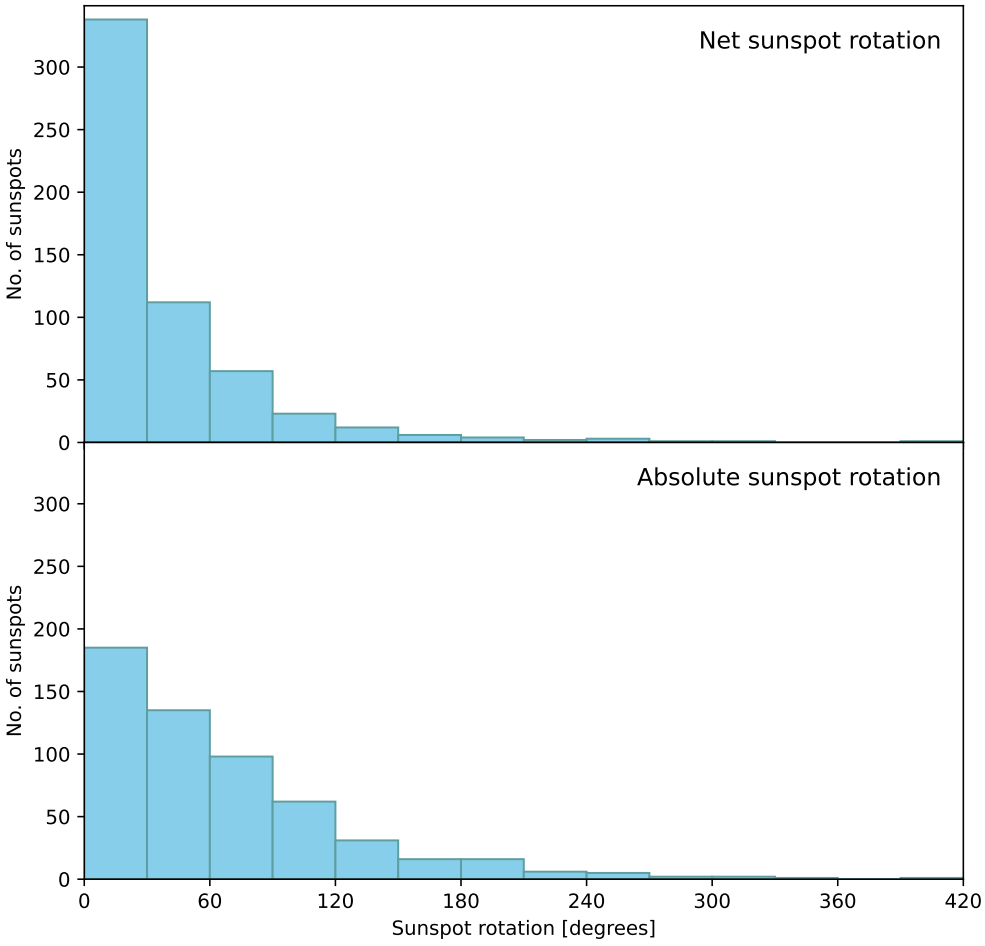

Figure 4.5: Histogram presenting the distribution of sunspot rotation within the twelve-month sample. The top figure shows the net sunspot rotation (R_{net}), and the bottom figure shows the absolute sunspot rotation (R_{abs}).

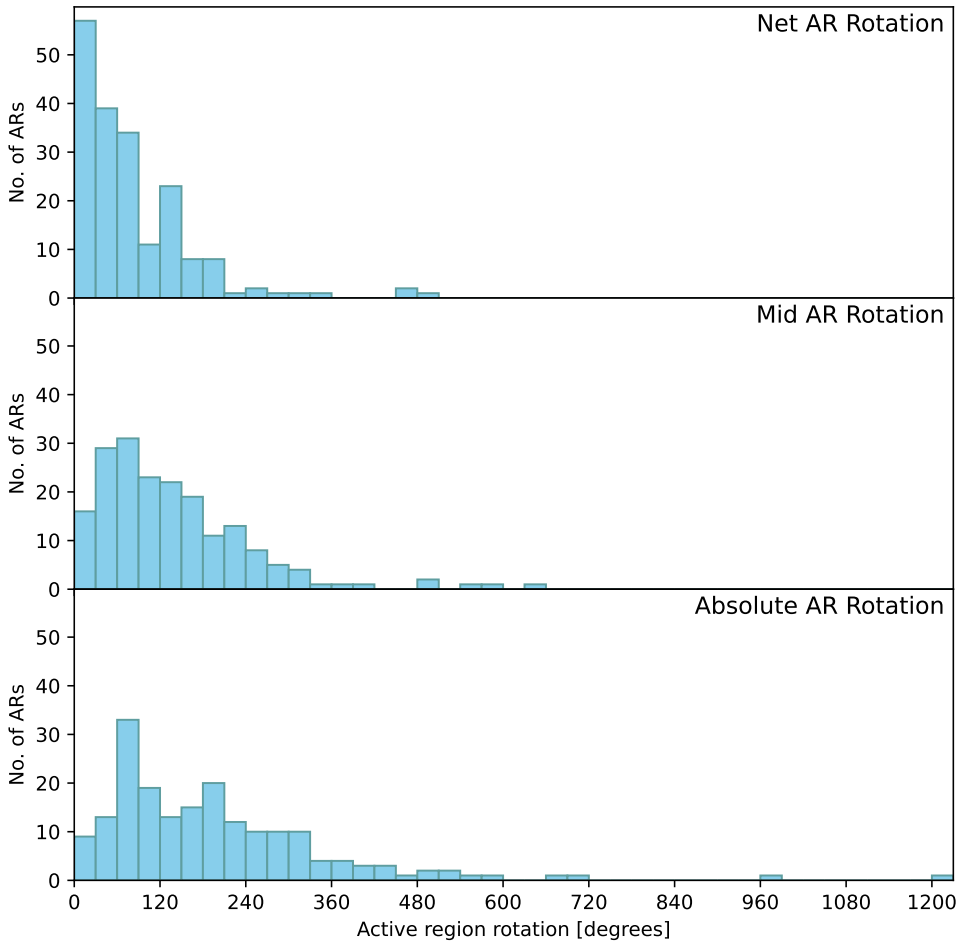

Figure 4.6: Histogram presenting the distribution of active region rotation within the twelve-month sample. The top figure shows the net active region rotation (R_{net}), the middle figure shows the mid active region rotation (R_{mid}), and the bottom figure shows the absolute active region rotation (R_{abs}).

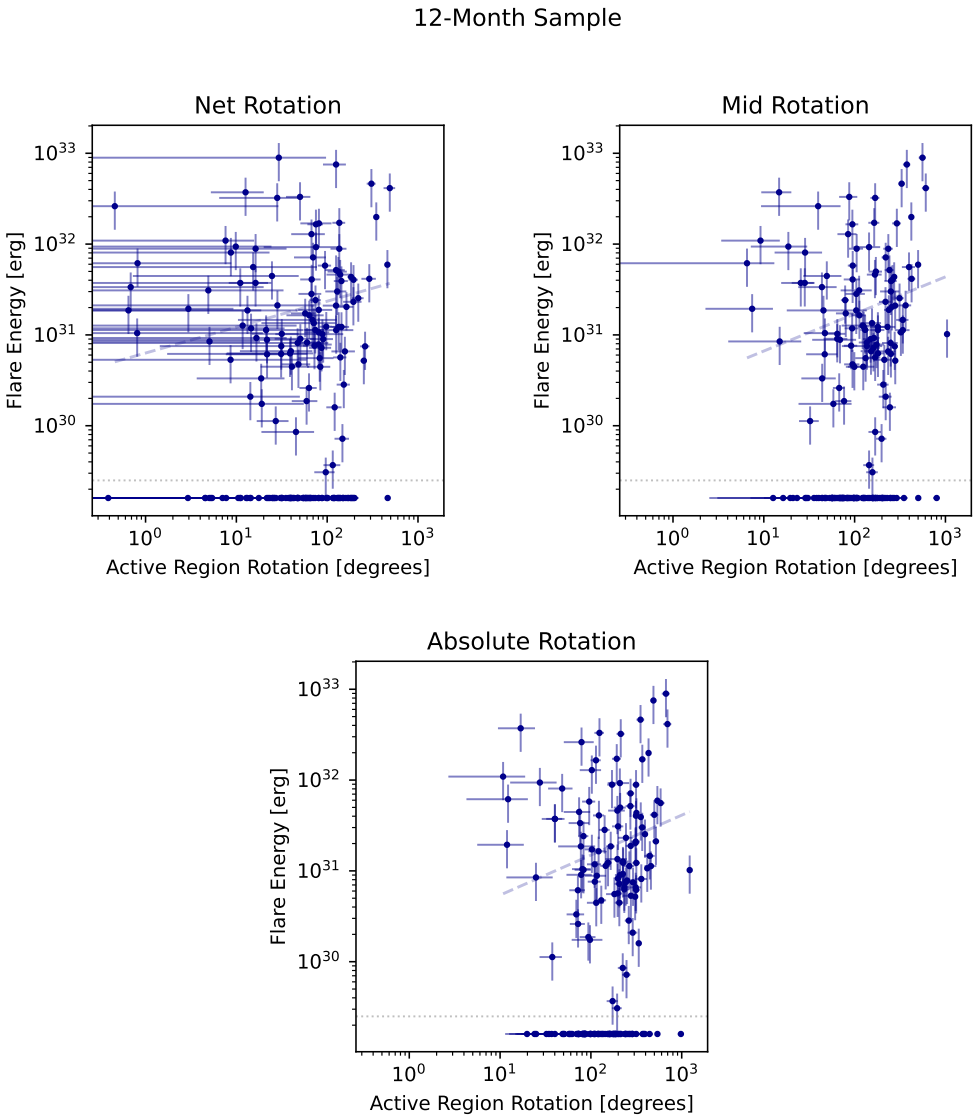

Figure 4.7: Active region rotation (degrees) versus bolometric flare energy (erg). The points below the dotted line represent active region rotations that do not have any assigned flares. The top left plot represents R_{net}, the top right plot represents R_{mid}, and the bottom plot represents R_{abs}. The blue dashed line shows the linear regression for each of the plots.

rotation of active regions that do not have flares assigned to them.

The K-S test from Figure 4.8 returns maximum probability differences of 0.16, 0.25, and 0.29 for the net, mid, and absolute rotations, respectively, with P-values 0.05, 0.001, and 2×10^{-5}. This shows that the results from the mid and absolute are significant and suggests that active regions that display less absolute rotation are more likely to be non-flaring regions.

The error from the net and absolute active region rotations varied between $6° - 74°$. This maximum error value is assigned to the rotation profile of AR 13500, which exhibits 980° of absolute rotation from eight sunspots. The most common error for the active regions was 26°. The error from the mid rotation profiles was similar the error associated with the net and absolute uncertainties. This error ranged from $5° - 74°$, with a typical value of approximately 26°.

Overall sunspot rotation does not show a correlation with flaring activity, but flaring and non-flaring active regions are two distinct populations in terms of mid and absolute rotation. The next section will apply the equations from section 2.3 to estimate the energy build-up in the active region to determine whether the rotation energy is sufficient to account for the bolometric flare energy.

The energy calculated from the net, mid and absolute rotation profiles of each active region from the sample period are presented in Table B.2, alongside the radiated flare energy from these active regions. The net rotation energy not only defines the minimum possible value for the energy, but also indicates the direction of rotation and helicity. Positive rotation energy correlates to anti-clockwise helicity, while negative rotation energy correlates to clockwise helicity. The 45% error on the flare energy comes from the conversion from optically thin energy to bolometric flare energy from Walker (2018).

The net rotation energy ranged between -24.7×10^{32} and 11.2×10^{32} erg, with an average energy of -0.2×10^{32}. The absolute rotation energy varied between

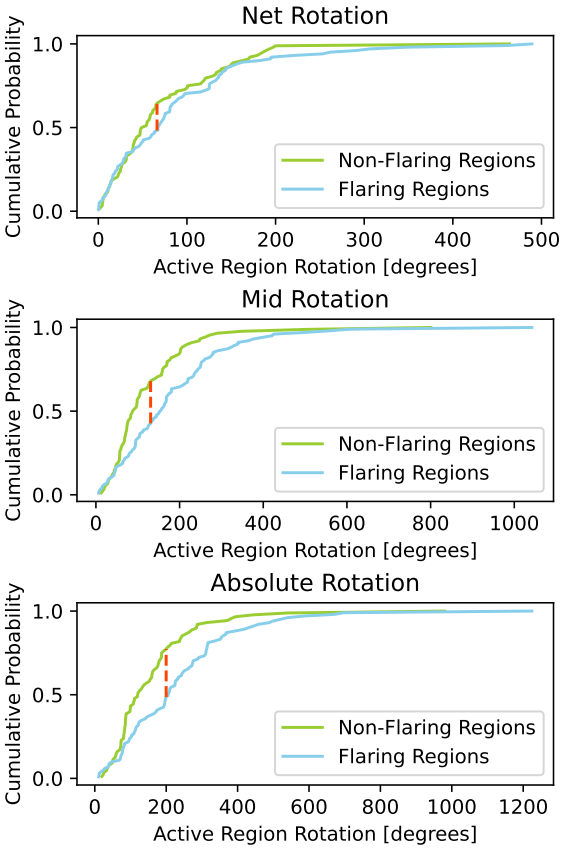

Figure 4.8: Cumulative distribution functions of the net, mid and absolute active region rotations for flaring and non-flaring active regions. The green lines are the distribution of the non-flaring regions, the blue lines are the distribution of the flaring regions, the red dashed lines are the Kolmogorov-Smirnov statistic. The KS value for the net, mid and absolute rotation distributions is 0.16, 0.25 and 0.29, respectively ($P = 0.05, 0.001, 2 \times 10^{-5}$).

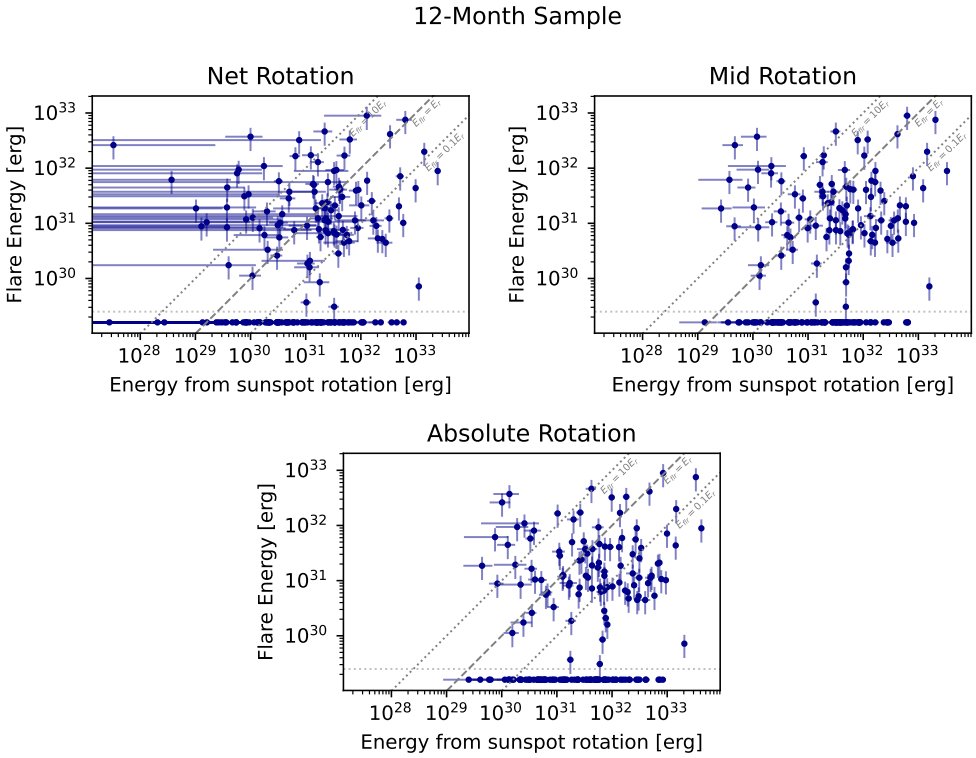

Figure 4.9: Energy from active region rotation (ergs) versus bolometric flare energy (erg). The points below the dotted line represent active region rotation energies that do not have any assigned flares. The top left plot represents E_{net}, the top right plot represents E_{mid}, and the bottom plot represents E_{abs}.

0.03×10^{32} and 41.6×10^{32} erg, with an average value of 1.7×10^{32} erg. The mid sunspot rotation range fell between the net and absolute values, ranging from 0.001×10^{32} to 33.0×10^{32} erg, with an average value of 1.3×10^{32} erg. The active region that exhibited the largest rotation energy values from the net, mid and absolute datasets was AR 13363, which had nine C-Class and 3 M-Class flares during the sample period. The error for the rotation energies varied between 8.8×10^{28} erg and 3×10^{32} erg, with average values of 0.2×10^{32} and 0.1×10^{32} erg for the net/absolute and mid rotations, respectively.

The active region flare energy ranged from 3.1×10^{29} to 8.9×10^{32} erg. The active region with the highest flare energy is AR 13576, this region had 98 C-Class flares, 23 M-Class flares and 1 X-Class flare. There are also 19 sunspots in this active region. Figure 4.9 shows the comparison between the net, absolute and mid rotation energies and the flare energy output tabulated in Table B.2. 72 active regions have excess energy due to absolute rotation, whilst 29 active regions do not generate enough energy to account for the solar flares. The net rotation figure shows significantly more scatter than the mid and absolute rotation profiles, but generally the points are scattered around the $E_r = E_{flr}$ line. The points at the base of the figures represent active regions that don't have any flares during the observed period. These active regions could have experienced flares before the active region became visible on the solar disc, and the rotation profile could be a relaxation of the active region following solar activity, or the active region could turn off the solar disc before the flares occurred.

Table 4.1: Table showing the distribution of flare energy and active region rotation ratios for the twelve month sample.

	$E_f > 10E_r$	$10E_r \geq E_f > E_r$	$E_r \geq E_f > 0.1E_r$	$0.1E_r \geq E_f$
Net	21	28	34	18
Mid	13	24	37	27
Abs	13	16	40	32

Table 4.1 shows the number of active regions that fall within different ranges of the radiated flare energy, when comparing the net, mid and absolute rotation energy. Most of the active regions fall within the $E_r \geq E_f > 0.1E_r$ range (34%, 37%, and 40%, respectively). The majority of the active regions generate more than enough energy to account for the flaring activity (51%, 63%, and 71% for net, mid, and absolute, respectively).

4.4 Conclusions

This chapter presented the results of a twelve-month statistical survey of observations from 1 March 2023 - 28 February 2024, covering the rise phase and initial peak of solar cycle 25. There are 560 sunspots that satisfy the sunspot criteria across 189 active regions. Out of these active regions 103 had solar flares. 730 solar flares were recorded in total, with six X-Class flares, ninety-eight M-Class flares and 626 C-Class flares.

The total area of each active region was compared to the bolometric flaring energy. The active region area ranged between $107 - 10819$ pixels. There was correlation between the active region area and the flare energy output. There is a slight trend towards larger active regions exhibiting more flare activity, and smaller active regions being more likely to not flare. A K-S test of the data (0.3, $P = 6 \times 10^{-11}$) showed that active regions with smaller umbral areas are less likely to release solar flares, and that flaring and non-flaring active regions are two distinct area populations.

From the tracked active region information, the rotation profiles of the sunspots were extracted. 80% of the sunspots exhibited less than 60° of net rotation, with the maximum absolute sunspot rotation exceeding 400°. When comparing active region rotation with the flare energy, the net rotation showed the largest scatter, however the net, mid and absolute rotation showed limited correlation with flare energy, with correlation coefficients of 0.25, 0.24, and 0.25 ($P = 0.1, 0.1, 0.1$). Figure 4.8 suggests that non-flaring active regions are less likely to experience large degrees of rotation. To quantify this relationship further, the energy build-up within the active region due to sunspot rotation was calculated and compared directly to the radiated bolometric flare energy.

The active region rotation energy shows a strong relationship with the bolometric flare energy. The data is more scattered when using the net rotation energy, with a

more compact distribution from the mid and absolute rotation energy. The sample shows that the rotation of sunspots within an active region can provide enough energy to the active region to account for the energy released during solar flares. For 64 active regions, the mid rotation energy exceeded that released by the solar flares, and for 27 of these active regions the mid rotation energy exceeded the flare energy by a factor of ten. As discussed in section 1.6, there are many different behaviours that contribute to the input and output of energy for an active region. This work only considers the build-up of energy due to sunspot rotation and the release of energy due to solar flares, or terms E_{rot} and E_{fl-rad} from Equation 1.10. The excess energy that is generated by sunspot rotation could be released in other ways, such as coronal mass ejections, or due to the flare energy calculation method not necessarily including all flares that could be assigned to the active region. The development of a flare detection and active region assignment program using SDO/AIA data could lead to more flares being assigned to the relevant active regions, and increased flare energy per active region.

One active region that was frequently highlighted by the results throughout this chapter was AR 13576. This active region had 19 sunspots, of which three had umbral areas exceeding 1000 pixels, the active region had the largest total umbral area (10819 pixels), and exhibited over 500° of mid rotation. The flaring activity from this active region was also high, there are 122 flares associated with this region, one of which is an X-Class flare. AR 13576 also had the highest radiated bolometric flare energy out of the sample, 8.9 erg, and the combined energy from absolute rotation accounts for this energy release. The next chapter will present two case studies of other active regions from the peak of solar cycle 25 that contained a high number of sunspots and released multiple X-Class flares.

Chapter 5

Investigating the rotation of sunspots within two high flaring active regions

5.1 Introduction

Following the analysis of the twelve-month sample (chapter 4), the tracking method is applied to two case study active regions that released a large amount of flares during 2024. The first active region, AR 13664, first rotated onto the solar disc in May 2024. 12 X-Class flares are associated with this region, and the associated CMEs were responsible for the May 2024 Gannon storm. AR 13664 was in the 99.5th percentile for active region area over 1874 May–2024, and the active region is in the 99.10th percentile for flux (Jaswal, Sinha & Nandy, 2025). The second active region, AR 13842 first appeared on the solar disc in September 2024, releasing 4 X-Class flares, leading to another solar storm in October 2024 (Xia et al., 2025). Both active regions have been the subject of many articles due to the intense auroral activity and geomagnetic storms that followed the increased solar activity (Hayakawa et al.,

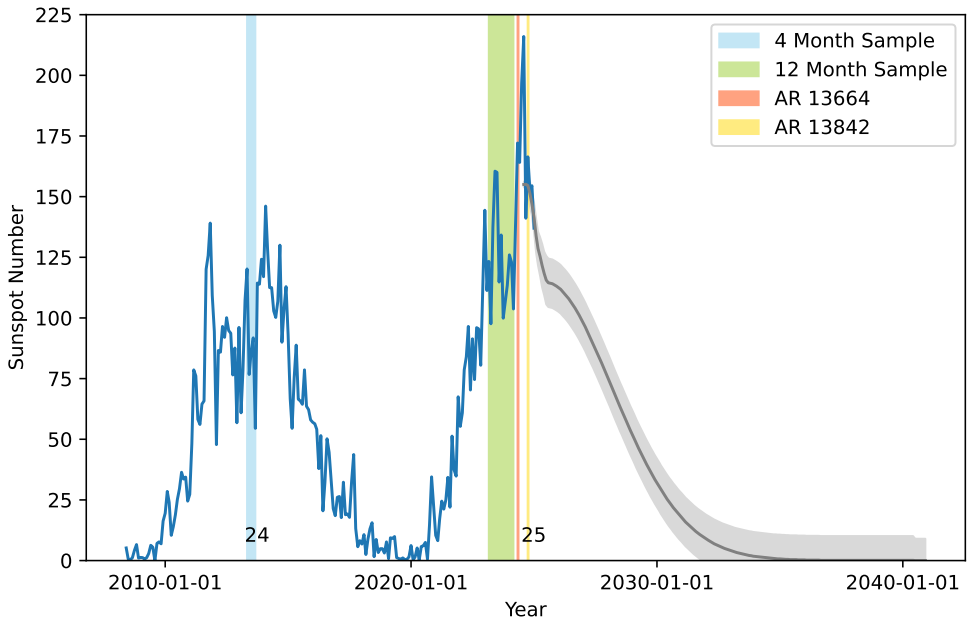

Figure 5.1: Solar cycles 24 and 25 presented using recorded and predicted sunspot number data from NOAA since 1 January 2008. The blue shaded region represents the four-month sample period, the green shaded region represents the twelve-month sample, the red shaded region represents AR 13664, and the yellow shaded region represents AR 13842.

2025).

The timings of the case study active regions can be seen in Figure 5.1. The red shaded region is AR 13664, and the yellow shaded region is AR 13842. Both of these periods fall during the peak of solar cycle 25.

5.2 Active Region 13664

Active region 13664 was first observed on 2 May 2024, and rotated off the solar disc on 14 May 2024. There are 39 sunspots in this active region that fulfil the analysis criteria from subsection 4.1.1. There are 100 GOES flares associated with

this active region, 36 C-Class, 52 M-Class, and 12 X-Class flares. The following section discusses the X-Class flares from this active region.

5.2.1 X-Class Solar Flares

Figures 5.2 and 5.3 show the active region in both SDO/HMI continuum and SDO/AIA 171 Å, the evolving nature of the sunspots in this active region is evident from the sequence. Flares occurring after 14 May 2024 00:00:00 are not included in these figures as the active region had rotated off-limb and useful photospheric measurements are not possible. Table 5.1 lists the GOES peak times and the flare class for each of the X-Class flares.

Table 5.1: X-Class flares associated with AR 13664

GOES Peak Time	GOES Flare Class
2024-05-08 05:09	X1.0
2024-05-08 21:40	X1.0
2024-05-09 09:13	X2.2
2024-05-09 17:44	X1.1
2024-05-10 06:54	X3.9
2024-05-11 01:23	X5.8
2024-05-11 11:44	X1.5
2024-05-12 16:26	X1.0
2024-05-14 02:09	X1.7
2024-05-14 12:55	X1.2
2024-05-14 16:51	X8.7
2024-05-15 08:37	X3.5

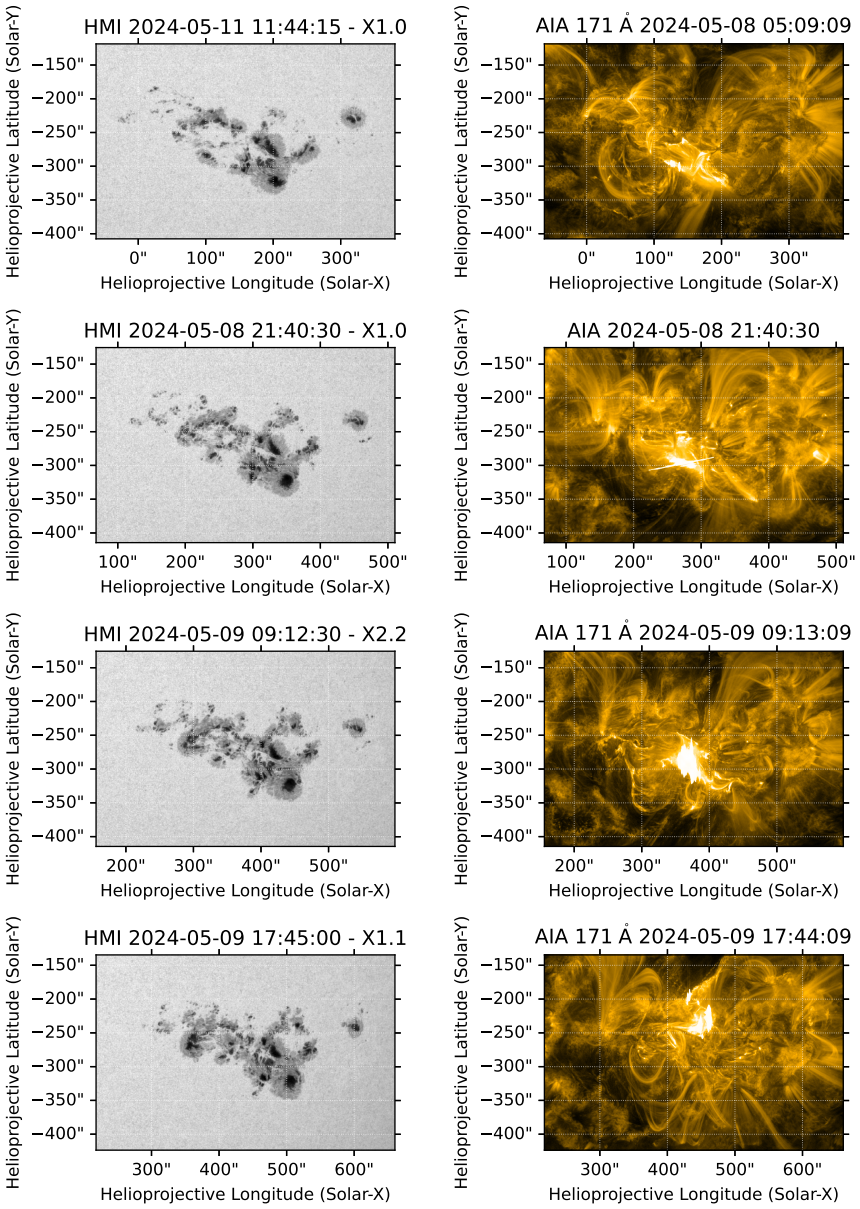

Figure 5.2: The left figures shows the SDO/HMI continuum image of AR 13664 during the peak time of the 8 May 2024 05:09 X1.0, 8 May 2024 21:40 X1.0, 9 May 2024 09:13 X2.2, and the 9 May 2024 17:14 X1.1 flares. The right figures shows the SDO/AIA 171 Å over the same period.

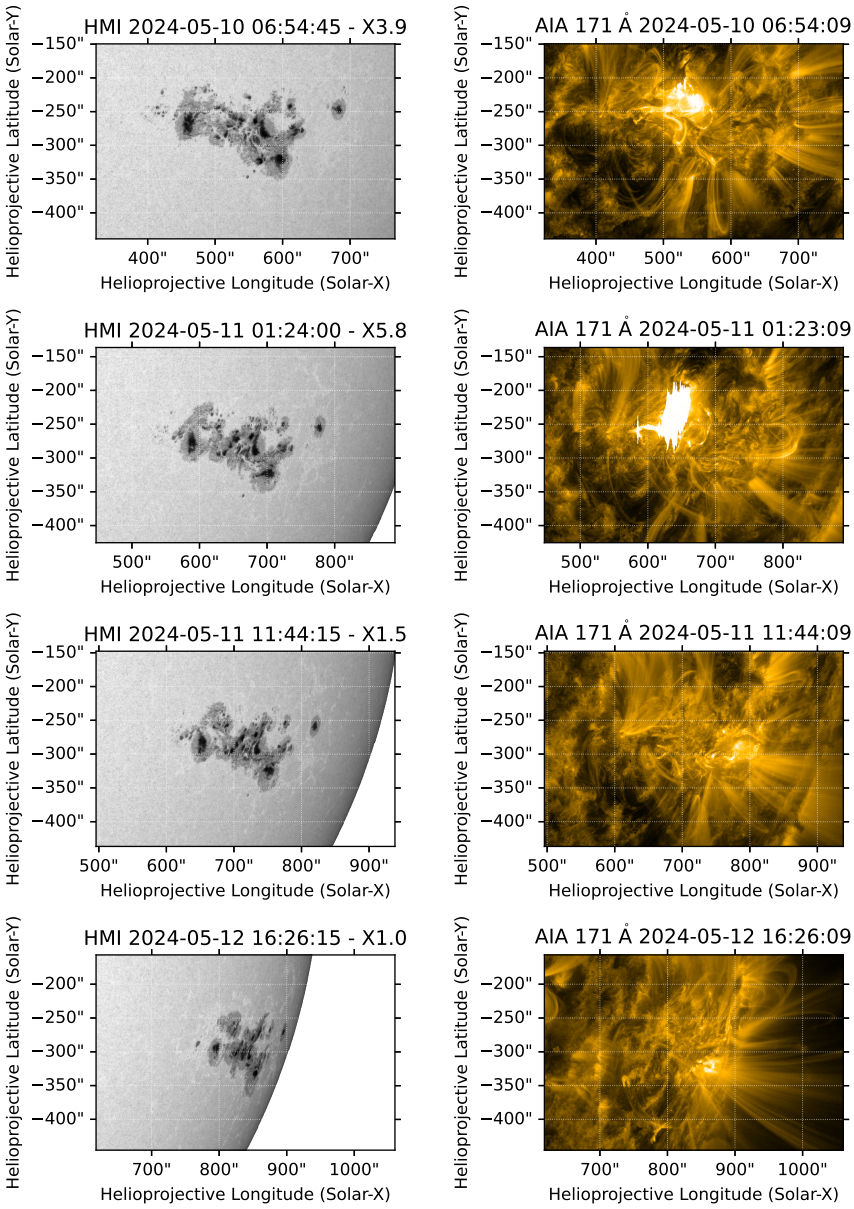

Figure 5.3: The left figures shows the SDO/HMI continuum image of AR 13664 during the peak time of the 10 May 2024 06:54 X3.9, 11 May 2024 01:23 X5.8, 11 May 2024 11:44 X1.5, and the 12 May 2024 16:26 X1.0 flares. The right figures shows the SDO/AIA 171 Å over the same period.

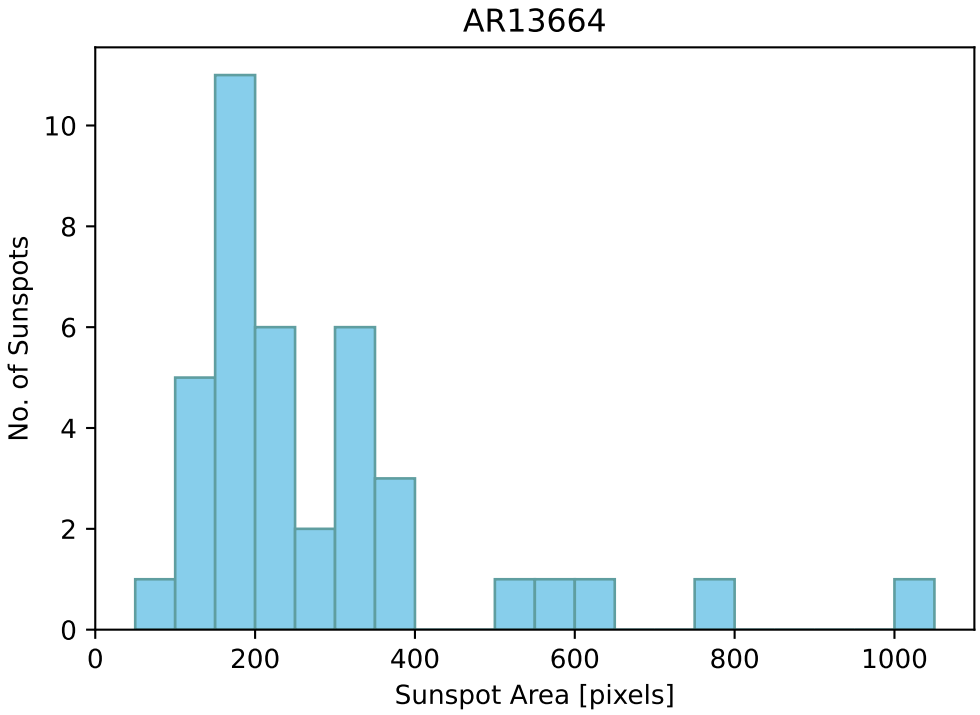

Figure 5.4: Histogram presenting the distribution of sunspot area within active region 13664.

5.2.2 Sunspot Properties

Active region 13664 has an incredibly complex structure and contains 39 sunspots that had an area greater than 49π pixels for at least 24 hours. The total sunspot umbral area for the active region is 11171 pixels, and the average sunspot umbral area is 286 pixels, with a standard deviation of 196 pixels. The largest sunspot has an area of 1043 pixels. Figure 5.4 shows the area distribution of sunspots within the active region. 44% of the sunspots have an area less than 200 pixels (17), and 13% have an area greater than 400 pixels (5).

There are multiple long-lasting sunspots within AR 13664. The shortest sunspot is tracked for 136 hours, and the longest lasting sunspot is tracked for 336 hour. The distribution of sunspot durations is presented in Figure 5.5. The sunspots in this active region are long-lasting, with 87% (34) of the sunspots from the active

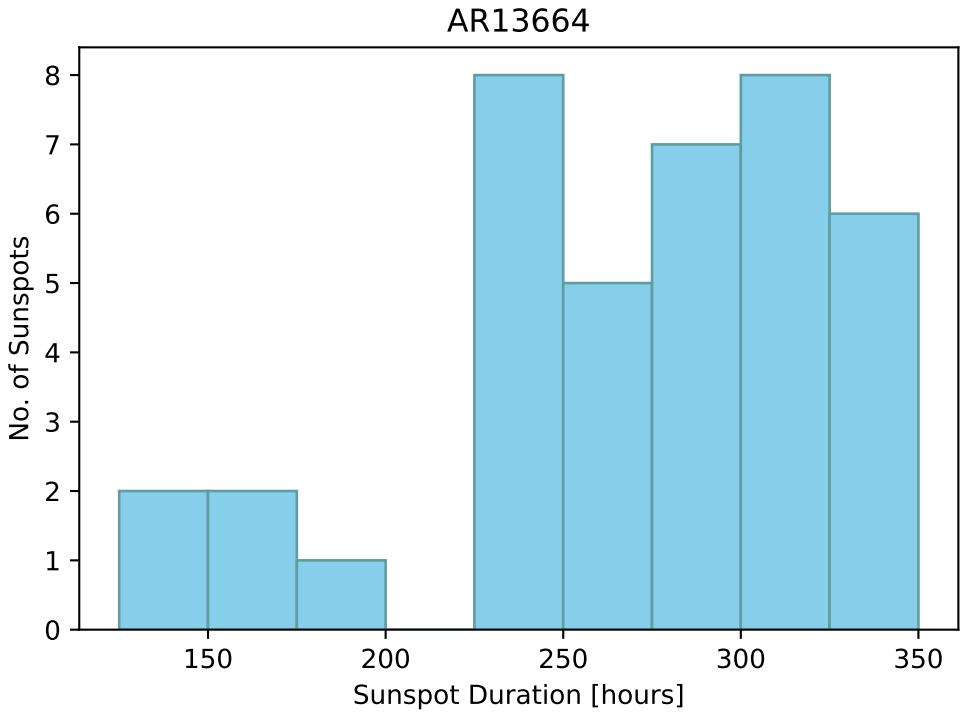

Figure 5.5: Histogram presenting the distribution of sunspot tracking duration within active region 13664.

region being tracked for more than 250 hours. Figure 5.6 shows the distribution of umbral area against duration for the sunspots in AR 13664. The figure shows a strong positive correlation, implying larger sunspots are more likely to be observed for a longer duration ($r = 0.59$, $P = 7 \times 10^{-5}$).

The rotation distributions for the sunspots in AR 13664 can be seen in Figure 5.7. Within the active region, 87%, 56%, and 46% of sunspots experienced $< 30°$ net, mid and absolute rotation, and 3%, 15%, and 26% of the sunspots experienced greater than 60° net, mid and absolute rotation, respectively. The net, mid and absolute rotation values ranged between $0.1° \pm 20.5°$ and $82° \pm 9.4°$, $8° \pm 7.0°$ and $90° \pm 8.1°$, and $12° \pm 9.3°$ and $133° \pm 33.2°$, respectively. The net rotation profiles of the active region are presented in Figure 5.8, the flares peak-times are also highlighted in the figure. Most of the high-energy flaring events occurred after 195 hours from the initial active

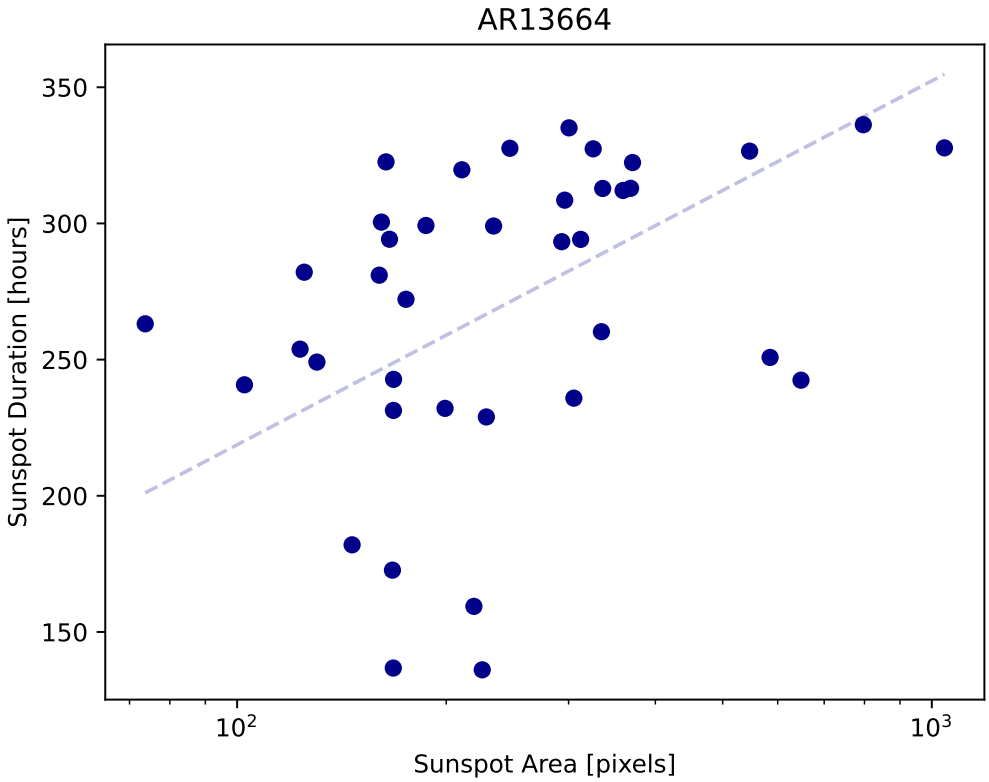

Figure 5.6: A scatter plot showing the relationship between the sunspot umbral area in pixels and the sunspot duration in hours. The dashed blue line is the linear regression of the distribution ($r = 0.59$, $P = 7 \times 10^{-5}$).

region identification. There is also a large amount of new sunspot emergence around this point. Although none of the sunspots exceed 150° net rotation, the high number of sunspots allows the rotation energy to build up over the duration of the active region. The next section will investigate the active region as a whole and determine if the rotation generated enough energy within the active region to account for the volume of solar flares.

5.2.3 Active Region Properties

The area, net, mid and absolute rotation profiles are combined across the active region to generate Figure 5.9. The largest combined sunspot umbra area is 8339 pixels, this maximum occurred 249 hours after the initial active region detection. The net, mid and absolute rotation had maximum values of $173° \pm 48°$, $1286° \pm 32°$, and $1794° \pm 24°$ respectively. These maximum rotation values occurred at 246, 336, and 336 hours. Five of the X-Class flares occurred during the rapid increase in area between 225 and 250 hours. The following three X-Class flares occurred after the change in net rotational direction, with the final three flares occurring on the 14 May 2024, after the active region rotated off disc.

Figure 5.10 shows the cumulative active region energy contribution from the net, mid and absolute rotation profiles, alongside the cumulative bolometric flaring energy for the region. From the figure, the flaring energy is initially higher than the rotation energy due to flaring events from before the sunspots rotated onto the solar disc. At this point the flares are releasing energy produced (by rotation or other mechanisms) before the active region rotations onto the solar disc. The rotation energy exceeds the flare energy at 80-100 hours. From this point on the active region rotation generates more than enough energy to account for the energy released by the solar flares, with an excess of energy 2-3 orders of magnitude larger than the amount emitted by the flares.

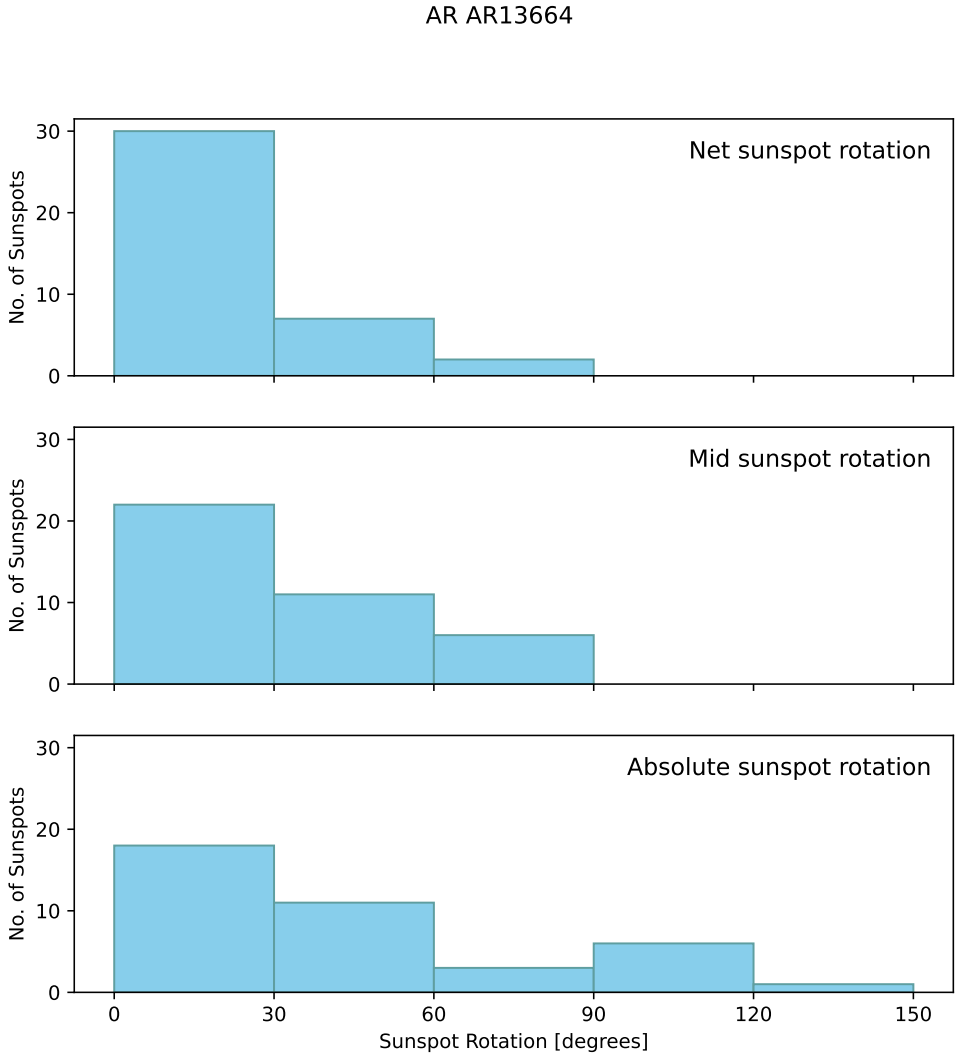

Figure 5.7: Histogram presenting the distribution of sunspot rotation within active region 13664. The top figure shows the net sunspot rotation (R_{net}), the middle figure shows the mid sunspot rotation (R_{mid}), and the bottom figure shows the absolute sunspot rotation (R_{abs}).

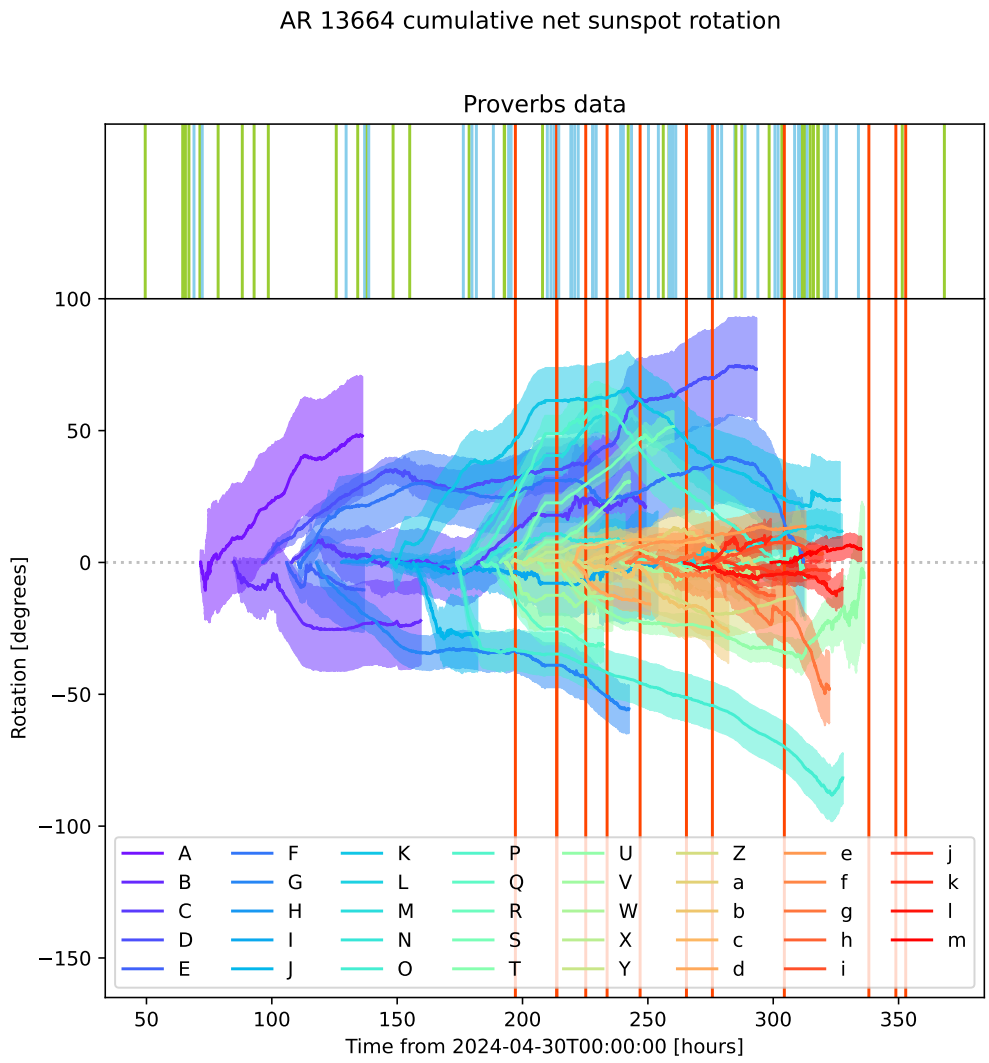

Figure 5.8: The top figure shows the GOES peak time of all flares associated with active region 13664. Green lines represent C-Class flares, blue lines represent M-Class flares, and red lines represent X-Class flares. The bottom figure shows the net rotation profile for each of the 39 sunspots within this active region. The shaded area is the uncertainty associated with each rotation profile.

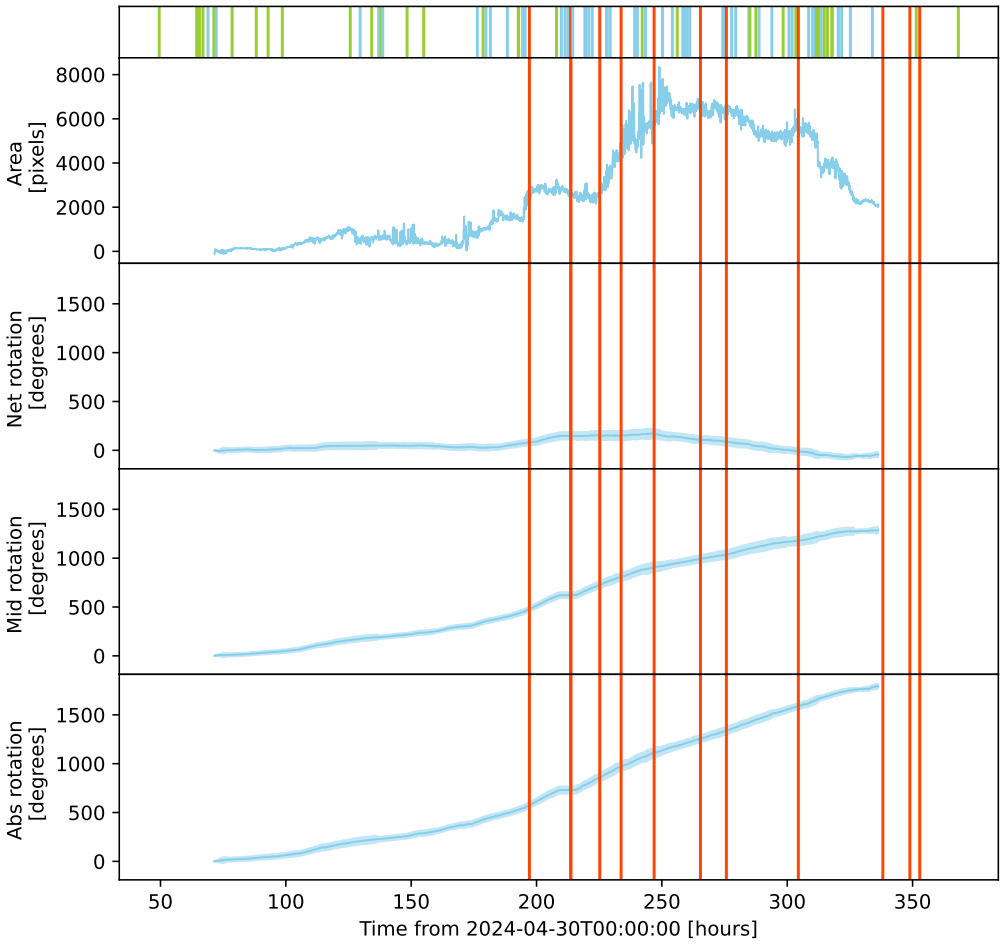

Figure 5.9: The top figure shows the GOES peak time of all flares associated with active region 13664. Green lines represent C-Class flares, blue lines represent M-Class flares, and red lines represent X-Class flares. The second figure shows the cumulative reprojected umbral active region area for the active region, and the third, fourth and fifth figure show the cumulative net, mid and absolute active region rotation profiles. The shaded region represents the uncertainty associated with the rotation profiles.

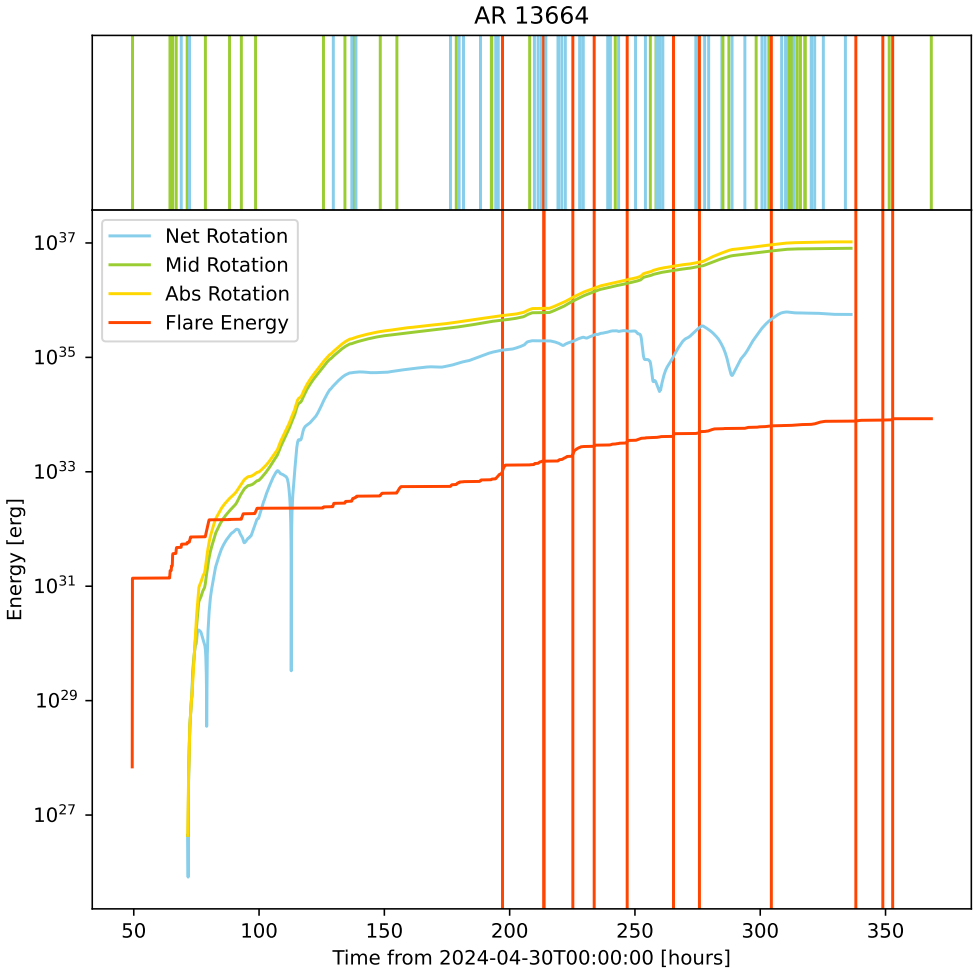

Figure 5.10: The top figure shows the GOES peak time of all flares associated with active region 13664. Green lines represent C-Class flares, blue lines represent M-Class flares, and red lines represent X-Class flares. The bottom figure shows the active region rotation energy and flaring energy profiles for AR 13664. The red line represents the radiated flare energy, the blue line represents the net rotation energy, the green line represents the mid rotation energy and the yellow line represents the absolute rotation energy.

5.3 Active Region 13842

Active region 13842 first rotated onto the solar disc on 26 September 2024 and rotated off the solar disc on 10 October 2024. There are 14 sunspots associated with this region that fulfil the Walker sunspot analysis criteria, and there are 50 GOES flares assigned to this active region. Four of these flares are X-Class, 27 M-Class, and 19 C-Class . The following section will discuss the X-Class flares that contributed to the October 2024 solar storm.

5.3.1 X-Class Solar Flares

Figure 5.11 shows active region 13842 in both SDO/HMI continuum and SDO/AIA 171 Å during three of the X-Class flares. The final X-Class flare is not included as it occurred on the limb and the active region had rotated off the solar disc so the sunspots were not visible. The figure also shows the evolution of the active region as there are multiple sunspot mergers and emergences. Table 5.2 lists the GOES peak times and flare class for each of the X-Class flares.

Table 5.2: X-Class flares associated with AR 13842

GOES Peak Time	GOES Flare Class
2024-10-01 22:20:00.000	X7.1
2024-10-03 12:18:00.000	X9.0
2024-10-07 19:13:00.000	X2.1
2024-10-09 15:47:00.000	X1.4

5.3.2 Sunspot Properties

Active region 13842 has a complex structure, with 50 flares being associated with the structure. The total sunspot area for this active region is 4872 pixels, and the average sunspot area is 348 pixels. The largest sunspot within this active region

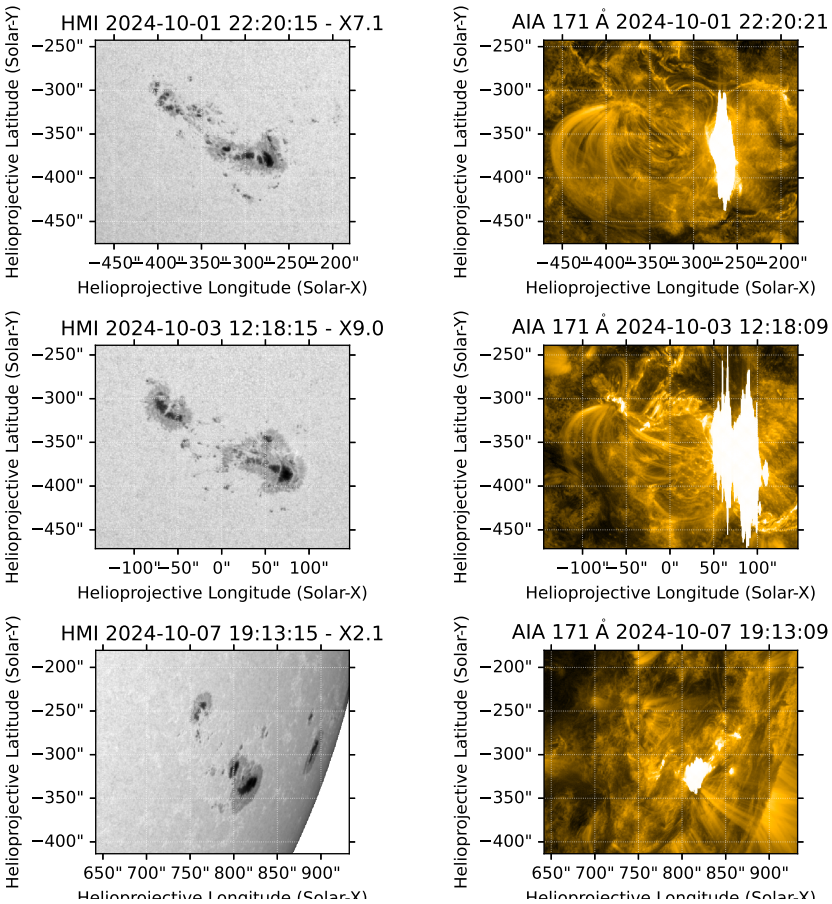

Figure 5.11: The left figures show the SDO/HMI continuum image of AR 13842 during the peak times of the 1 October 2024 X7.1, 3 October 2024 X9.0, and the 7 October 2024 X2.1 flares. The right figures show the SDO/AIA 171 Å over the same period.

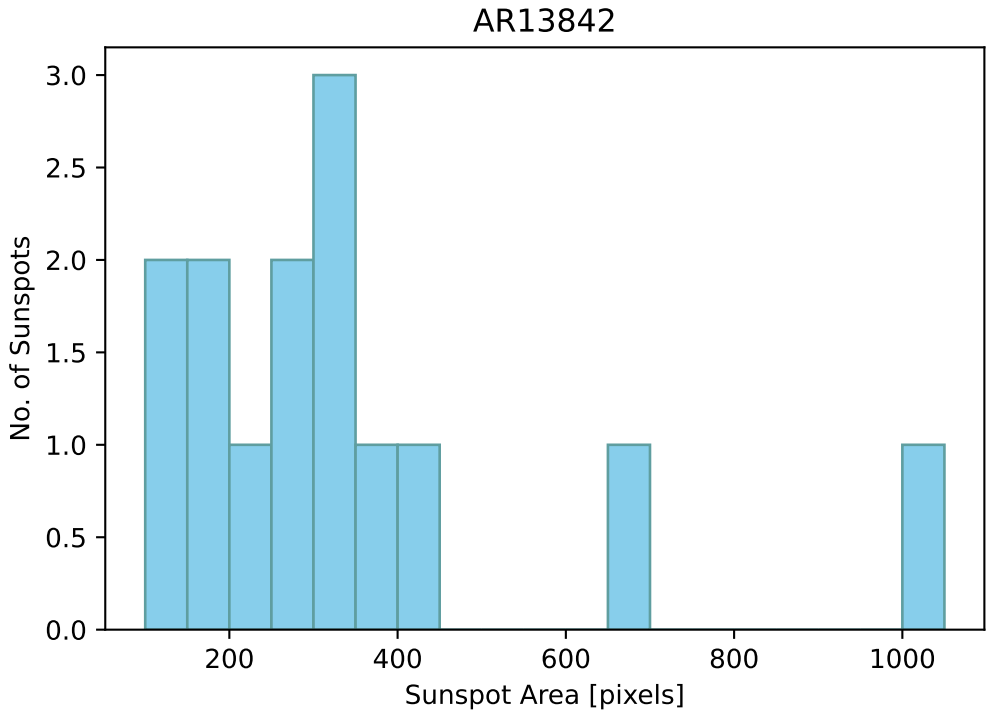

Figure 5.12: Histogram showing the distribution of sunspot area within active region 13842.

had a maximum umbral area of 1046 pixels. Figure 5.12 shows the distribution of sunspot areas within active region 13842. Within the sample, 29% of the sunspots had an area less than 200 pixels (4), and 21% had an area greater than 400 pixels (3).

The shortest sunspot duration within this sample is 132.9 hours, and the longest duration is 299.8 hours. Figure 5.13 shows the distribution of sunspot durations within the active region, and 57% of the sunspots are tracked for at least 225 hours (8). Figure 5.14 shows the relationship between sunspot umbral area and duration for this active region. Linear regression analysis of this distribution returns a negative correlation coefficient ($r = -0.15$), however the P-Value is large for this figure ($P = 0.6$), suggesting there is limited correlation overall.

Figure 5.15 shows the distribution of the net, mid and absolute sunspot rotations

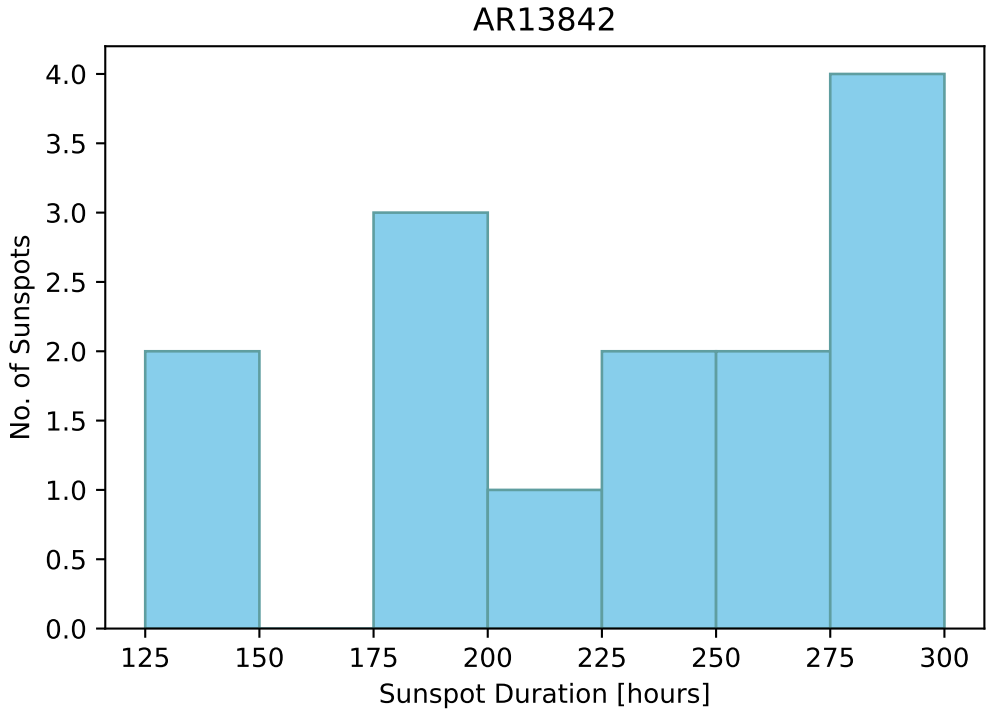

Figure 5.13: Histogram showing the distribution of sunspot duration within active region 13842

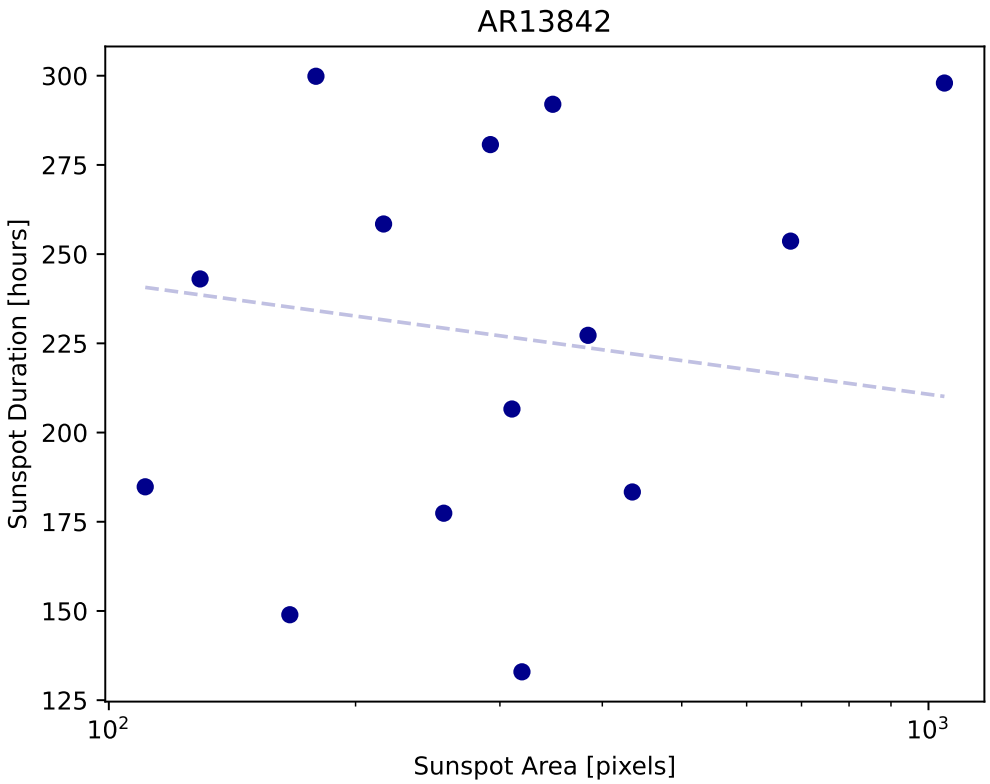

Figure 5.14: A scatter plot showing the relationship between the sunspot umbral area in pixels and the sunspot duration in hours. The dashed blue line is the linear regression of the distribution ($r = -0.15$, $P = 0.6$).

for the 14 sunspots within this active region. Within the active region, 79%, 57%, and 43% of the sunspots exhibited less than 30° of net, mid and absolute rotation (11, 8, and 6 sunspots, respectively), and 7%, 21%, and 36% of the sunspots exhibited more than 60° of net, mid and absolute rotation (1, 3, and 5 sunspots, respectively). The net, mid and absolute rotation values range between $2.5° \pm 25°$ and $139° \pm 15°$, $5.9° \pm 3.5°$ and $166° \pm 18.6°$, and $8.9° \pm 4.3°$ and $193° \pm 18.6°$, respectively. The net rotation profiles for the sunspots within AR 13842 are shown in Figure 5.16. From the figure, one sunspot (sunspot A) exhibits more than 100° of rotation, and lasts almost the full tracking period of the active region. There is also a large amount of sunspot emergence beginning from 120 hours, 12 sunspots emerge between 120-200 hours. The following section will investigate the active region as a whole and determine if the sunspot rotation generated enough energy to account for the flaring activity assigned to the region.

5.3.3 Active Region Properties

Figure 5.17 shows the evolution of the umbral area, net, mid and absolute rotation profiles of the sunspots within active region 13842. The maximum active region umbral area is 4049 pixels, occurring at 250 hours. The net, mid and absolute active region rotation had maximum values of $163° \pm 28°$, $576° \pm 26°$, and $743° \pm 25°$, occurring at 244, 299, and 300 hours, respectively. These maximum rotation values occur before the final two X-Class flares occur. There is also a considerable difference between the net and the absolute rotation values. The net rotation of the active region changes direction on two occasions. The second direction change occurs alongside the third X-Class flare (Figure 5.17).

The cumulative flare, net, mid, and absolute rotation energy profiles for AR 13842 are shown in Figure 5.18. The first flares associated with this active region

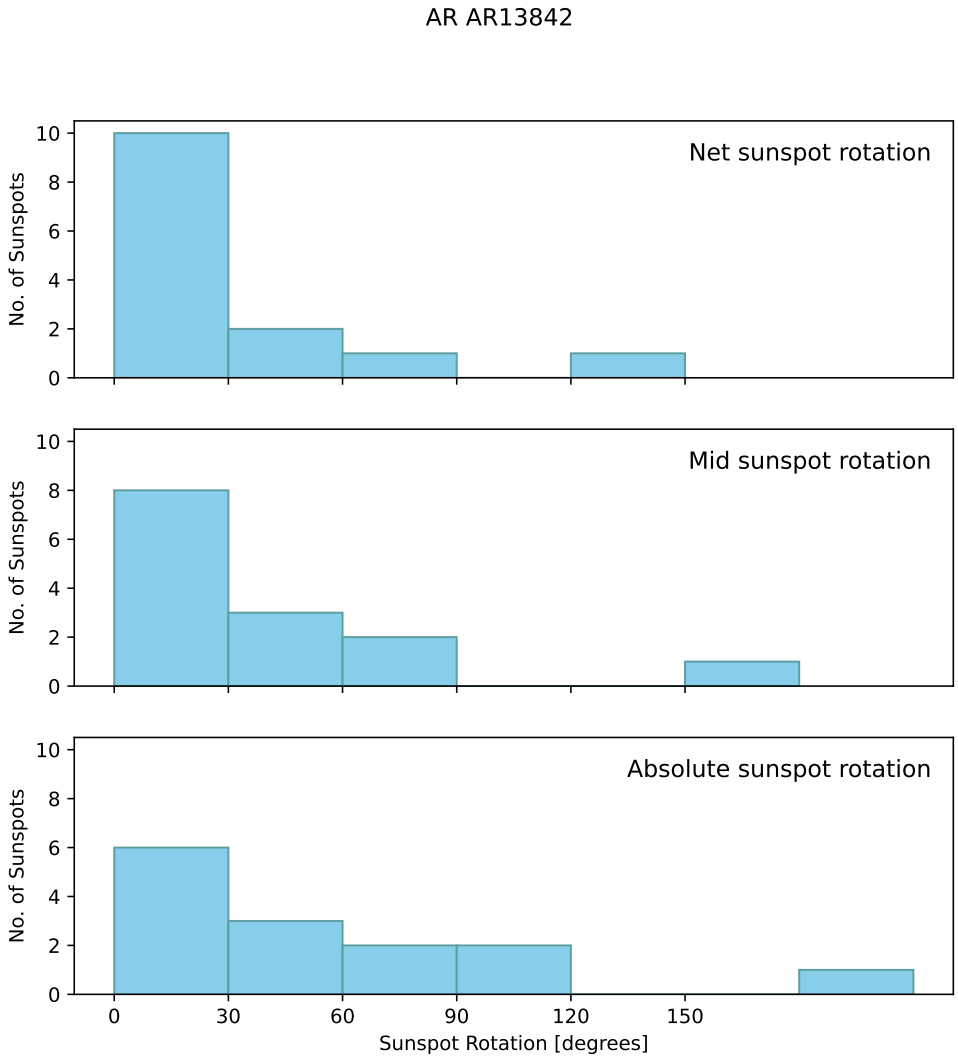

Figure 5.15: Histogram presenting the distribution of sunspot rotation within active region 13842. The top figure shows the net sunspot rotation (R_{net}), the middle figure shows the mid sunspot rotation (R_{mid}), and the bottom figure shows the absolute sunspot rotation (R_{abs}).

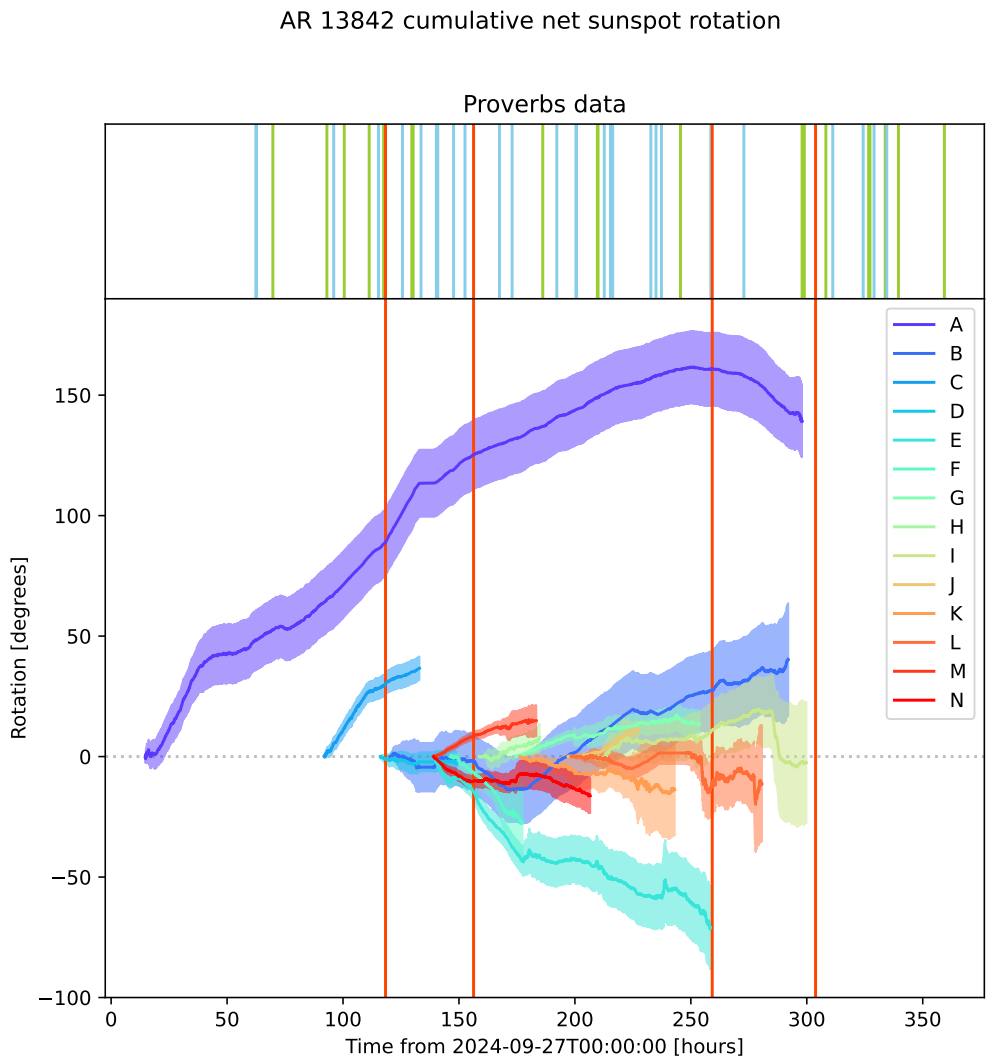

Figure 5.16: The top figure shows the GOES peak time of all flares associated with active region 13842. Green lines represent C-Class flares, blue lines represent M-Class flares, and red lines represent X-Class flares. The bottom figure shows the net rotation profile for each of the 14 sunspots within this active region. The shaded area is the uncertainty associated with each rotation profile.

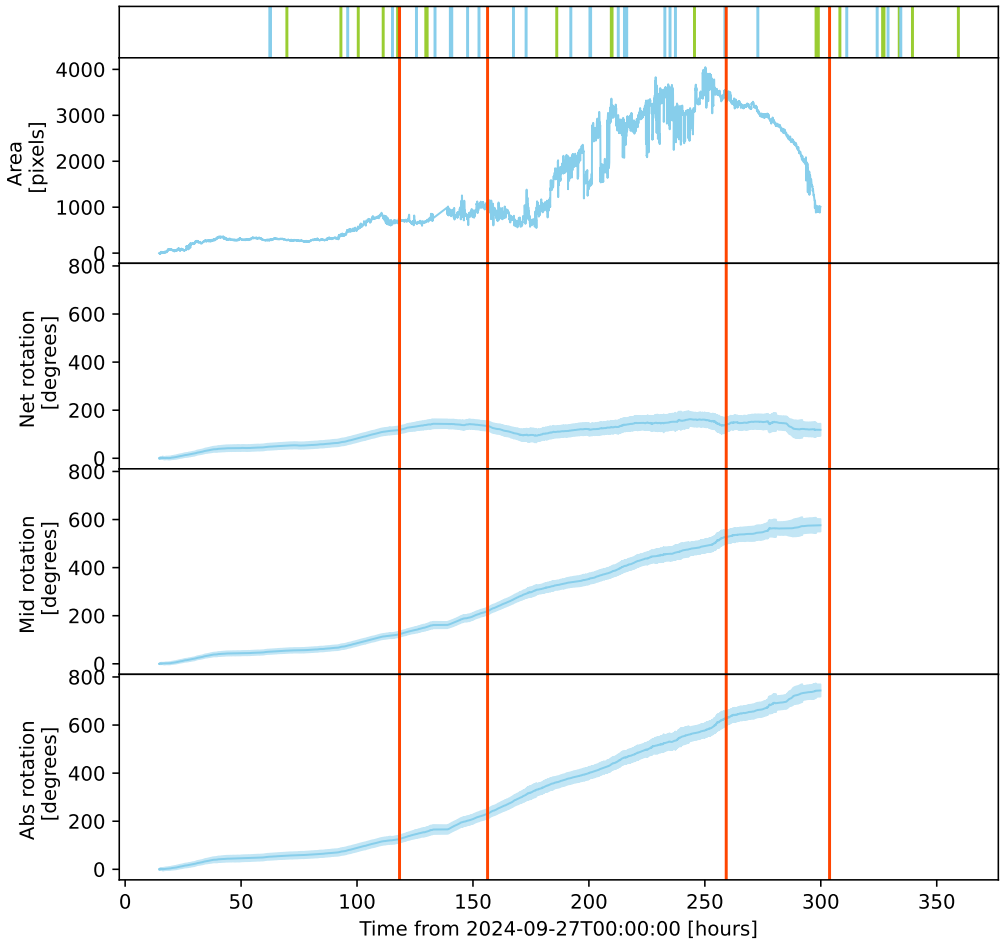

Figure 5.17: The top figure shows the GOES peak time of all flares associated with active region 13842. Green lines represent C-Class flares, blue lines represent M-Class flares, and red lines represent X-Class flares. The second figure shows the cumulative reprojected umbral active region area for the active region, and the third, fourth and fifth figure show the cumulative net, mid and absolute active region rotation profiles. The shaded region represents the uncertainty associated with the rotation profiles.

occur after the sunspots within AR 13842 are first identified. Throughout the observed period the energy due to sunspot rotation consistently exceeds the energy output by solar flares.

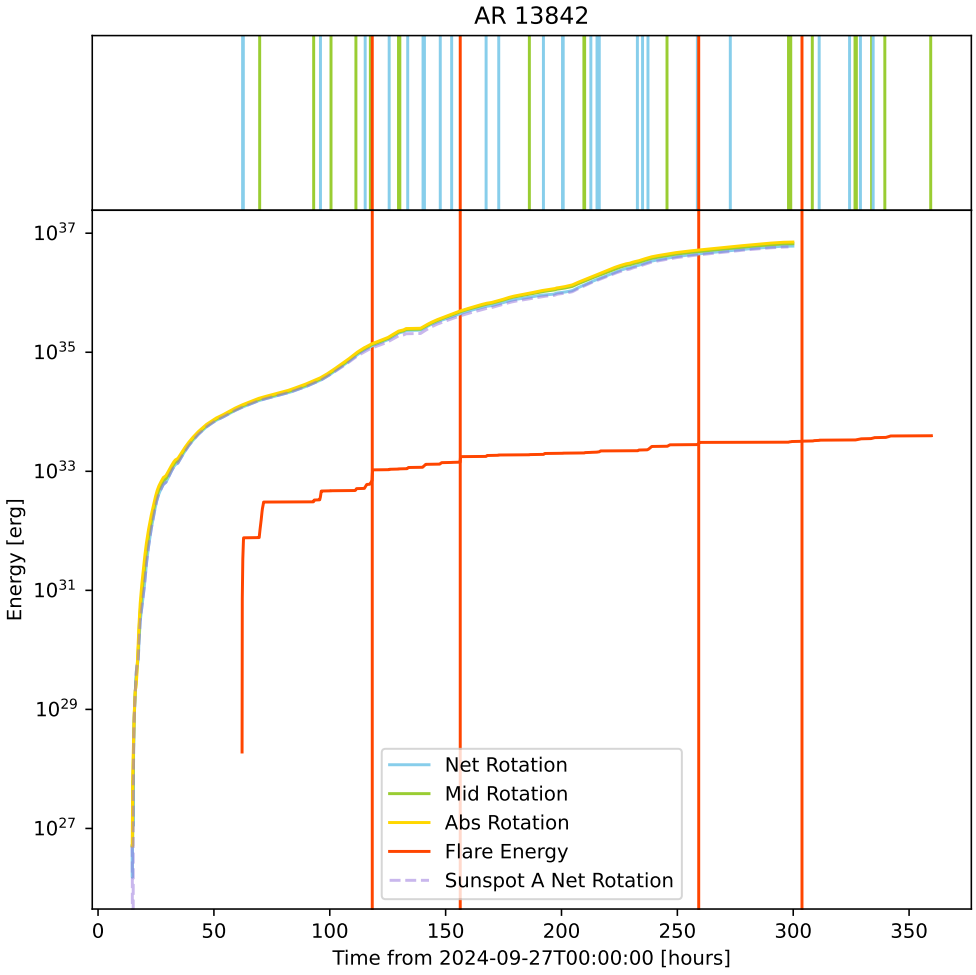

Figure 5.18: The top figure shows the GOES peak time of all flares associated with active region 13842. Green lines represent C-Class flares, blue lines represent M-Class flares, and red lines represent X-Class flares. The bottom figure shows the active region rotation energy and flaring energy profiles for AR 13842. The red line represents the radiated flare energy, the blue line represents the net rotation energy, the green line represents the mid rotation energy and the yellow line represents the absolute rotation energy. The dashed purple line is the energy contribution from the net rotation of sunspot A.

5.4 Conclusions

This chapter presented the analysis of two large active regions from the maximum of solar cycle 25, AR 13664, and AR 13842. Both of these active regions released coronal mass ejections that triggered large solar storms on Earth, and contained 39 and 14 sunspots, respectively. Both of the active regions experience multiple X-Class flares, with 12 flares assigned to AR 13664, and 4 assigned to AR 13842.

The largest sunspots from both active regions have similar sizes, with 1043 pixels area for AR 13664, and 1046 pixels area for AR 13842. Sunspots in active region 13842 tended to have a larger area than those in active region 13664, 21% of sunspots within AR 13842 had an area exceeding 400 pixels, and 29% of sunspots had an area less than 200 pixels. Whilst 13% of sunspots in AR 13664 had an area greater than 400 pixels, and 44% had an area less than 200 pixels. Although the sunspots in AR 13664 are smaller, the large amount of sunspots causes the maximum observed umbral area of the active region to total 8780 pixels. The maximum observed umbral area for AR 13842 was 4651 pixels. Both case study active regions contained many small sunspots (< 200 pixels) that were observed for over 225 hours, and one large (> 1000 pixels) sunspot that evolves over the full active region observation period.

The majority of the sunspots within AR 13664 experience less than 60° of rotation, specifically 97%, 92%, and 87% of sunspots experience $< 60°$ of net, mid, and absolute rotation. Within AR 13842 the rotation was slightly higher per sunspot, with 93%, 79%, and 64% of sunspots experience $< 60°$ of net, mid, and absolute rotation. Despite the relatively small amount of rotation from AR 13664, the overall rotation energy contribution remained high. This suggests that the volume of sunspots within the active region compensates for the small amount of rotation per sunspot. The majority of the rotation from AR 13842 is contributed by sunspot A, which experiences 257° absolute rotation.

The cumulative rotation and flare energy profiles for AR 13664 show that the

flare energy exceeds the active region energy contribution from the net, mid and absolute rotation profiles until 75 hours. There is some recorded flaring activity from GOES from before the first observation of a sunspot that fulfils the Walker analysis criteria that accounts for this difference. Once the sunspots pass the criteria and begin rotating the rotation energy exceeds the radiated flare energy. The energy profiles for AR 13842 show that the rotation energy consistently exceeds the flare energy throughout the observational period. The net, mid and absolute energy profiles are very similar for AR 13842, this is most likely due to sunspot A being the main contributor to the energy build-up. This sunspot had both the largest area and the largest rotation, reaching over 150° net rotation, whilst the other smaller sunspots do not exceed 75° of rotation. Solar flares are not the only mechanism for an active region to expel built-up energy, as shown in Equation 1.10, other forms of solar activity such as coronal mass ejections could account for the excess of active region rotation energy.

The following chapter will investigate how sunspots interact with each other within an active region through co-rotation. This analysis will be applied to all active regions covered within this work.

Chapter 6

A method to measure sunspot corotation in active regions

6.1 Introduction

Corotation is the rotation of two sunspots about each other. This chapter will discuss a method to measure the corotation of sunspot pairs within active regions as individual pairs, alongside the bulk corotation of whole active regions. An additional criteria is placed on the sunspots to allow corotation analysis. Each sunspot pair must be tracked on the same observations for at least twenty-four hours. Roll periods of SDO are also removed from the dataset as the blurring of the sunspot umbral and penumbral boundary increases the uncertainty of the sunspot area and centre of mass, and the effect of the rolling motion on the centre of mass interferes with the corotation calculations.

6.2 Measuring sunspot corotation

This section will discuss the method used to calculate the corotation of sunspots within an active region. The active region database created using the Proverbs

method is used to identify sunspots from the same active region that are visible on the solar disc at the same time for at least 24 hours. The following process is applied to each joint observation of each sunspot pairing within the active region.

The weighted centre of mass (in pixels) is extracted for both sunspots (s_1, s_2). The location of the centre pixels of the Sun is also extracted ($\underline{\mathbf{v}}_s$) along with the radius of the Sun (r_S). For this analysis the centre of the Sun is considered to be (0,0). The relative location (x_{rel}, y_{rel}) of the sunspots under analysis are given by

$$x_{rel} = s_x - x_S \tag{6.1}$$

$$y_{rel} = s_y - y_S \tag{6.2}$$

where $s_{x,y}$ is the original pixel location of the sunspots, and (x_S, y_S) is the original pixel location of the centre of the Sun. The z-component of the sunspot locations is calculated using

$$z_{rel} = \sqrt{r_S^2 - x_{rel}^2 - y_{rel}^2} \tag{6.3}$$

The midpoint between the two sunspot locations (weighted with sunspot umbral area) is determined, and the relative location of the midpoint is calculated using equations 6.1, 6.2 and 6.3.

These relative pixel locations are combined to generate the sunspot location vectors $\underline{\mathbf{v}}_1$ and $\underline{\mathbf{v}}_2$:

$$\underline{\mathbf{v}}_{i,rel} = \begin{bmatrix} x_{n,rel} \\ y_{n,rel} \\ z_{n,rel} \end{bmatrix} \tag{6.4}$$

and the vector of the midpoint between the two sunspots is defined as

$$\underline{\mathbf{v}}_{mid} = \frac{w_1\underline{\mathbf{v}}_1 + w_2\underline{\mathbf{v}}_2}{w_1 + w_2} \tag{6.5}$$

where w_i is the weighting, which in this case is the reprojected area of the sunspot.

The relative midpoint location is used to define two inverse rotation matrices, $\underline{\mathbf{A}}$ and $\underline{\mathbf{B}}$, to transform the relative midpoint location to the centre of the solar disc.

A and B are defined by

$$A = \begin{bmatrix} \cos(\alpha) & 0 & -\sin(\alpha) \\ 0 & 1 & 0 \\ \sin(\alpha) & 0 & \cos(\alpha) \end{bmatrix} \tag{6.6}$$

$$B = \begin{bmatrix} 1 & 0 & 0 \\ 0 & \cos(\beta) & \sin(\beta) \\ 0 & \sin(\beta) & \cos(\beta) \end{bmatrix} \tag{6.7}$$

which are the same rotation matrices from section 2.2, where

$$\sin\alpha = \frac{x_{mid}}{\sqrt{r_S^2 - y_{mid}^2}} \tag{6.8}$$

$$\sin\beta = -\frac{y_{mid}}{r_S} \tag{6.9}$$

Equations 6.6 and 6.7 are applied to the two sunspot location matrices to rotate them to their relative location on the solar disc if $\underline{\mathbf{v}}_{mid}$ is at the centre of the image, the resulting matrices are

$$\bar{\underline{\mathbf{v}}}_i = \underline{\mathbf{BA}\mathbf{v}}_{i,rel} \tag{6.10}$$

The two reprojected sunspot location matrices ($\bar{\underline{\mathbf{v}}}_i$) were used to determine the angle between the sunspots. The angle (θ) is given by

$$\tan\theta = \frac{\bar{y}_1 - \bar{y}_2}{\bar{x}_1 - \bar{x}_2}. \tag{6.11}$$

The associated uncertainty for θ is given by

$$\sigma_\theta^2 = \frac{y^2\sigma_{\Delta x}^2 + x^2\sigma_{\Delta y}^2}{x^2(x^2+y^2)} \tag{6.12}$$

where

$$\sigma_{\Delta x} = \sqrt{\sigma_{x_1}^2 + \sigma_{x_2}^2} \tag{6.13}$$

$$\sigma_{\Delta y} = \sqrt{\sigma_{y_1}^2 + \sigma_{y_2}^2} \tag{6.14}$$

and $x = \bar{x}_1 - \bar{x}_2$, $y = \bar{y}_1 - \bar{y}_2$.

The angle between the sunspots along with the associated uncertainty is calculated for each observation of the sunspot pair, for each combination that fulfil the criteria within the active region. The 360° discrepancy within the data is removed to provide a continuous corotation signal. This method is applied to each suitable active region from the four and twelve-month sample, and the two case study active regions (AR 13664 and AR 13842). The following section will present the corotation results for the sunspots within these active regions.

6.3 Results

This section will discuss the sunspot corotation for all suitable active regions from the four-month and twelve month sample, alongside the two case study active regions from chapter 5.

6.3.1 Sunspot Corotation

Within the 240 active regions covered in this thesis, there are 887 sunspot pairs that satisfy the corotation criteria. Figure 6.1 shows the number of sunspot pairs that exhibit different amounts of corotation. There are 71 sunspot pairs within the four-month sample (chapter 3), and the net and absolute corotation ranges between $-188° \pm 1.5°$ and $337° \pm 0.05°$, and $0.05° \pm 0.005°$ and $796° \pm 1.5°$. Within this sample, 85% (63) and 66% (47) sunspot pairs exhibit $< 60°$ of net and absolute corotation, and 6% (4) and 20% (14) sunspot pairs exhibit $> 120°$ of net and absolute rotation.

The twelve-month sample (chapter 4) contains 447 sunspot pairs that fulfil the corotation selection criteria. The net and absolute corotation values range between $-603° \pm 0.03°$ and $33° \pm 0.05°$, and $0.06° \pm 0.002°$ and $1934° \pm 0.1°$. Within the

twelve-month sample, 89% (399) and 64% (275) of the sunspot pairs exhibited less than 60° of corotation, and 4% (16) and 20% (91) sunspot pairs exhibited more than 120° of rotation.

The two case study active regions (AR 13664 and AR 13842) contain 369 sunspot pairs that corotate. The net corotation ranges between $-143° \pm 0.1°$ and $471° \pm 0.01$, and the absolute corotation ranges between $0.5° \pm 0.002°$ and $969° \pm 0.5°$. Within the case study active regions, 61% (224) and 49% (181) of the sunspot pairs exhibited less than 60° net and absolute rotation, and 36% (133) and 41% (150) sunspot pairs exhibit more than 120° of corotation.

There is a wide distribution of sunspot numbers per active region, leading to the large case study active regions containing more sunspot pairs than the four-month sample. The following section will show the distribution of corotation summed over the active regions.

6.3.2 Active Region Corotation

The net and absolute corotation values are summed across each active region, Figure 6.2 shows the different amount of corotation recorded for different active regions. Out of the 240 active regions, 118 active regions have at least one sunspot pair that satisfy the conditions for corotation analysis. This includes 20 active regions from the four-month sample, 96 sunspots from the twelve-month sample, and the two case study active regions. The net active region corotation ranges from $-542° \pm 0.1°$ to $44922° \pm 0.7°$, and the absolute corotation ranges from $0.05° \pm 0.006°$ to $59074° \pm 0.7°$. The active region that exhibits the largest net and absolute corotation is AR 13664. Out of the 118 active region sample, 87% (103) and 50% (59) of the active regions exhibit less than 60° of net and absolute rotation, and 2% (2) and 33% (39) of the active regions exhibit over 120° of corotation.

Figure 6.3 shows the relationship between the net and absolute active region

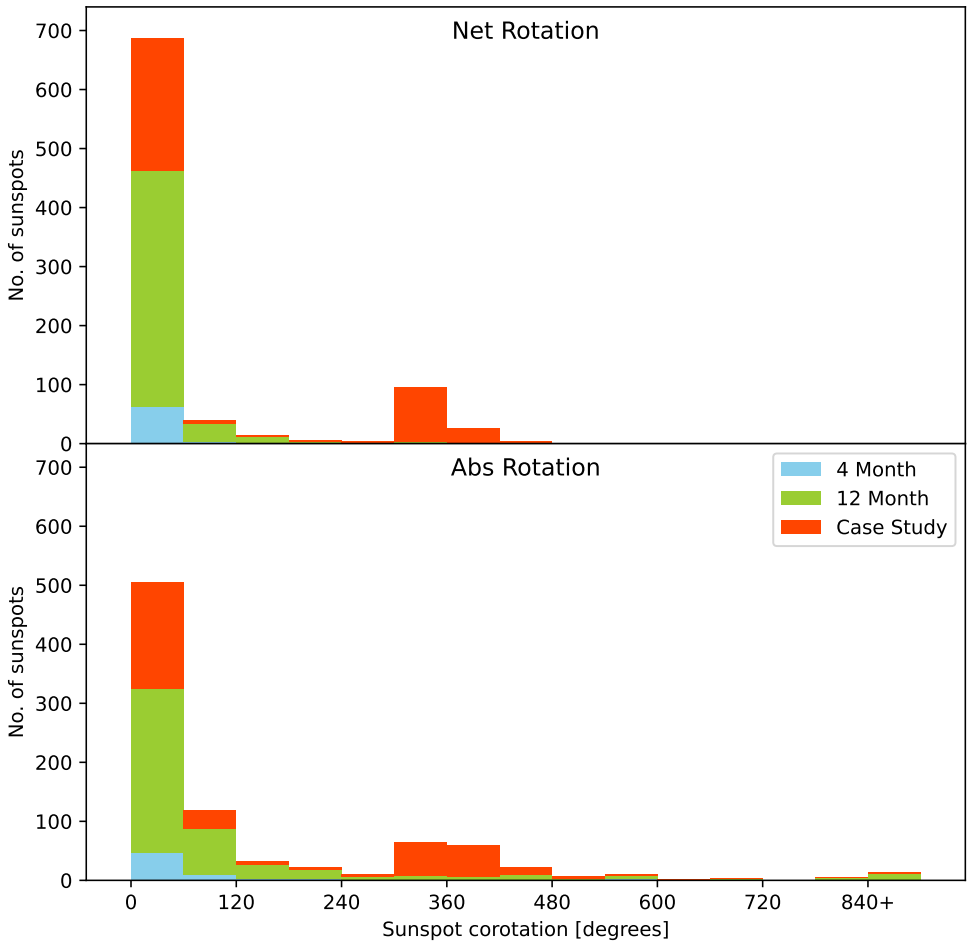

Figure 6.1: A histogram showing the number of sunspot pairs that exhibit different amounts of corotation. Blue represents sunspots from the four-month sample, green represents sunspot pairs from the twelve-month sample, and red represents sunspot pairs from the case study active regions.

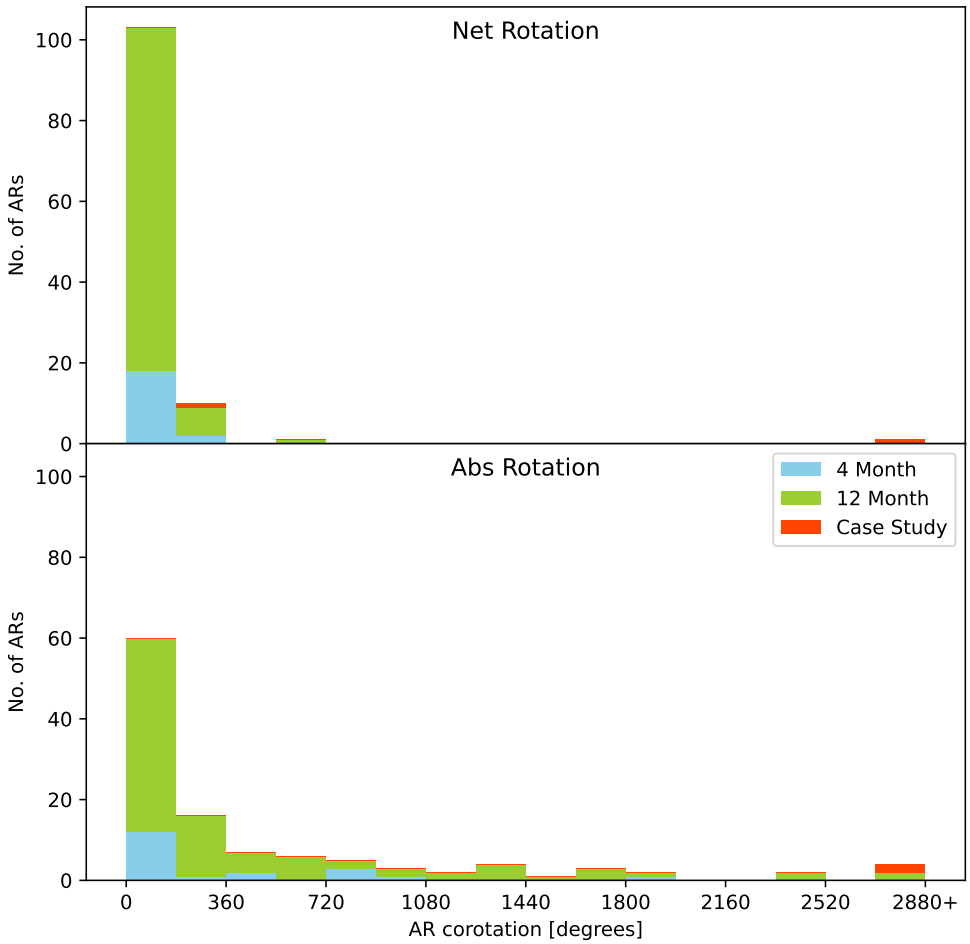

Figure 6.2: A histogram showing the number of active regions that exhibit different amounts of corotation. Blue represents active regions from the four-month sample, green represents active regions from the twelve-month sample, and red represents the case study active regions.

corotation and the bolometric flare energy. Net corotation is on the boundary of statistical significance between sunspot corotation and radiated flare energy ($r = 0.2$, $P = 0.06$), suggesting if she shearing and corotating sunspots were treated separately, there may be a correlation. The absolute corotation figure does not show a strong correlation ($r = 0.1$, $P = 0.26$). The two case study active regions have the largest absolute corotation values, and some of the highest radiated flare energy. The most extreme point on the net and absolute figures is assigned to active region AR 13664, which contains 39 sunspots that pass the sunspot rotation criteria. Most points are distributed between 10^1 - 10^3 degrees for net corotation. The absolute corotation has a wider distribution, with active regions mostly ranging between 10^0 - 10^4 degrees.

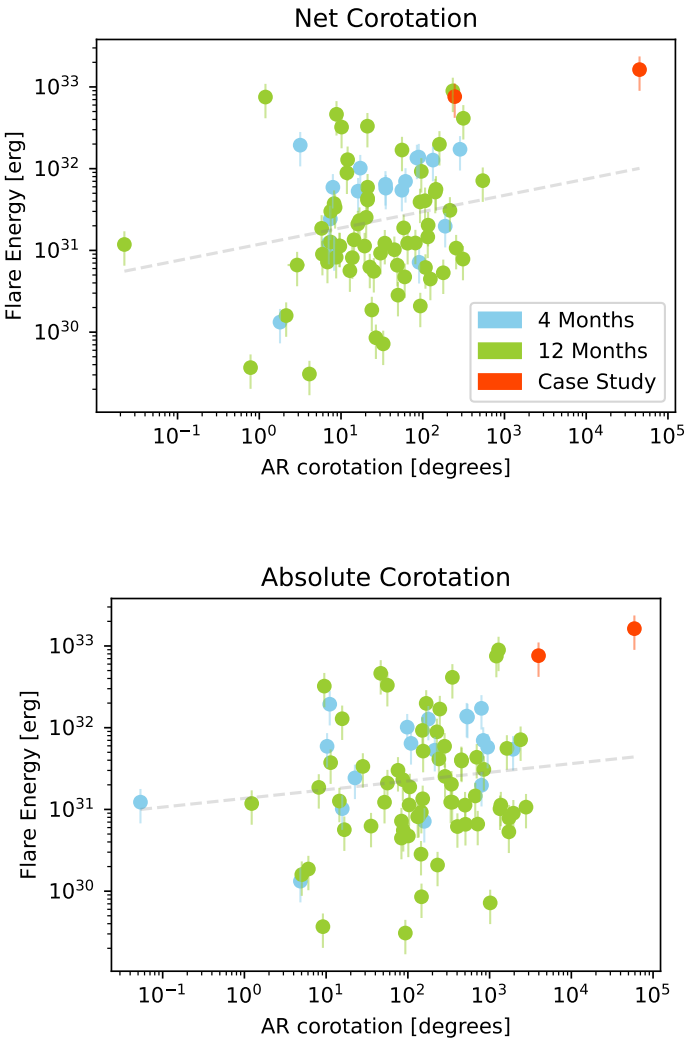

Figure 6.3: Active region corotation (degrees) versus bolometric flare energy (erg). The blue points represent active regions from the four-month sample, the green points represent active regions from the twelve-month sample, and the red points represent the case study active regions. The grey dashed line shows the linear regression for the plot. The upper figure shows the net corotation ($r = 0.2$, $P = 0.06$), and the bottom figure shows the absolute corotation ($r = 0.1$, $P = 0.26$).

6.4 Conclusion

This chapter presented a method to measure the corotation of sunspot pairs within active regions. The method was applied to all suitable active regions from the three samples (chapter 3, 4, and 5). 118 of the active regions were suitable for analysis, including both case study active regions that displayed an extreme amount of solar activity.

The four-month sample only contains 71 suitable sunspot pairs, this is because 22 active regions within this sample only contain one sunspot, and 5 active regions contain more than one sunspot but have no overlapping observations. The twelve-month sample contained 447 sunspot pairs, and the two case study active regions contain 369 suitable sunspot pairs. Across all sunspot pairs, 29% exhibited more than 120° of absolute rotation, the distributions of the twelve-month and case study samples are similar, with 20% of these samples exhibiting $> 120°$ absolute corotation and 66% and 64% exhibiting $< 60°$ absolute corotation. The four-month sample has fewer high-corotating sunspots than the other two samples. There are two populations within Figure 6.1, one centred around 30° and another centred around 330°, many of the cases within the first population may not be corotating sunspots, but could be shearing past each other. Further work could investigate this further and separate out the true corotators.

When comparing the active region corotation results, the majority of active regions exhibit less than 180° of corotation (87% net and 51% absolute). There is also a much notable difference between the net and the absolute distribution of active region corotations. Two of the largest corotation active regions are AR 13664 and AR13842, which both exceed 3000° of absolute corotation, with AR 13664 exceeding $55000° \pm 0.2°$. This active region contains 39 sunspots, all of which contribute to this very large corotation value. Comparisons between active region corotation and the radiated flare energy shows a positive correlation ($r = 0.2$, $P = 0.06$) with net

corotation but this is not statistically significant, however the relationship between absolute corotation and the flare energy shows no correlation. These results suggest that sunspots that exhibit large amounts of sunspot corotation could be more likely to flare, however further work is needed to confirm this. Future work could also focus on estimating the energy build up within active regions due to sunspot corotation, to determine if this type of dynamic could provide enough energy to account for the radiated flare energy.

Chapter 7

Summary and Future Work

7.1 Summary

This thesis aimed to statistically analyse the relationship that different forms of sunspot dynamics, specifically sunspot rotation and corotation, have with solar flares. To achieve this, a fully automatic method to identify and track sunspots was developed and tested on a previously analysed series of observations falling over the peak of solar cycle 24. The method was then applied to a 12-month dataset falling over the rise phase and initial peak of solar cycle 25 and two case study active regions (AR 13664 and AR 13842) that released an extremely large amount of bolometric flare energy. The summary of these results is presented in this chapter.

7.1.1 Four-Month Testing Sample

The automatic sunspot identification and tracking method was applied to a four-month statistical sample covering sunspots visible in SDO/HMI data from 1 May 2013 - 31 August 2013. This period has been previously analysed using a semi-automatic method by Walker (2018). Three characteristics of the two datasets were compared: the number of sunspots identified, the duration of each commonly

identified sunspot and the rotation profile of the commonly identified sunspots.

The Proverbs method was able to identify 54 of the 56 sunspots identified using the Walker method, alongside 53 additional sunspots that were not identified by Walker. The missing sunspots from the Proverbs dataset are due to a difference in the handing of sunspot splitting from the two methods and the missing sunspots are found, but do not meet Walkers size or duration criteria. The Proverbs method was generally able to track sunspots for longer by identifying them earlier and tracking them beyond the final observation recorded in the Walker dataset. The rotation of overlapping sunspot observations also showed good agreement, with only two sunspots having more than a 45° difference in the final rotation profile, and these differences in rotation were generally traced back to the different approaches to due to sunspot substructure.

Overall the Proverbs method has a few key advantages over the Walker method. The Proverbs method is fully automatic and tries to find all sunspots in the data, whereas the Walker method requires the location of the sunspot to be manually identified in the first observation. Due to the automatic nature of the Proverbs method, smaller sunspots are identified, leading to more sunspots being found per active region. The automatic method of sunspot identification also enables sunspots to be identified earlier, and tracked for longer. This has knock on effects to the rotation profiles of the sunspots, as the rotation can be tracked over a longer duration. Finally, the Proverbs method is also able to successfully identify splits and mergers within the sunspot sample, allowing the dynamics of more complex active regions to be monitored.

7.1.2 Twelve-Month Statistical Sample

The twelve-month sample covers observations from 1 March 2023 - 28 February 2024, which falls over the peak of solar cycle 25. Within this series of observations,

560 sunspots were identified across 189 active regions. 103 of these active regions experience solar flares, with over 700 flares associated with the sample. There is a wide range in active region area within the sample, ranging between 107 pixels - 10819 pixels. There is a positive correlation between active region umbral area and the radiated flare energy ($r = 0.4$, $P = 0.0002$), and a Kolmogorov-Smirnov test shows that active regions with smaller umbral areas are more likely to not have any solar flares associated with the active region.

The net, mid, and absolute active region rotation appear to have a positive correlation with the outputted flare energy ($r = 0.25, 0.24, 0.25$, $P = 0.1, 0.1, 0.1$), however this is not significant so there is no discernable correlation. A Kolmogorov-Smirnov test also showed that the active regions that do not flare are more likely to exhibit smaller amounts of mid and absolute rotation. This relationship was not significant with the net rotation profiles. Figure 7.1 shows the active region rotation energy versus the estimated flare energy for all active regions from the four-month and twelve-month sample, and the two case study active regions. When comparing the energy contributed to the active region by rotation, the majority of active regions generated enough energy to account for the flare activity. For the three rotation profiles (net, mid and absolute), 51%, 63%, and 71% of active regions generated more rotation energy than required for the observed flare activity, and 18%, 27%, and 32% of active regions generated 10 times the amount of energy outputted by solar flares during the observed period. As discussed in section 1.6, there are many methods of building up and releasing energy within an active region that are not considered in this work. The discrepancy in energies could be due to sunspot corotation and shearing, or the release of energy during coronal mass ejections. One active region within the twelve-month sample was frequently highlighted throughout the analysis due to the large umbral area and rotation, this active region has 19 sunspots is associated with 122 solar flares. To investigate this further, two extreme case study

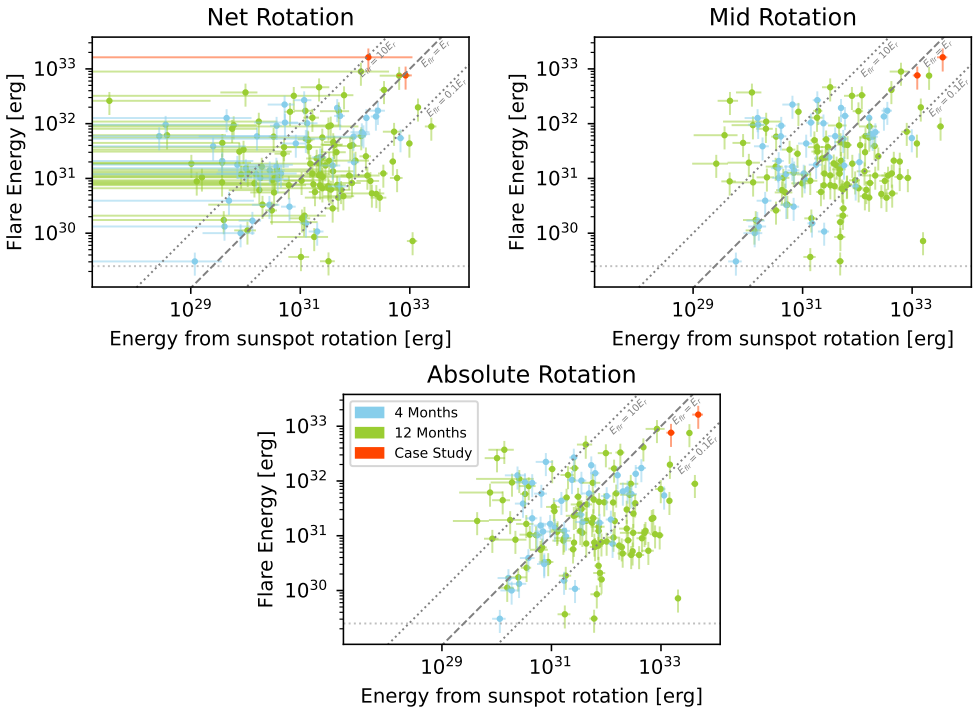

Figure 7.1: Energy from active region rotation (ergs) versus bolometric flare energy (erg). The points below the dotted line represent active region rotation energies that do not have any assigned flares. The top left plot represents E_{net}, the top right plot represents E_{mid}, and the bottom plot represents E_{abs}. The blue points represent active regions from the four-month sample, green points represent active regions from the twelve-month sample, and red points represent the case study active regions.

active regions from 2024 were analysed.

7.1.3 Case Study Active Regions

Two case study active regions were studied in chapter 5 to investigate the sunspot dynamics that preceded two extreme space weather events in 2024. The first active region studied is AR 13664 which has a Mount Wilson classification of $\beta\gamma\delta$ and caused the extreme G5 10 May solar storm (Elvidge & Themens, 2025). AR 13664 also contains 39 sunspots that passed the rotation analysis criteria and has 12 associated X-Class flares. The second active region is AR 13842, this region also has a $\beta\gamma\delta$ classification and released CMEs that triggered one of the most intense solar storms since the 2003 Halloween solar storm (Xia et al., 2025). This active region is also attributed to the orbital decay of multiple Starlink satellites (Oliveira, Zesta & Nandy, 2025). There are 14 sunspots within this active region that surpass the analysis criteria, and there are 4 X-Class flares associated with this region.

Both of the case study active regions contain large sunspots that have an umbral area of over 1000 pixels that are observed for the full duration of the active region. AR 13664 contains more small sunspots ($<$ 400 pixels) than AR 13842. Most sunspots within AR 13664 exhibited less than 60° of rotation (97% net and 87% of absolute), whereas the largest sunspot in AR 13842 exhibited over 150° of net rotation over the observation period.

The rotation energy time series for AR 13664 is initially less than the flare energy profile, this could be due to sunspot rotation or dynamics that occurred before the active region rotated onto the solar disc. Between 80-100 hours the rotation energy exceeds the flare energy. There is a large difference between the net rotation energy and the mid and absolute energy for AR 13664. This is most likely because the sunspots are rotating in both directions, resulting in the net rotation profile having a much smaller magnitude than the mid and absolute rotation profiles. This is not

the case for AR 13642, where the rotation energy profiles are very similar and exceed the flare energy throughout the observation period. The energy contribution for this active region is dominated by the rotation profile of the largest sunspot (A) that also exhibited a large amount of rotation in comparison to the other sunspots in the region.

Overall these active regions build-up rotation energy differently, but both AR 13664 and AR 13842 are able to generate sufficient energy within the active region by sunspot rotation to account for the large amount of energy released by solar flares in the lead up to the two large solar storms of 2024.

7.1.4 Corotation

Chapter 6 introduces a new method to measure sunspot pair corotation using the dataset created by the automatic sunspot identification and tracking method. This method was applied to all of the active regions analysed within this body of work. The four-month sample was found to exhibit less sunspot pair corotation than other active regions under analysis, 66% of sunspot pairs exhibit $< 60^{\circ}$ of absolute corotation, versus 56% of sunspot pairs across the full sample. When summing the sunspot pair corotation across active regions, most active regions exhibited less than 180° of corotation (51%). The active regions that exhibited the most sunspot pair corotation were AR 13664 and AR 13842, this was expected due to the unusually high complexity of these active regions. Overall net active region corotation appeared to have a positive correlation with the flare energy output of an active region ($r = 0.2$, $P = 0.06$) but the results were not statistically significant, and absolute rotation did not present a strong enough relationship to identify any correlation ($r = 0.1$, $P = 0.26$). This method measured the angular change between sunspots pairs, rather than strictly corotation. The ability to extract truly corotating sunspots pairs would be useful, which could be a focus of future work.

7.2 Conclusion

In this work we applied an automatic sunspot identification and tracking technique to a twelve-month dataset of active regions to generate a large sample of active region rotation profiles. In total the rotation profiles of 560 sunspots were measured over 189 active regions. We found a strong positive correlation between active region umbral area and radiated flare energy, and for both active region area and rotation, we found that flaring and non-flaring active regions can be considered two distinct populations, with flaring active regions more likely to experience higher rotation and to have a larger active region area than non-flaring regions. The majority of active regions (51%, 63%, 71% net, mid and absolute respectively) were able to build-up enough rotational energy to account for the radiated flare energy, but there was not a significant correlation between sunspot rotation and radiated flare energy, suggesting that rotation alone is not correlated to the flaring energy, and that it also depends on other active region properties, such as umbral area and flux. There are also multiple extreme cases where an active region generated $< 10\%$ or $> 1000\%$ of the energy released by solar flares. This work only considers one method of energy generation (sunspot rotation) and one method of energy release (solar flares), however the excess and lack of input energy suggests that a number of other factors may contribute, such as sunspot corotation and CMEs.

7.3 Future Work

This work has investigated whether the rotation of sunspots can build-up enough energy within an active region to account for that released by a solar flare a twelve-month sample. Future work could focus on applying this method to other periods of the solar cycle. The four-month sample falls over the peak of solar cycle 24, and the twelve-month sample falls over the peak of solar cycle 25. As SDO has observed

the entirety of solar cycle 24, the method could be applied to the rise and fall phases of the solar cycle. This would provide insights as to how sunspot dynamics vary at different points of the solar cycle when the amount of solar activity is changing. A comparison could also be drawn between the sunspot activity during equivalent periods of solar cycle 24 and 25 as the data become available.

Walker (2018) generated a statistical sample of all X-Class flaring active regions observed by SDO/HMI for the first seven years of the mission (February 2010 - March 2017). Since this point, there have been many more X-Class solar flares that could be analysed using the Proverbs method to expand this database. The main limiting factor for the number of active regions that can be studied isn't related to processing power, but rather the amount of SDO/HMI FITS files that can be stored locally. If access to the JSOC database was granted, the method could be applied to every observation from SDO/HMI since launch. This would cover over 15 years of data and the entirety of solar cycle 24.

Another of avenue of investigation could be the development of a method to estimate the amount of energy built-up within an active region due to the corotation of sunspot pairs. This work found that the amount of corotation within an active region correlates with increasing flare energy, however there is not currently a metric to calculate how much energy these dynamics are providing to the active region. Research in this area could also be applied to other forms of sunspot interactions, such as shear and mergers to determine how much energy these motions can contribute to an active region.

The sunspot identification and tracking method could be adapted for use with other space missions, such as Solar Orbiter's Polarimetric and Helioseismic Imager (SO/PHI) (Solanki et al., 2020). The High Resolution Telescope on SO/PHI collects high-resolution continuum data of the photosphere, but this data is not continuous. The method would need to be adapted to work with the varying location of SO/PHI

with respect to the Sun, and to ensure than the variations in pixel scaling due to the SO/PHI orbit was accounted for. There is currently one set of observations that could be used alongside this method, a 5-hour sample with a one-minute cadence where a single sunspot is visible. Another observation series is currently unreleased, but includes a sunspot that is observed by both SO/PHI and SDO/HMI which could present an interesting case study. Other instruments such as the National Science Foundation's (NSF) Daniel K. Inouye Solar Telescope (DKIST) may provide interesting opportunities to analyse high-resolution ground-based observations of sunspot dynamics over multiple hours (Rimmele et al., 2020).

Many of the active regions studied using the Proverbs method exceed the amount of energy output from the active region by solar flares. This discrepancy is most likely because solar flares are not the only way that active regions release energy and events such as coronal mass ejections are not included in this analysis. The development of a tool that could automatically assign solar flares and coronal mass ejections to active regions, and estimate their energy output would allow a more thorough analysis of the energy balancing within an active region.

7.4 Closing Remarks

This thesis has studied 720 sunspots across 240 active regions using data from the Solar Dynamics Observatory's Helioseismic and Magnetic Imager. Statistical analysis of these active regions has found that 71% of the active regions potentially generate enough energy due to sunspot rotation to account for the energy released by solar flares, with 32% of active regions exceeding the required rotation energy by at least 10 times. We also studied the corotation of sunspots and the relationship that this form of sunspot dynamic forms with flaring activity. We found that sunspots that exhibit high levels of corotation are more likely to release higher energy solar flares.

Bibliography

Aulanier G., Janvier M., Schmieder B., 2012, Astronomy and Astrophysics, 543, A110

Babcock H. W., 1961, Astrophysical Journal, 133, 572

Beckers J. M., Schröter E. H., 1969, *Sol. Phys.*, 10, 384

Berger M. A., 1984, Geophysical and Astrophysical Fluid Dynamics, 30, 79

Blessy W. H., Rahman A. M., Inbanathan S. S. R., Prasad P. G., 2024, Geomagnetism and Aeronomy, 64, 592

Brown D., Walker A., 2021, Solar Physics, 296, 48

Brown D. S., Nightingale R. W., Alexander D., Schrijver C. J., Metcalf T. R., Shine R. A., Title A. M., Wolfson C. J., 2003, Solar Physics, 216, 79

Burkepile J. T., St. Cyr O. C., 1993, A revised and expanded catalogue of mass ejections observed by the Solar Maximum Mission coronagraph

Cho K., Chae J., Madjarska M. S., 2021, *Astron. Astrophys.*, 656, A86

Cliver E. W., Dietrich W. F., 2013, Journal of Space Weather and Space Climate, 3, A31

Cowling T. G., 1946, *Mon. Not. R. Astron. Soc.*, 106, 446

Cox D. P., Tucker W. H., 1969, Astrophysical Journal, 157, 1157

Dhakal S. K., Zhang J., 2024, Astrophysical Journal, 960, 36

Elvidge S., Themens D. R., 2025, Space Weather, 23, 2024SW004113

Emslie A. G. et al., 2012, Astrophysical Journal, 759, 71

Evershed J., 1910, Monthly Notices of the Royal Astronomical Society, 70, 217

Fang T.-W. et al., 2022, Space Weather, 20, e2022SW003193

Forbes T. G. et al., 2006, , 123, 251

Foukal P. V., 2004, Solar Astrophysics, 2nd, Revised Edition

Gnevyshev M. N., 1938, Mitteilungen der Nikolai-Hauptsternwarte zu Pulkowo, 16, B36

Grimes R., Pintér B., Morgan H., 2020, Solar Physics, 295, 87

Hale G. E., 1908, *Astrophys. J.*, 28, 315

Hale G. E., Ellerman F., Nicholson S. B., Joy A. H., 1919, Astrophysical Journal, 49, 153

Hale G. E., Nicholson S. B., 1925, Astrophysical Journal, 62, 270

Hayakawa H. et al., 2025, Astrophysical Journal, 979, 49

Howard R. A., Sheeley, Jr. N. R., Michels D. J., Koomen M. J., 1985, *J. Geophys. Res.*, 90, 8173

Howard R. F., 1992, *Sol. Phys.*, 137, 51

James A. W., Green L. M., Barnes G., van Driel-Gesztelyi L., Williams D. R., 2024, *Astrophys. J.*, 975, 52

James A. W. et al., 2017, *Sol. Phys.*, 292, 71

James A. W., Green L. M., van Driel-Gesztelyi L., Valori G., 2020, *Astron. Astrophys.*, 644, A137

James A. W., Williams D. R., O'Kane J., 2022, *Astron. Astrophys.*, 665, A37

Jaswal P., Sinha S., Nandy D., 2025, Astrophysical Journal, 979, 31

Kallenrode M.-B., 2004, Space Physics: An Introduction to Plasmas and Particles in the Heliosphere and Magnetospheres. Springer

Kazachenko M. D., Canfield R. C., Longcope D. W., Qiu J., Des Jardins A., Nightingale R. W., 2009, Astrophysical Journal, 704, 1146

Kliem B., Török T., 2006, Phys. Rev. Lett., 96, 255002

Kumar P., Park S.-H., Cho K. S., Bong S. C., 2013, Solar Physics, 282, 503

Lagg A., Solanki S. K., van Noort M., Danilovic S., 2014, *Astron. Astrophys.*, 568, A60

Leka K. D., Canfield R. C., McClymont A. N., van Driel-Gesztelyi L., 1996, *Astrophys. J.*, 462, 547

Leka K. D., Skumanich A., 1998, *Astrophys. J.*, 507, 454

Lemen J. R. et al., 2012, *Sol. Phys.*, 275, 17

Li A., Liu Y., 2015, SOLAR PHYSICS, 290, 2199

Li L., Zhang J., 2009, Astrophysical Journal, 706, L17

Li W., Ai C., Wang H., 2001, in IAU Symposium, Vol. 203, Recent Insights into the Physics of the Sun and Heliosphere: Highlights from SOHO and Other Space Missions, Brekke P., Fleck B., Gurman J. B., eds.

Lites B. W., Scharmer G. B., Skumanich A., 1990, Astrophysical Journal, 355, 329

Liu C. et al., 2016, Nature Communications, 7, 13104

Livingston W., 2002, Solar Physics, 207, 41

Longcope D. W., Welsch B. T., 2000, Astrophysical Journal, 545, 1089

Löptien B., Lagg A., van Noort M., Solanki S. K., 2018, *Astron. Astrophys.*, 619, A42

—, 2020, *Astron. Astrophys.*, 635, A202

Louis R. E., Puschmann K. G., Kliem B., Balthasar H., Denker C., 2014, Astronomy and Astrophysics, 562, A110

Masson S., Klein K. L., Bütikofer R., Flückiger E., Kurt V., Yushkov B., Krucker S., 2009, Solar Physics, 257, 305

McIntosh P. S., 1981, in The Physics of Sunspots, Cram L. E., Thomas J. H., eds., pp. 7–54

Nagovitsyn Y. A., Ivanov V. G., Skorbezh N. N., 2019, Astronomy Letters, 45, 396

Oliveira D. M., Zesta E., Nandy D., 2025, Frontiers in Astronomy and Space Sciences, 11, 1522139

Parker E. N., 1979, *Astrophys. J.*, 230, 905

Petrovay K., van Driel-Gesztelyi L., 1997, *Sol. Phys.*, 176, 249

Priest E., 2014, Magnetohydrodynamics of the Sun

Priest E. R., Forbes T., 2002, The Astronomy and Astrophysics Review, 10, 313

Régnier S., Priest E. R., 2007, *Astrophys. J. Lett.*, 669, L53

Rimmele T. R. et al., 2020, Solar Physics, 295, 172

Ritter S., Rotko D., Halpin S., Nawal A., Farias A., Patel K., Diggewadi A., Hill H., 2020, New Space, 8, 23

Scharmer G. B. et al., 2008, Astrophysical Journal, 689, L69

Scherrer P. H. et al., 2012, *Sol. Phys.*, 275, 207

Schou J. et al., 2012, Solar Physics, 275, 229

Schrijver C. J., Aulanier G., Title A. M., Pariat E., Delannée C., 2011, Astrophysical Journal, 738, 167

Schuck P. W., 2006, Astrophysical Journal, 646, 1358

Shea M. A., Smart D. F., 2006, Advances in Space Research, 38, 313

Singh A. K., Singh R., 2003, INDIAN JOURNAL OF PHYSICS AND PROCEEDINGS OF THE INDIAN ASSOCIATION FOR THE CULTIVATION OF SCIENCE B, 77, 611

Siscoe G., 2000, Journal of Atmospheric and Solar-Terrestrial Physics, 62, 1223

Siu-Tapia A., Lagg A., van Noort M., Rempel M., Solanki S. K., 2019, Astronomy and Astrophysics, 631, A99

Solanki S. K. et al., 2020, Astronomy and Astrophysics, 642, A11

Spörer G., 1880, Publikationen des Astrophysikalischen Observatoriums zu Potsdam, 2, 1

Sturrock Z., Hood A. W., Archontis V., McNeill C. M., 2015, Astronomy and Astrophysics, 582, A76

Su Y., Veronig A. M., Holman G. D., Dennis B. R., Wang T., Temmer M., Gan W., 2013, Nature Physics, 9, 489

Svestka Z., Jackson B. V., Machado M. E., 1992, Eruptive Solar Flares, Vol. 399

Thomas J. H., Weiss N. O., 1992, in NATO Advanced Study Institute (ASI) Series C, Vol. 375, Sunspots. Theory and Observations, Thomas J. H., Weiss N. O., eds., p. 3

—, 2012, Sunspots and Starspots

Tiwari S. K., van Noort M., Solanki S. K., Lagg A., 2015, *Astron. Astrophys.*, 583, A119

Török T., Temmer M., Valori G., Veronig A. M., van Driel-Gesztelyi L., Vršnak B., 2013, Solar Physics, 286, 453

Tziotziou K., Georgoulis M. K., Raouafi N.-E., 2012, Astrophysical Journal, 759, L4

Vemareddy P., Ambastha A., Maurya R. A., 2012, Astrophysical Journal, 761, 60

Vemareddy P., Cheng X., Ravindra B., 2016, Astrophysical Journal, 829, 24

Wachter R., Schou J., Rabello-Soares M. C., Miles J. W., Duvall T. L., Bush R. I., 2012, Solar Physics, 275, 261

Waldmeier M., 1955, Ergebnisse und Probleme der Sonnenforschung.

Walker A., 2018, PhD thesis, University of Central Lancashire

Webb D. F., Howard T. A., 2012, Living Reviews in Solar Physics, 9, 3

White S. M., Thomas R. J., Schwartz R. A., 2005, Solar Physics, 227, 231

Wilson A., Maskelyne N., 1774, Philosophical Transactions of the Royal Society of London Series I, 64, 1

Woods T. N. et al., 2012, *Sol. Phys.*, 275, 115

Xia X., Hu X., Wang H., Zhang K., 2025, Remote Sensing, 17, 394

Yan X. L., Qu Z. Q., 2007, *Astron. Astrophys.*, 468, 1083

Yan X. L., Qu Z. Q., Kong D. F., 2008, Monthy Notices of the Royal Astronomical Society, 391, 1887

Yan X. L., Qu Z. Q., Kong D. F., Xu C. L., 2012, Astrophysical Journal, 754, 16

Yan X. L., Qu Z. Q., Xu C. L., 2008, Astrophysical Journal, 682, L65

Yan X. L., Wang J. C., Pan G. M., Kong D. F., Xue Z. K., Yang L. H., Li Q. L., Feng X. S., 2018, Astrophysical Journal, 856, 79

Zhang Y., Huang J., Liu J., Yang S., Yang Y., Tan B., 2025, Astrophysical Journal, 979, 165

Zhu C., Alexander D., Tian L., 2012, Solar Physics, 278, 121

Zwaan C., 1968, , 6, 135

Appendix A

4 Month Profiles

A.1 Walker Comparison

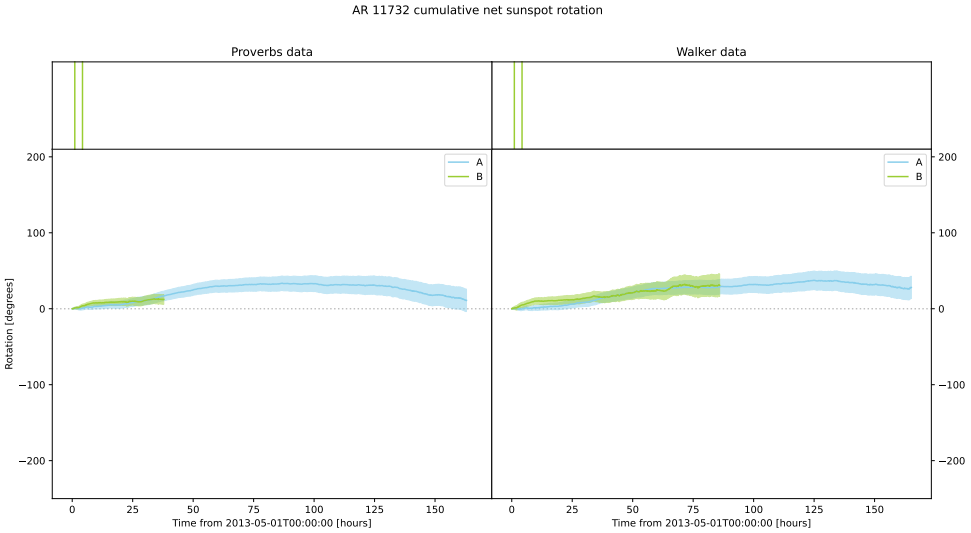

(i) AR 11732

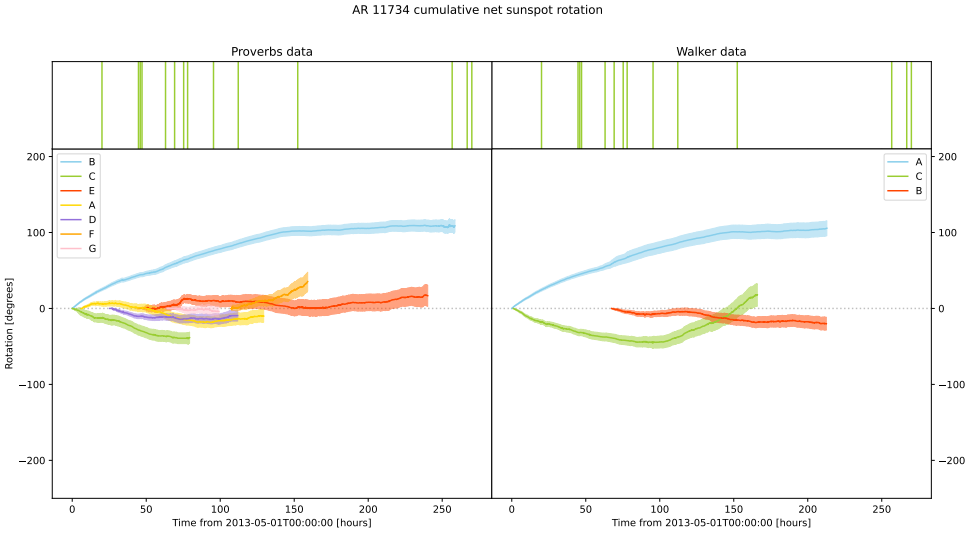

(ii) AR 11734

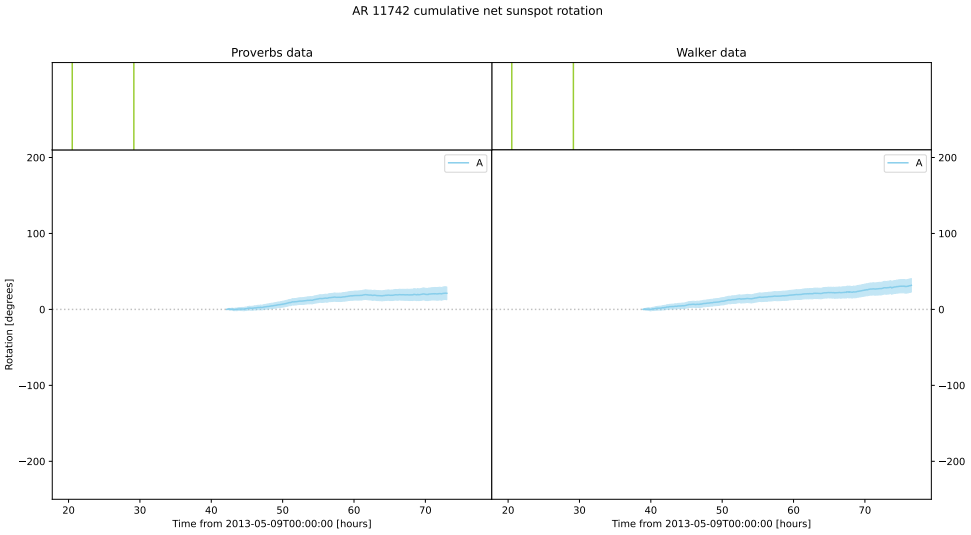

(iii) AR 11742

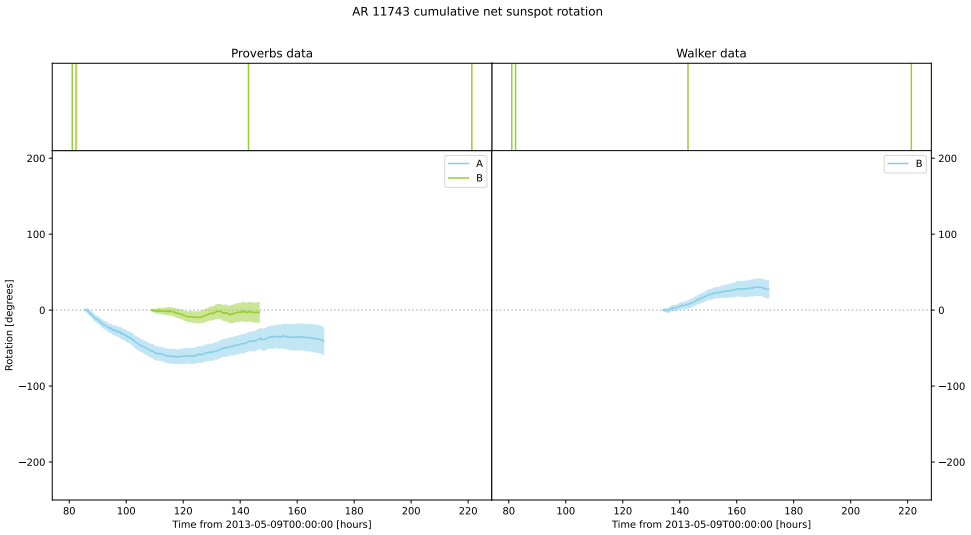

(iv) AR 11743

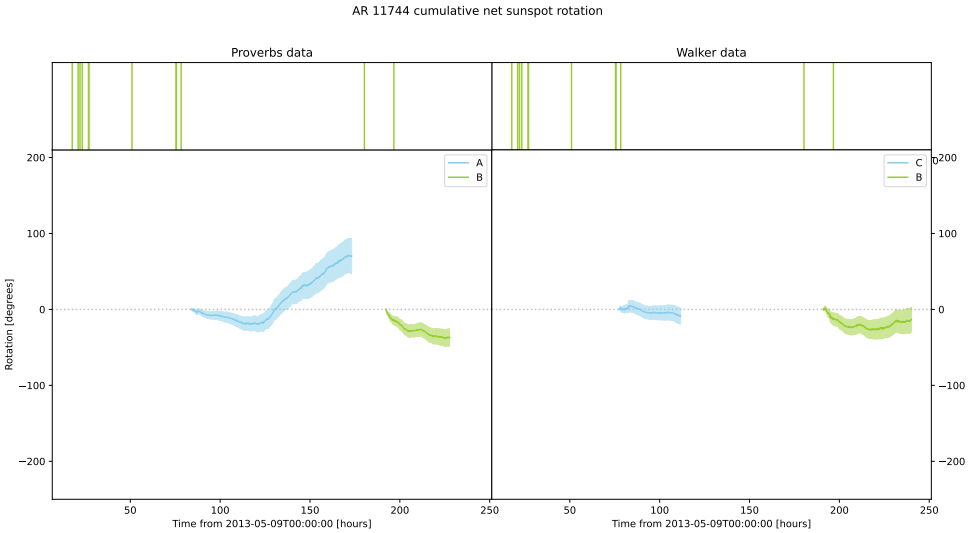

(v) AR 11744

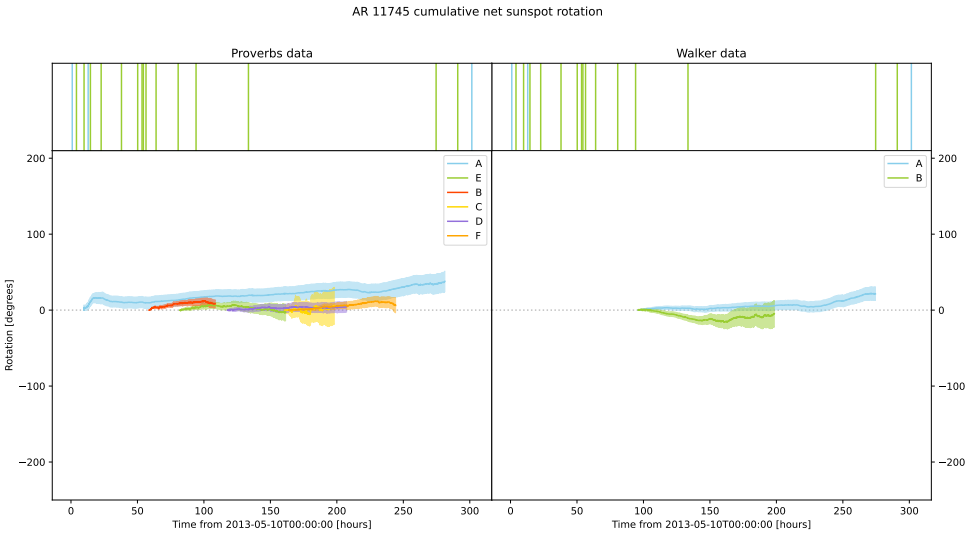

(vi) AR 11745

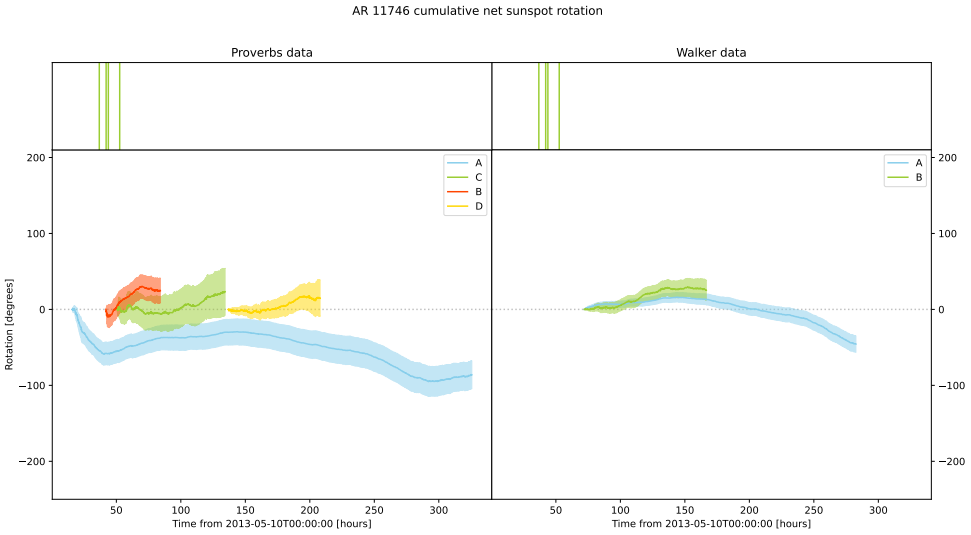

(vii) AR 11746

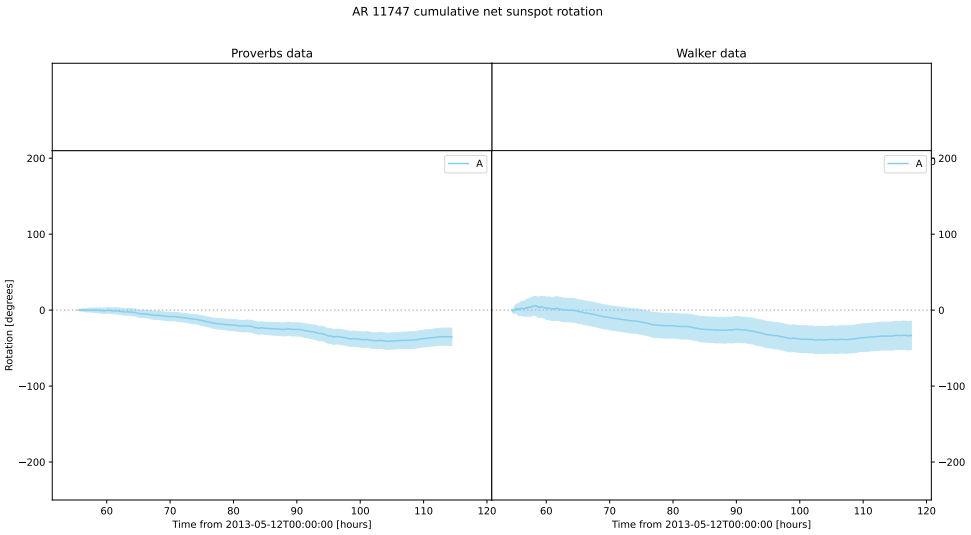

(viii) AR 11747

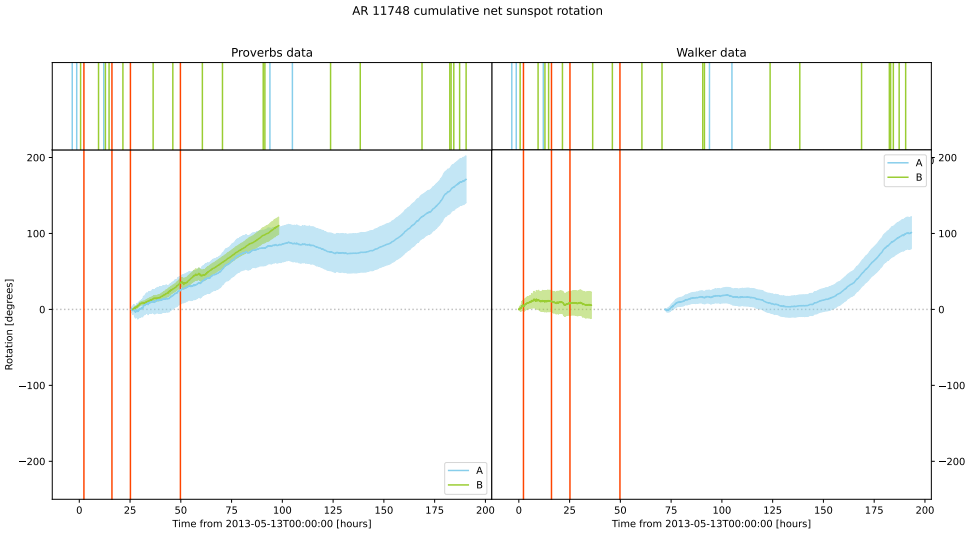

(ix) AR 11748

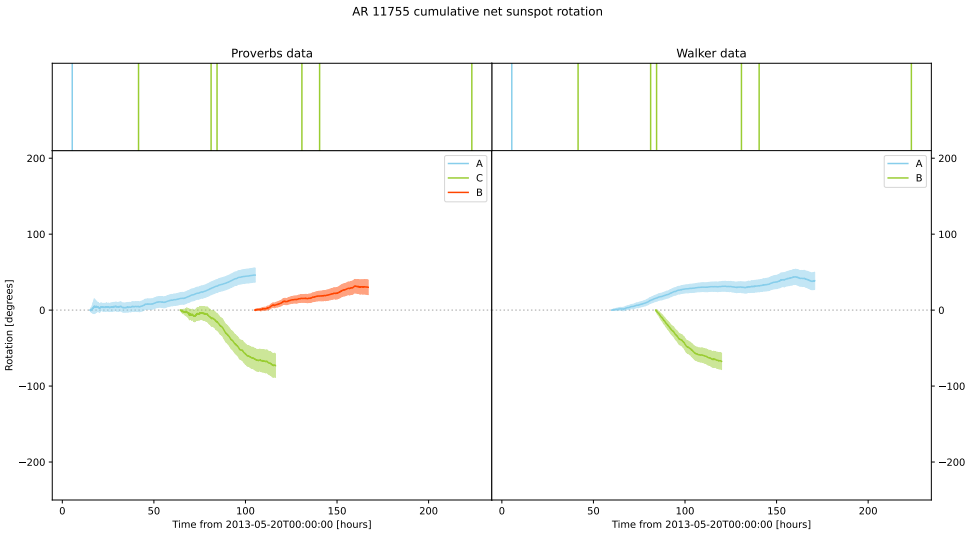

(x) AR 11755

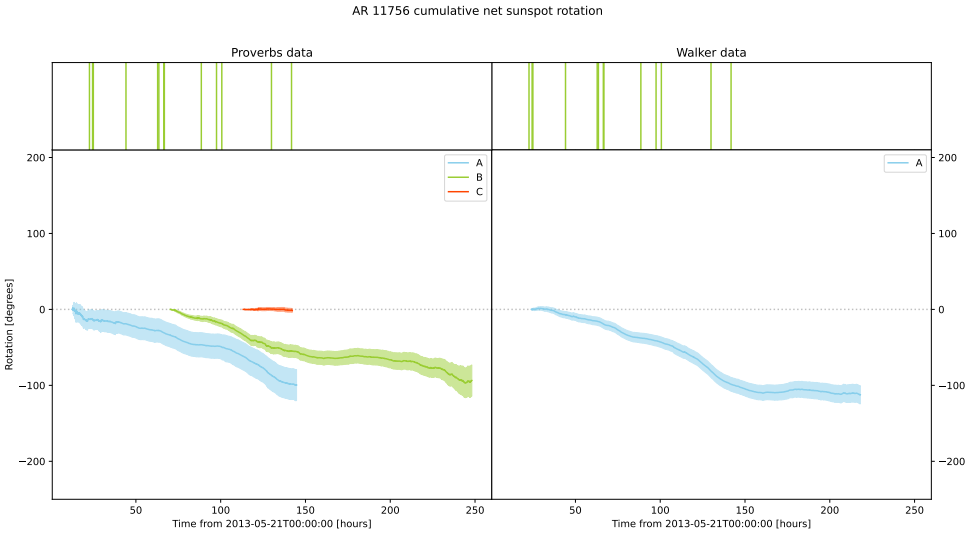

(xi) AR 11756

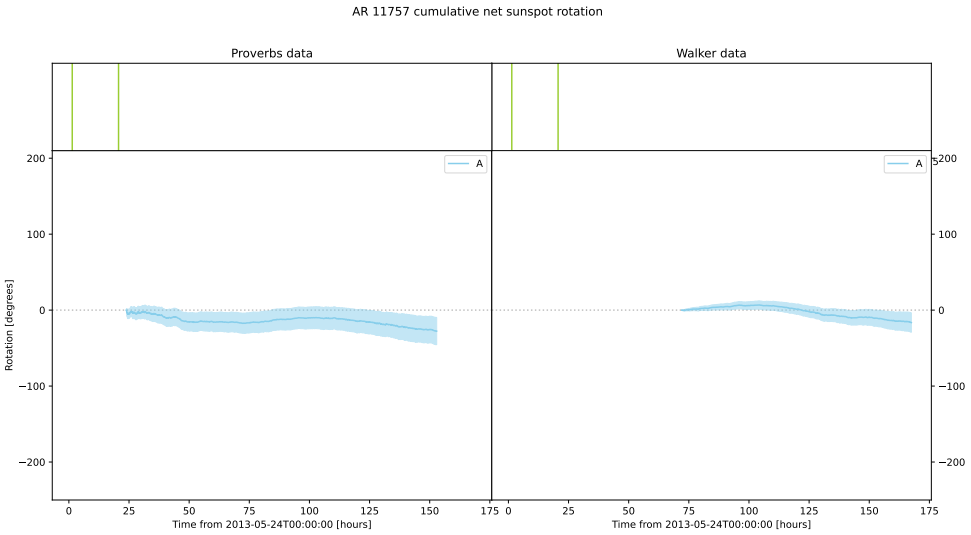

(xii) AR 11757

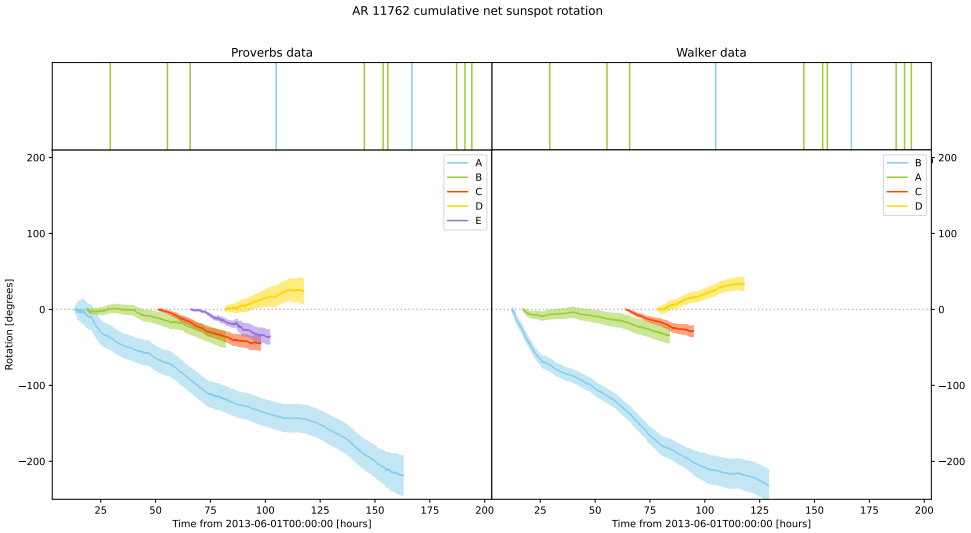

(xiii) AR 11762

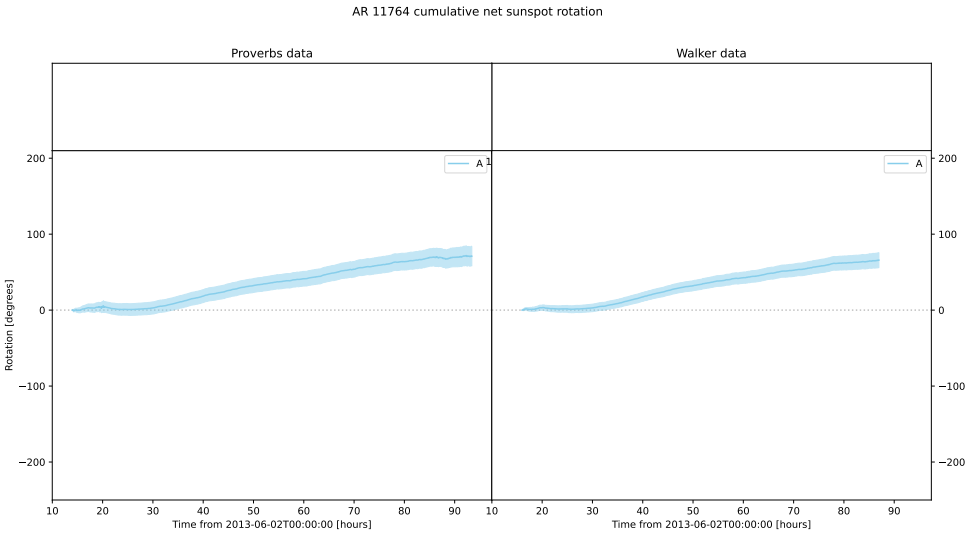

(xiv) AR 11764

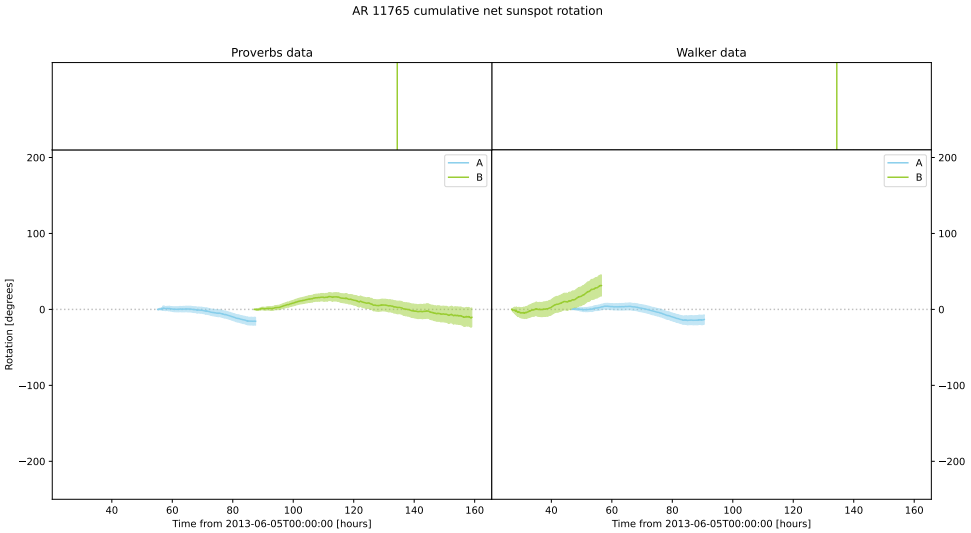

(xv) AR 11765

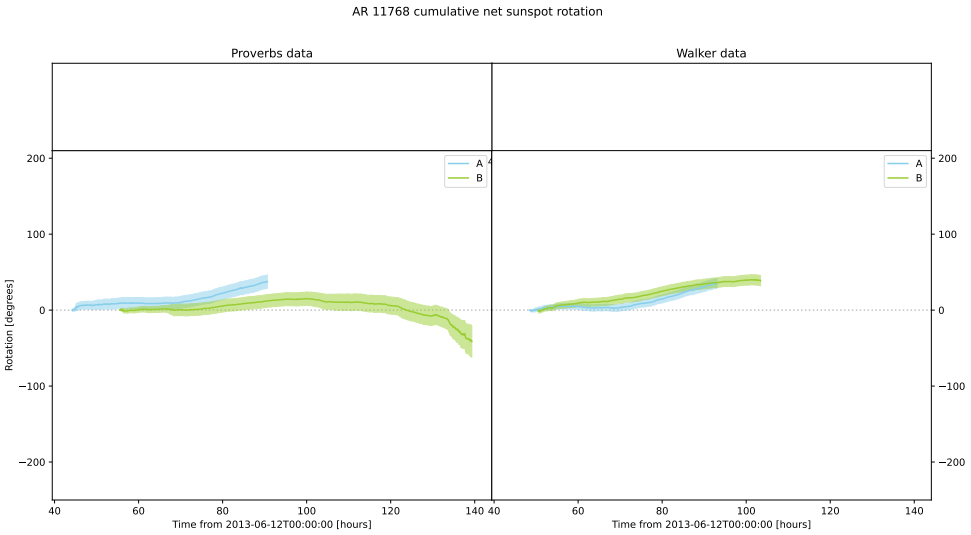

(xvi) AR 11768

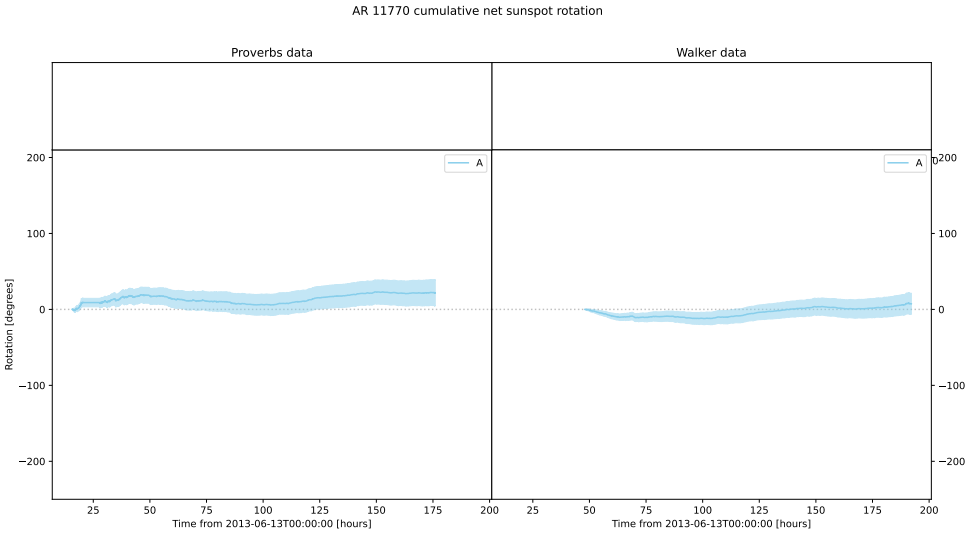

(xvii) AR 11770

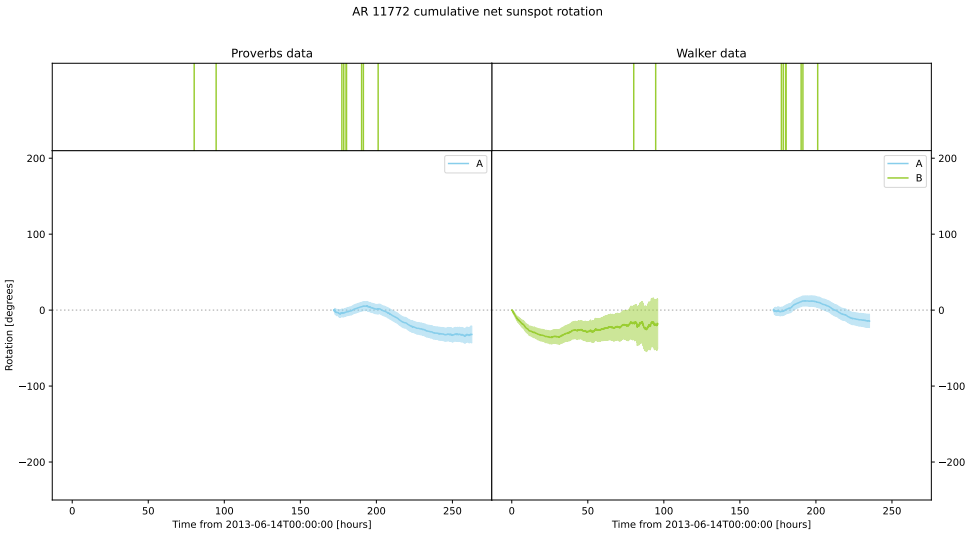

(xviii) AR 11772

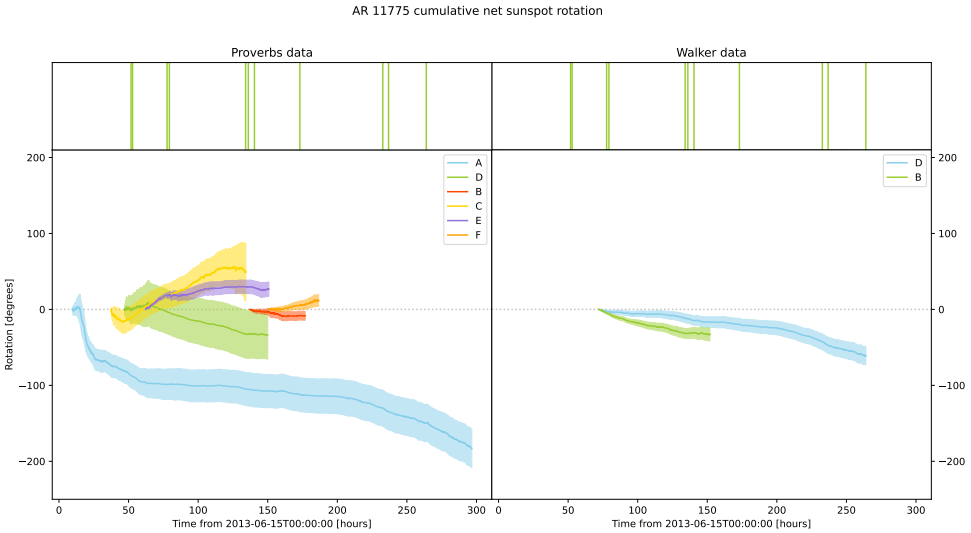

(xix) AR 11775

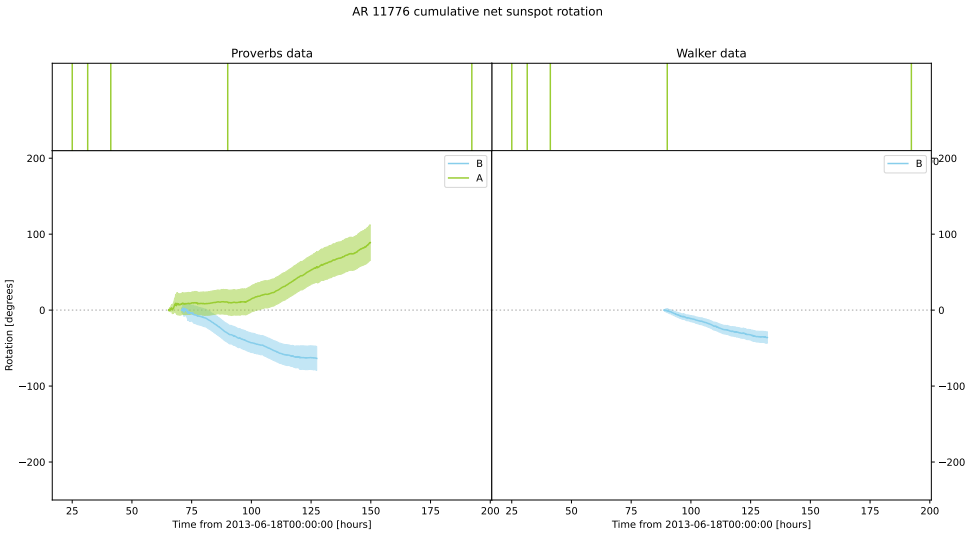

(xx) AR 11776

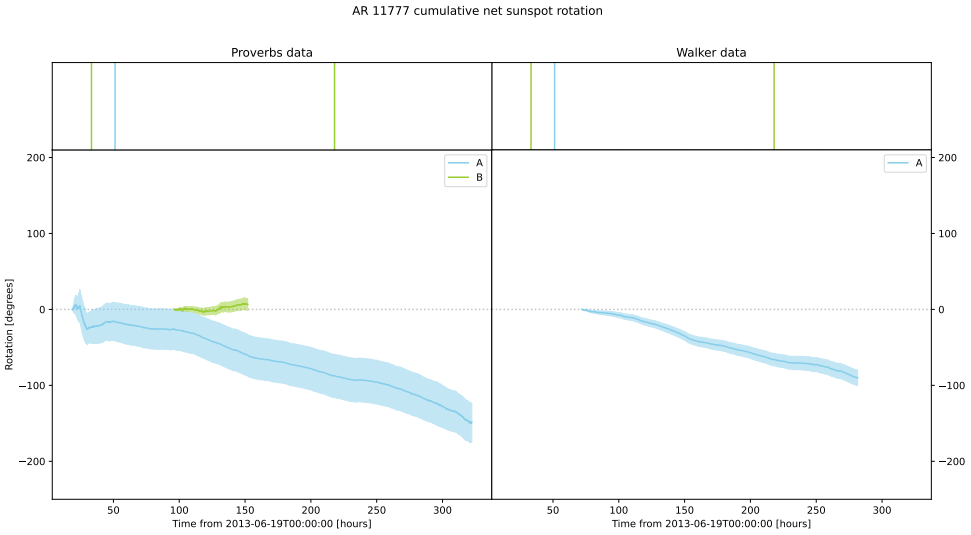

(xxi) AR 11777

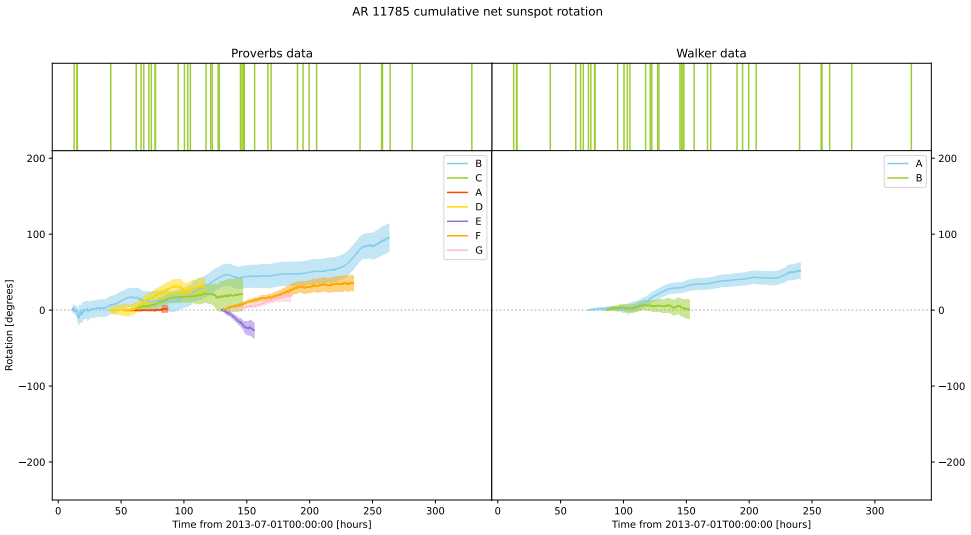

(xxii) AR 11785

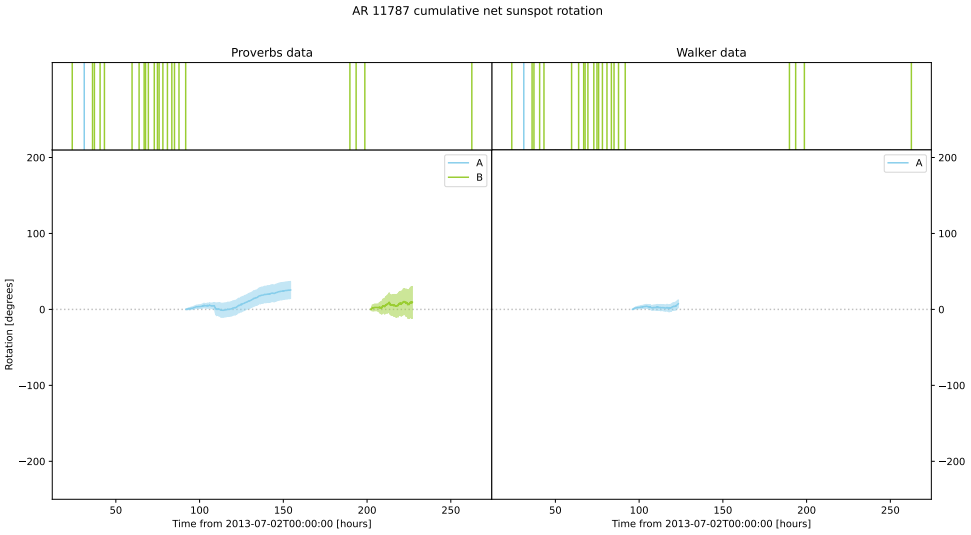

(xxiii) AR 11787

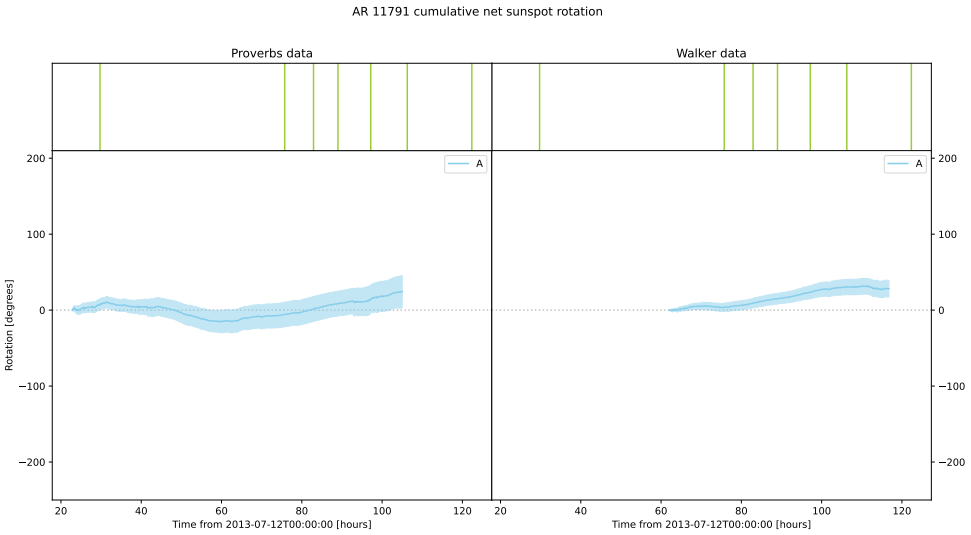

(xxiv) AR 11791

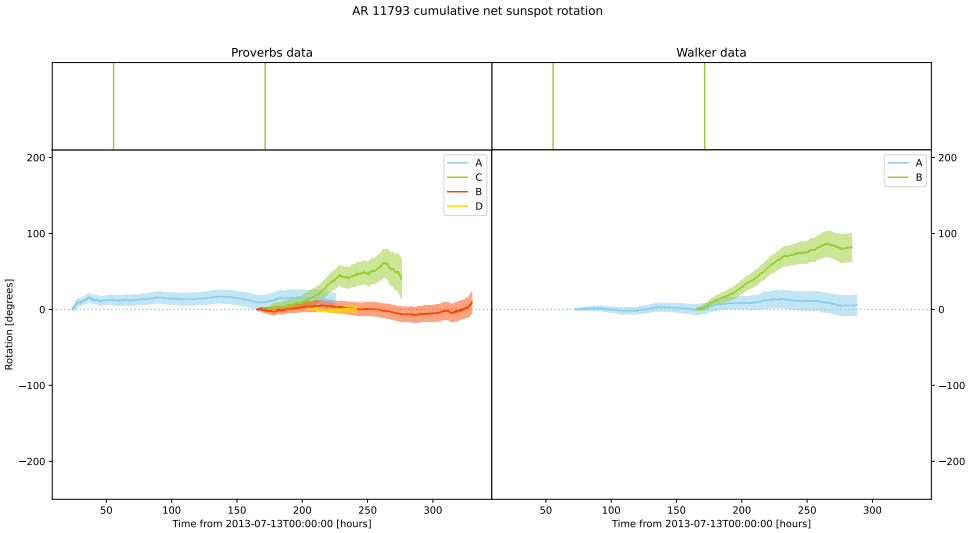

(xxv) AR 11793

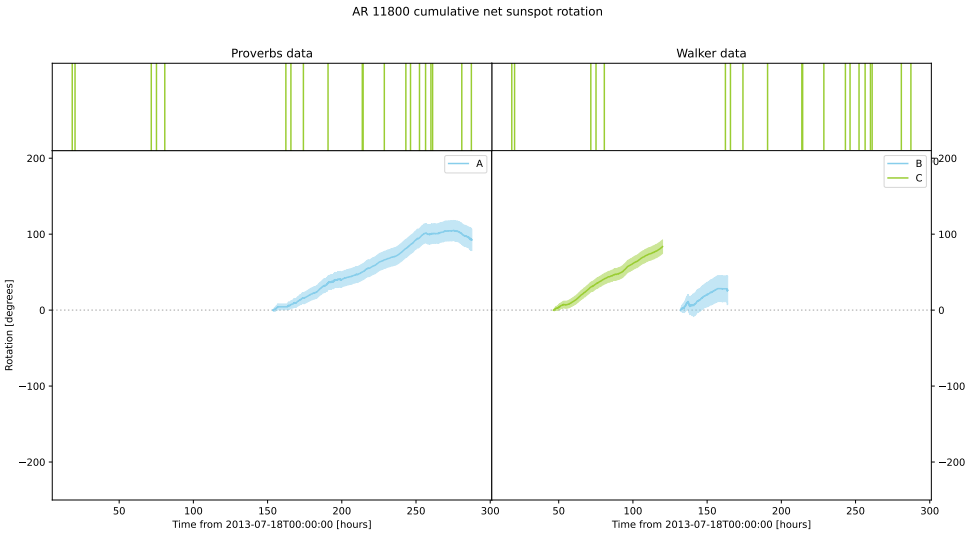

(xxvi) AR 11800

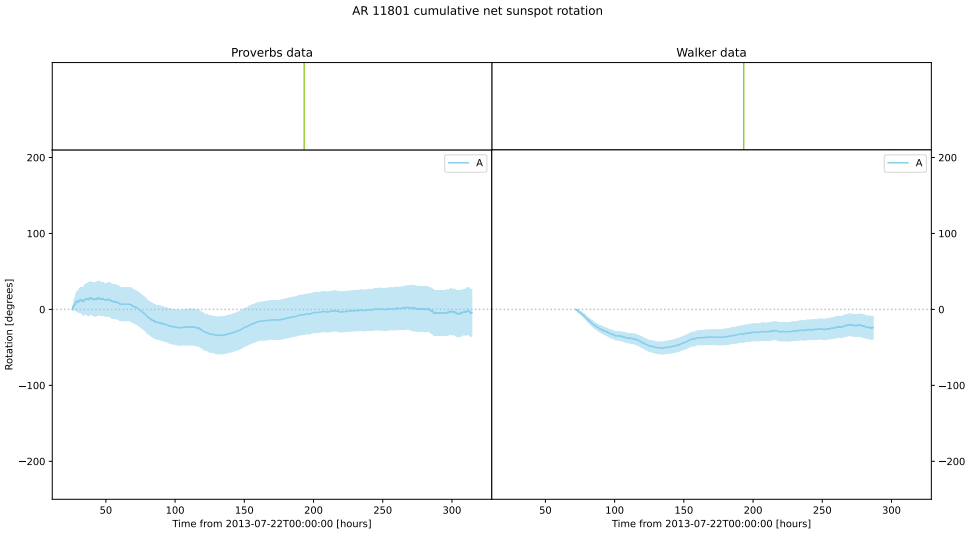

(xxvii) AR 11801

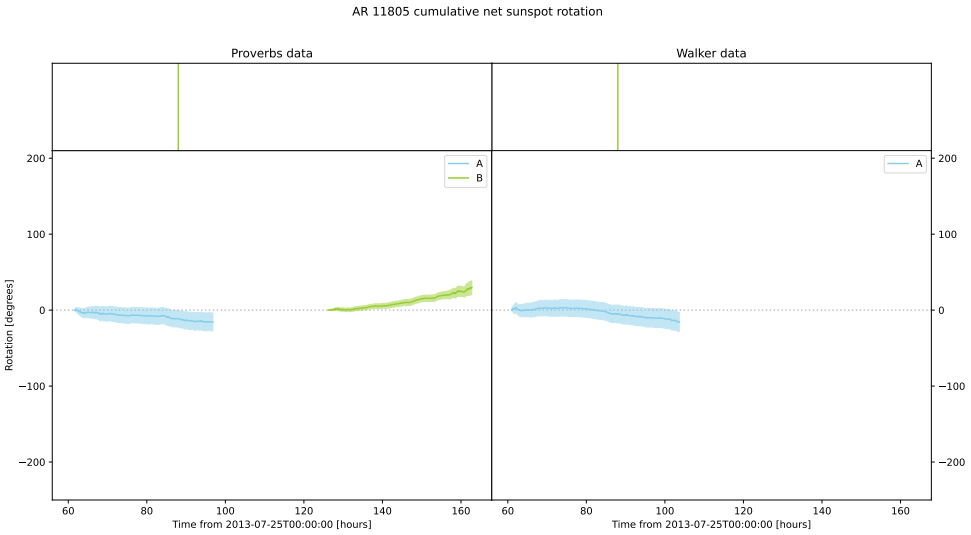

(xxviii) AR 11805

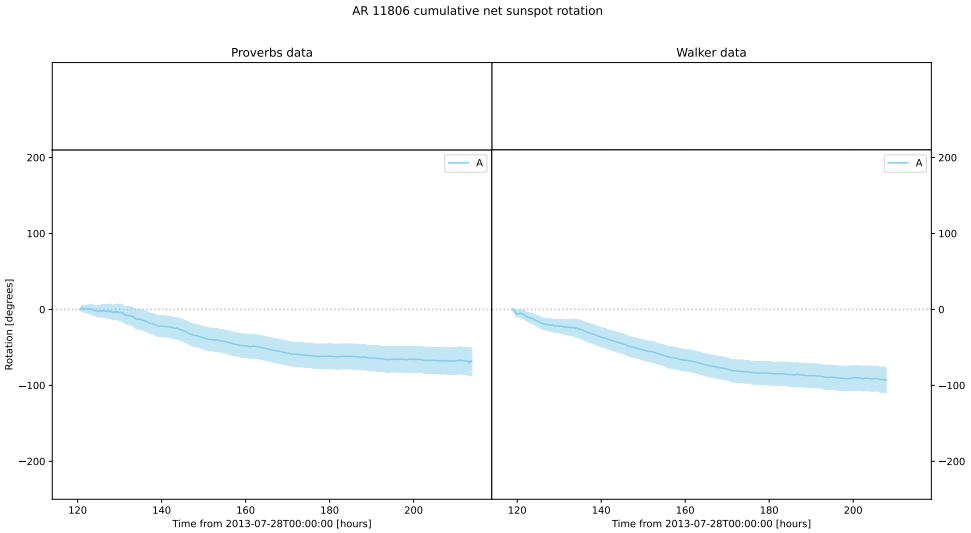

(xxix) AR 11806

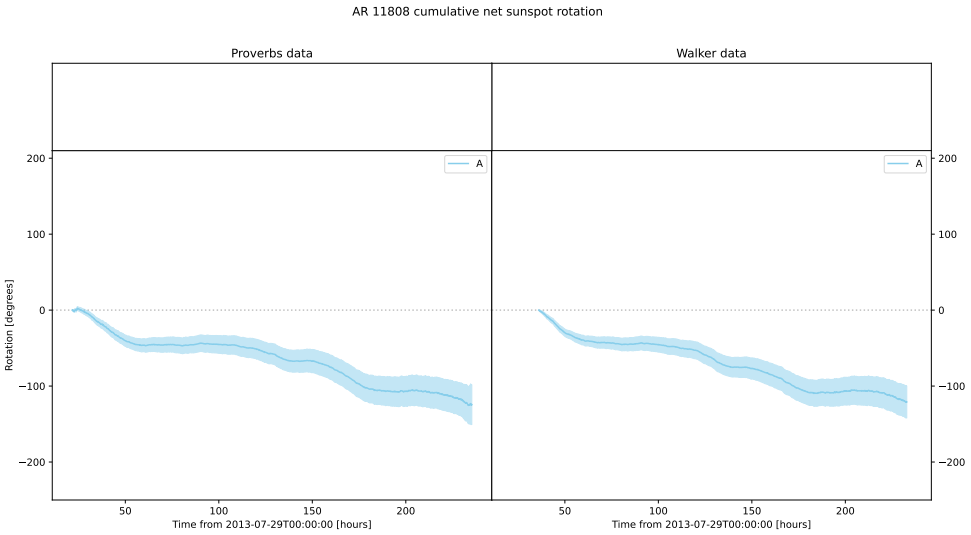

(xxx) AR 11808

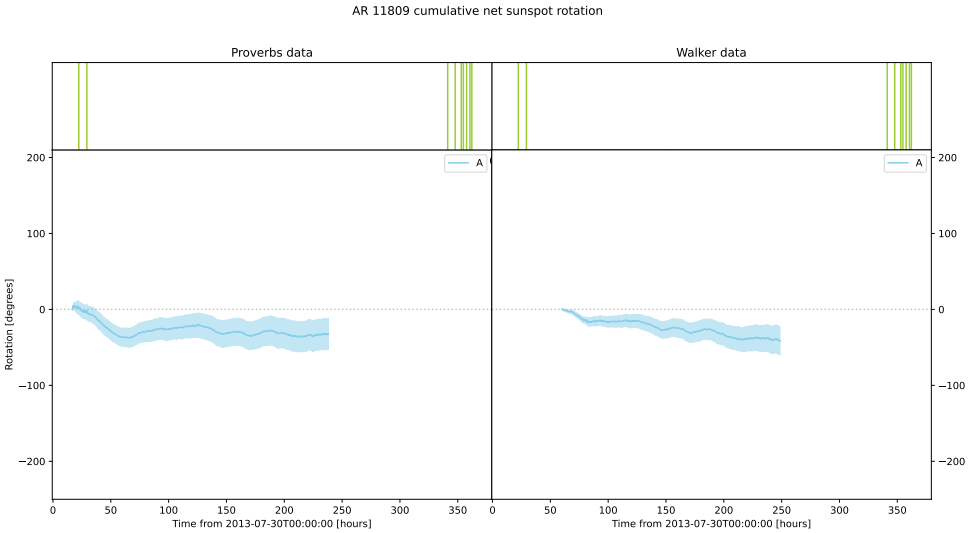

(xxxi) AR 11809

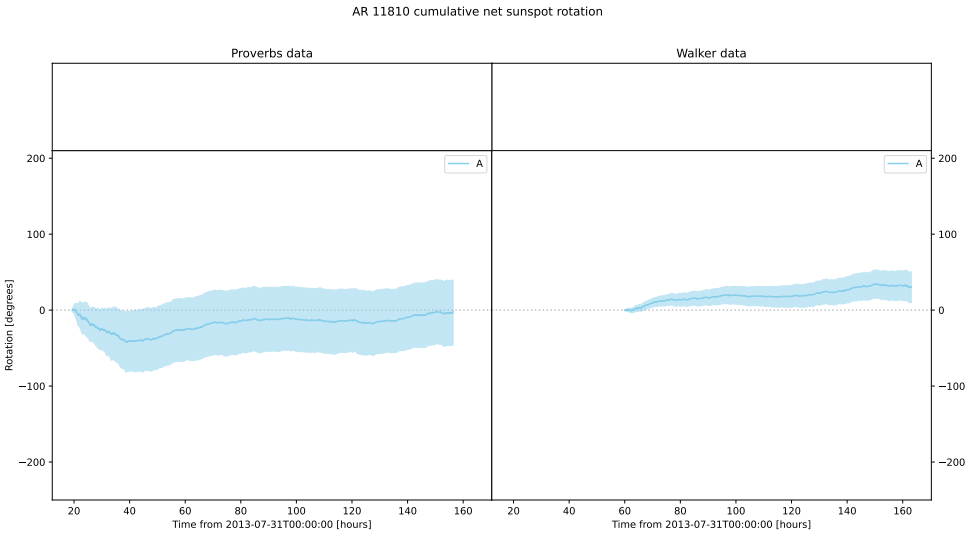

(xxxii) AR 11810

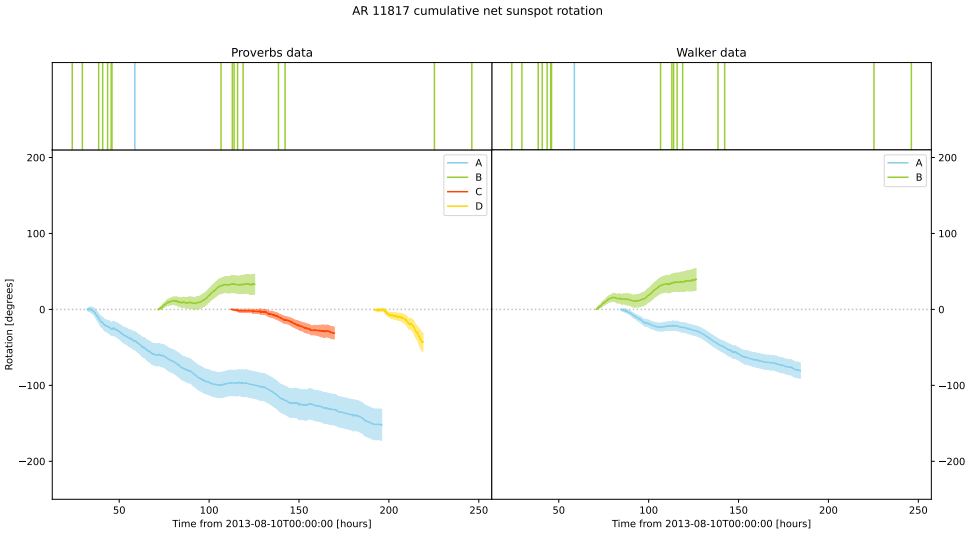

(xxxiii) AR 11817

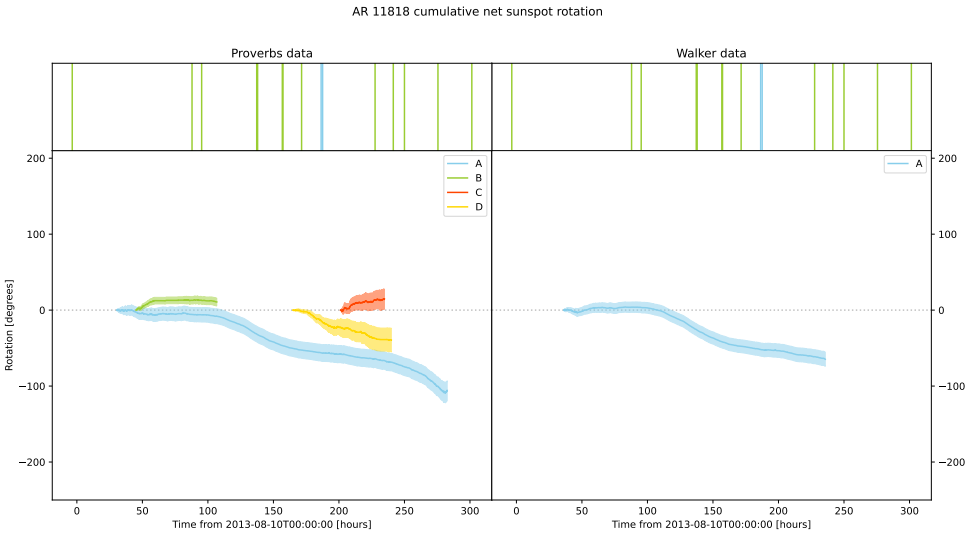

(xxxiv) AR 11818

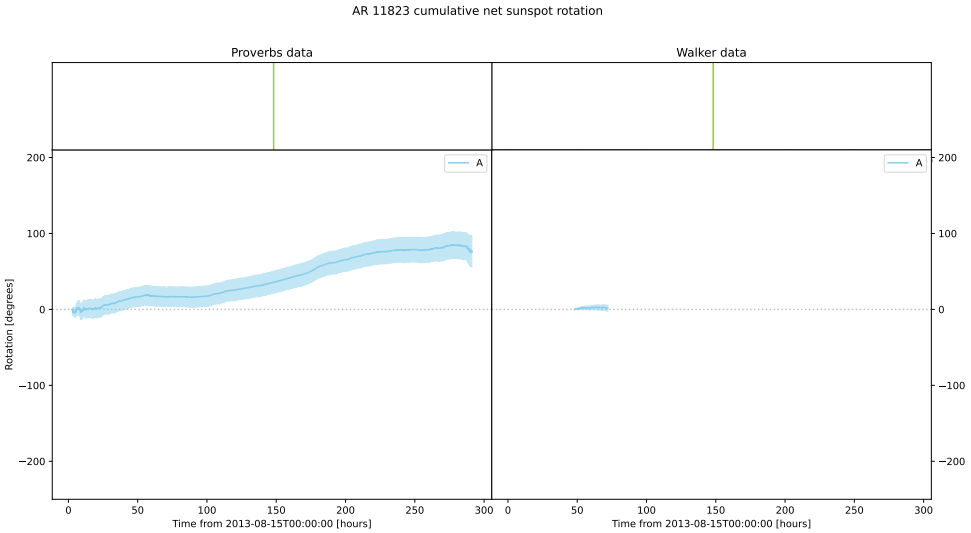

(xxxv) AR 11823

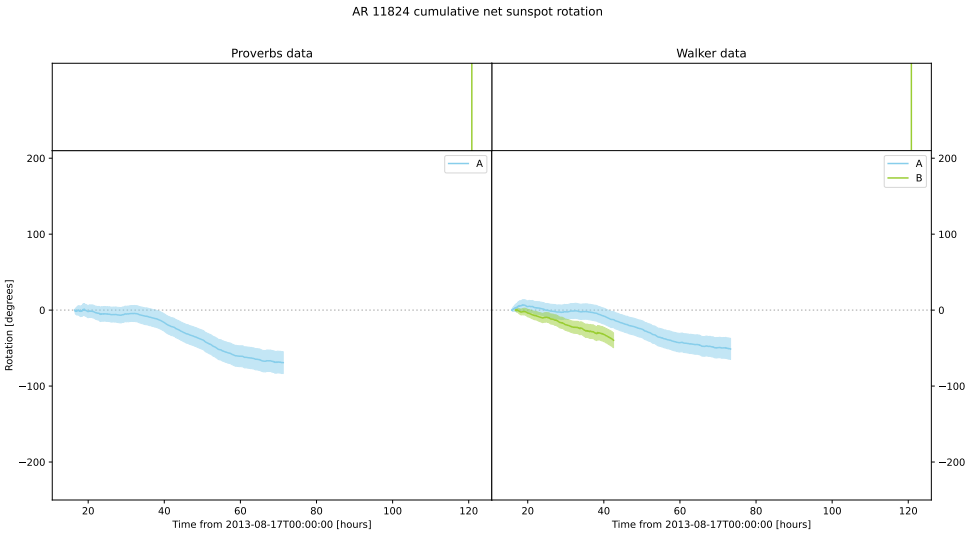

(xxxvi) AR 11824

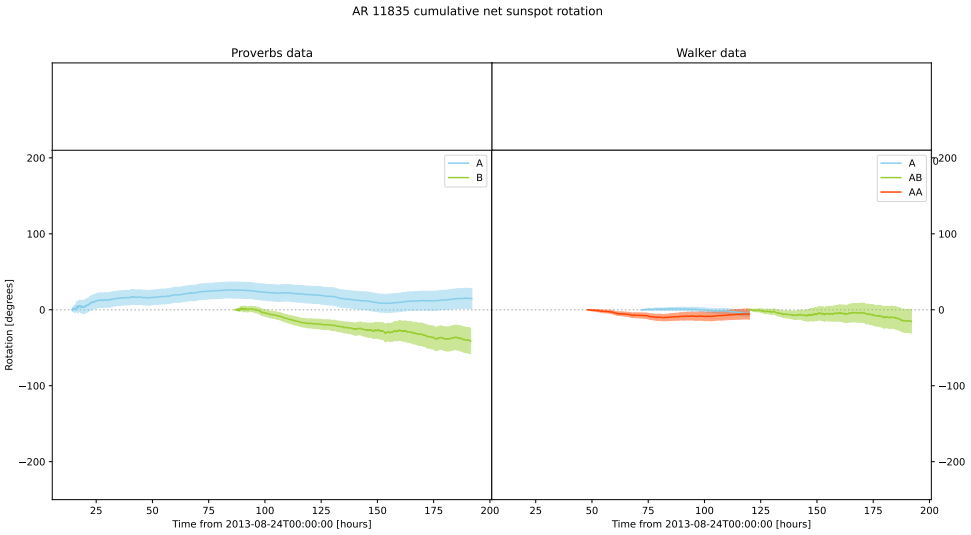

(xxxvii) AR 11835

A.2 Additional Proverbs Active Regions

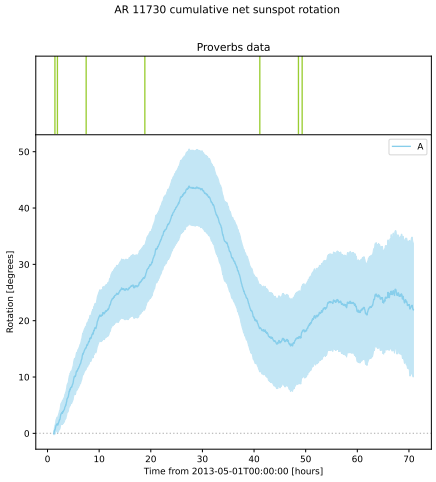

(i) AR 11730

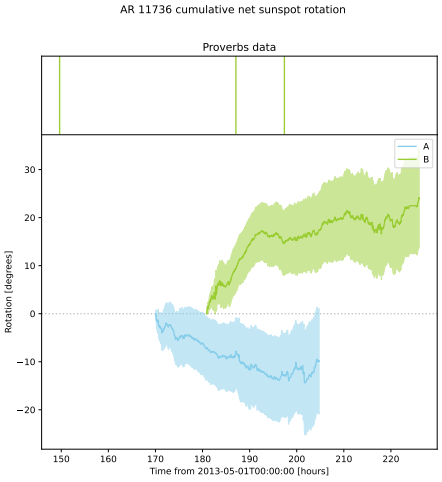

(ii) AR 11736

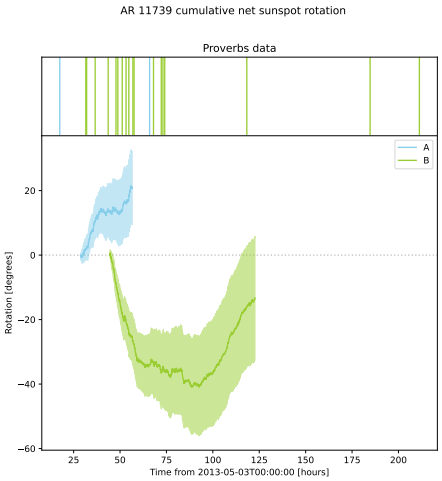

(iii) AR 11739

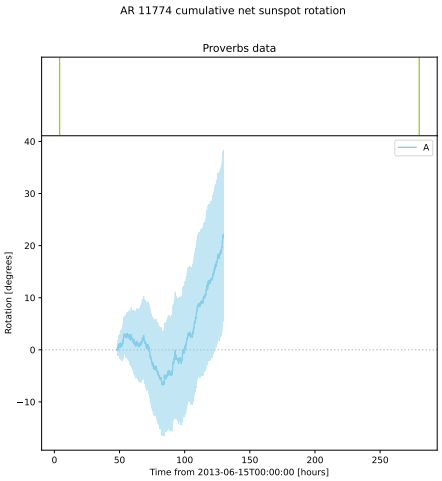

(iv) AR 11774

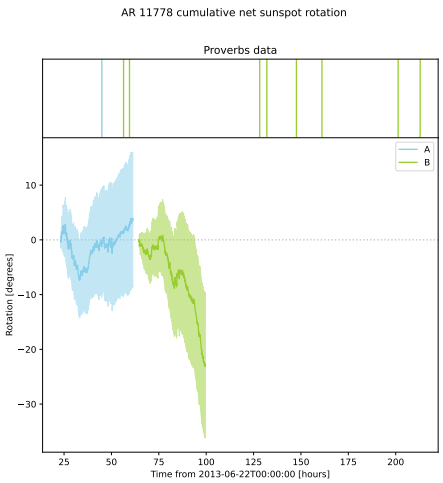

(v) AR 11778

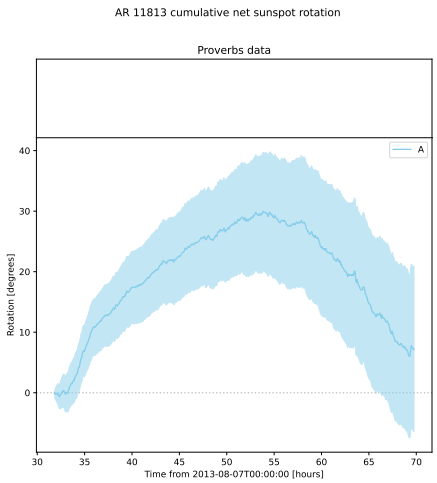

(vi) AR 11813

(vii) AR 11814

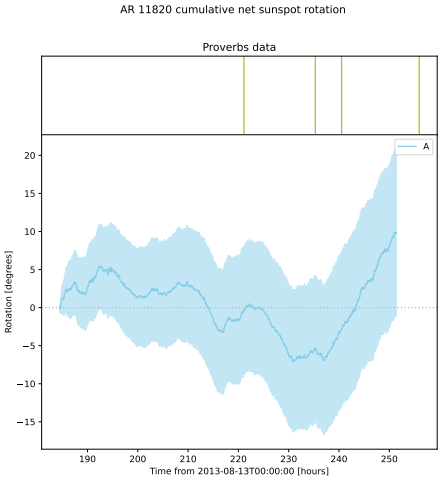

(viii) AR 11820

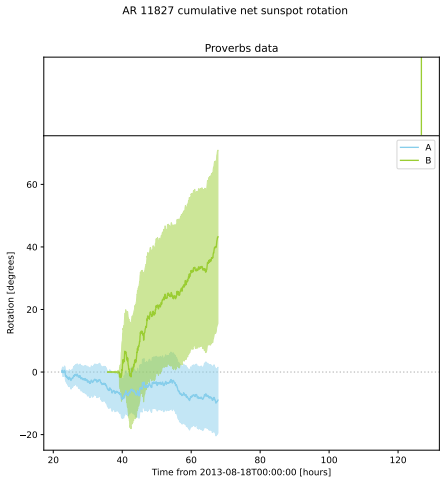

(ix) AR 11827

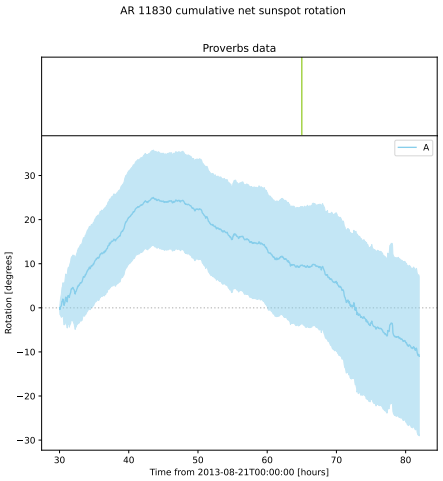

(x) AR 11830

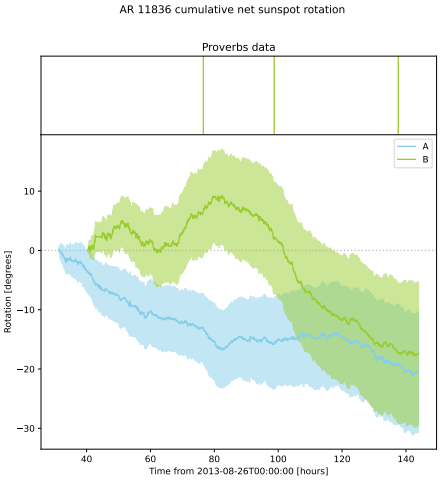

(xi) AR 11836

Appendix B

12 Month Profiles

B.1 Active Region Figures

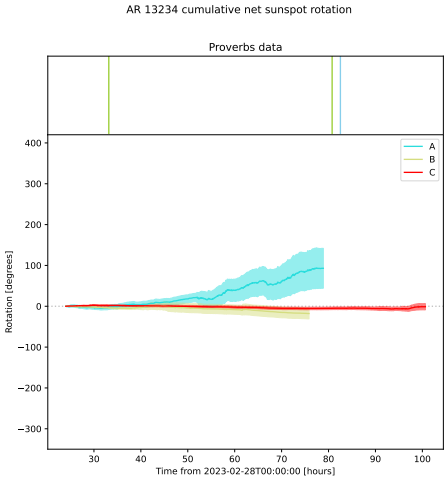

(i) AR 13234

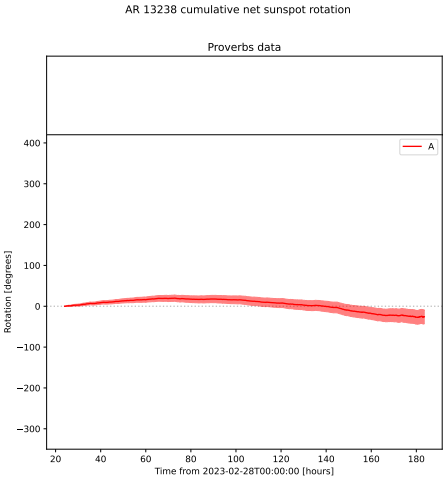

(ii) AR 13238

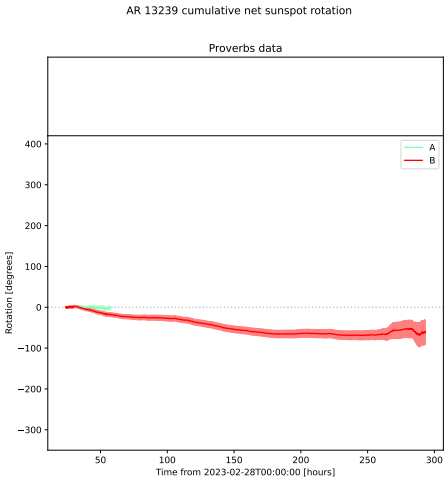

(iii) AR 13239

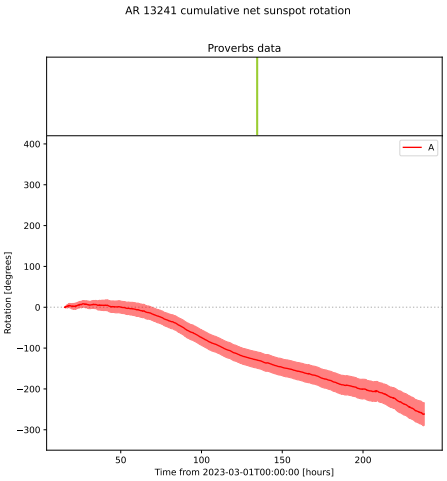

(iv) AR 13241

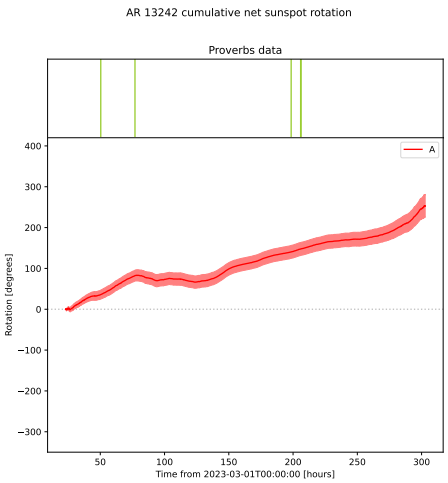

(v) AR 13242

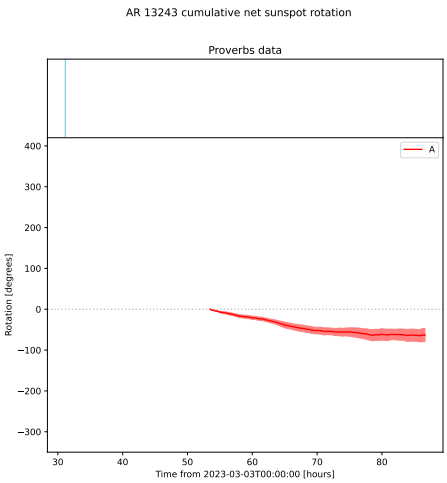

(vi) AR 13243

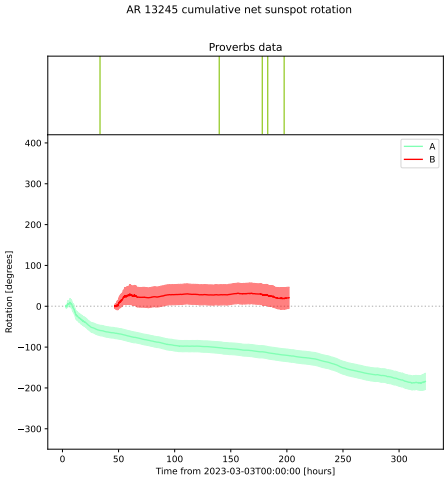

(vii) AR 13245

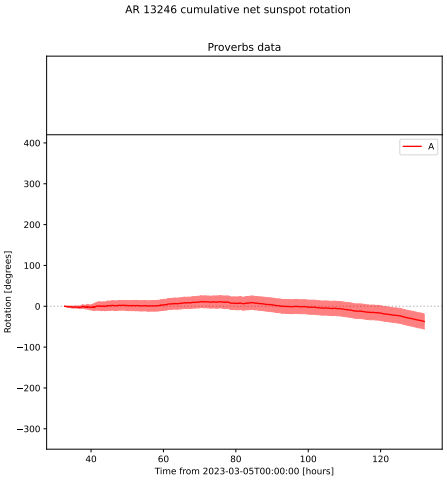

(viii) AR 13246

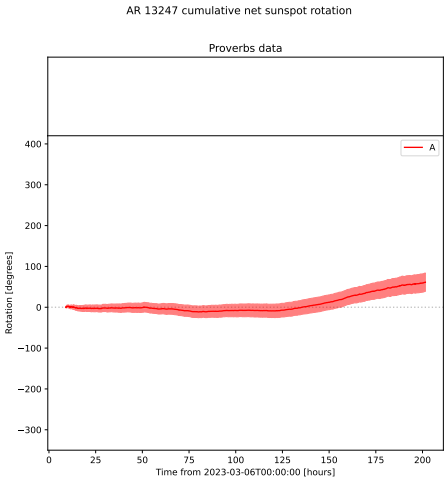

(ix) AR 13247

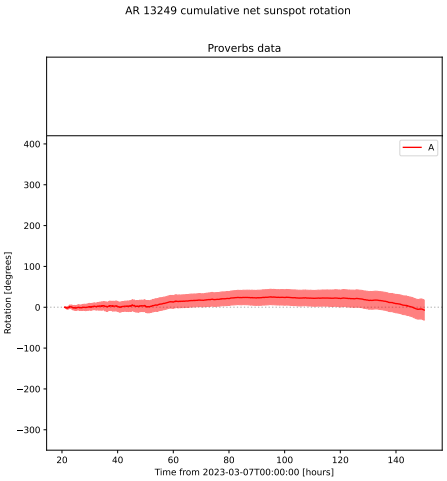

(x) AR 13249

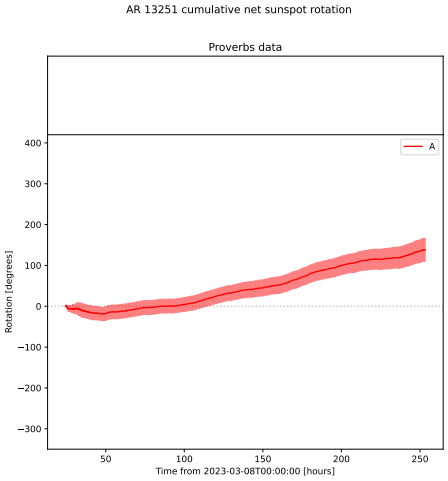

(xi) AR 13251

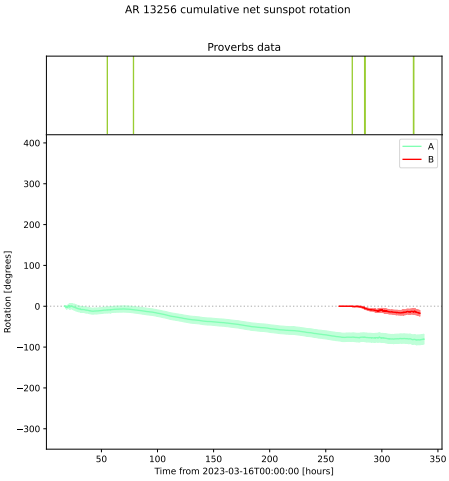

(xii) AR 13256

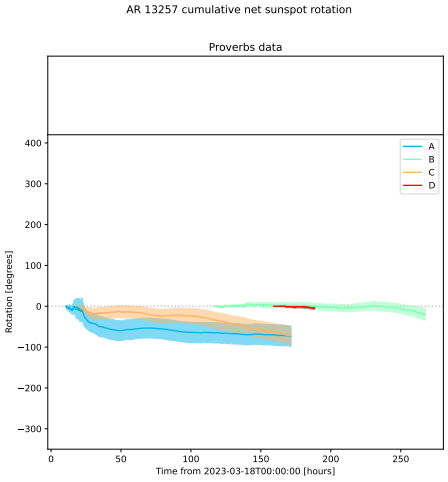

(xiii) AR 13257

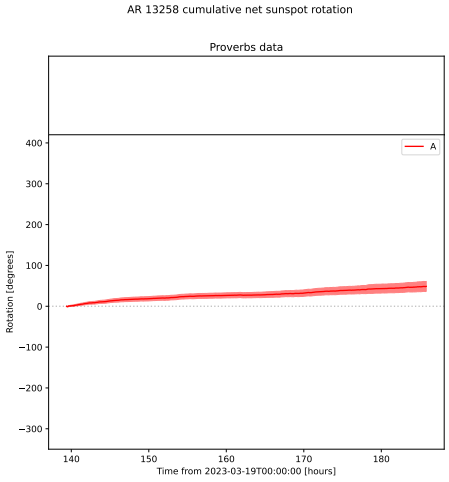

(xiv) AR 13258

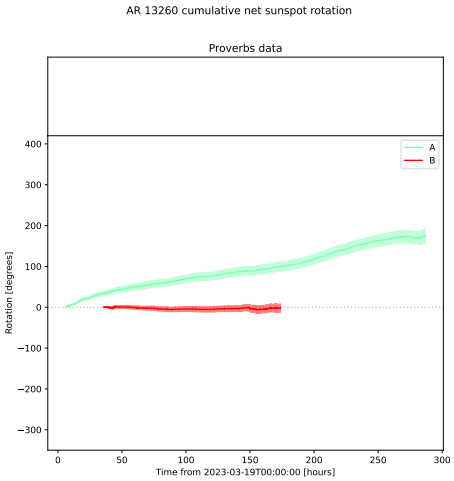

(xv) AR 13260

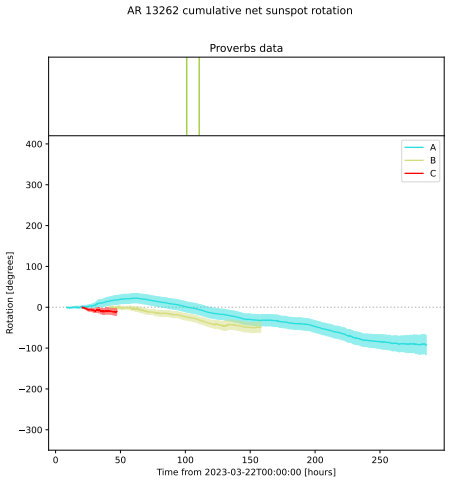

(xvi) AR 13262

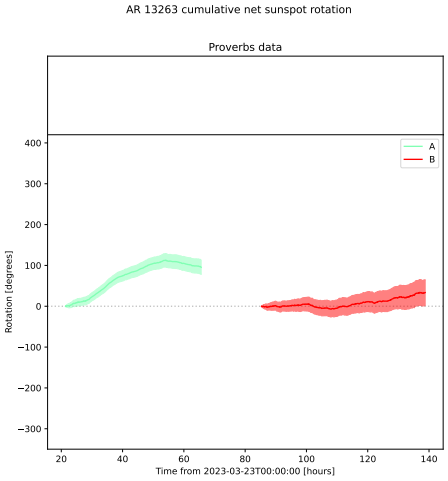

(xvii) AR 13263

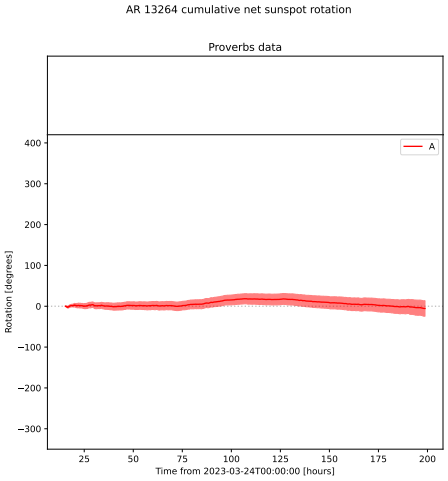

(xviii) AR 13264

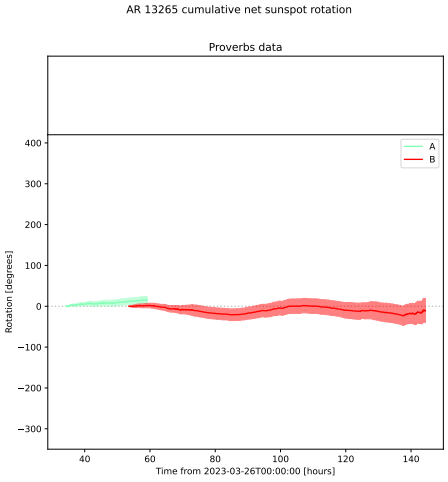

(xix) AR 13265

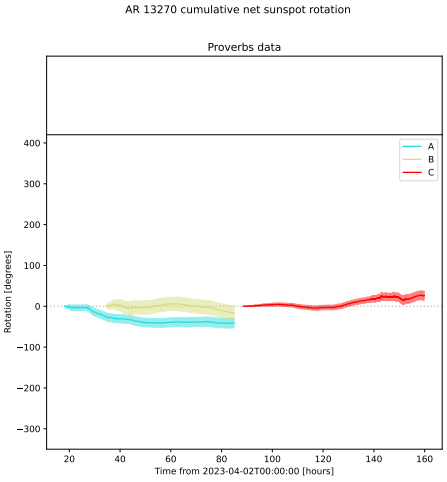

(xx) AR 13270

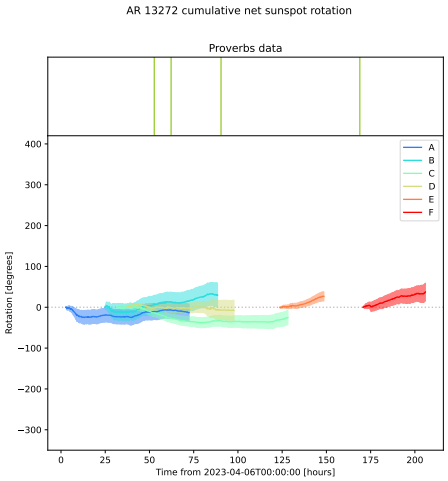

(xxi) AR 13272

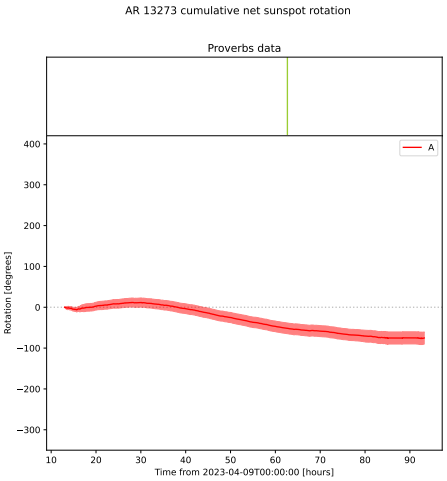

(xxii) AR 13273

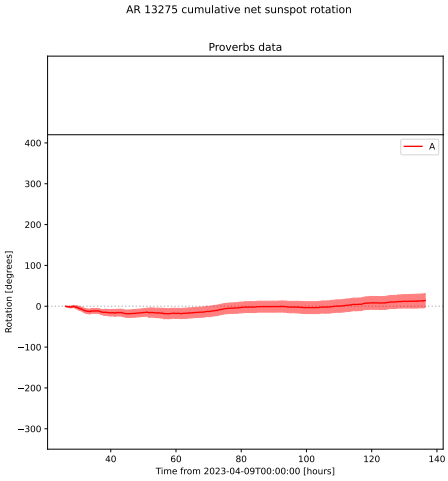

(xxiii) AR 13275

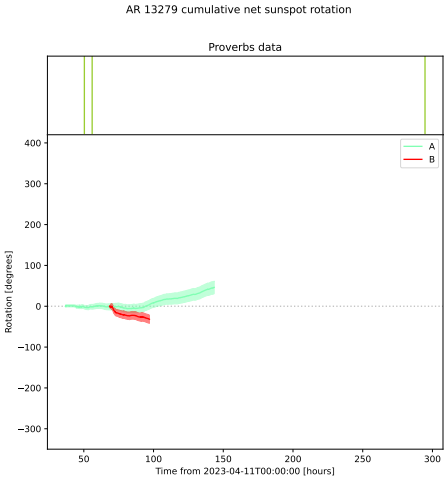

(xxiv) AR 13279

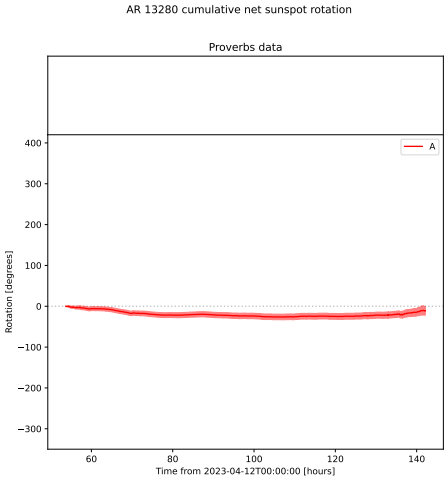

(xxv) AR 13280

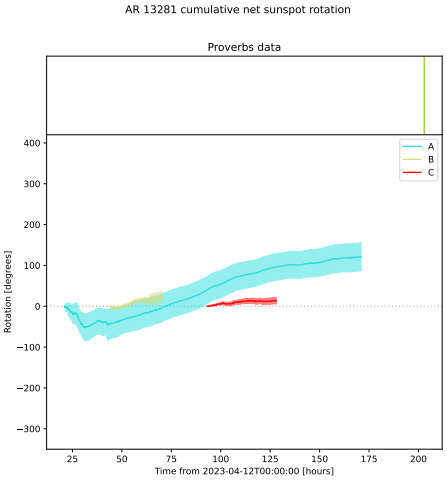

(xxvi) AR 13281

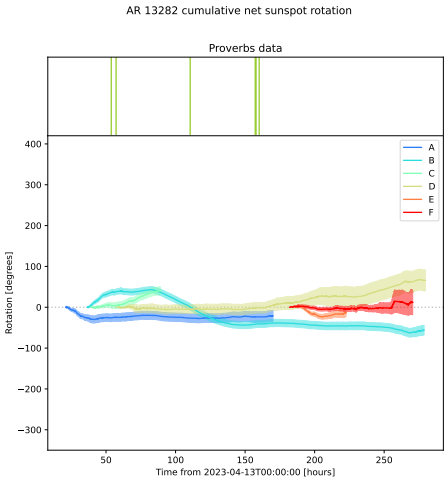

(xxvii) AR 13282

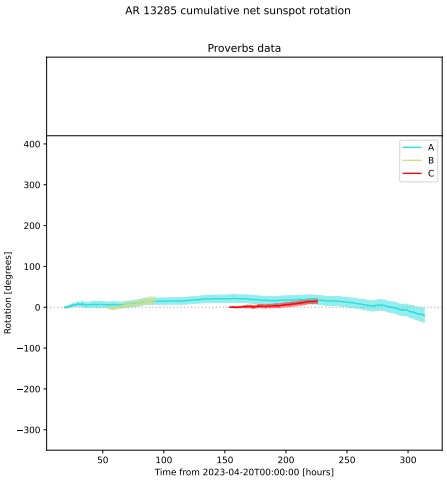

(xxviii) AR 13285

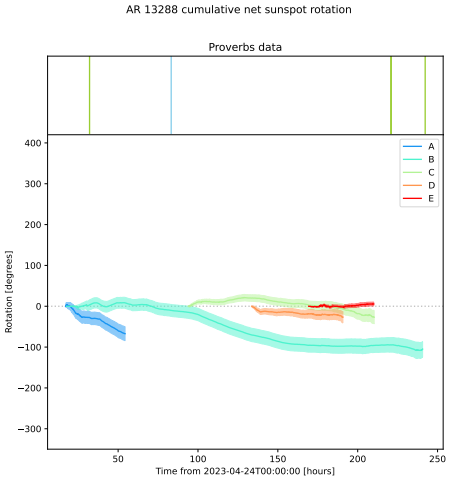

(xxix) AR 13288

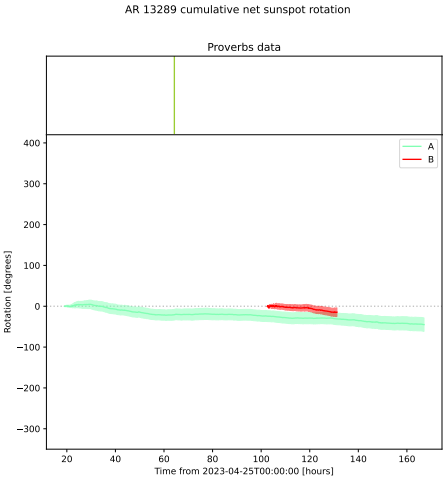

(xxx) AR 13289

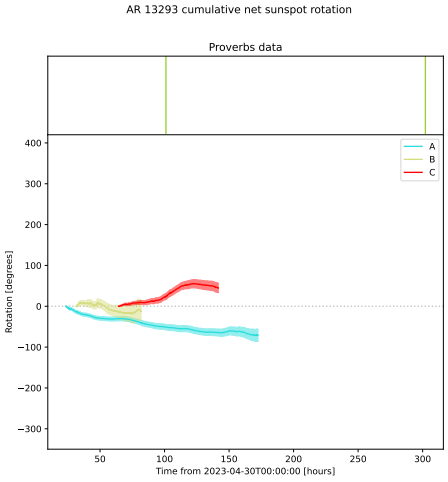

(xxxi) AR 13293

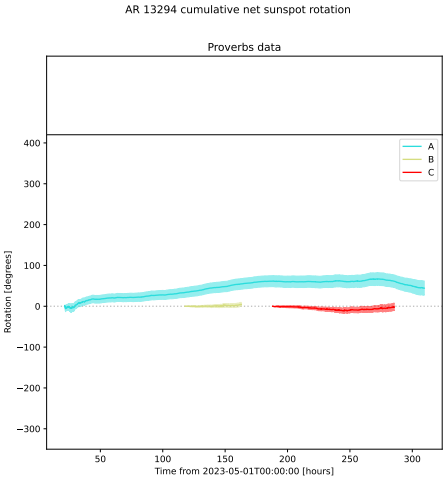

(xxxii) AR 13294

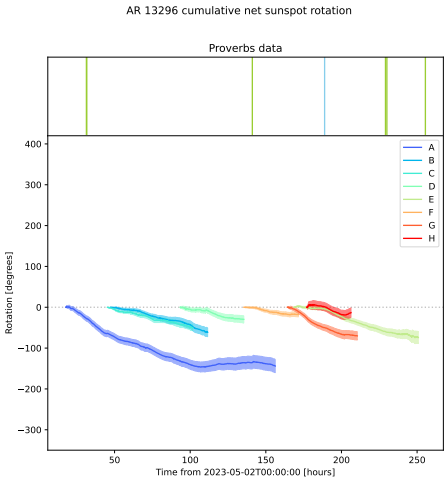

(xxxiii) AR 13296

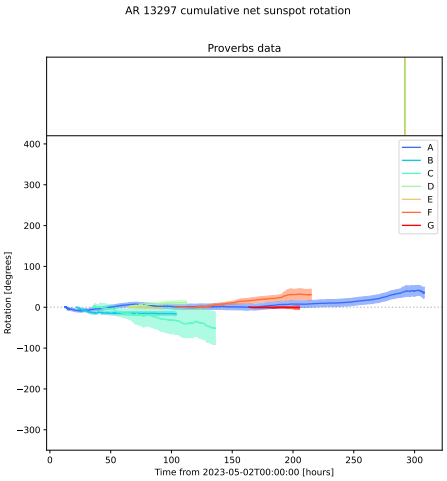

(xxxiv) AR 13297

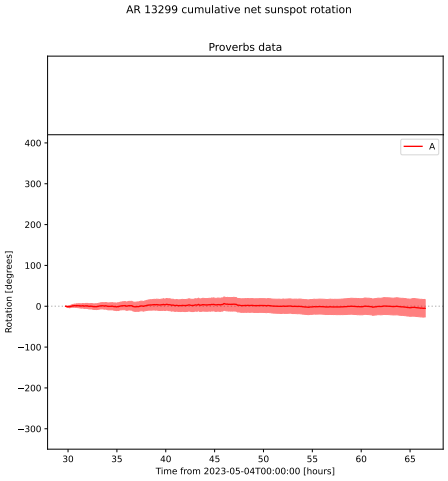

(xxxv) AR 13299

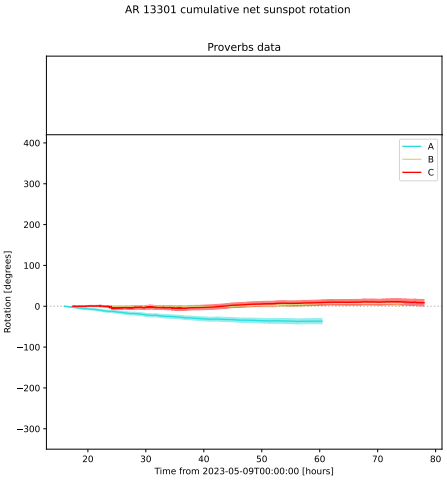

(xxxvi) AR 13301

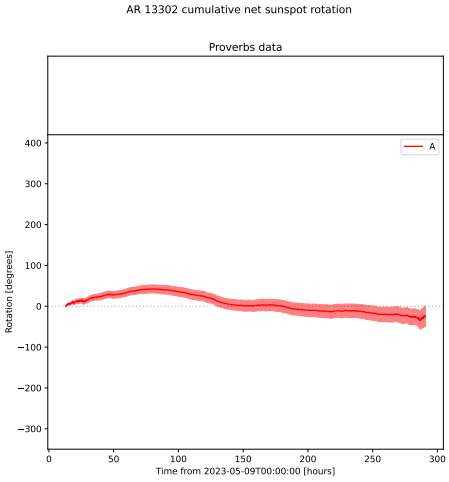

(xxxvii) AR 13302

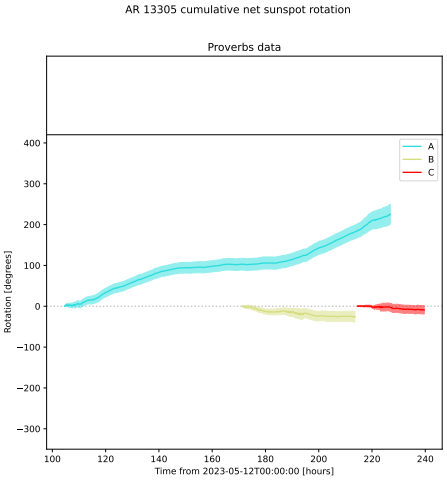

(xxxviii) AR 13305

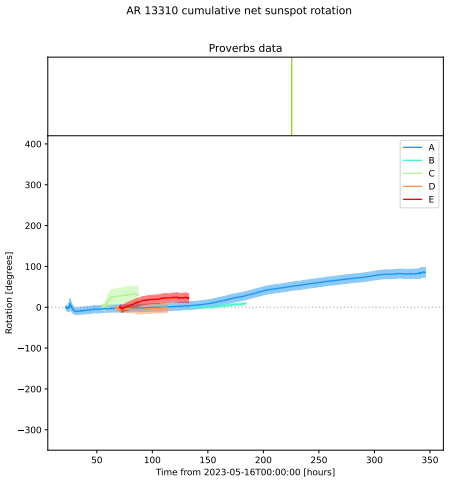

(xxxix) AR 13310

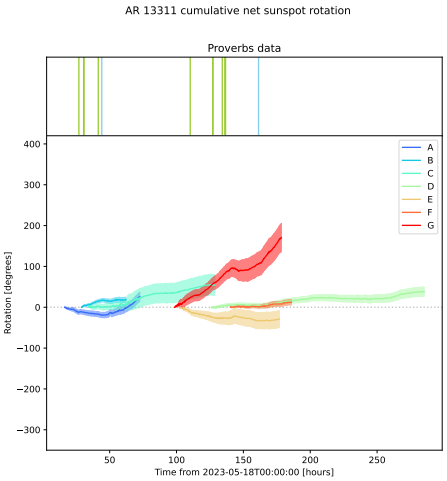

(xl) AR 13311

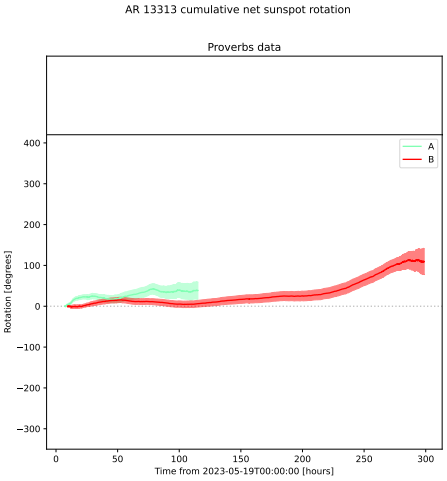

(xli) AR 13313

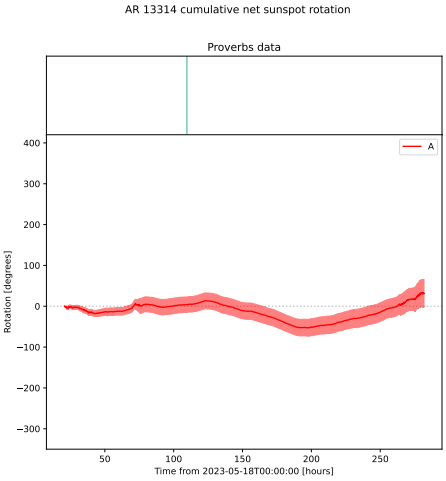

(xlii) AR 13314

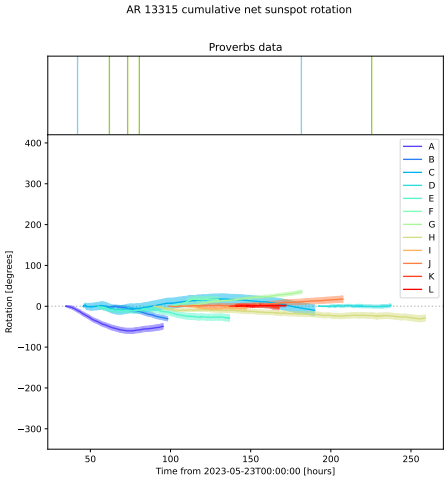

(xliii) AR 13315

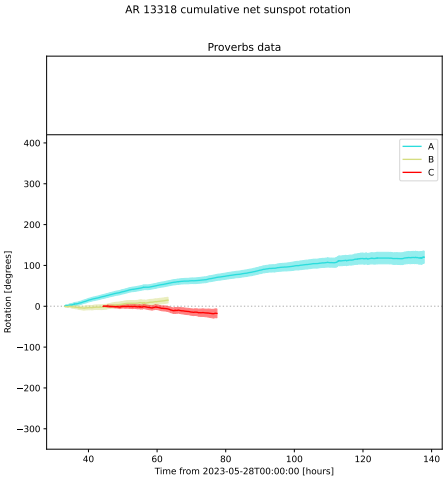

(xliv) AR 13318

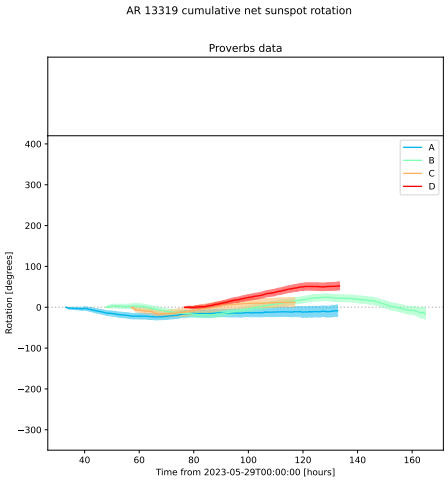

(xlv) AR 13319

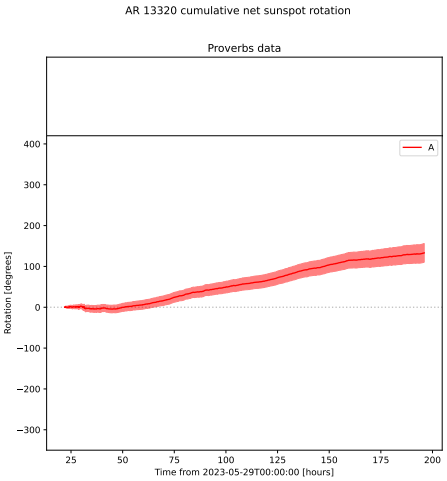

(xlvi) AR 13320

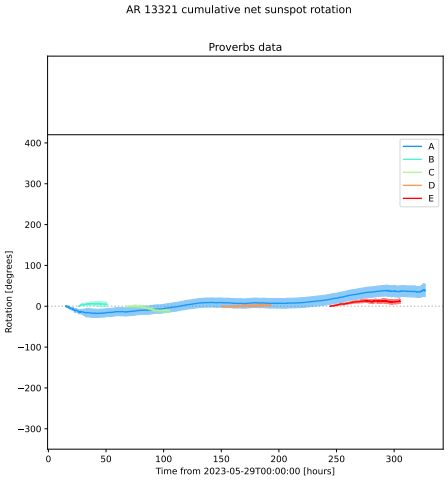

(xlvii) AR 13321

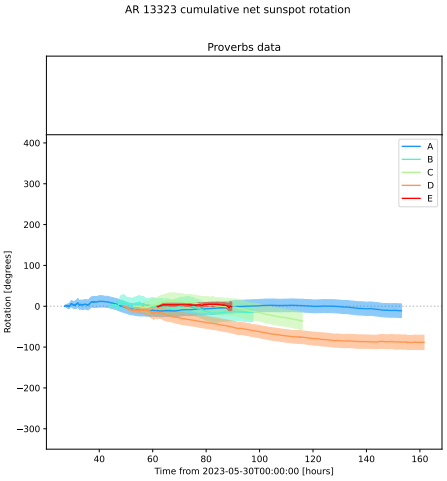

(xlviii) AR 13323

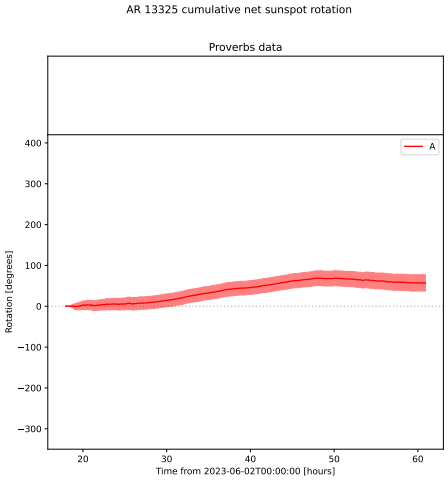

(xlix) AR 13325

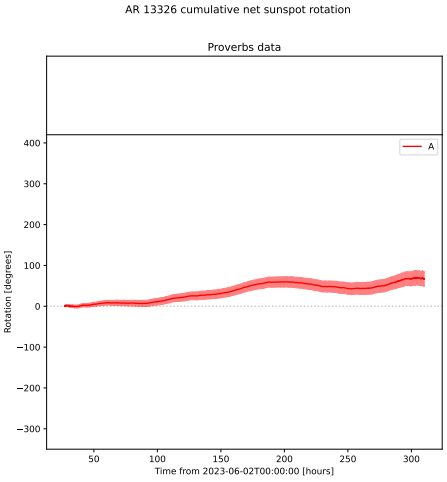

(l) AR 13326

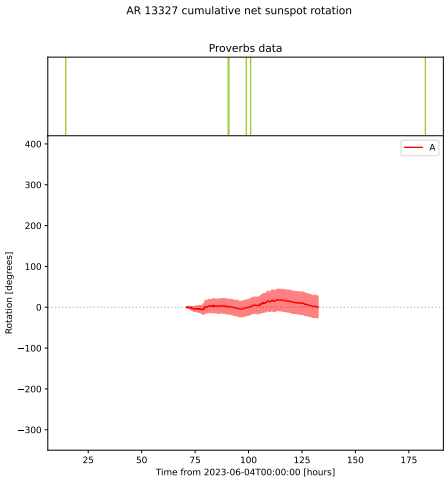

(li) AR 13327

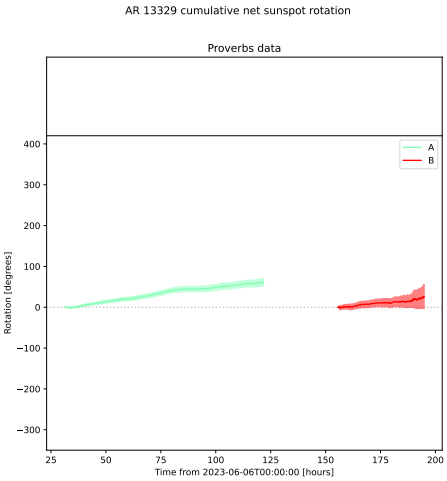

(lii) AR 13329

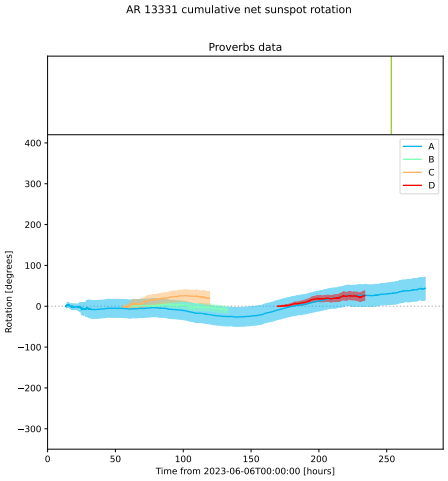

(liii) AR 13331

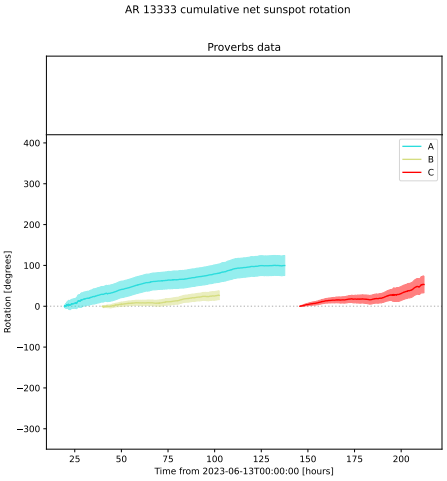

(liv) AR 13333

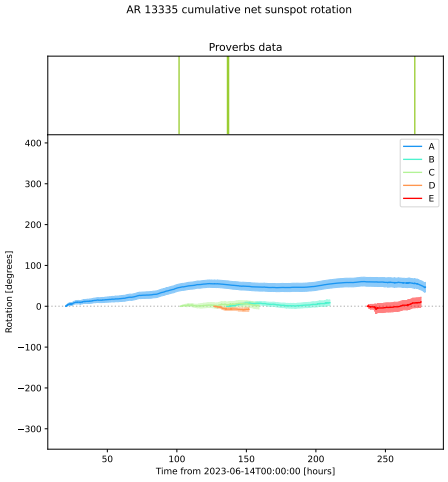

(lv) AR 13335

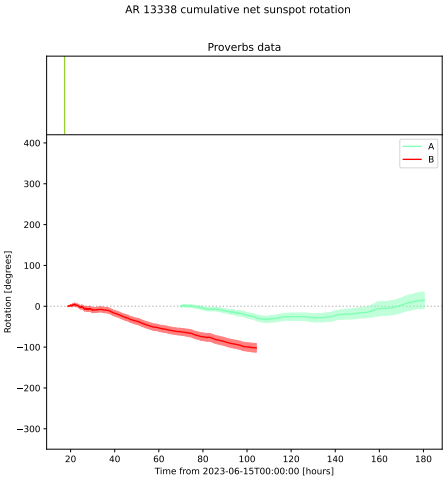

(lvi) AR 13338

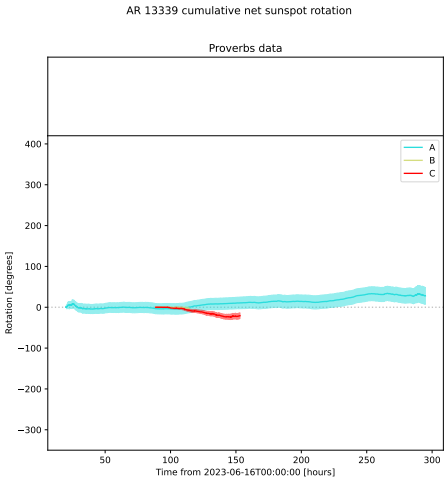

(lvii) AR 13339

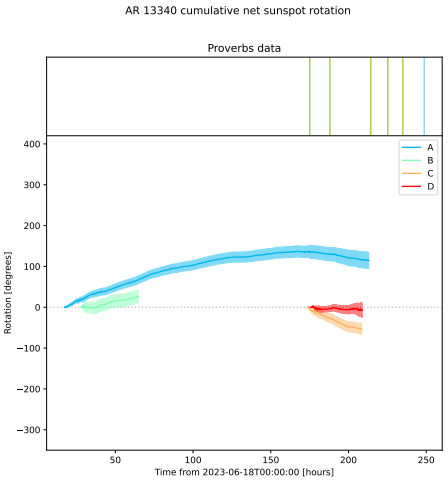

(lviii) AR 13340

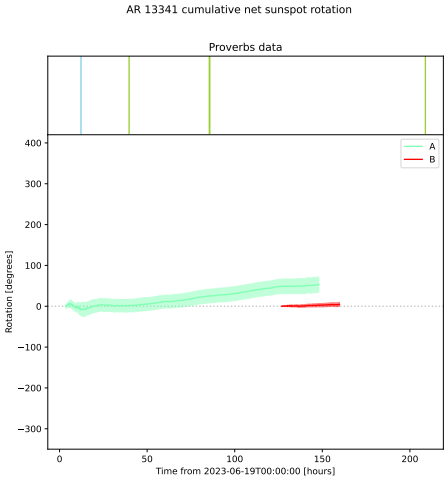

(lix) AR 13341

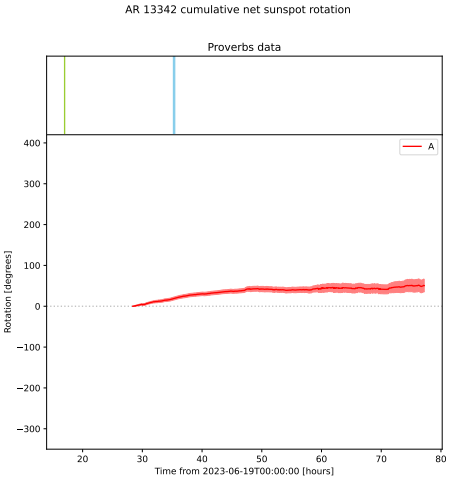

(lx) AR 13342

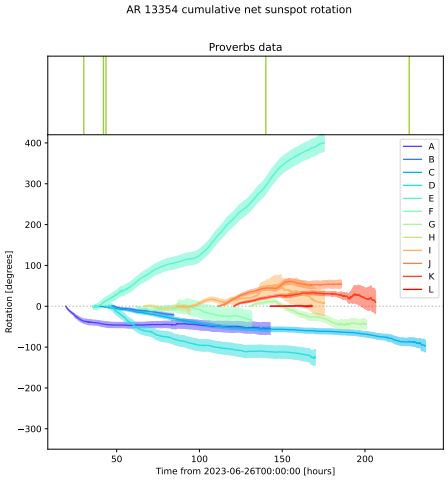

(lxi) AR 13354

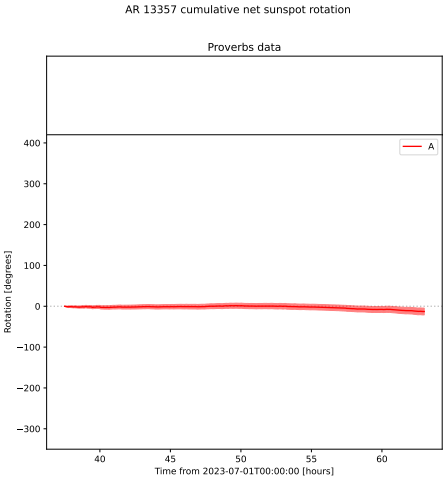

(lxii) AR 13357

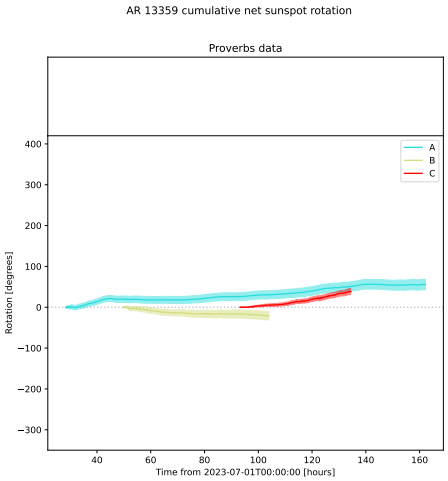

(lxiii) AR 13359

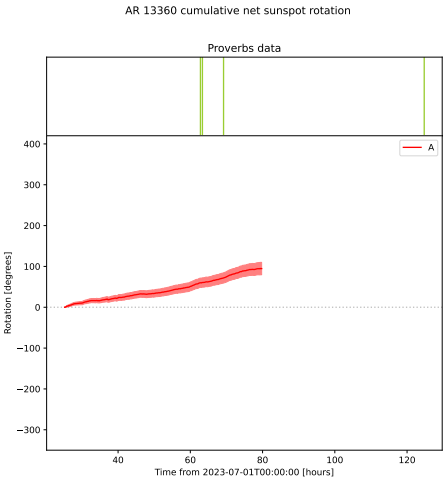

(lxiv) AR 13360

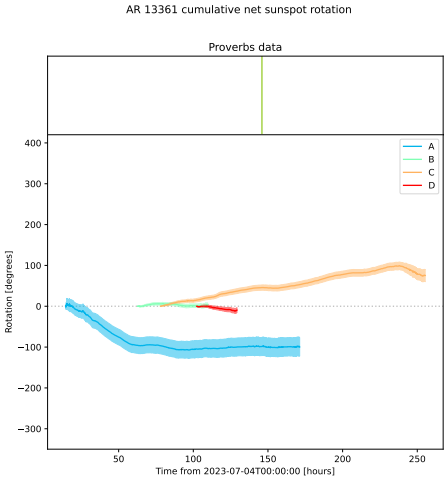

(lxv) AR 13361

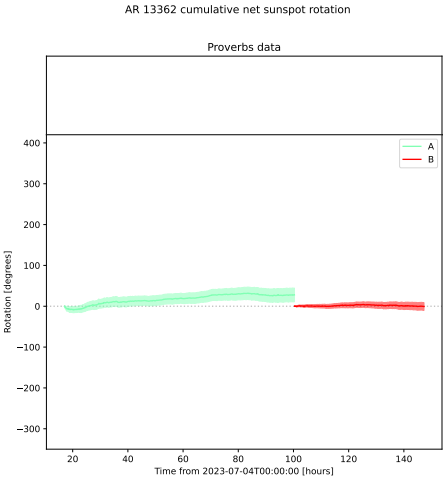

(lxvi) AR 13362

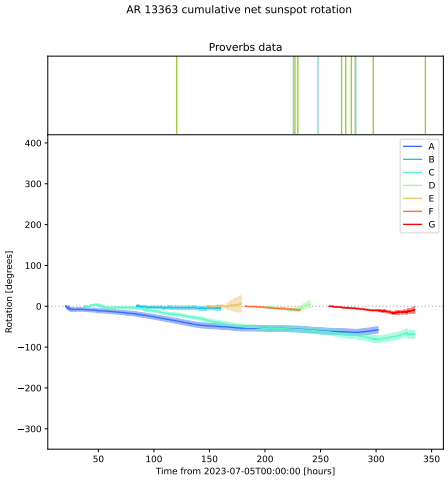

(lxvii) AR 13363

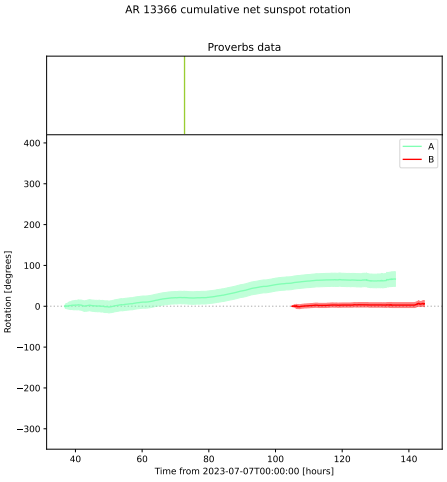

(lxviii) AR 13366

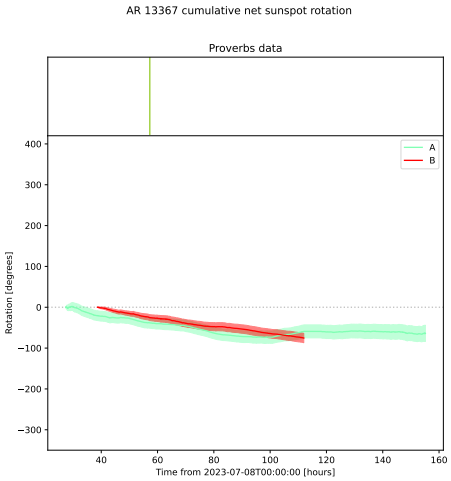

(lxix) AR 13367

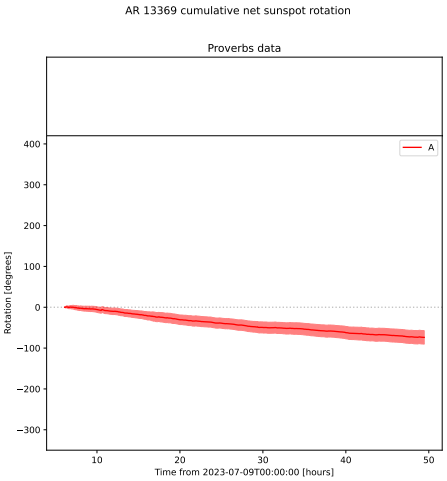

(lxx) AR 13369

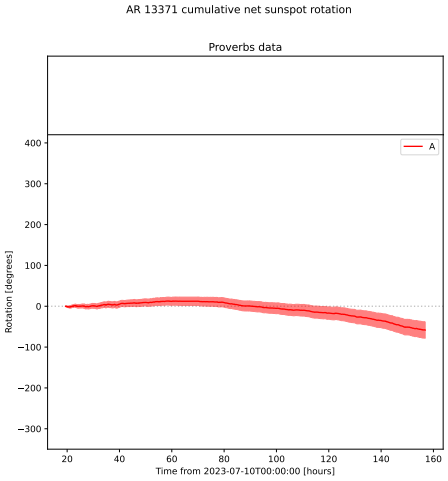

(lxxi) AR 13371

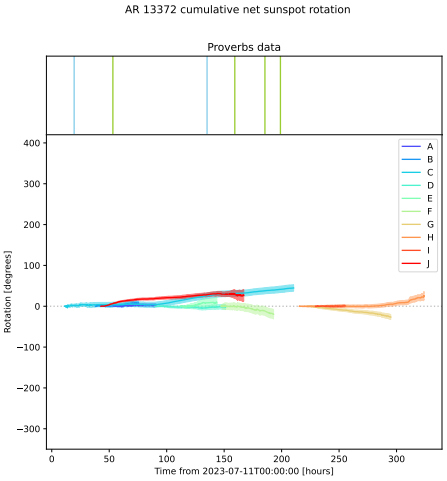

(lxxii) AR 13372

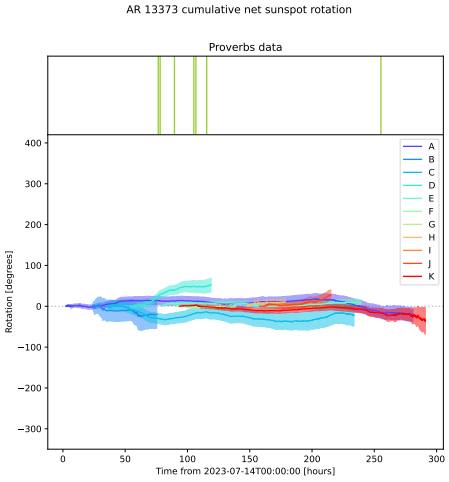

(lxxiii) AR 13373

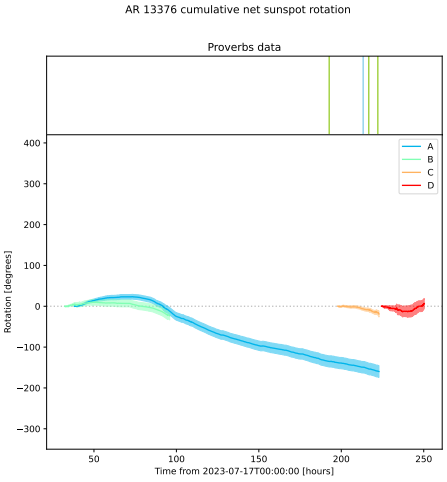

(lxxiv) AR 13376

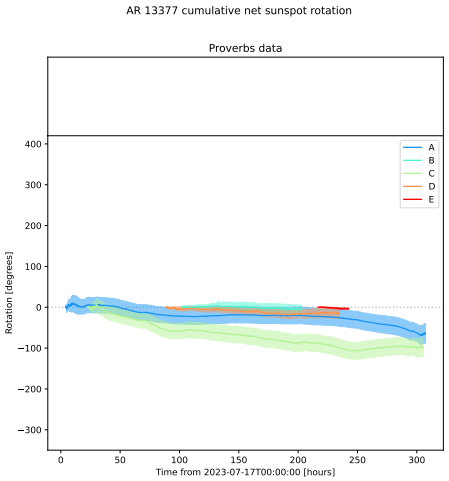

(lxxv) AR 13377

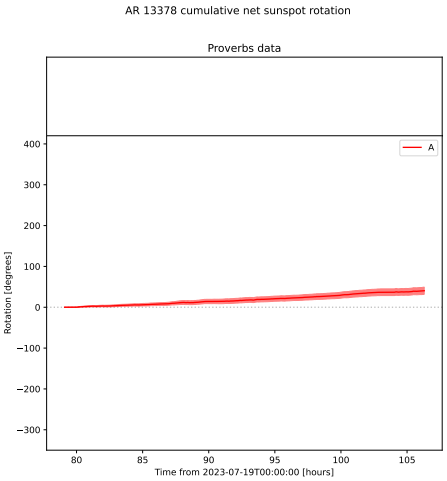

(lxxvi) AR 13378

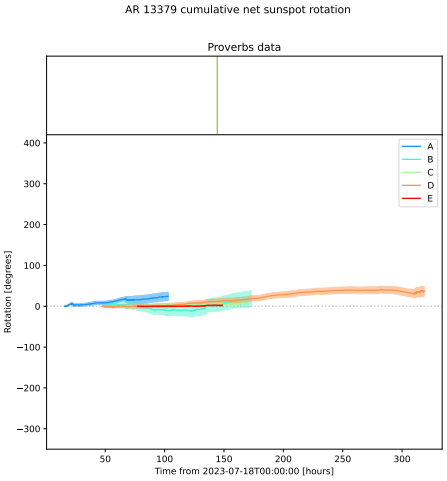

(lxxvii) AR 13379

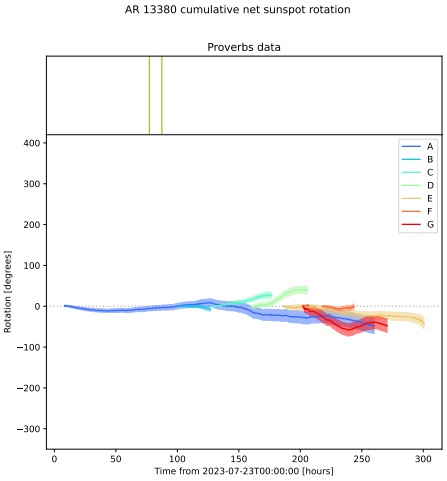

(lxxviii) AR 13380

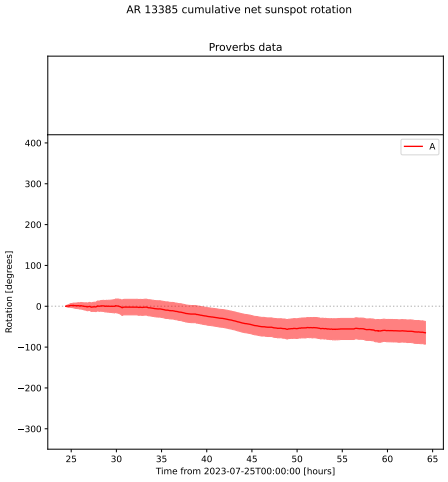

(lxxix) AR 13385

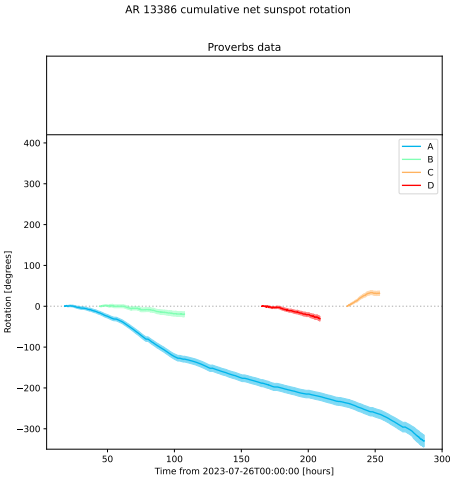

(lxxx) AR 13386

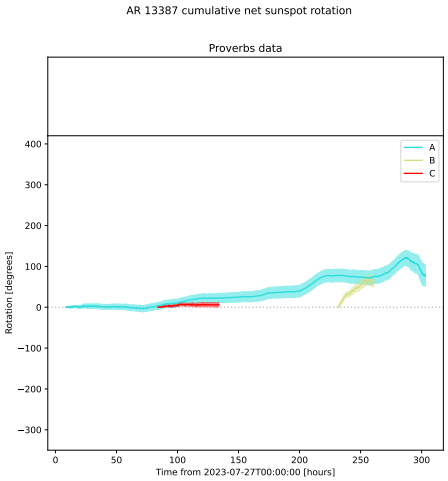

(lxxxi) AR 13387

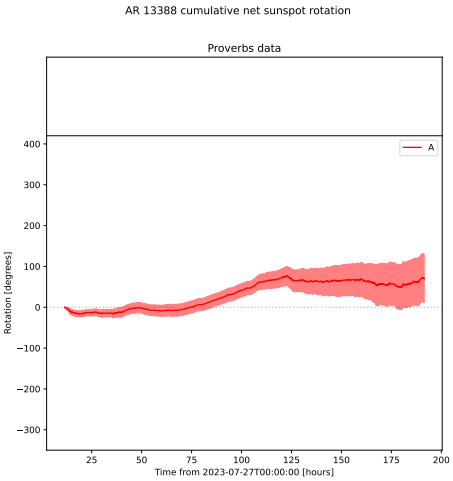

(lxxxii) AR 13388

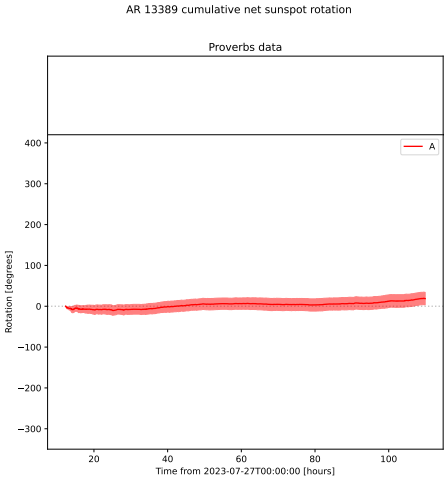

(lxxxiii) AR 13389

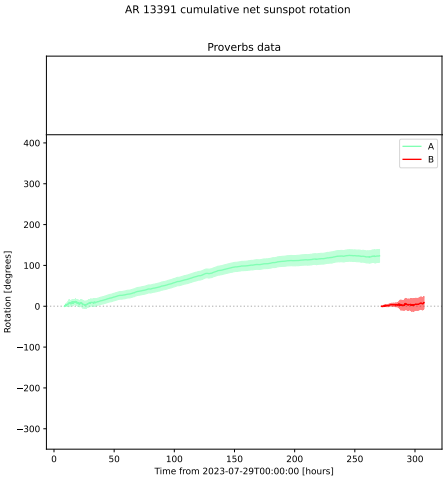

(lxxxiv) AR 13391

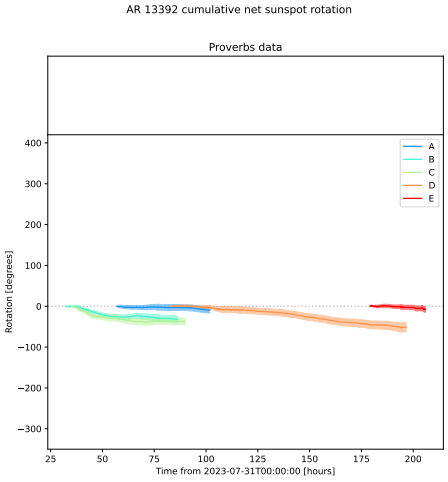

(lxxxv) AR 13392

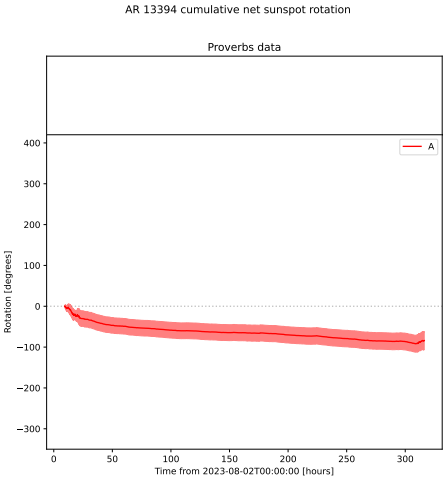

(lxxxvi) AR 13394

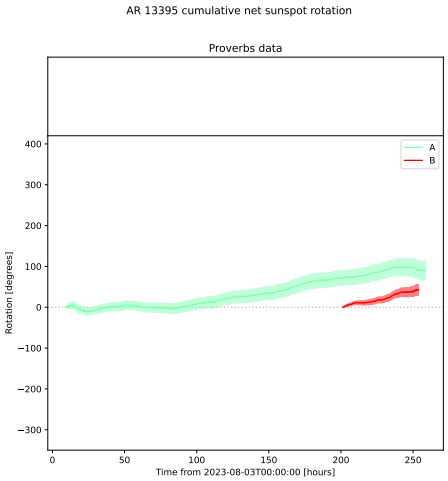

(lxxxvii) AR 13395

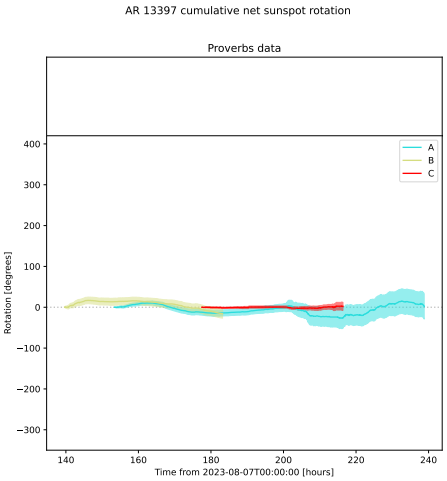

(lxxxviii) AR 13397

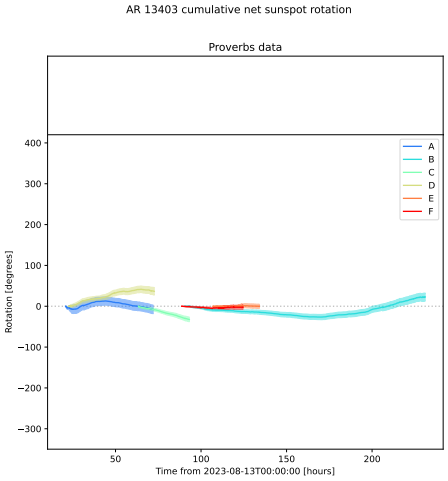

(lxxxix) AR 13403

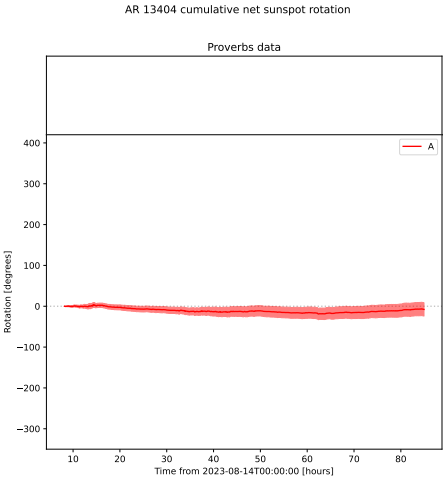

(xc) AR 13404

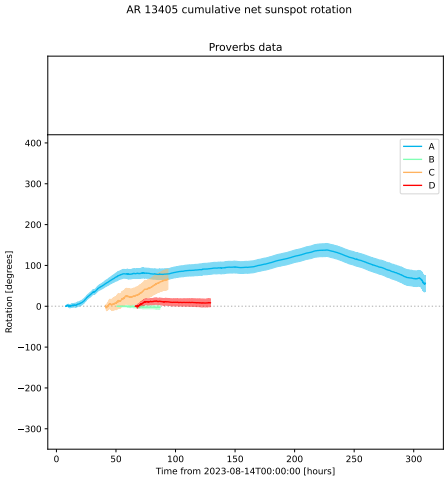

(xci) AR 13405

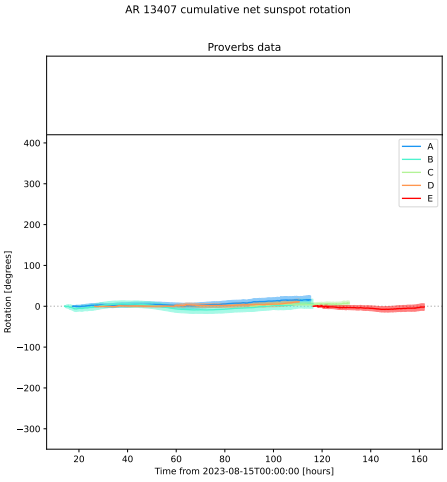

(xcii) AR 13407

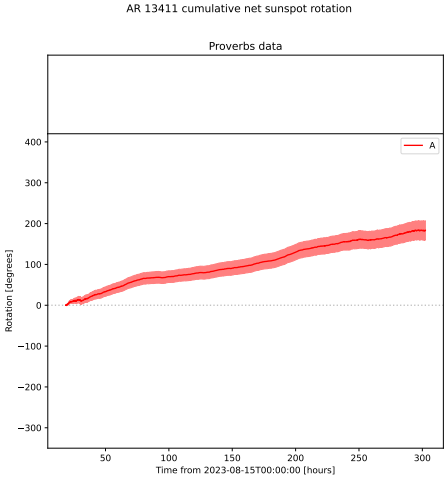

(xciii) AR 13411

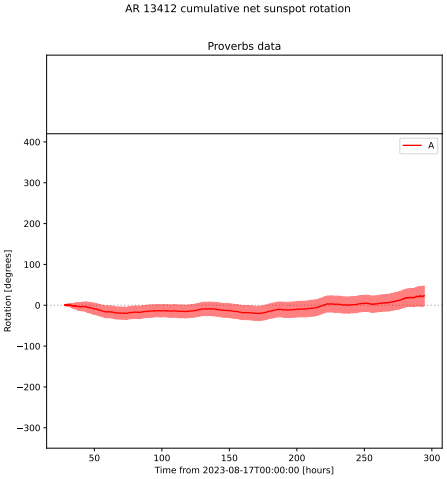

(xciv) AR 13412

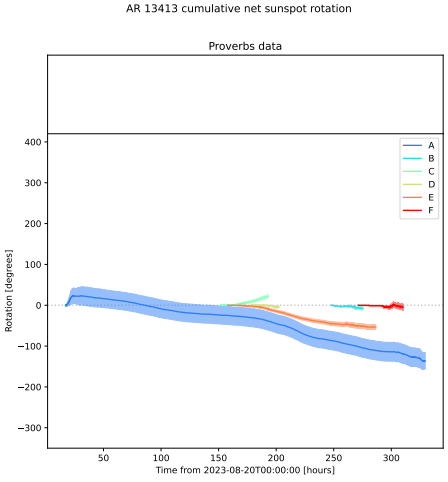

(xcv) AR 13413

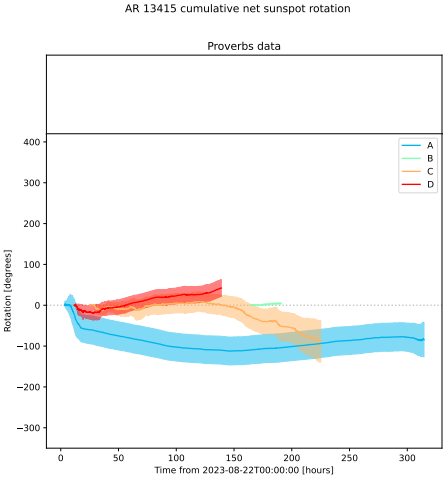

(xcvi) AR 13415

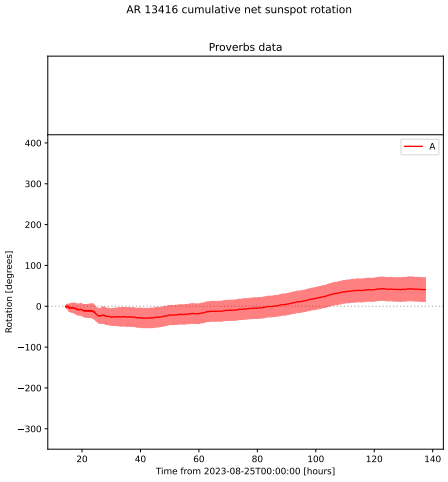

(xcvii) AR 13416

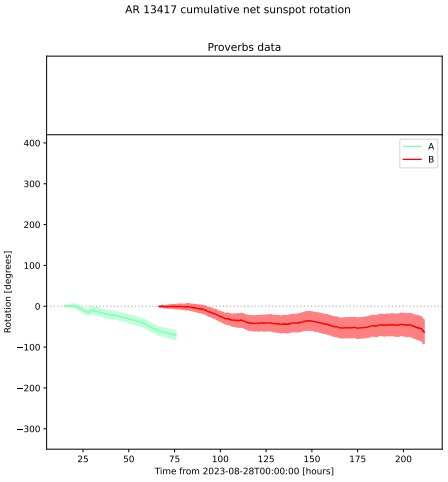

(xcviii) AR 13417

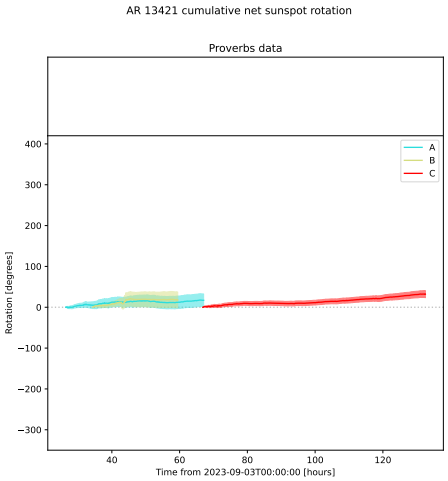

(xcix) AR 13421

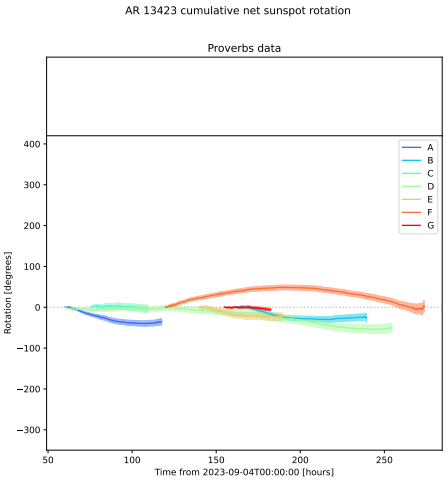

(c) AR 13423

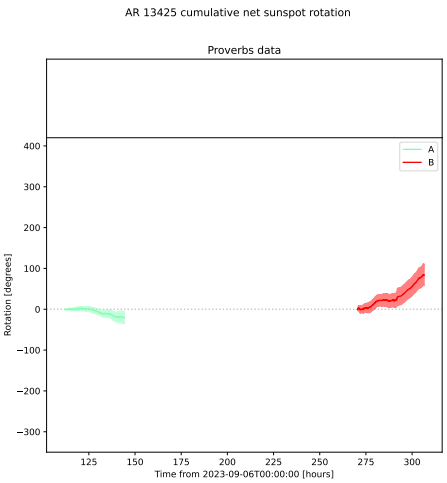

(ci) AR 13425

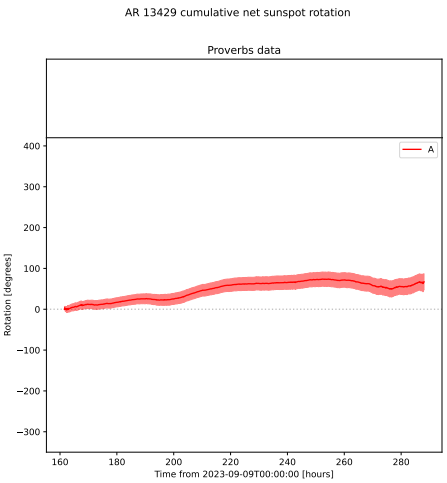

(cii) AR 13429

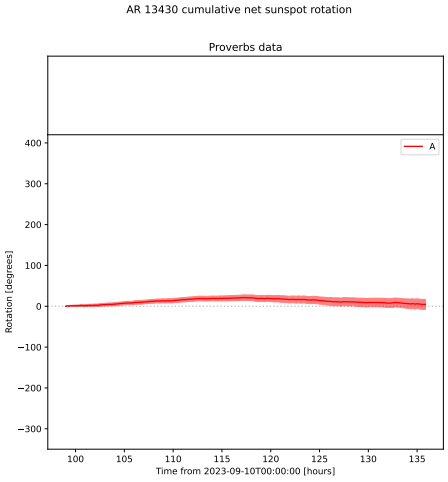

(ciii) AR 13430

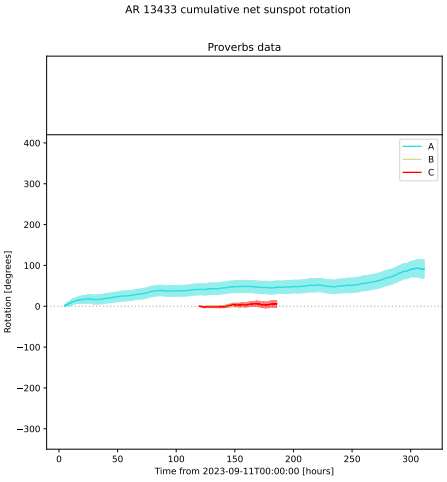

(civ) AR 13433

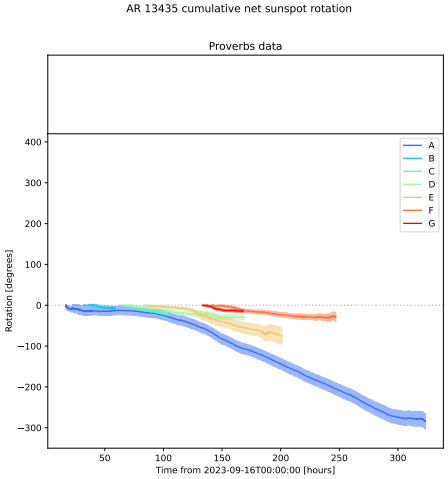

(cv) AR 13435

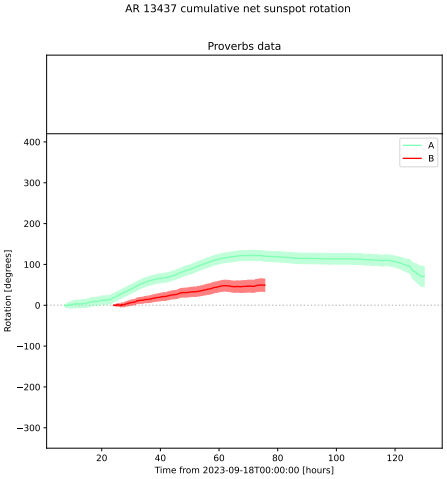

(cvi) AR 13437

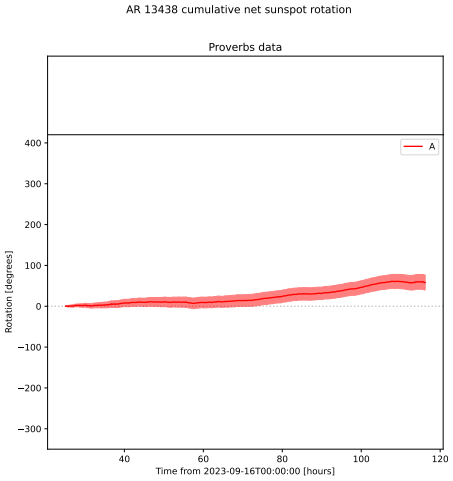

(cvii) AR 13438

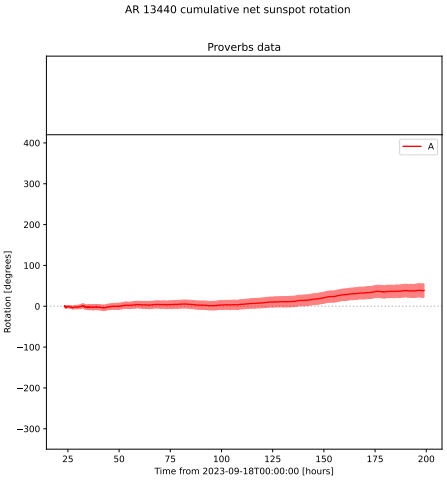

(cviii) AR 13440

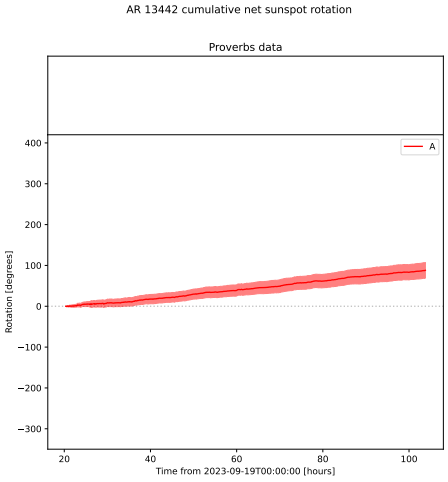

(cix) AR 13442

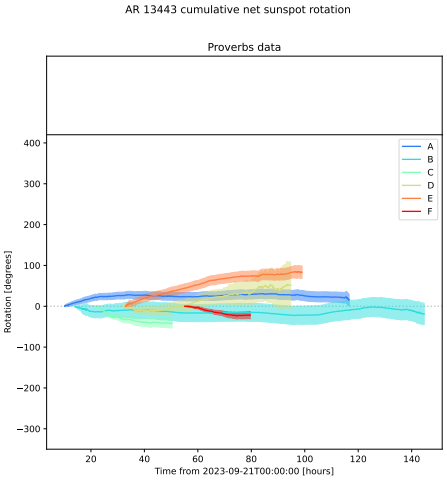

(cx) AR 13443

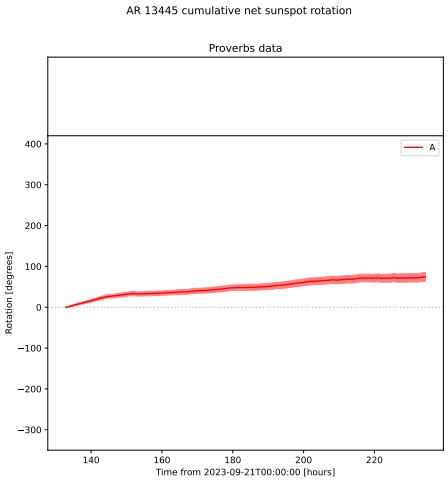

(cxi) AR 13445

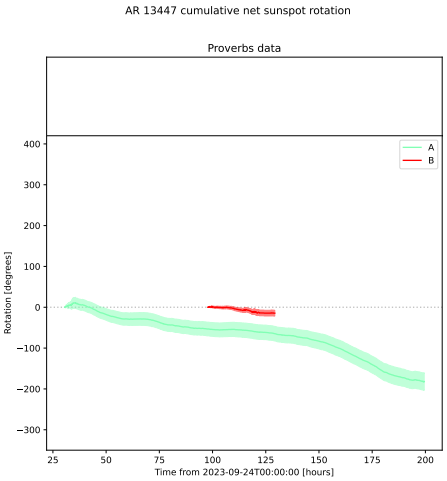

(cxii) AR 13447

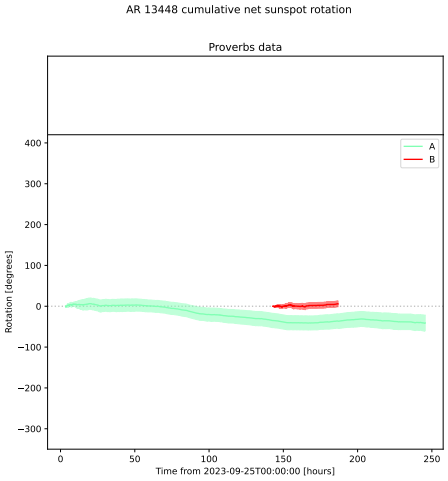

(cxiii) AR 13448

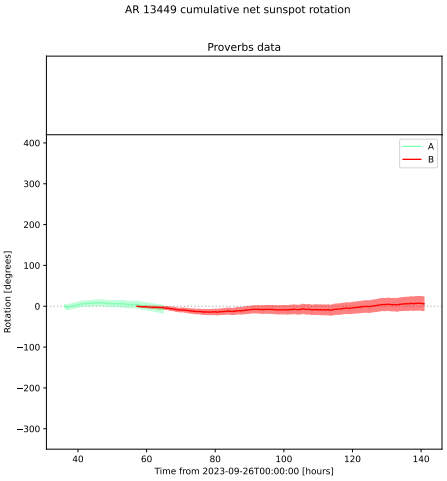

(cxiv) AR 13449

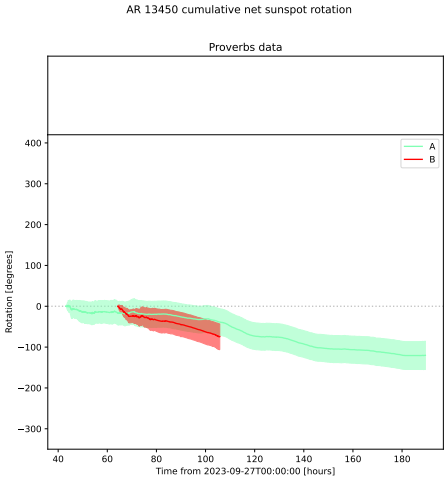

(cxv) AR 13450

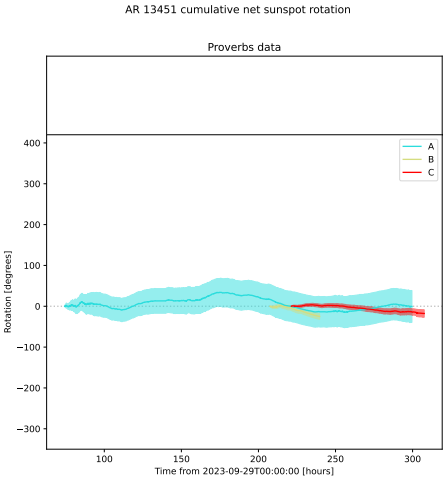

(cxvi) AR 13451

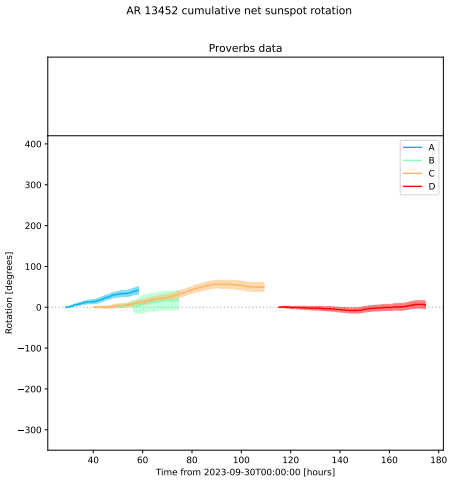

(cxvii) AR 13452

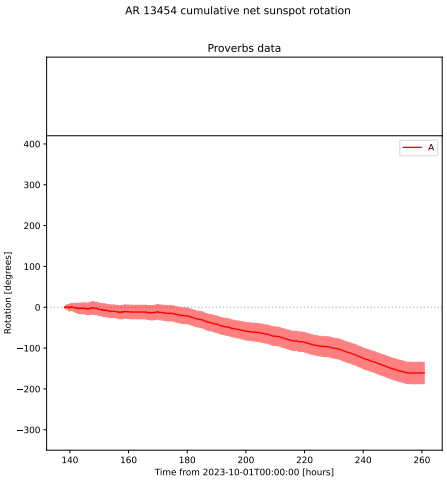

(cxviii) AR 13454

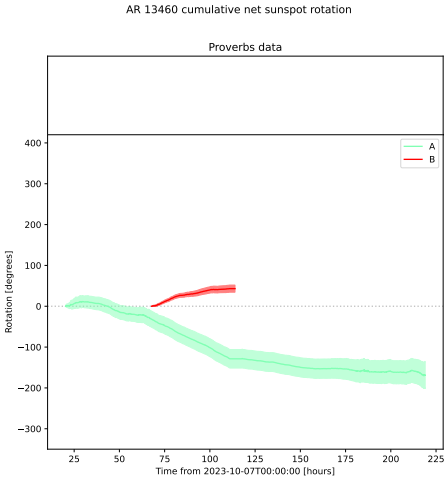

(cxix) AR 13460

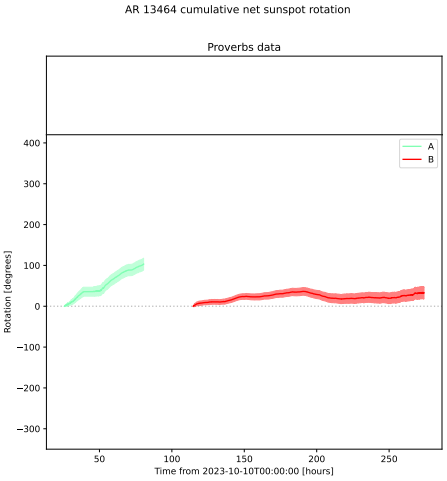

(cxx) AR 13464

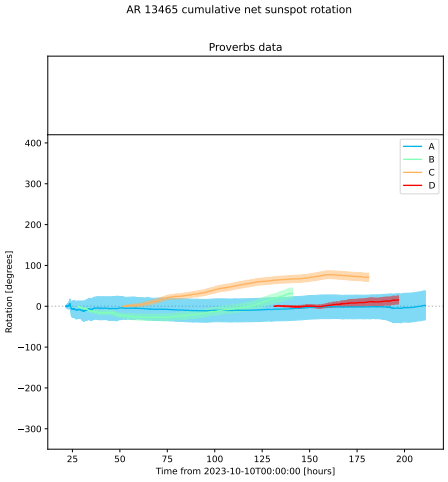

(cxxi) AR 13465

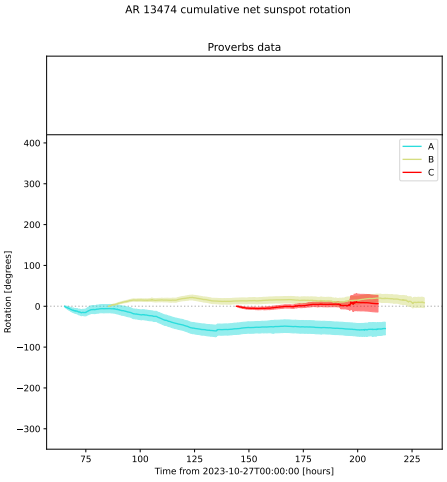

(cxxii) AR 13474

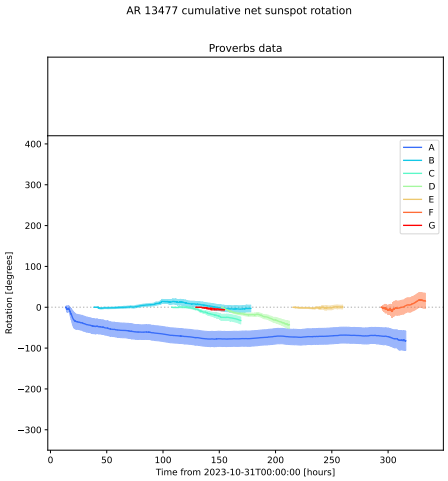

(cxxiii) AR 13477

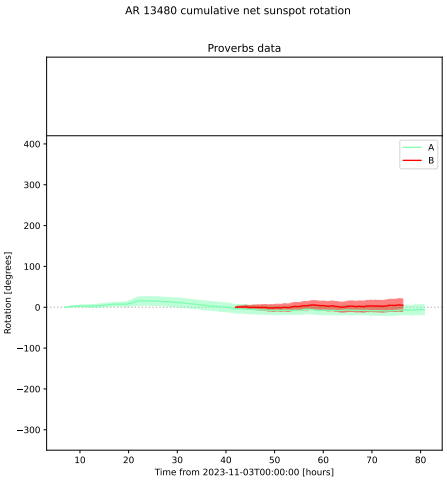

(cxxiv) AR 13480

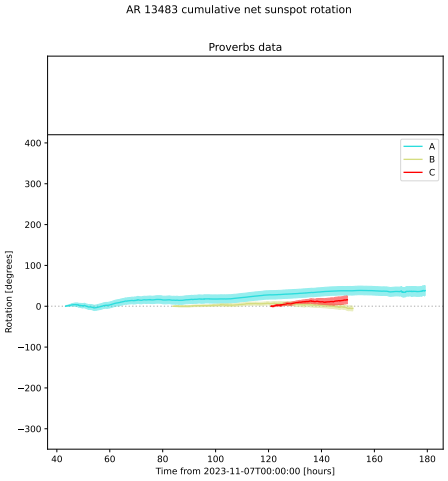

(cxxv) AR 13483

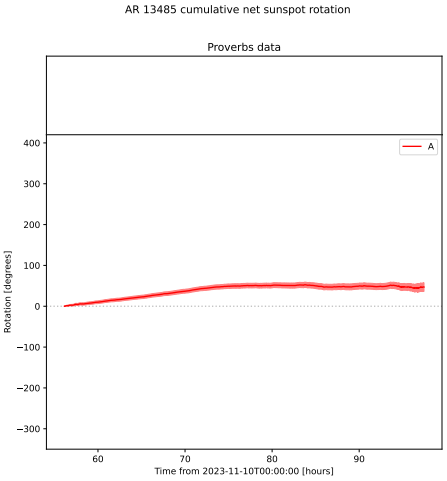

(cxxvi) AR 13485

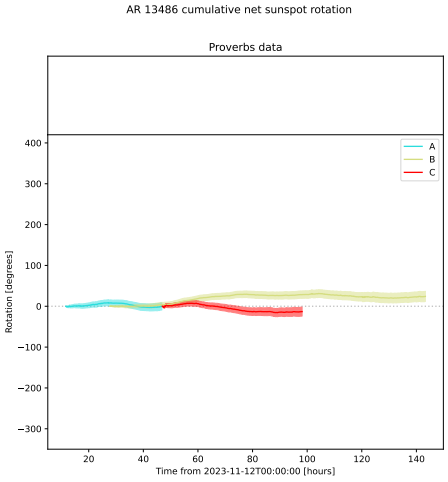

(cxxvii) AR 13486

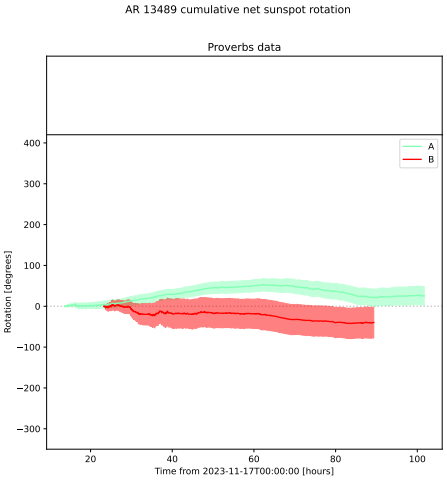

(cxxviii) AR 13489

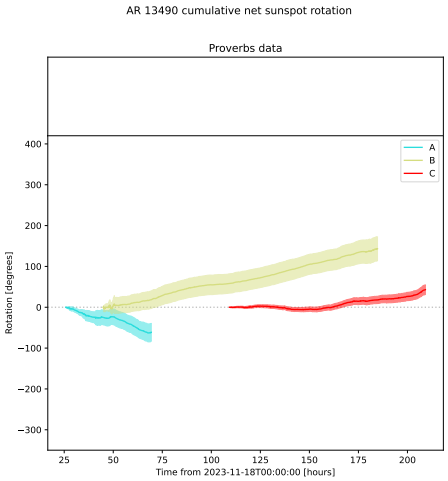

(cxxix) AR 13490

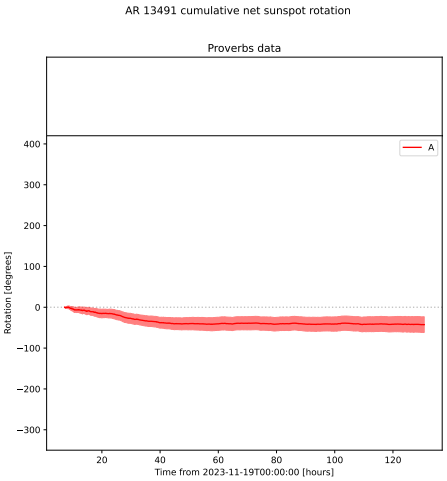

(cxxx) AR 13491

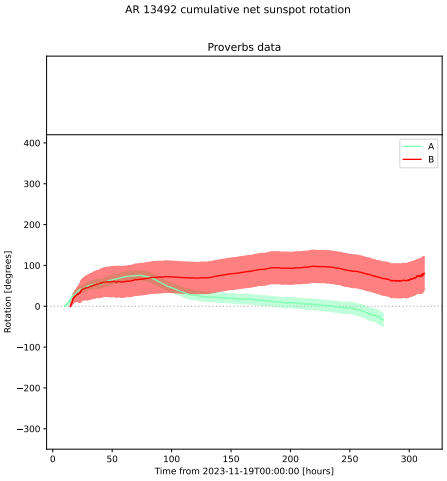

(cxxxi) AR 13492

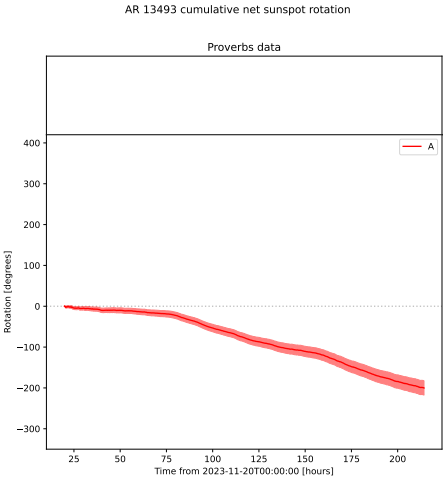

(cxxxii) AR 13493

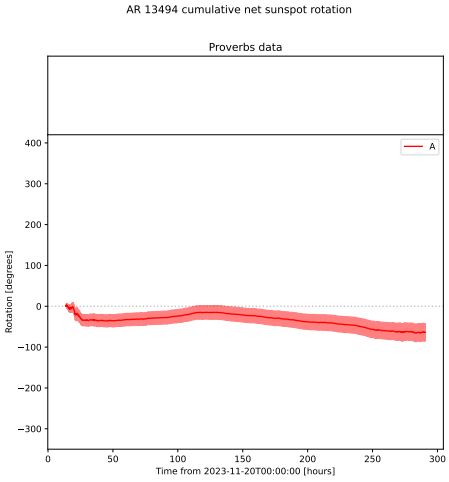

(cxxxiii) AR 13494

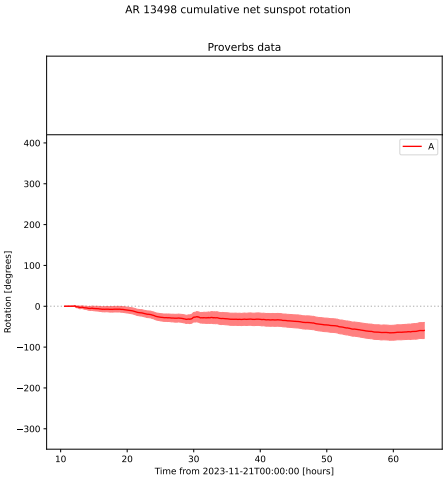

(cxxxiv) AR 13498

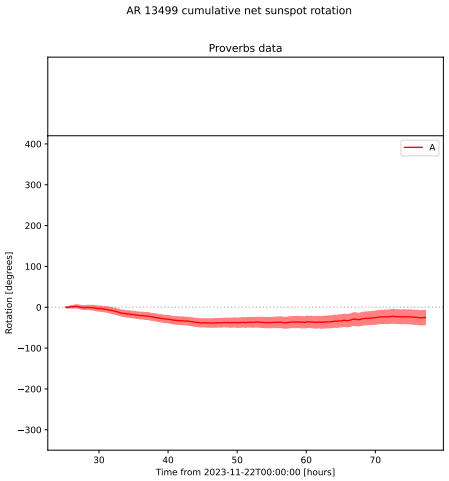

(cxxxv) AR 13499

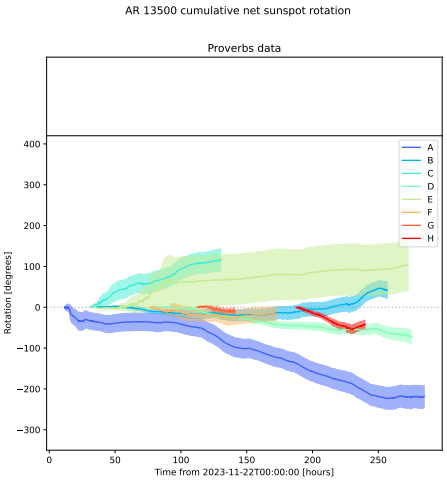

(cxxxvi) AR 13500

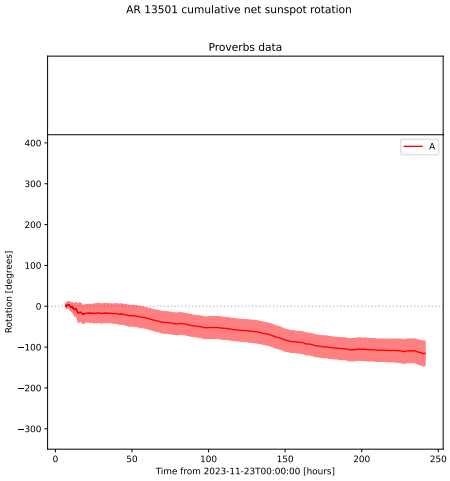

(cxxxvii) AR 13501

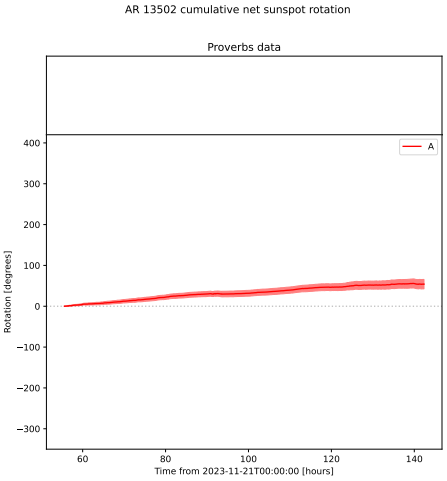

(cxxxviii) AR 13502

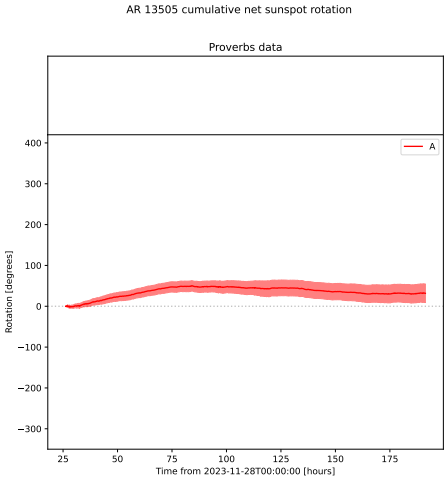

(cxxxix) AR 13505

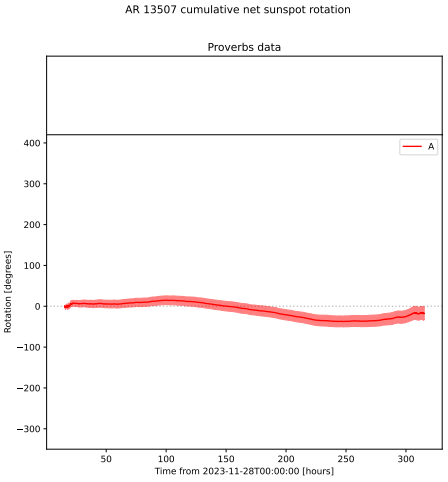

(cxl) AR 13507

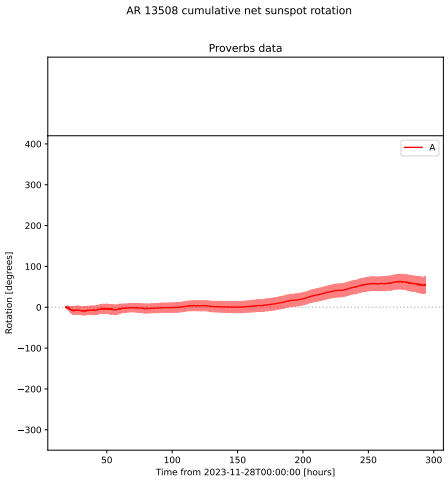

(cxli) AR 13508

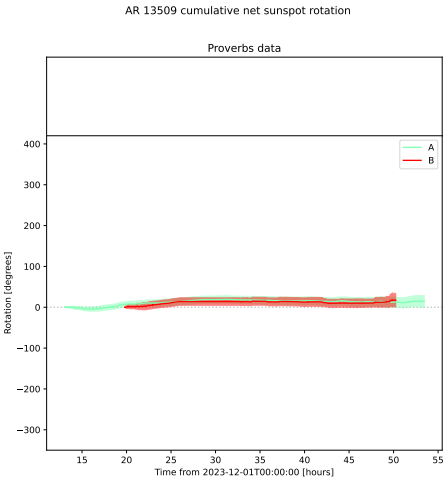

(cxlii) AR 13509

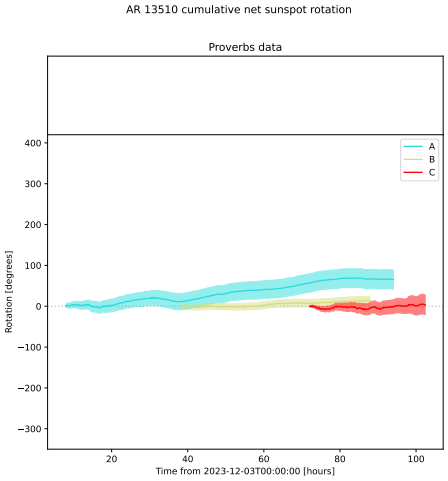

(cxliii) AR 13510

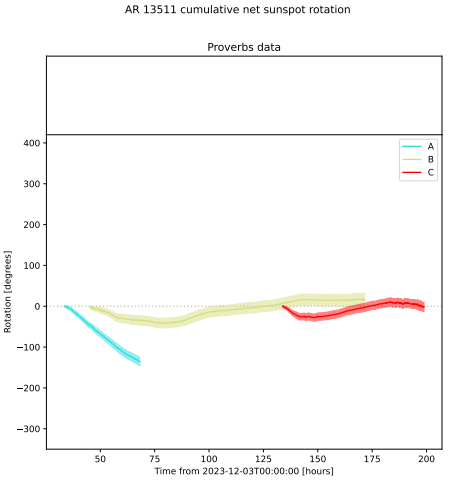

(cxliv) AR 13511

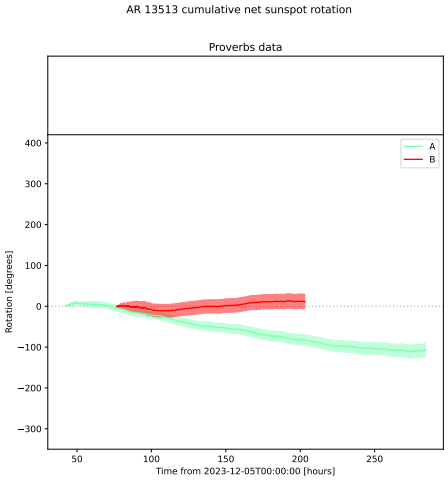

(cxlv) AR 13513

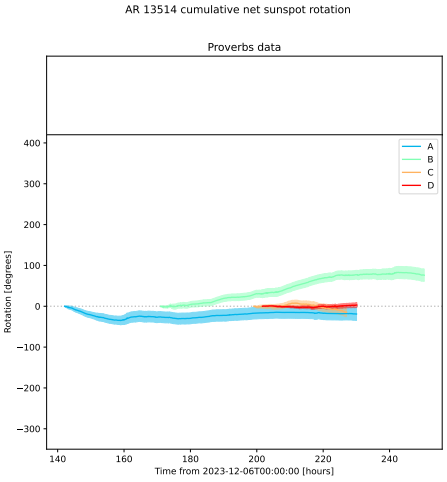

(cxlvi) AR 13514

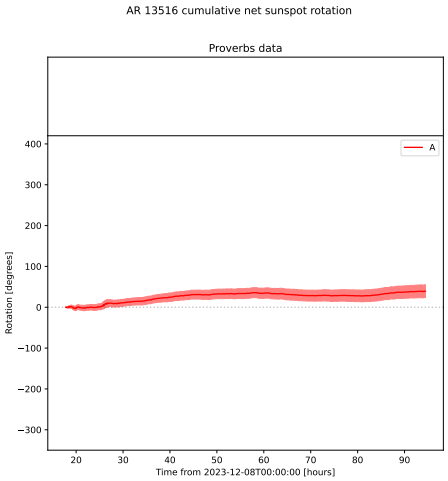

(cxlvii) AR 13516

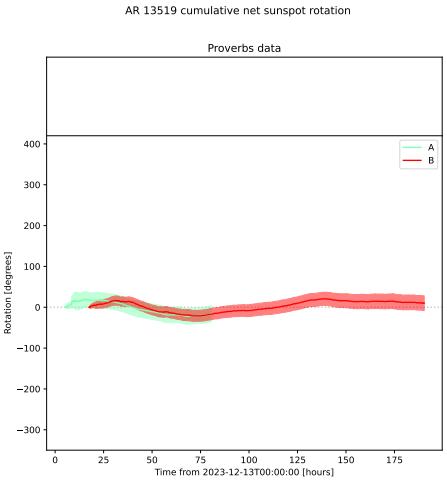

(cxlviii) AR 13519

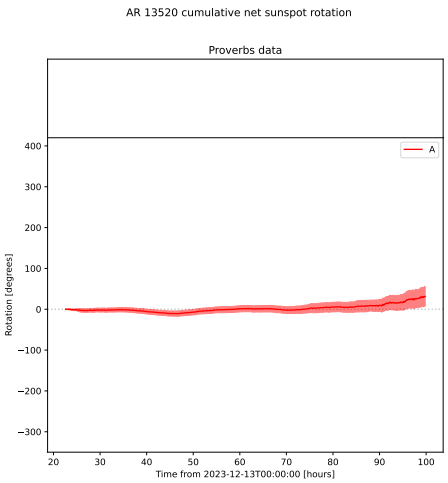

(cxlix) AR 13520

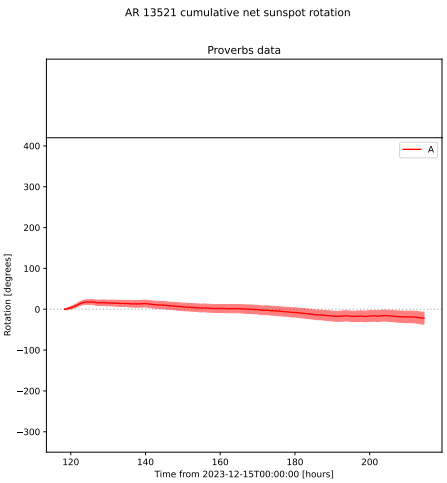

(cl) AR 13521

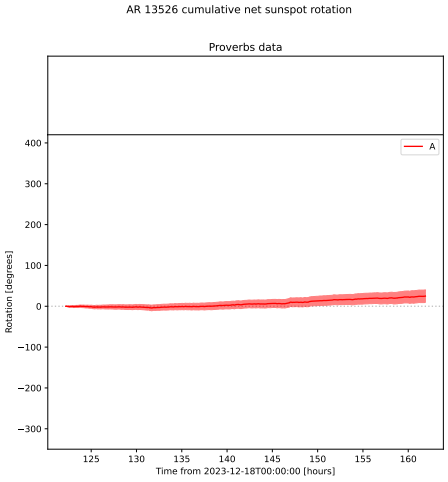

(cli) AR 13526

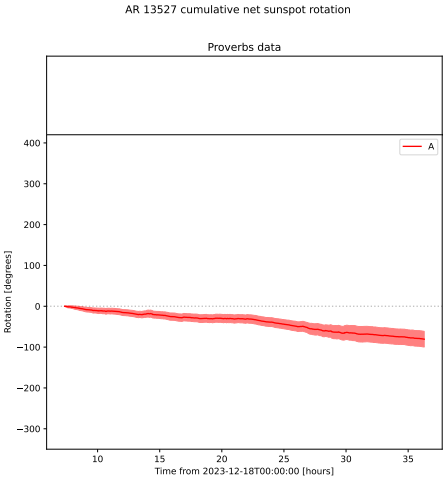

(clii) AR 13527

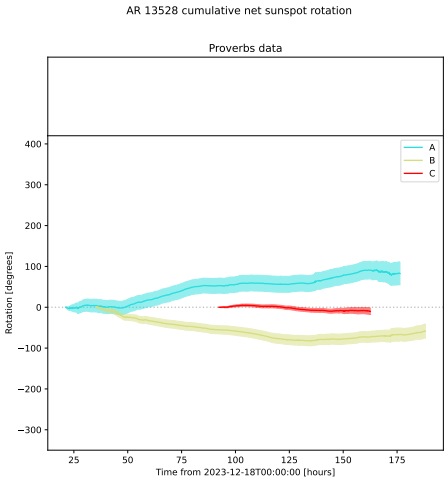

(cliii) AR 13528

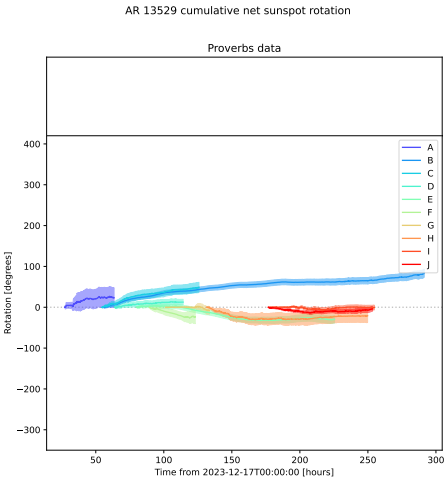

(cliv) AR 13529

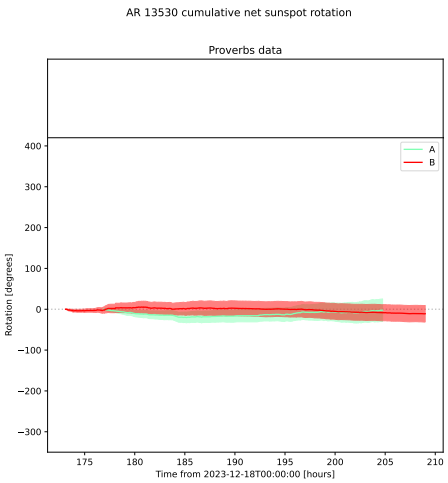

(clv) AR 13530

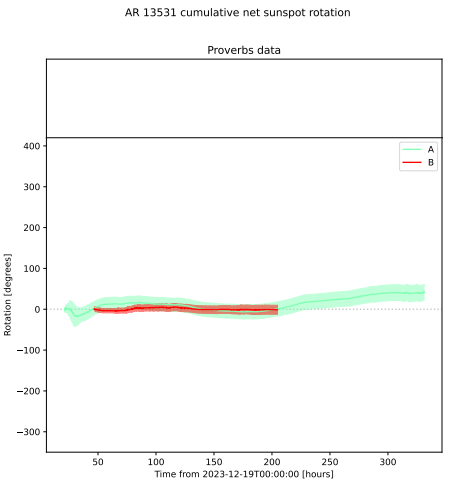

(clvi) AR 13531

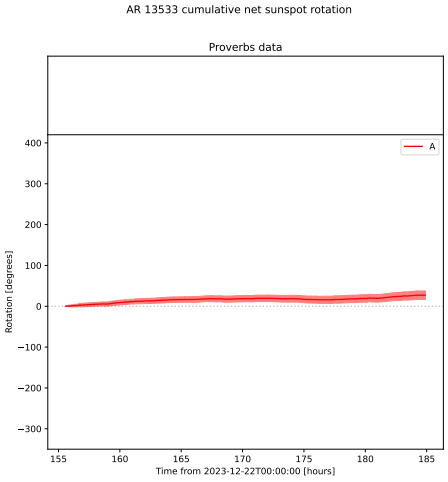

(clvii) AR 13533

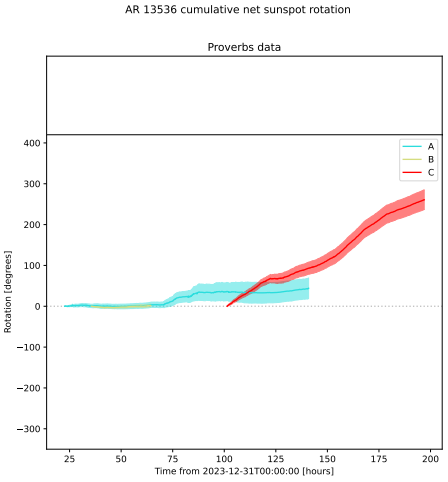

(clviii) AR 13536

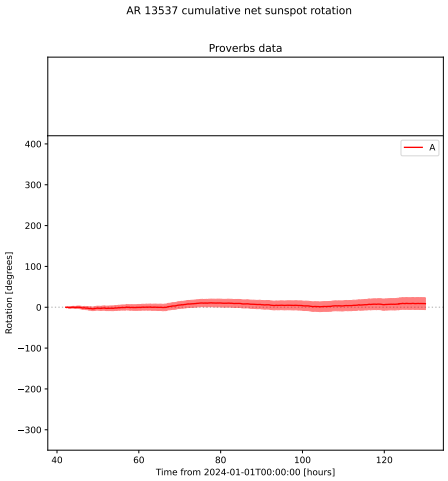

(clix) AR 13537

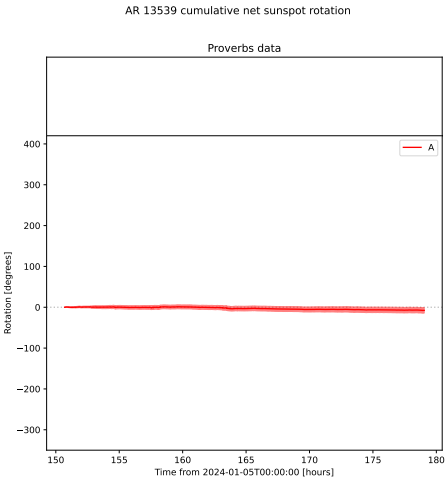

(clx) AR 13539

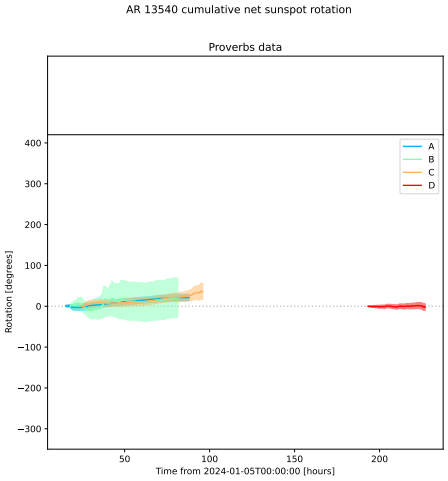

(clxi) AR 13540

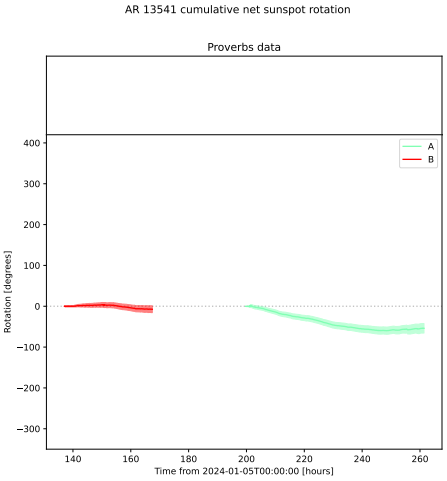

(clxii) AR 13541

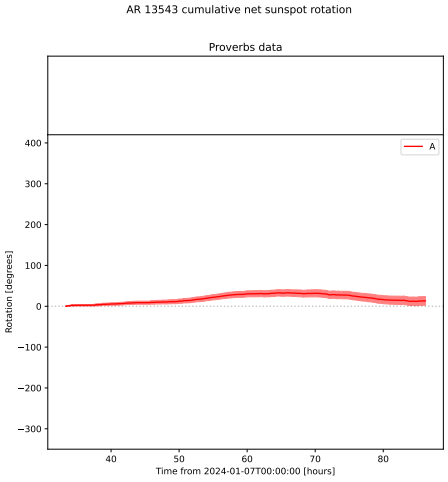

(clxiii) AR 13543

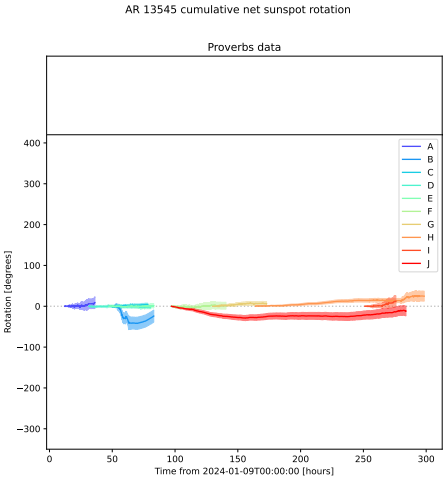

(clxiv) AR 13545

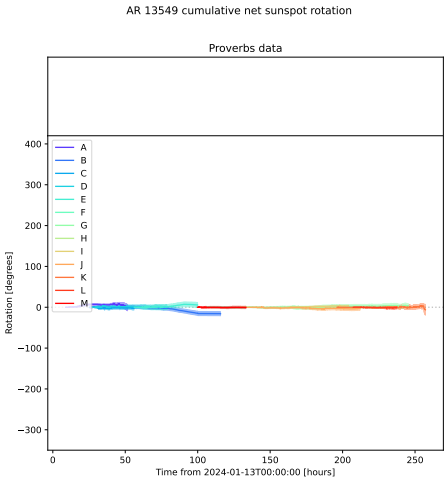

(clxv) AR 13549

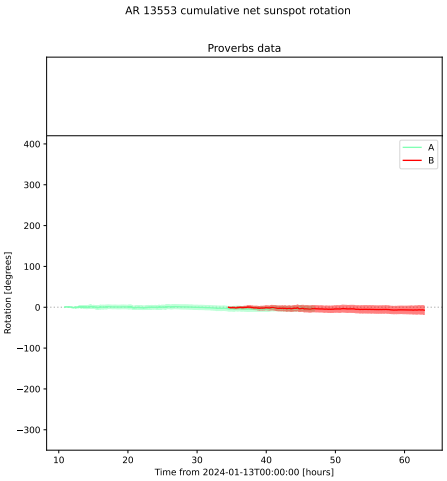

(clxvi) AR 13553

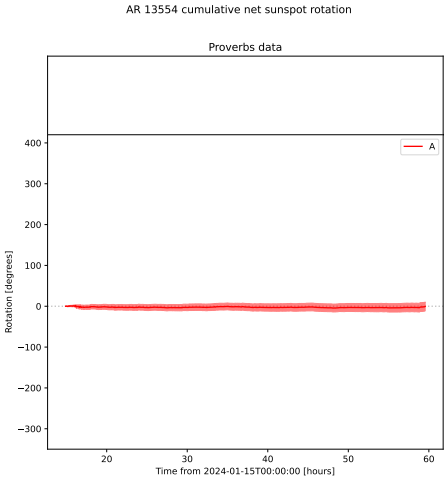

(clxvii) AR 13554

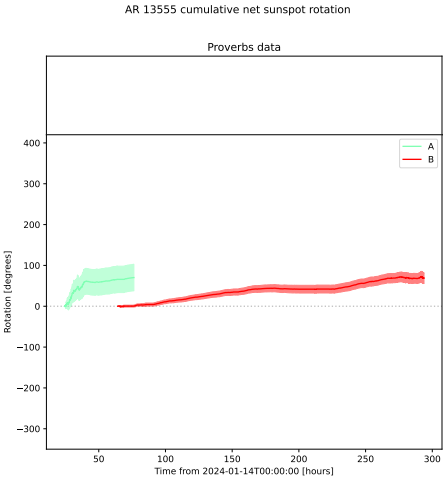

(clxviii) AR 13555

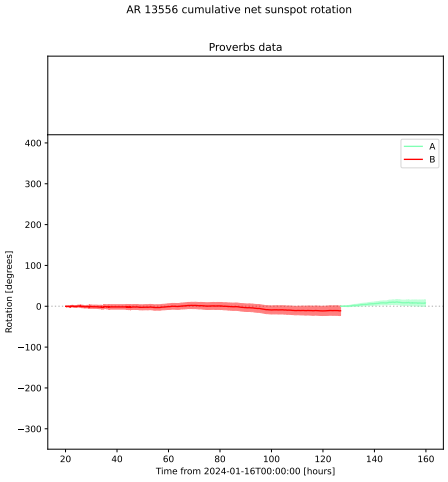

(clxix) AR 13556

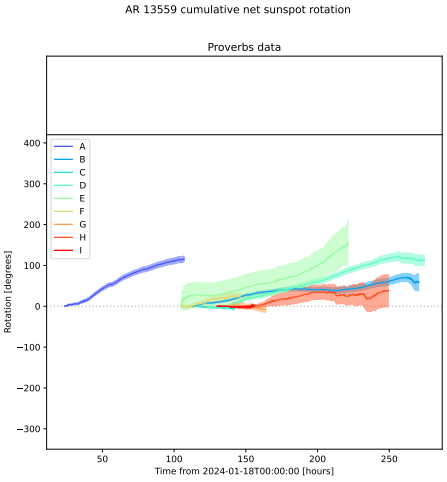

(clxx) AR 13559

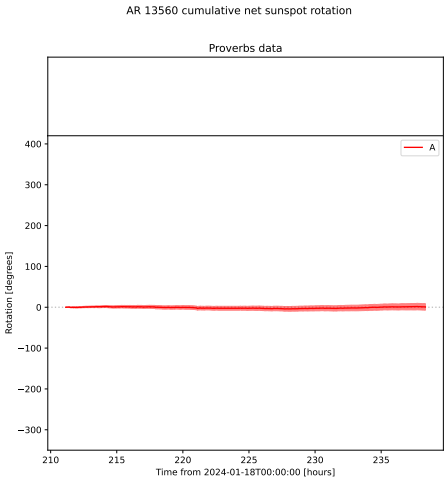

(clxxi) AR 13560

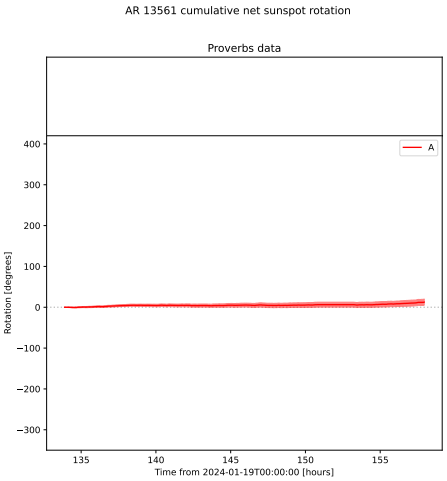

(clxxii) AR 13561

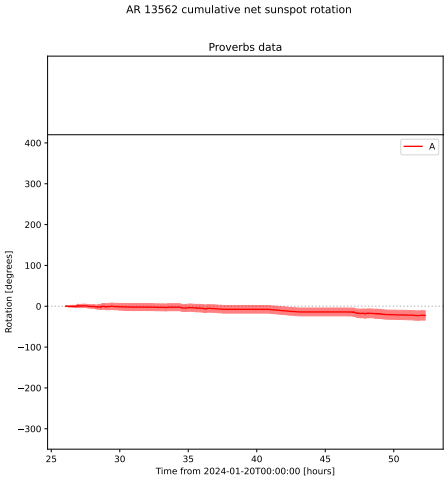

(clxxiii) AR 13562

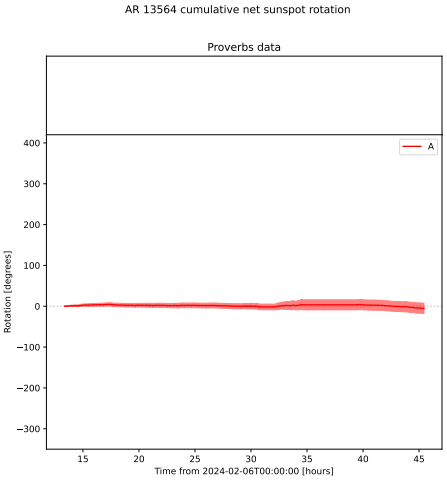

(clxxiv) AR 13564

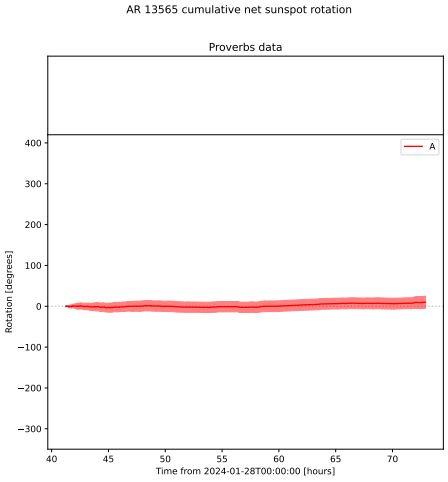

(clxxv) AR 13565

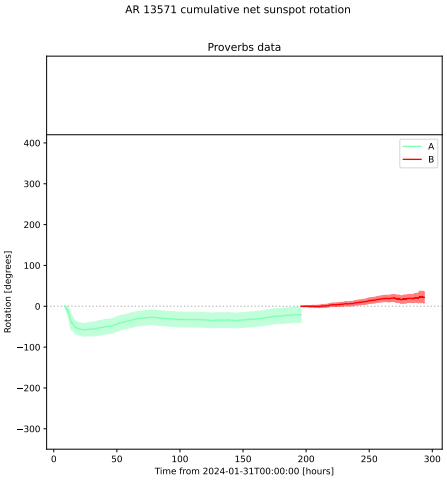

(clxxvi) AR 13571

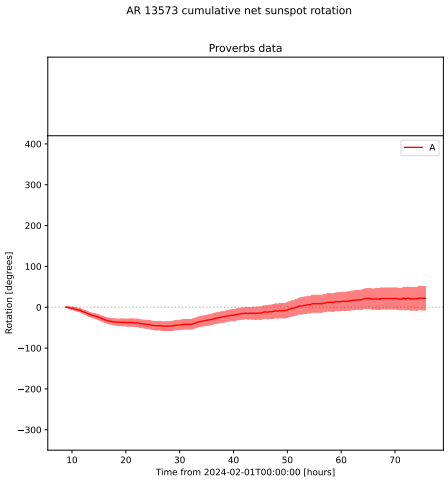

(clxxvii) AR 13573

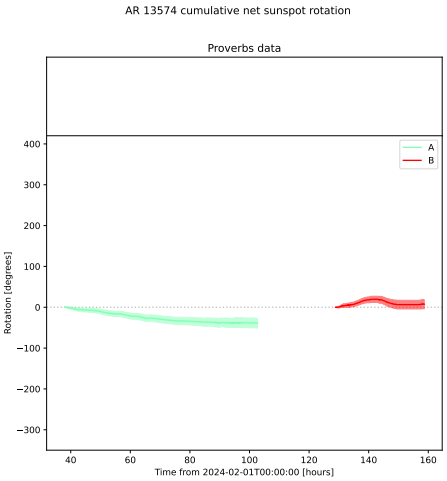

(clxxviii) AR 13574

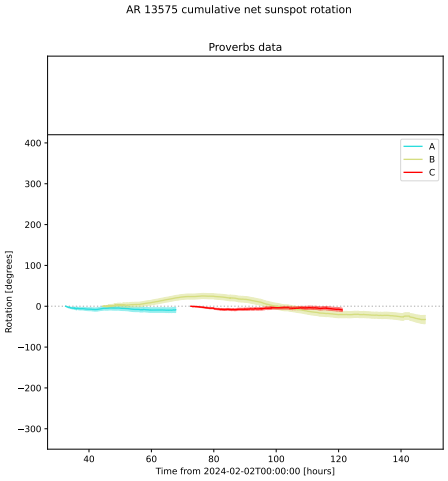

(clxxix) AR 13575

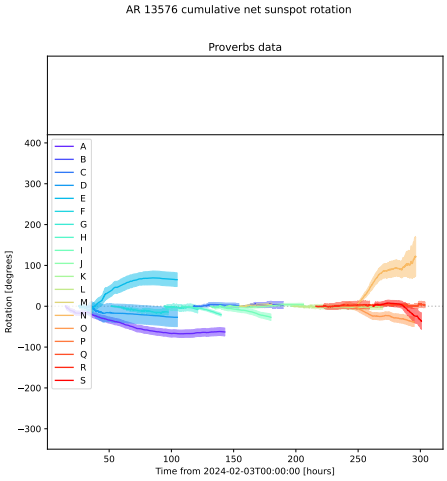

(clxxx) AR 13576

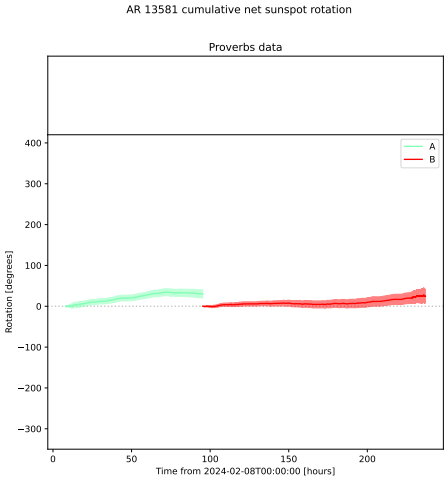

(clxxxi) AR 13581

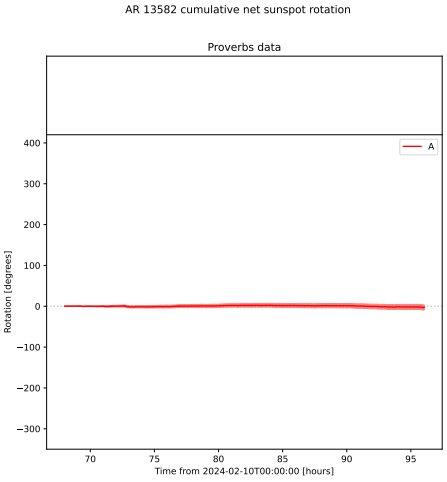

(clxxxii) AR 13582

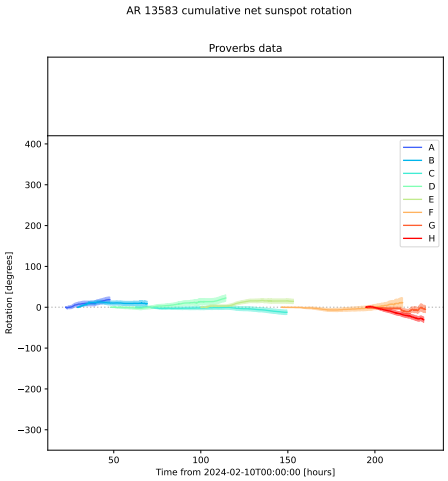

(clxxxiii) AR 13583

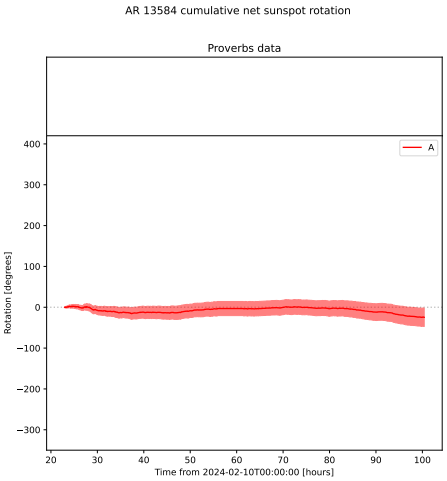

(clxxxiv) AR 13584

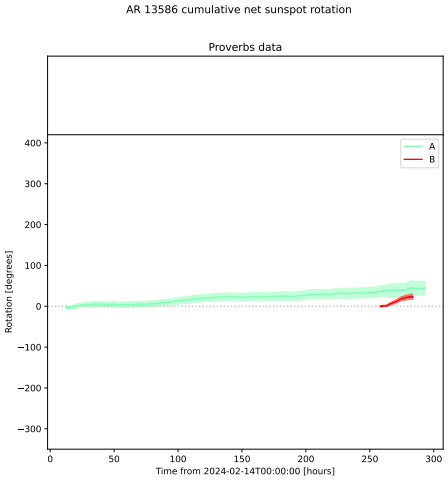

(clxxxv) AR 13586

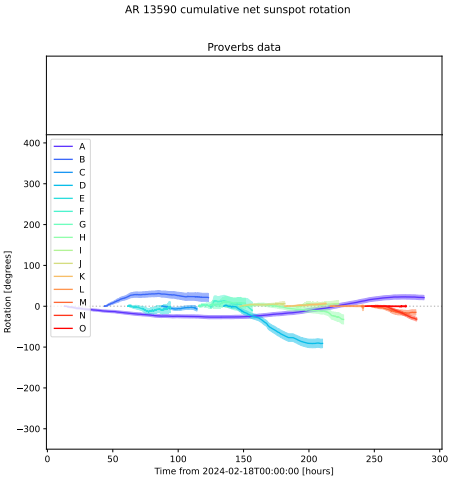

(clxxxvi) AR 13590

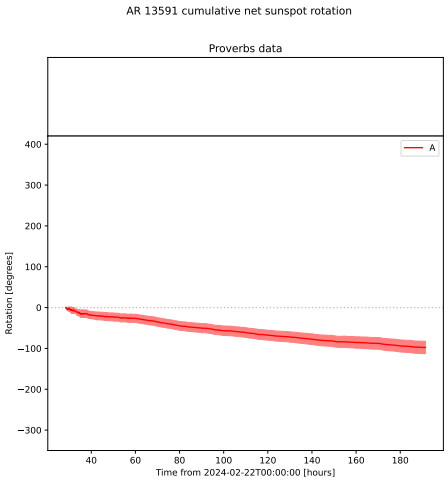

(clxxxvii) AR 13591

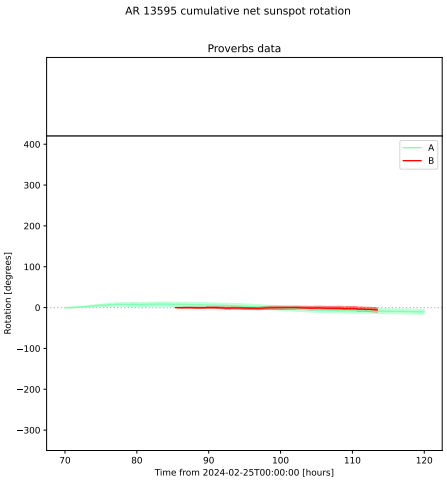

(clxxxviii) AR 13595

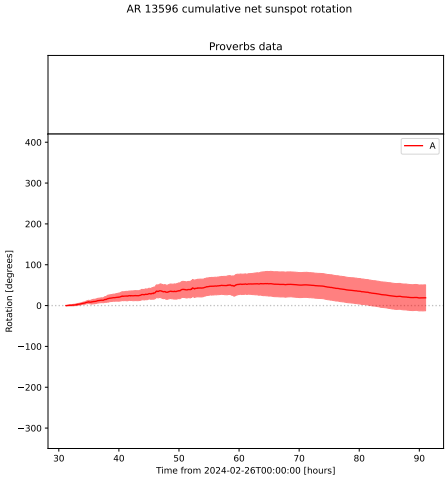

(clxxxix) AR 13596

B.2 Data Tables

Table B.1: Active regions with their first and final observation times, the number of sunspots visible (N_S),the net, mid and absolute rotation (degrees), and the number of flares associated with the active region.

AR	Start Time	End Time	N_S	Sunspot Rot (°)			Flare		
				R_{net}	R_{mid}	R_{abs}	C	M	X
13234	28-Feb-2023 23:59	4-Mar-2023 04:38	3	71.24	155.42	196.09	2	1	0
13238	28-Feb-2023 23:59	7-Mar-2023 15:29	1	-25.97	55.79	85.62	0	0	0
13239	28-Feb-2023 23:59	12-Mar-2023 05:14	2	-65.04	104.33	143.62	0	0	0
13241	1-Mar-2023 15:14	10-Mar-2023 21:53	1	-261.47	276.31	291.16	3	0	0
13242	1-Mar-2023 22:59	13-Mar-2023 14:47	1	253.35	280.22	307.08	5	0	0
13243	5-Mar-2023 05:29	6-Mar-2023 14:38	1	-63.08	67.66	72.23	0	1	0
13245	3-Mar-2023 02:56	16-Mar-2023 11:26	2	-163.05	257.49	310.22	5	0	0
13246	6-Mar-2023 08:41	10-Mar-2023 12:02	1	-37.38	62.58	87.78	0	0	0
13247	6-Mar-2023 08:59	14-Mar-2023 09:32	1	61.4	91.17	120.95	0	0	0
13249	7-Mar-2023 20:56	13-Mar-2023 06:08	1	-7.04	53.2	99.35	0	0	0
13251	9-Mar-2023 00:26	18-Mar-2023 13:17	1	138.14	162.57	187.01	0	0	0
13256	16-Mar-2023 16:59	30-Mar-2023 01:35	2	-97.75	126.11	154.47	7	0	0
13257	18-Mar-2023 10:32	29-Mar-2023 03:35	4	-169.33	228.16	286.98	0	0	0
13258	24-Mar-2023 19:23	26-Mar-2023 17:47	1	48.68	48.72	48.75	0	0	0
13260	19-Mar-2023 06:08	30-Mar-2023 22:53	2	170.85	208.8	241.54	0	0	0
13262	22-Mar-2023 08:29	2-Apr-2023 21:38	3	-152.43	206.84	261.24	2	0	0
13263	23-Mar-2023 21:23	28-Mar-2023 18:44	2	128.93	170.0	211.08	0	0	0
13264	24-Mar-2023 15:23	1-Apr-2023 06:44	1	-5.41	44.06	82.72	0	0	0
13265	27-Mar-2023 10:11	1-Apr-2023 00:23	2	4.53	68.71	110.78	0	0	0

Continued on next page

Table B.1 - Continued from previous page

AR	Start Time	End Time	N_S	Sunspot Rot (°)			Flare		
				R_{net}	R_{mid}	R_{abs}	C	M	X
13270	2-Apr-2023 18:08	8-Apr-2023 15:50	3	-30.54	128.04	172.55	0	0	0
13272	6-Apr-2023 02:41	14-Apr-2023 13:56	6	47.28	249.4	359.0	4	0	0
13273	9-Apr-2023 12:59	12-Apr-2023 21:11	1	-75.22	94.48	113.74	1	0	0
13275	10-Apr-2023 02:08	14-Apr-2023 16:23	1	14.16	43.8	73.43	0	0	0
13279	12-Apr-2023 12:47	16-Apr-2023 23:29	2	14.51	94.0	109.98	3	0	0
13280	14-Apr-2023 05:41	17-Apr-2023 22:08	1	-11.18	30.57	49.96	0	0	0
13281	12-Apr-2023 21:02	19-Apr-2023 02:59	3	156.67	234.03	311.4	1	0	0
13282	13-Apr-2023 21:02	24-Apr-2023 15:38	6	28.32	364.29	520.04	7	0	0
13285	20-Apr-2023 18:44	3-May-2023 01:14	3	10.98	106.27	160.72	0	0	0
13288	24-Apr-2023 17:05	4-May-2023 00:38	5	-220.06	312.59	394.05	4	1	0
13289	25-Apr-2023 18:59	1-May-2023 23:02	2	-59.35	76.54	93.74	1	0	0
13293	30-Apr-2023 23:26	7-May-2023 04:26	3	-38.98	180.88	233.19	2	0	0
13294	1-May-2023 21:20	13-May-2023 21:32	3	47.27	121.89	193.12	0	0	0
13296	2-May-2023 17:44	12-May-2023 10:47	8	-460.6	500.1	539.6	6	1	0
13297	2-May-2023 12:05	14-May-2023 19:56	7	8.63	212.44	275.73	1	0	0
13299	5-May-2023 05:44	6-May-2023 18:32	1	-5.04	20.97	36.9	0	0	0
13301	9-May-2023 15:56	12-May-2023 05:59	3	-21.67	67.88	84.18	0	0	0
13302	9-May-2023 12:59	21-May-2023 02:44	1	-26.27	101.32	176.38	0	0	0
13305	16-May-2023 08:35	21-May-2023 23:35	3	191.36	272.09	284.52	0	0	0
13310	16-May-2023 22:02	30-May-2023 09:53	5	147.22	198.18	246.71	1	0	0
13311	18-May-2023 16:17	29-May-2023 21:14	7	290.95	423.92	498.99	10	2	0
13313	19-May-2023 06:56	31-May-2023 10:44	2	147.91	201.62	255.33	0	0	0

Continued on next page

Table B.1 - Continued from previous page

AR	Start Time	End Time	N_S	Sunspot Rot (°)			Flare		
				R_{net}	R_{mid}	R_{abs}	C	M	X
13314	18-May-2023 20:38	29-May-2023 17:47	1	31.23	136.78	242.32	1	1	0
13315	24-May-2023 10:38	2-Jun-2023 18:59	12	-80.75	323.18	417.53	4	2	0
13318	29-May-2023 09:02	2-Jun-2023 17:50	3	117.46	169.74	186.93	0	0	0
13319	30-May-2023 09:05	4-Jun-2023 20:50	4	39.5	176.92	265.06	0	0	0
13320	29-May-2023 21:53	6-Jun-2023 03:59	1	133.23	146.5	159.78	0	0	0
13321	29-May-2023 14:53	11-Jun-2023 14:56	5	47.06	124.76	180.89	0	0	0
13323	31-May-2023 02:56	5-Jun-2023 17:32	5	-151.82	261.65	371.49	0	0	0
13325	2-Jun-2023 17:56	4-Jun-2023 12:53	1	57.15	72.02	86.9	0	0	0
13326	3-Jun-2023 02:56	14-Jun-2023 22:05	1	66.77	98.46	130.15	0	0	0
13327	6-Jun-2023 22:53	9-Jun-2023 12:32	1	0.46	39.66	78.86	6	0	0
13329	7-Jun-2023 07:11	14-Jun-2023 02:53	2	87.48	97.97	108.46	0	0	0
13331	6-Jun-2023 13:14	17-Jun-2023 14:20	4	80.55	174.49	250.72	1	0	0
13333	13-Jun-2023 19:26	21-Jun-2023 20:14	3	179.67	189.79	199.91	0	0	0
13335	14-Jun-2023 20:05	25-Jun-2023 14:44	5	60.0	136.38	198.07	4	0	0
13338	15-Jun-2023 18:47	22-Jun-2023 12:20	2	-86.74	161.32	205.58	1	0	0
13339	16-Jun-2023 19:53	28-Jun-2023 06:50	3	5.23	105.01	159.27	0	0	0
13340	18-Jun-2023 17:20	26-Jun-2023 21:02	4	80.81	237.98	274.27	5	1	0
13341	19-Jun-2023 03:32	25-Jun-2023 15:47	2	57.29	79.9	102.51	4	1	0
13342	20-Jun-2023 04:23	22-Jun-2023 05:11	1	50.65	64.35	78.06	1	2	0
13354	26-Jun-2023 19:14	5-Jul-2023 20:29	12	88.59	1041.99	1224.22	5	0	0
13357	2-Jul-2023 13:29	3-Jul-2023 14:59	1	-12.85	16.33	19.81	0	0	0
13359	2-Jul-2023 04:23	7-Jul-2023 18:08	3	73.91	130.5	145.45	3	0	0

Continued on next page

Table B.1 - Continued from previous page

AR	Start Time	End Time	N_S	Sunspot Rot (°)			Flare		
				R_{net}	R_{mid}	R_{abs}	C	M	X
13360	2-Jul-2023 01:11	4-Jul-2023 07:44	1	94.71	95.26	95.82	4	0	0
13361	4-Jul-2023 14:26	14-Jul-2023 15:17	4	-31.13	251.0	315.14	1	0	0
13362	4-Jul-2023 16:59	10-Jul-2023 03:17	2	27.26	57.08	85.64	0	0	0
13363	5-Jul-2023 20:38	18-Jul-2023 22:41	7	-135.98	235.07	314.19	9	3	0
13366	8-Jul-2023 12:44	13-Jul-2023 00:35	2	72.45	91.44	110.42	1	0	0
13367	9-Jul-2023 03:23	14-Jul-2023 11:08	2	-139.7	168.37	197.04	1	0	0
13369	9-Jul-2023 06:05	11-Jul-2023 01:26	1	-73.78	73.39	72.99	0	0	0
13371	10-Jul-2023 19:23	16-Jul-2023 12:50	1	-58.37	83.13	107.89	0	0	0
13372	11-Jul-2023 10:59	24-Jul-2023 11:53	10	69.92	219.9	273.35	4	2	0
13373	14-Jul-2023 02:17	26-Jul-2023 02:59	11	15.31	397.1	585.7	7	0	0
13376	18-Jul-2023 08:11	27-Jul-2023 10:17	4	-195.07	261.18	313.33	5	1	0
13377	17-Jul-2023 04:11	29-Jul-2023 19:14	5	-187.2	290.37	393.54	0	0	0
13378	22-Jul-2023 07:05	23-Jul-2023 10:17	1	40.47	40.31	40.15	0	0	0
13379	18-Jul-2023 15:41	31-Jul-2023 06:38	5	90.35	149.86	209.37	1	0	0
13380	23-Jul-2023 08:08	4-Aug-2023 12:35	7	-81.14	291.68	368.27	11	5	0
13385	26-Jul-2023 00:23	27-Jul-2023 16:11	1	-64.92	75.05	85.17	0	0	0
13386	26-Jul-2023 17:56	6-Aug-2023 22:38	4	-347.41	421.28	431.38	1	2	0
13387	27-Jul-2023 08:26	8-Aug-2023 15:05	3	143.74	230.03	316.32	2	0	0
13388	27-Jul-2023 11:26	3-Aug-2023 23:26	1	70.24	157.39	244.54	0	0	0
13389	27-Jul-2023 12:17	31-Jul-2023 13:53	1	18.77	43.94	69.12	1	0	0
13391	29-Jul-2023 08:38	10-Aug-2023 19:29	2	132.63	158.9	185.17	0	0	0
13392	1-Aug-2023 08:17	8-Aug-2023 13:53	5	-139.1	159.13	179.17	0	0	0

Continued on next page

Table B.1 - Continued from previous page

AR	Start Time	End Time	N_S	Sunspot Rot (°)			Flare		
				R_{net}	R_{mid}	R_{abs}	C	M	X
13394	2-Aug-2023 09:14	15-Aug-2023 04:11	1	-84.01	99.27	114.52	2	0	0
13395	3-Aug-2023 09:14	13-Aug-2023 18:32	2	134.1	180.38	226.67	4	0	0
13397	12-Aug-2023 19:38	16-Aug-2023 22:47	3	-11.73	122.7	225.3	1	0	0
13403	13-Aug-2023 20:47	22-Aug-2023 15:02	6	16.64	163.32	224.92	1	0	0
13404	14-Aug-2023 08:08	17-Aug-2023 12:56	1	-7.72	29.38	51.03	0	0	0
13405	14-Aug-2023 07:50	26-Aug-2023 21:47	4	129.02	250.47	367.44	5	0	0
13407	15-Aug-2023 14:05	21-Aug-2023 17:59	5	39.01	98.55	154.76	0	0	0
13411	15-Aug-2023 18:38	27-Aug-2023 14:23	1	183.28	198.76	214.25	0	0	0
13412	18-Aug-2023 03:56	29-Aug-2023 06:20	1	23.34	74.19	125.03	0	0	0
13413	20-Aug-2023 17:02	2-Sep-2023 17:26	6	-183.4	272.65	317.42	2	1	0
13415	22-Aug-2023 03:08	4-Sep-2023 02:29	4	-125.62	339.59	458.08	1	0	0
13416	25-Aug-2023 14:26	30-Aug-2023 17:29	1	40.84	75.98	111.11	0	0	0
13417	28-Aug-2023 14:56	5-Sep-2023 19:20	2	-132.74	171.42	210.11	1	0	0
13421	4-Sep-2023 02:23	8-Sep-2023 12:32	3	67.21	84.81	102.42	4	1	0
13423	6-Sep-2023 11:50	15-Sep-2023 09:41	7	-143.54	251.94	354.03	4	1	0
13425	10-Sep-2023 15:50	18-Sep-2023 18:32	2	63.53	113.01	121.59	3	0	0
13429	15-Sep-2023 17:32	21-Sep-2023 00:02	1	67.2	104.41	141.62	2	1	0
13430	14-Sep-2023 02:59	15-Sep-2023 15:50	1	4.56	19.55	34.53	0	0	0
13433	11-Sep-2023 04:47	23-Sep-2023 23:32	3	100.7	131.25	161.8	0	0	0
13435	16-Sep-2023 16:41	29-Sep-2023 11:23	7	-463.84	502.12	540.39	0	0	0
13437	18-Sep-2023 07:20	23-Sep-2023 09:56	2	119.74	179.11	238.48	0	0	0
13438	17-Sep-2023 01:05	20-Sep-2023 20:11	1	58.16	70.98	83.81	0	0	0

Continued on next page

Table B.1 - Continued from previous page

AR	Start Time	End Time	N_S	Sunspot Rot (°)			Flare		
				R_{net}	R_{mid}	R_{abs}	C	M	X
13440	18-Sep-2023 23:17	26-Sep-2023 06:53	1	38.66	59.66	80.67	0	0	0
13442	19-Sep-2023 20:20	23-Sep-2023 07:47	1	88.06	87.56	87.07	0	0	0
13443	21-Sep-2023 10:08	27-Sep-2023 00:41	6	68.82	339.34	445.42	1	0	0
13445	26-Sep-2023 12:50	30-Sep-2023 18:23	1	74.37	78.64	82.92	6	0	0
13447	25-Sep-2023 06:29	2-Oct-2023 07:26	2	-196.26	216.88	237.5	0	0	0
13448	25-Sep-2023 03:23	5-Oct-2023 05:29	2	-35.06	83.37	120.17	0	0	0
13449	27-Sep-2023 12:02	1-Oct-2023 20:50	2	-0.81	47.08	80.63	3	0	0
13450	28-Sep-2023 19:05	4-Oct-2023 21:29	2	-194.39	218.88	243.37	8	0	0
13451	2-Oct-2023 02:14	11-Oct-2023 19:32	3	-43.22	157.02	270.82	6	0	0
13452	1-Oct-2023 04:50	7-Oct-2023 06:35	4	115.22	144.28	173.35	1	0	0
13454	6-Oct-2023 18:11	11-Oct-2023 20:47	1	-160.62	169.04	177.47	0	0	0
13460	7-Oct-2023 20:14	16-Oct-2023 02:59	2	-125.35	241.85	272.07	4	0	0
13464	11-Oct-2023 01:47	21-Oct-2023 10:05	2	136.03	164.3	192.57	1	0	0
13465	10-Oct-2023 21:29	18-Oct-2023 18:59	4	120.62	203.15	285.69	0	0	0
13474	29-Oct-2023 17:14	5-Nov-2023 14:35	3	-39.82	151.4	233.31	1	0	0
13477	31-Oct-2023 13:35	13-Nov-2023 21:08	7	-149.51	248.74	315.58	0	0	0
13480	3-Nov-2023 06:50	6-Nov-2023 08:44	2	-0.69	43.65	76.14	1	0	0
13483	8-Nov-2023 19:17	14-Nov-2023 11:11	3	48.25	94.81	130.14	1	0	0
13485	12-Nov-2023 08:08	14-Nov-2023 01:26	1	46.99	60.43	73.86	0	0	0
13486	12-Nov-2023 11:35	17-Nov-2023 23:17	3	10.5	85.81	133.77	0	0	0
13489	17-Nov-2023 13:38	21-Nov-2023 05:41	2	-14.39	126.12	187.1	0	0	0
13490	19-Nov-2023 01:47	26-Nov-2023 17:08	3	125.12	279.6	311.62	2	0	0

Continued on next page

Table B.1 - Continued from previous page

AR	Start Time	End Time	N_S	Sunspot Rot (°)			Flare		
				R_{net}	R_{mid}	R_{abs}	C	M	X
13491	19-Nov-2023 07:11	24-Nov-2023 10:44	1	-42.4	57.05	71.71	0	0	0
13492	19-Nov-2023 09:56	2-Dec-2023 00:32	2	47.7	247.44	381.2	0	0	0
13493	20-Nov-2023 19:50	28-Nov-2023 22:14	1	-200.17	202.02	203.86	0	0	0
13494	20-Nov-2023 13:41	2-Dec-2023 02:41	1	-63.96	108.09	152.21	0	0	0
13498	21-Nov-2023 10:35	23-Nov-2023 16:38	1	-59.19	70.08	80.98	0	0	0
13499	23-Nov-2023 01:11	25-Nov-2023 05:14	1	-25.03	47.38	69.74	0	0	0
13500	22-Nov-2023 11:38	3-Dec-2023 20:50	8	-100.52	800.68	979.61	0	0	0
13501	23-Nov-2023 06:38	3-Dec-2023 01:26	1	-115.45	140.37	165.29	0	0	0
13502	23-Nov-2023 07:35	26-Nov-2023 22:20	1	54.16	57.16	60.15	0	0	0
13505	29-Nov-2023 02:14	5-Dec-2023 23:17	1	31.71	65.47	99.22	0	0	0
13507	28-Nov-2023 15:17	11-Dec-2023 03:14	1	-17.67	68.61	119.56	0	0	0
13508	28-Nov-2023 18:38	10-Dec-2023 05:35	1	54.94	95.91	136.88	0	0	0
13509	1-Dec-2023 13:02	3-Dec-2023 05:26	2	31.79	56.52	81.25	0	0	0
13510	3-Dec-2023 07:53	7-Dec-2023 06:23	3	82.72	132.15	181.58	1	0	0
13511	4-Dec-2023 09:29	11-Dec-2023 06:50	3	-120.92	244.51	336.45	2	0	0
13513	6-Dec-2023 18:26	16-Dec-2023 20:05	2	-96.46	157.1	194.47	1	0	0
13514	11-Dec-2023 22:05	16-Dec-2023 10:26	4	45.32	168.47	224.22	1	0	0
13516	8-Dec-2023 17:47	11-Dec-2023 22:26	1	39.45	56.13	72.81	0	0	0
13519	13-Dec-2023 04:53	20-Dec-2023 22:20	2	-4.91	112.17	199.25	3	0	0
13520	13-Dec-2023 22:35	17-Dec-2023 03:47	1	31.54	46.94	62.33	0	0	0
13521	19-Dec-2023 22:17	23-Dec-2023 22:32	1	-21.78	46.86	71.93	1	0	0
13526	23-Dec-2023 02:11	24-Dec-2023 17:53	1	24.95	28.69	32.44	0	0	0

Continued on next page

Table B.1 - Continued from previous page

AR	Start Time	End Time	N_S	Sunspot Rot (°)			Flare		
				R_{net}	R_{mid}	R_{abs}	C	M	X
13527	18-Dec-2023 07:20	19-Dec-2023 12:17	1	-80.64	81.61	82.58	0	0	0
13528	18-Dec-2023 21:14	25-Dec-2023 20:08	3	14.25	219.87	288.62	1	0	0
13529	18-Dec-2023 03:05	29-Dec-2023 03:23	10	80.65	349.38	442.99	0	0	0
13530	25-Dec-2023 05:05	26-Dec-2023 16:59	2	-13.25	45.39	77.53	4	0	0
13531	19-Dec-2023 21:02	1-Jan-2024 19:05	2	40.93	124.52	205.68	1	0	0
13533	28-Dec-2023 11:35	29-Dec-2023 16:53	1	27.14	32.35	37.57	1	0	0
13536	31-Dec-2023 22:35	8-Jan-2024 04:56	3	306.92	329.46	351.99	46	6	1
13537	2-Jan-2024 18:08	6-Jan-2024 10:02	1	8.7	28.49	48.27	6	0	0
13539	11-Jan-2024 06:41	12-Jan-2024 11:02	1	-7.6	9.2	10.79	13	1	0
13540	5-Jan-2024 15:14	14-Jan-2024 10:50	4	75.36	144.18	208.42	13	0	0
13541	10-Jan-2024 17:02	15-Jan-2024 21:23	2	-61.43	73.75	86.07	13	0	0
13543	8-Jan-2024 09:20	10-Jan-2024 14:11	1	13.19	35.68	58.17	0	0	0
13545	9-Jan-2024 12:02	21-Jan-2024 10:26	10	21.26	180.64	264.9	2	0	0
13549	13-Jan-2024 08:56	23-Jan-2024 17:08	13	-16.29	105.29	170.71	4	0	0
13553	13-Jan-2024 10:50	15-Jan-2024 14:50	2	-11.04	25.53	40.02	3	0	0
13554	15-Jan-2024 14:53	17-Jan-2024 11:32	1	-0.39	12.67	24.94	0	0	0
13555	15-Jan-2024 00:14	26-Jan-2024 05:47	2	139.08	167.36	195.64	1	0	0
13556	16-Jan-2024 20:05	22-Jan-2024 15:47	2	-2.93	38.16	57.34	0	0	0
13559	18-Jan-2024 23:38	29-Jan-2024 10:23	9	489.15	607.46	697.11	38	6	0
13560	26-Jan-2024 19:08	27-Jan-2024 22:20	1	0.82	6.53	12.24	5	0	0
13561	24-Jan-2024 13:53	25-Jan-2024 13:56	1	12.62	14.74	16.86	30	14	0
13562	21-Jan-2024 02:02	22-Jan-2024 04:17	1	-22.48	23.22	23.96	0	0	0

Continued on next page

Table B.1 - Continued from previous page

AR	Start Time	End Time	N_S	Sunspot Rot (°)			Flare		
				R_{net}	R_{mid}	R_{abs}	C	M	X
13564	6-Feb-2024 13:20	7-Feb-2024 21:26	1	-5.06	14.95	24.84	1	1	0
13565	29-Jan-2024 17:14	31-Jan-2024 00:53	1	9.85	18.63	27.42	7	0	0
13571	31-Jan-2024 08:35	12-Feb-2024 05:35	2	0.65	104.2	165.29	10	1	0
13573	1-Feb-2024 08:50	4-Feb-2024 03:38	1	21.74	69.0	116.27	1	0	0
13574	2-Feb-2024 13:56	7-Feb-2024 14:38	2	-31.62	64.45	82.99	1	0	0
13575	3-Feb-2024 08:29	8-Feb-2024 03:44	3	-50.25	87.27	124.29	13	5	1
13576	3-Feb-2024 14:50	15-Feb-2024 15:44	19	-29.33	558.76	670.86	98	23	1
13581	8-Feb-2024 08:08	17-Feb-2024 20:56	2	54.89	77.15	99.4	0	0	0
13582	12-Feb-2024 19:59	14-Feb-2024 00:02	1	-2.96	7.44	11.92	2	1	0
13583	10-Feb-2024 22:26	19-Feb-2024 12:59	8	28.17	168.31	213.2	19	0	0
13584	10-Feb-2024 22:56	14-Feb-2024 04:23	1	-24.66	49.4	74.14	5	0	0
13586	14-Feb-2024 12:02	26-Feb-2024 05:17	2	67.54	95.05	122.57	2	0	0
13590	18-Feb-2024 12:59	29-Feb-2024 23:59	15	-125.31	375.72	488.46	58	10	3
13591	23-Feb-2024 04:26	29-Feb-2024 23:23	1	-97.54	97.66	97.79	0	0	0
13595	27-Feb-2024 21:56	29-Feb-2024 23:59	2	-16.28	28.26	40.24	3	0	0
13596	27-Feb-2024 07:11	29-Feb-2024 19:02	1	19.04	58.34	97.65	2	0	0

Table B.2: Active regions with the calculated energy due to net, mid, and absolute sunspot rotation (E_{net}, E_{mid}, E_{abs}, respectively, in ergs. The calculated flare energy (ergs) is also presented per active region.

AR	Rot. Energy (10^{32} erg)			Flare Energy
	E_{net}	E_{mid}	E_{abs}	(10^{32} erg)
13234	-0.397	1.35	2.371	0.135
13238	-0.033	0.077	0.123	0.0
13239	-0.485	0.819	1.169	0.0
13241	-0.229	0.244	0.258	0.075
13242	2.449	2.74	3.035	0.052
13243	-0.03	0.033	0.035	0.026
13245	-4.9	5.941	6.777	0.204
13246	-0.02	0.035	0.051	0.0
13247	0.061	0.095	0.13	0.0
13249	-0.002	0.023	0.046	0.0
13251	0.108	0.129	0.151	0.0
13256	-3.287	4.24	5.216	0.123
13257	-1.02	1.379	1.749	0.0
13258	0.058	0.058	0.058	0.0
13260	2.294	2.722	3.144	0.0
13262	-0.39	0.554	0.723	0.028
13263	0.019	0.023	0.027	0.0
13264	-0.005	0.057	0.114	0.0
13265	0.003	0.028	0.048	0.0
13270	-0.033	0.327	0.472	0.0

Continued on next page

Table B.2 - Continued from previous page

AR	Rot. Energy (10^{32} erg)			Flare Energy
	E_{net}	E_{mid}	E_{abs}	(10^{32} erg)
13272	-0.015	0.098	0.165	0.081
13273	-0.065	0.084	0.103	1.651
13275	0.009	0.033	0.059	0.0
13279	-0.008	0.11	0.127	0.118
13280	-0.097	0.299	0.517	0.0
13281	0.333	0.521	0.716	0.066
13282	-1.018	4.625	7.242	0.211
13285	0.05	0.732	1.181	0.0
13288	-1.579	2.408	3.136	0.254
13289	-0.107	0.144	0.183	0.019
13293	-0.362	0.548	0.625	0.063
13294	0.34	0.87	1.43	0.0
13296	-1.298	1.409	1.521	0.593
13297	2.031	4.325	5.882	0.053
13299	-0.0	0.001	0.003	0.0
13301	-0.125	0.327	0.414	0.0
13302	-0.045	0.202	0.375	0.0
13305	0.412	0.515	0.538	0.0
13310	11.25	15.827	20.475	0.007
13311	0.417	0.584	0.742	0.415
13313	0.618	0.832	1.052	0.0
13314	0.062	0.321	0.607	0.075

Continued on next page

Table B.2 - Continued from previous page

AR	Rot. Energy (10^{32} erg)			Flare Energy
	E_{net}	E_{mid}	E_{abs}	(10^{32} erg)
13315	0.256	5.933	7.809	0.107
13318	0.334	0.384	0.413	0.0
13319	-0.086	1.131	2.011	0.0
13320	0.07	0.078	0.086	0.0
13321	1.113	2.721	4.146	0.0
13323	-0.5	0.68	0.874	0.0
13325	0.008	0.011	0.013	0.0
13326	0.253	0.389	0.531	0.0
13327	0.0	0.005	0.01	2.615
13329	0.262	0.28	0.299	0.0
13331	0.174	0.649	1.018	0.078
13333	0.188	0.199	0.21	0.0
13335	0.88	1.701	2.513	0.083
13338	-0.322	0.384	0.432	0.072
13339	0.001	0.477	0.756	0.0
13340	0.221	0.37	0.433	0.189
13341	0.288	0.418	0.553	0.173
13342	0.106	0.138	0.171	0.091
13354	-5.863	8.353	9.478	0.102
13357	-0.008	0.011	0.013	0.0
13359	0.22	0.319	0.366	0.114
13360	0.033	0.033	0.033	0.58

Continued on next page

Table B.2 - Continued from previous page

AR	Rot. Energy (10^{32} erg)			Flare Energy
	E_{net}	E_{mid}	E_{abs}	(10^{32} erg)
13361	0.555	1.459	1.921	0.062
13362	0.014	0.032	0.052	0.0
13363	-24.698	33.041	41.639	0.889
13366	0.471	0.642	0.819	0.076
13367	-0.185	0.216	0.248	0.057
13369	-0.022	0.022	0.021	0.0
13371	-0.03	0.045	0.06	0.0
13372	5.163	7.974	9.919	0.713
13373	-0.252	1.647	2.675	0.558
13376	-0.899	1.125	1.339	0.405
13377	-1.831	2.919	4.055	0.0
13378	0.032	0.032	0.032	0.0
13379	1.906	3.172	4.497	0.09
13380	-0.504	1.047	1.394	1.691
13385	-0.003	0.004	0.004	0.0
13386	-14.104	14.398	14.556	1.985
13387	0.233	0.473	0.727	0.122
13388	0.007	0.018	0.03	0.0
13389	0.02	0.053	0.087	0.033
13391	0.745	0.884	1.025	0.0
13392	-0.576	0.655	0.736	0.0
13394	-2.823	3.401	3.988	0.045

Continued on next page

Table B.2 - Continued from previous page

AR	Rot. Energy (10^{32} erg)			Flare Energy
	E_{net}	E_{mid}	E_{abs}	(10^{32} erg)
13395	0.167	0.25	0.336	0.123
13397	-0.011	0.069	0.13	0.127
13403	-0.031	0.91	1.358	0.093
13404	-0.003	0.012	0.022	0.0
13405	0.458	1.382	2.369	0.301
13407	0.162	0.422	0.698	0.0
13411	0.292	0.32	0.347	0.0
13412	0.037	0.133	0.239	0.0
13413	-9.83	12.214	14.27	0.435
13415	-1.679	3.634	5.003	0.113
13416	0.015	0.029	0.045	0.0
13417	-0.14	0.164	0.189	0.498
13421	0.166	0.183	0.2	1.287
13423	-0.816	2.061	3.374	0.392
13425	0.02	0.032	0.035	0.164
13429	0.049	0.081	0.113	0.283
13430	0.002	0.008	0.015	0.0
13433	0.451	0.588	0.73	0.0
13435	-5.948	6.457	6.973	0.0
13437	0.284	0.531	0.791	0.0
13438	0.022	0.027	0.032	0.0
13440	0.061	0.098	0.138	0.0

Continued on next page

Table B.2 - Continued from previous page

AR	Rot. Energy (10^{32} erg)			Flare Energy
	E_{net}	E_{mid}	E_{abs}	(10^{32} erg)
13442	0.023	0.023	0.023	0.0
13443	0.037	0.478	0.727	0.146
13445	0.247	0.263	0.279	0.241
13447	-0.398	0.443	0.488	0.0
13448	-0.192	0.382	0.564	0.0
13449	-0.002	0.022	0.04	0.105
13450	-0.199	0.228	0.256	0.231
13451	-0.189	0.354	0.536	nan
13452	0.103	0.138	0.175	0.004
13454	-0.048	0.051	0.054	0.0
13460	-0.136	0.269	0.307	0.517
13464	0.124	0.193	0.265	1.715
13465	0.68	1.353	2.096	0.0
13474	-0.253	1.054	1.727	0.066
13477	-4.475	6.368	8.341	0.0
13480	-0.009	0.058	0.11	0.336
13483	0.613	1.371	2.0	0.047
13485	0.088	0.116	0.145	0.0
13486	0.043	0.148	0.238	0.0
13489	0.0	0.024	0.038	0.0
13490	0.337	0.505	0.579	0.21
13491	-0.046	0.064	0.083	0.0

Continued on next page

Table B.2 - Continued from previous page

AR	Rot. Energy (10^{32} erg)			Flare Energy
	E_{net}	E_{mid}	E_{abs}	(10^{32} erg)
13492	0.151	1.653	2.751	0.0
13493	-0.493	0.498	0.503	0.0
13494	-0.154	0.276	0.405	0.0
13498	-0.012	0.014	0.016	0.0
13499	-0.004	0.007	0.011	0.0
13500	-1.084	2.365	2.921	0.0
13501	-0.163	0.203	0.244	0.0
13502	0.165	0.175	0.185	0.0
13505	0.021	0.047	0.075	0.0
13507	-0.186	0.845	1.569	0.0
13508	0.211	0.393	0.585	0.0
13509	0.015	0.03	0.047	0.0
13510	0.033	0.048	0.063	0.055
13511	-0.118	0.487	0.822	0.016
13513	-0.328	0.485	0.601	0.003
13514	0.18	0.49	0.673	0.009
13516	0.03	0.045	0.06	0.0
13519	-0.008	0.187	0.355	0.309
13520	0.03	0.046	0.064	0.0
13521	-0.018	0.042	0.068	0.061
13526	0.005	0.005	0.006	0.0
13527	-0.014	0.014	0.014	0.0

Continued on next page

Table B.2 - Continued from previous page

AR	Rot. Energy (10^{32} erg)			Flare Energy
	E_{net}	E_{mid}	E_{abs}	(10^{32} erg)
13528	-0.119	0.545	0.769	0.021
13529	3.609	6.02	7.393	0.0
13530	-0.001	0.003	0.004	0.186
13531	0.493	1.636	2.858	0.045
13533	0.011	0.013	0.016	0.011
13536	0.22	0.319	0.423	4.624
13537	0.006	0.021	0.038	0.807
13539	-0.017	0.022	0.026	1.092
13540	0.36	0.463	0.568	0.926
13541	-0.096	0.115	0.135	nan
13543	0.008	0.025	0.043	0.0
13545	0.781	2.119	3.109	0.113
13549	-0.327	1.666	2.806	0.89
13553	-0.051	0.183	0.327	0.373
13554	-0.0	0.01	0.021	0.0
13555	0.399	0.493	0.589	0.461
13556	-0.014	0.058	0.093	0.0
13559	3.381	4.18	4.773	4.134
13560	0.0	0.004	0.008	0.615
13561	0.01	0.012	0.014	3.717
13562	-0.006	0.006	0.006	0.0
13564	-0.004	0.012	0.022	0.085

Continued on next page

Table B.2 - Continued from previous page

AR	Rot. Energy (10^{32} erg)			Flare Energy
	E_{net}	E_{mid}	E_{abs}	(10^{32} erg)
13565	0.006	0.012	0.019	0.939
13571	-0.152	0.809	1.432	0.186
13573	0.001	0.005	0.008	0.088
13574	-0.034	0.044	0.052	0.103
13575	-0.629	1.205	1.812	3.309
13576	-1.279	6.255	8.449	8.941
13581	0.133	0.183	0.235	0.0
13582	-0.004	0.01	0.018	0.194
13583	-0.076	0.795	0.986	3.226
13584	-0.004	0.008	0.013	0.445
13586	0.414	0.662	0.922	0.408
13590	6.392	20.404	33.09	7.521
13591	-0.337	0.337	0.338	0.0
13595	-0.145	0.289	0.442	0.374
13596	0.004	0.014	0.025	0.017